Synthesis and characterization of Sn-based electrolytes for F-ion batteries

Briséïs Mercadier

To cite this version:

Briséïs Mercadier. Synthesis and characterization of Sn-based electrolytes for F-ion batteries. Analytical chemistry. Sorbonne Université, 2023. English. NNT : 2023SORUS686 . tel-04550062

HAL Id: tel-04550062
https://theses.hal.science/tel-04550062v1

Submitted on 17 Apr 2024

Thèse de Doctorat

Mention : Chimie
Spécialité : Chimie des Solides et Science de Matériaux

présentée à ***l'Ecole Doctorale en Chimie Physique et Chimie Analytique Paris centre (ED388)***

de Sorbonne Université

par

Briséïs Mercadier

Le 17 octobre 2023

pour obtenir le grade de Docteur de Sorbonne Université

Synthesis and characterization of Sn-based electrolytes for F-ion batteries

D. Carlier, Professeur, Université de Bordeaux	**Rapporteure**
P. Rozier, MC, HDR, Université de Toulouse	**Rapporteur**
A. Demourgues, Directeur de Recherche, Université de Bordeaux	**Président du Jury**
S. Mariyappan, Chargée de recherche, CNRS	**Examinatrice**
R. Dominko, Professeur, National Institute of Chemistry	**Examinateur**
M. Morcrette, Directeur de recherche, CNRS	**Examinateur**
D. Dambournet, MC, HDR, Sorbonne Université	**Directeur de thèse**
C. Masquelier, Professeur, UPJV, Amiens	**Directeur de thèse**

Acknowledgements

Ces trois années de thèses ont été un grand plaisir pour moi, tant du point de vue humain que scientifique, et je voudrais donc remercier les personnes qui ont rendu cela possible, à commencer par mes deux directeurs de thèse, Damien et Christian, pour leur disponibilité, leur patience, leur volonté de me donner toutes les opportunités possibles, et leur grande écoute pendant ces 3 ans (3 ans et demi pour Damien !). C'était un vrai plaisir de travailler avec vous et je vous suis très reconnaissante.

Je remercie aussi les membres permanents de PHENIX et du LRCS qui m'ont apporté de l'aide : Sandrine Leclerc, Mathieu Morcrette, Jean-Noël Chotard, Arash Jamali, Virginie Viallet, Raynald Lesieur, José Gomes, Ana-Gabriela Porras-Gutierrez, Anne-Laure Rollet, Vincent Seznec, Loïc Dupont, ainsi que les équipes administratives qui ont permis le bon déroulement de ma thèse (et facilité les nombreux déplacements Paris/Amiens), Gérard Guillard, Brigitte Carrez, Daphné Boursier.

I of course would also like to thank all of the people who collaborated with us on this project, who were a delight to work with and from whom I learned a lot: Samuel Coles and Benjamin Morgan from Bath, Mathieu Duttine from ICMCB, Theodosios Famprikis from the Reactor Institute Delft, Christophe Legein and Monique Body from IMMM.

Je remercie aussi les doctorants et postdocs qui ont pris du temps pour m'aider, en particulier Mickaël, Matheus, Cédric, et Clément.

I am very grateful to my office mates Kriti, Lydia, Kyle, Lucile, and Sunkyu, from both PHENIX and LRCS, who made the (few) difficult times less difficult and the (many) good times even better.

The same goes for all of the colleagues who have become more than just that made during that time. Thank you Noura, Sorina, Fenu, Adolfo, Julien, Julie, Arina, Junghan, Dennis, UV, Iris, Hélène, Darcy, Lucie, Melisa, Eunike, Linh, Dhanush, Nikhil, and everyone else.

Merci aussi à mes amis en dehors du laboratoire, François, Morgane, Allan, Hugues, qui m'ont soutenue pendant ces années.

Un grand merci aussi et bien sûr à ma famille, à ma sœur Kyra, experte Word de renommée mondiale, à mes frères Hector et Darius, ainsi qu'à leurs conjoints Marjorie, Camille et Yegor.

Merci à mes parents, à Caro, à ma chère tante Mania et à tous mes oncles, tantes, cousines et cousins, toujours pleins d'intérêt pour mon travail.

Finally, I wish to thank Matheus, with whom I look forwards to discussing German German Sheperds sheperds until one of us finally decides to learn grammar (and possibly still a little bit after that).

Contents

Bibliographic Introduction ... 7
0.1.General context ... 9
0.2.General principles of battery operation ... 11
0.3.History of Fluoride-ion batteries ... 12
    0.3.1. The early days ... 12
    0.3.2. Re-discovery ... 13
    0.3.3. Recent breakthrough in FIB research ... 18
0.4.Electrolytes for FIB ... 19
    0.4.1. Electrolyte requirements ... 19
    0.4.2. General conduction process ... 21
    0.4.3. Important solid electrolytes for FIB ... 24
0.5.Scope of the thesis ... 30
Chapter I
Dynamic Lone Pairs and Fluoride-Ion Disorder in Cubic-BaSnF$_4$ ... 33
Introduction ... 35
I.1. Methods ... 37
    I.1.1. Synthesis of Cubic BaSnF$_4$ ... 37
    I.1.2. Impedance Spectroscopy ... 37
    I.1.3. X-Ray Diffraction ... 37
    I.1.4. ^{119}Sn Mössbauer Spectroscopy ... 38
    I.1.5. ^{19}F Solid-State NMR ... 38
    I.1.6. Pair-Distribution Functions ... 38
    I.1.7. Molecular-Dynamics Simulations ... 39
I.2. Results and discussion ... 40
    I.2.1. The fluorite structure, cation disorder and stereoactive lone pairs ... 40
    2.2. Fluoride-ion dynamics ... 54
    2.3. Sn lone pair dynamics ... 57
Summary and Conclusions ... 62
Chapter II
Effect of the cation nature in MSnF$_4$ (M = Ba, Sr) on the stereoactivity of tin lone pairs and dynamics of the fluoride-ion sublattice ... 65
Introduction ... 67
II.1. Comparative study: from c-BaSnF$_4$ to c-SrSnF$_4$ ... 68
    II.1.1. Synthesis route of c-SrSnF$_4$ ... 68
    II.1.2. Local structure study of c-SrSnF$_4$ ... 73
    II.1.3 Transport properties evolution with the substitution of barium for strontium in c-MSnF$_4$ ... 79
II.2. A perspective: introducing additional cationic disorder in the Ba$_{1-x}$Sr$_x$SnF$_4$ mixed cation solid solution ... 83

II.2.1. Synthesis of cubic $Ba_{1-x}Sr_xSnF_4$ 83
II.2.2. Conductivity in $Ba_{1-x}Sr_xSnF_4$ 85
Conclusion 87

Chapter III

Synthesis-originated structural variations in t-$BaSnF_4$ 89
Introduction 91
III.1. Revisiting the Ball-milling/high temperature route 92
III.1.1. Methods 92
III.1.2. Results and discussion 93
III.2. A new route to produce $BaSnF_4$: Spark "Plasma" Sintering 95
III.2.1 SPS working principle 96
III.2.2 Methodology of the SPS synthesis 97
III.2.3. SPS synthesis 97
Conclusions 119

Chapter IV

Electrochemical properties of Sn-based solid electrolytes 121
Introduction 123
IV.1. Testing of possible reference electrodes through symmetrical cells 124
IV.1.1. Using tin as a reference electrode in symmetrical cells 125
IV.1.2. Using lithium as a reference electrode in symmetrical cells 129
IV.2. Electrochemical Stability Window (ESW) of $MSnF_4$ 133
IV.2.1. Prediction of the ESW through thermodynamics 133
IV.2.2. Experimental ESW 134
Conclusions and Perspectives 146
Perspective: FIB reference electrode in the litterature 146
Conclusions and perspectives 149
Annexe 1 153
References 159

Bibliographic Introduction

Table of Contents

0.1.General context 9
0.2.General principles of battery operation 11
0.3.History of Fluoride-ion batteries 12
    0.3.1. The early days 12
    0.3.2. Re-discovery 13
        0.3.2.1. Conversion electrodes 14
        0.3.2.2. Insertion electrodes 16
    0.3.3. Recent breakthrough in FIB research 18
0.4.Electrolytes for FIB 19
    0.4.1. Electrolyte requirements 19
    0.4.2. General conduction process 21
        0.4.2.1. Atomic scale transport 21
        0.4.2.2. Particle-scale transport 23
    0.4.3. Important solid electrolytes for FIB 24
        0.4.3.1. $La_{1-x}Ba_xF_{3-x}$ (LBF) 25
        0.4.3.2. Sn-based $MSnF_4$ electrolytes 26
            Structure 26
            Transport mechanism 28
            Doping $MSnF_4$ 29
0.5.Scope of the thesis 30

0.1. General context

According to the Intergovernmental Panel on Climate Change (IPCC)'s Sixth Assessment Report, "Climate Change 2022: Mitigation of Climate Change", in order to keep global temperature increase below 1.5°C above pre-industrial levels, there needs to be a decrease of transport-related greenhouse gas emission of 47% by 2050. Strategies to reach this goal include improving public transit services, decarbonizing fuels (e.g.: biofuels), and electrification. At present time, electrification of personal vehicles is undergoing particularly rapid development. This advance will be doubly beneficial, as it should provide additional storage supporting the increasingly fluctuating power grid.

Currently, car battery technology is heavily reliant on lithium, an element that is not abundant enough to fulfil the rising supply needs, in addition to yielding systems limited in terms of safety.[1]

Presently, however, no battery can compete with lithium-ion batteries (LIB)'s years of development and funding, as industrial state-of-the-art recently reached a power density of 500 Wh/kg.[2] This breakthrough was previously thought of at best, very far off in the future, and at worst, as an impossible goal on the industrial scale. While this is an

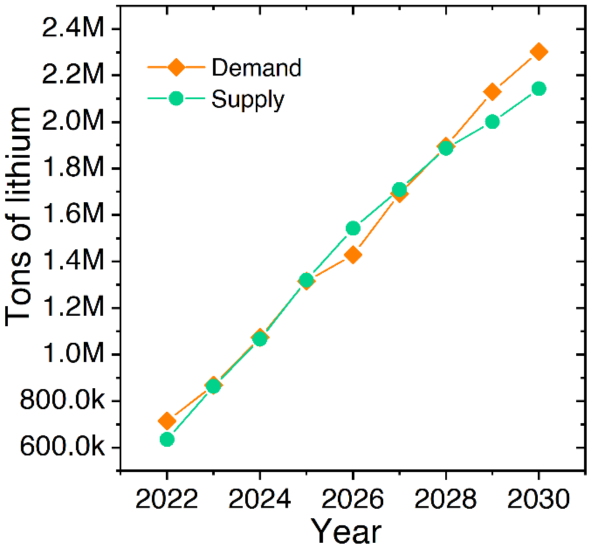

Figure 0.1 Global Lithium demand and supply. Benchmark Mineral Intelligence, dec.2022

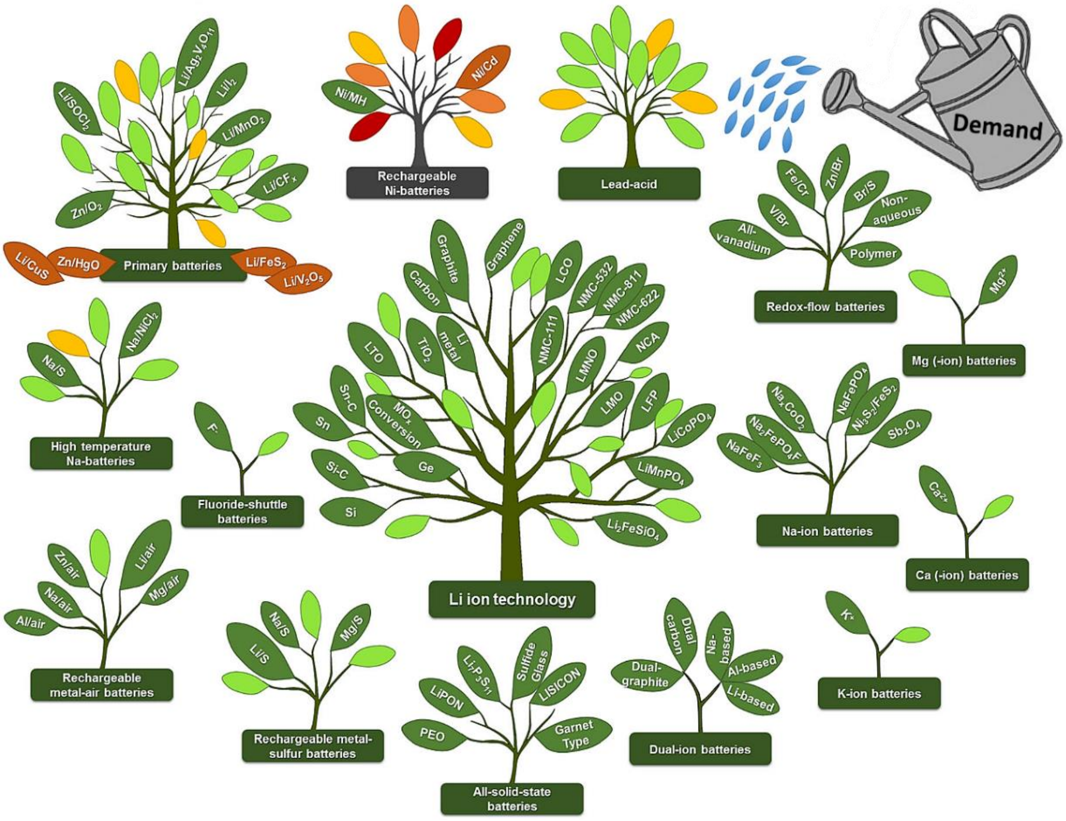

Figure 0.2. Battery cell chemistries which are considered in R&D to have technological relevance today and tomorrow, reproduced from ref. 4

example of what can be accomplished when pushing a technology, it does not solve the lithium supply issue, and may in fact worsen it, as such high capacities allow for additional applications in the aviation and shipping. Lithium demand and supply projections shown in **Figure 0.1** highlight the projected upcoming supply deficit, which will drive lithium prices up.[3]

In order to make up for the lack of lithium, a great number of alternatives are under development, as seen in **Figure 0.2**. Each system has its own strengths and weaknesses, and would be used as replacements for LIBs in its different applications, though none has quite caught up with the level of maturity LIBs have reached. [4]

One of the chemistries presented in **Figure 0.2.** to be in the very early stages of research is the Fluoride-ion (or Fluoride-shuttle) battery (FIB), a type of All-Solid-State Battery (ASSB). FIB are based on an abundant element, are inherently dendrite-free and may theoretically reach very high volumetric and gravimetric capacities (**Figure 0.3**), which explains our interest in them. [5]

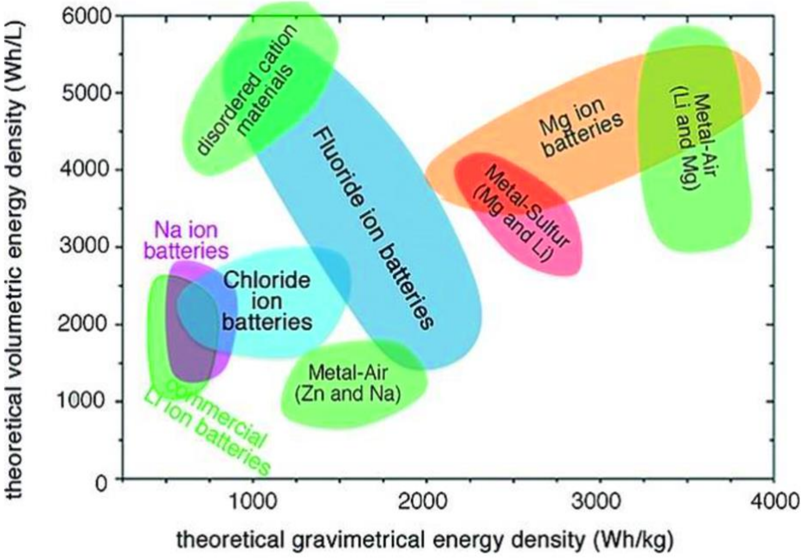

Figure 0.3 Comparison of the energy densities of various battery chemistries, extracted from ref.5

0.2. General principles of battery operation

Batteries work by converting stored chemical energy into electrical energy. A battery is technically an assembly of cells, but the term is often used to designate single cells as well. Batteries may be either rechargeable or single-use, though we will here focus on rechargeable systems. A general schematic of an electrochemical cell is presented in **Figure 0.4.**

A battery consists of two electrodes, a positive and a negative, separated by an electrolyte (or separator). Both electrodes have a different intrinsic electrochemical potential. The difference between electrode potentials generates the voltage of the battery. During discharge, electrons flow, as is thermodynamically favoured, from the electrode with the highest potential (negative) to the positive, through the external circuit. Upon charging, electrons are driven into the negative electrode. Electrons are then stored and released through reversible oxidation and reduction reactions occurring in the electrodes, thus the battery accumulates or dispenses energy. Ions need to flow

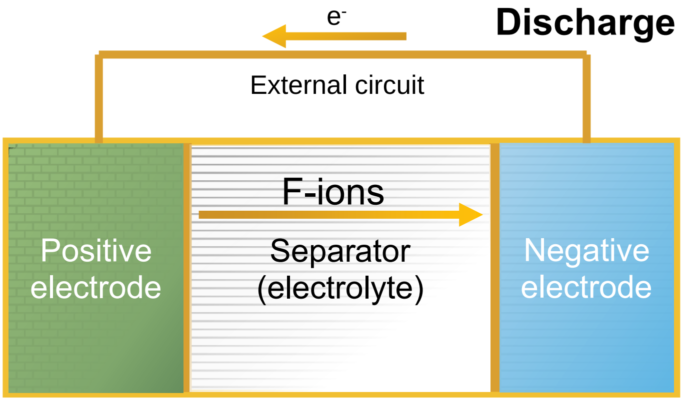

Figure 0.4 General schematic of a fluoride-ion

from one electrode to another to maintain charge neutrality. In doing so they pass through a separator, which must be conductive to these ions: the electrolyte.All batteries are based on these principles, but have different specificities. For instance, the charge carrier is usually a cation, as is the case in Lithium-ion batteries or sodium-ion batteries. One of the few systems based around anionic charge carriers in the electrolyte and within the electrodes is the Fluoride-Ion Battery (FIB), which recently started to generate interest due to its high potential theoretical gravimetrical and volumetric energy densities (**Figure 0.3**).[5]

0.3. History of Fluoride-ion batteries

Though FIB development is currently in its relative infancy, it has roots which may be traced back to the 1970s, which we will discuss here.

0.3.1. The early days

Interestingly, the very first FIB were originally not built to function as batteries, to be charged or discharged. “Galvanic cells”, as they were called, were utilized in order to calculate standard molar free energy (ΔG°) through the Electromotive Force Method, described by Lorenz in 1909.[6,7] Briefly, ΔG° may be deduced from the open-circuit voltage of a galvanic cell, comprised of two electrodes and a solid electrolyte, using the relation : $\Delta G^0 = -nFE$, where n is the number of electrons exchanged in the cell reaction, F the faraday constant, and E the open-circuit voltage of the cell. To measure this intrinsic constant for various fluorides, galvanic cells were built in 1974 by Kessler et al., using fluorite CaF_2 as an electrolyte. [8]

The first report of the electrochemical cycling of a cell came in 1976, with a symmetric $Bi|PbF_2|Bi$ configuration. The cell was polarized and a change in the appearance of the Bi electrodes was observed but no cycling data was provided. [9]

Shortly after, in 1978, a thin film FIB was presented by Danto et al., with Pb and Bi/BiF_3 as electrodes and PbF_2 as the electrolyte. The battery was cycled 10 times but once again there was no data shown, or information given about the capacity after cycling or the shape of the voltage-composition profiles. [10]

All aforementioned systems are all-solid-state batteries, as at the time there were no known liquid with adequate properties to be used as FIB electrolytes.

0.3.2. Re-discovery

FIB were then mostly forgotten from 1981 to 2011, though key studies on F-electrolytes continued to be published in the meantime, often considering the materials as options for sensors rather than for batteries. [11–13]

In 2011, electrochemical cycling data was reported for the first time for an all-solid-state FIB battery by Reddy and Fichtner.[14] The ionic conductivity of several electrolytes was measured before selecting $La_{0.9}Ba_{0.1}F_{2.9}$ as the solid electrolyte and several fluorides tested as cathode materials, including a CuF_2 composite, which showed the highest discharge capacity.

Because of the low ionic conductivity of LBF and slow F-diffusion kinetics in fluorides, the batteries needed to be cycled at 150°C, as shown in **Figure 0.5**. One should note that in spite of the severe capacity loss upon cycling, the battery could still be considered to be rechargeable. This study revived the field and generated interest around the world. Current FIB work

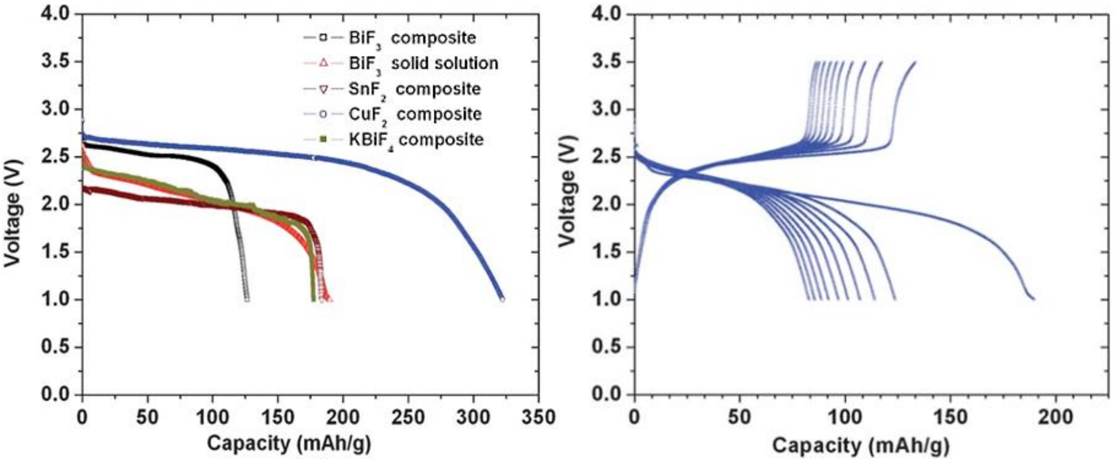

Figure 0.5 Highlights of the reintroduction of FIB a) cycling of various metal fluorides vs Ce metal, at 150°C, with $La_{0.9}Ba_{0.1}F_{2.9}$ solid electrolyte, at 10μA.cm^{-2}, b) cycling of Bi/BiF_3 composite vs Ce metal (same conditions). Extracted from ref.14

Though FIBs are still far from being able to compete with other, more mature systems, significant advances were made since 2011, with a particular focus on electrode and electrolyte material research and screening.

0.3.2.1. Conversion electrodes

The most heavily represented class of electrode materials in recent FIB publications function through conversion reactions, and are thus referred to as ‘conversion electrodes’. Both cathode and anode materials are often metal-based and the conversion itself consists of the fluorination and defluorination of the metal during battery operation, as follows (example: during charge) :

$$\textbf{Anode} : M + xF^{-} \rightarrow MF_x + xe^{-}$$

$$\textbf{Cathode} : M'F_y + ye^{-} \rightarrow M' + yF^{-}$$

Since most of the elements in the periodic table may be fluorinated, the number of theoretically possible M-M’ combinations is very high.[15] Additionally, conversion materials can typically store higher numbers of ions and engage in multi-electronic reactions, which results in theoretical gravimetric and volumetric energy densities that outperform current commercial lithium-ion batteries. This generates interest in FIB.

Table 0.1. Volume change of various materials upon defluorination and fluorination (extracted from [16])

Reaction	$\Delta V(MFx \rightarrow M)$	$\Delta V(M \rightarrow MFx)$
$FeF_2 \rightarrow Fe$	-68%	+210%
$FeF_3 \rightarrow Fe$	-77%	+342%
$CuF_2 \rightarrow Cu$	-66%	+192%
$BiF_3 \rightarrow Bi$	-36%	-
$CeF_3 \rightarrow Ce$	-36%	+56%

However, conversion materials tend to suffer from the same critical flaw: lack of cyclability. This is generally attributed to the volumetric changes that occur upon battery operation. [17] **Table 0.1** lists some examples of the volume expansion and contraction which occur upon cycling. These variations induce the formation of voids and cracks in the electrodes, which may lead to the loss of active material and subsequent capacity decay. In extreme cases, it can even precipitate the mechanical failure of the cell.[18,19]

To circumvent this issue, as well as the low ionic conductivity of F-electrolytes, many groups chose to preferentially study thin-film FIB. [15,19,20] Thin-film systems are also a solution to the second major issue encountered when using fluorides as conversion materials, which lies in the difficulty in attaining the full theoretical capacity (C_{th}). Taking Cu/CuF_2 electrodes as an example, the battery closest to reaching C_{th} was a thin-film battery operated at 150°C, and still only achieved 80% C_{th}.[19] A similar system cycled at 25°C reached 30% C_{th}, and no room-temperature bulk battery based on Cu/CuF_2 could be found in the literature. For thin films, it has been suggested that only the first 10nm in contact with the electrolyte undergo the conversion reaction.[21]

Other investigations suggest that the fluorination process of Cu is kinetically limited due to the lattice mismatch between the metal and the fluoride, making the phase boundary difficult to pass for the fluorine-ions. Attempts made to lessen the mismatch by creating a Cu-Au alloy resulted in improved performances.[22,23] Another solution to obtain better M/MF_2 interface was to start cycling from a half-discharged state, with the anode being a mix of M and MF_2.[24] This strategy is now widely adopted.

Lastly, most fluorides are both poor ionic and electronic conductors, which also impedes further reaction as F-ions cannot easily hop from the electrolyte through the fluorine to reach the unreacted material.[14] A schematic summarizing these processes is shown in **Figure 0.6**.

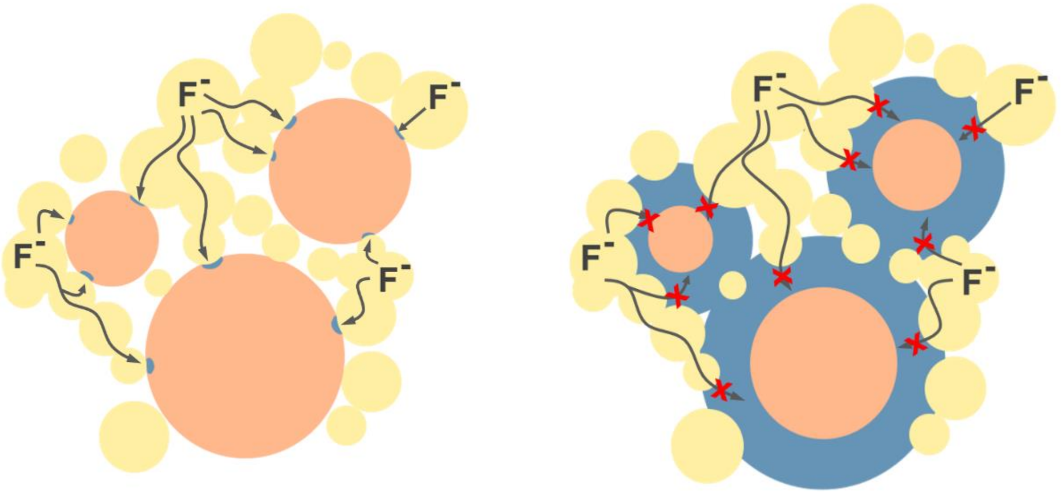

Figure 0.6. schematic of the incomplete fluorination reaction. Electrolyte particles are drawn in yellow, while the active material M is in orange and the fluorinated M is blue. On the right is the beginning of operation, on the left when the reaction cannot occur anymore, despite unreacted material still being present. Usually, electrode composites also include carbon for electronic conductivity but it was omitted here for simplicity.

0.3.2.2. Insertion electrodes

As another category of materials, insertion electrodes are currently investigated as alternatives to conversion-based chemistries. Though these materials are the most commons for LIBs, making up the entirety of commercial LIB electrodes, their development for FIB is still in its early stages of development.

The first insertion electrodes were based on the Ruddlesden-Popper structure, a layered distortion of perovskites with the general formula $A_{n+1}M_nO_{3n+1}$, where fluoride may be reversibly intercalated, as shown in **Figure 0.7.** panels a) and b). Examples include $LaSrMnO_4$, $Sr_2TiO_3F_2$, $Sr_4Fe_{3-x}Cr_xO_{10}$, $La_2NiO_3F_2$, and La_2CoO_4.[25–28] They are usually suitable for high-voltages, and can lead to fully reversible reactions.[25] However, they suffer from comparatively lower gravimetric capacities, with theoretical capacities in the range of 130-160 $mAh.g^{-1}$, similar to that of LIBs ($LiFePO_4$ theoretical capacity : 170 $mAh.g^{-1}$)[29]. These theoretical values are however not truly representative of the battery's potential, as fully charging and discharging induces rapid capacity fading, forcing a trade-off between capacity cut-off and cyclability, illustrated in **Figure 0.7** panel c). The lower reversibility at high cut-offs is attributed to inhomogeneities in the fluorination of the material, which lead to local overpotentials, thus enabling the irreversible fluorination of the carbon matrix, yielding particularly stable CF_x.[30]

These side reactions have been the focus of a number of studies. Grenier *et al.* studied the formation of CF_x in active material/electrolyte/Carbon composites. They showed that in $LaF_3/La_{0.95}Ba_{0.05}F_{2.95}$/Carbon, there is no reaction upon ball-milling of the composite, but upon cycling, CF_x side-reactions are present. [31] McTaggart et al. later additionally found

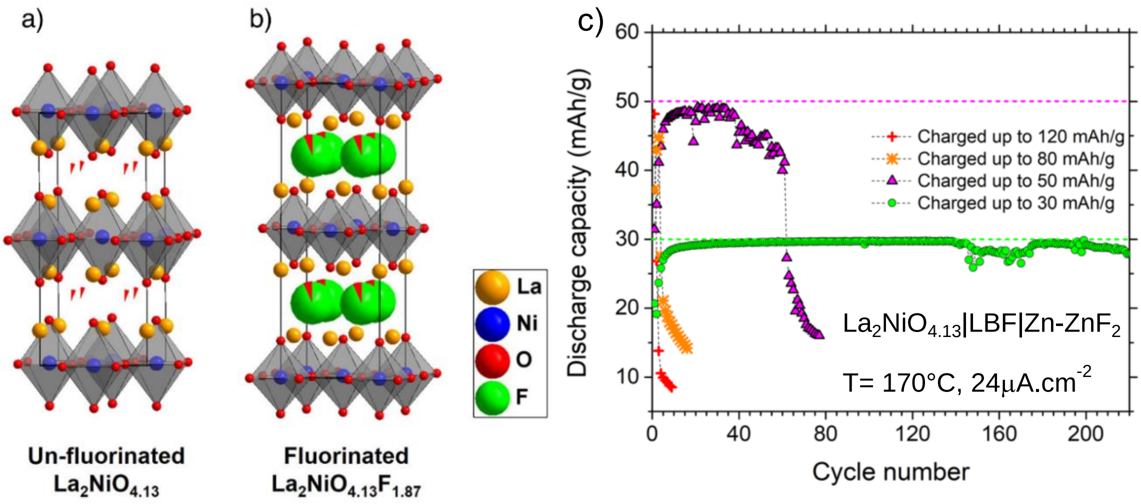

Figure 0.7. example of an intercalation material a) unfluorinated Ruddlesden-popper-type structure b) fluorinated structure (expansion along the c-axis) c) reversibility at different cut-off capacities extracted from ref.25

through thermodynamic calculations that lanthanides are prone to form MC_x carbides due to their high electropositivity. [32]

It should be noted that thus far, the theoretical improved cyclability of FIB insertion electrodes has only been shown to be true for Ruddlesden-Popper-type materials. Even then, it could be argued that it is not a fair comparison, as no study on conversion material investigates the effect of cut-off capacity on capacity fading. Furthermore, other reports of possible insertion materials often do not include enough cycling data to draw any general conclusions.[33,34] As such, insertion electrodes currently appear to require further investigations before they may rival conversion materials.

0.3.3. Recent breakthrough in FIB research

The current state of the art for FIB was set in 2021 by Wang et al., with a follow-up article reporting on a slight improvement by the same group in 2022.[35,36]

At the core of these articles is the synthesis and characterization of a new solid electrolyte, $CsPb_{1-x}K_xF_{3-x}$, of perovskite structure. It is not the first perovskite F-electrolyte synthetized, [37] but it is the most conductive by far, around 2 orders of magnitude above others from the same family. Various compositions were synthetized through mechanosynthesis and later, simple heat treatment of the precursors. The best ionic conductivity was obtained in both cases for $CsPb_{0.9}K_{0.1}F_{2.9}$, reaching 2.2 x 10^{-3} $S.cm^{-1}$ at 25 °C, which is around three orders of magnitude higher than the most common FIB electrolyte $La_{0.9}Ba_{0.1}F_{2.9}$. Its electrochemical stability was evaluated at round 1.8 V.

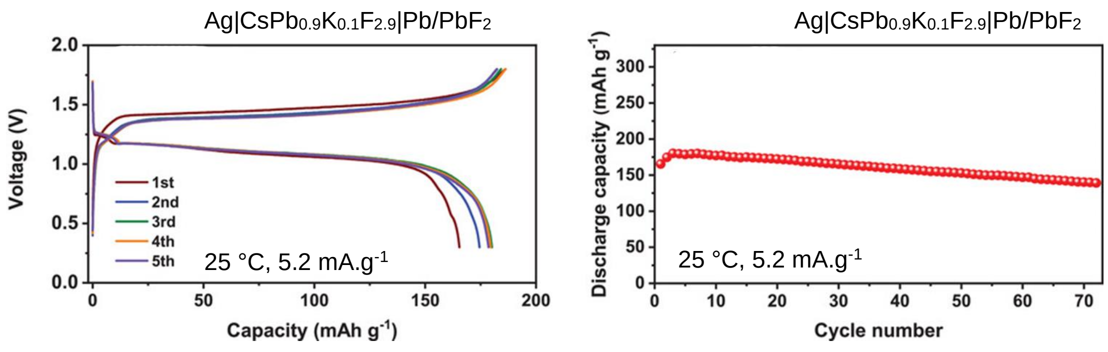

Figure 0.8 Room-temperature performances of the cells constructed using $CsPb_{0.9}K_{0.1}F_{2.9}$ a) charge/discharge curves for the first five cycles of the Ag|$CsPb_{0.9}K_{0.1}F_{2.9}$|Pb/PbF+ cell at 5.2 mA g−1. d) Discharge capacities of the same cell after different numbers of cycles at 5.2 mA g^{-1}. Adapted from ref. 35

Ag|$CsPb_{0.9}K_{0.1}F_{2.9}$|Pb/PbF_2 cells were assembled and cycled at 25°C, see **Figure 0.8**. The discharge capacity reached 190 mAh.g^{-1}, with 80% capacity retention after 100 cycles. These results are exceptional for a FIB, and were attributed to the improved ionic conductivity of the electrolyte, as well as the good chemical compatibility with the electrodes, forming conductive and stable interfaces. These results highlight the key role played by the electrolyte in FIB, which we will now describe in greater detail.

0.4. Electrolytes for FIB

0.4.1. Electrolyte requirements

There are many kinds of electrolytes: liquids, aqueous, polymers, solid-state (SSE)… All need to have the same key characteristics.

Firstly, electrolytes need high ionic conductivity, as one of the main roles of the electrolyte is to transport ions. Historically, liquid electrolytes had superior ionic conductivity, but recently solid-state has caught up and it is possible to operate ASSB at room temperature. Target values of ionic conductivity needed for battery use are usually set around 10^{-4} to 10^{-2} S.cm^{-1}.

One of the advantages SSE hold over liquid electrolytes is selective ionic conduction. In liquid electrolytes, all ions may move easily, which creates concentration gradients during operation, drastically limiting current densities and increasing charging times. On the other hand, in most SSEs only one ion is mobile, which consequently could enable faster charging.[38] There are still examples of materials where the framework ions are not static. In some cases, they rotate around,[39] which can be beneficial to the transport of the desired ion. In other instances, both anions and cations are mobile.[40] Such materials are better suited for other applications.

Another fundamental property for electrolytes is the ability to block electrons. This attribute is essential, as an electron-conducting separator would immediately cause a short-circuit, effectively rendering the battery unusable.

Ideally, electrolytes should be electrochemically, chemically and thermally stable. This point is subject to more caveats, but is still of major interest. Some materials may degrade when subjected to a high current or high potential. Contact with electrodes, even in the absence of current, may also result in degradation. Finally, the high temperature required for some systems to function and the overheating of others necessitates a higher level of heat resistance.

Solid-state electrolytes were initially thought to have higher stability compared to liquids, thus having the potential to enable the use of high-voltage electrodes, and high capacity electrodes like Lithium metal. This was however later disproved, as further investigation showed narrow windows of electrochemical stability for many solid-state electrolytes,[41] and demonstrated the propagation of Lithium dendrites through ceramics grain boundaries.[42] Nevertheless, there are many ways to compensate for a low-stability electrolyte: choosing chemically compatible electrodes, coating of the electrode or of the electrolyte, using additives… Some electrolytes are unstable only with respect to the formation of degradation products which form a stable and conductive interface. This turns an advantage into a disadvantage, as these products form a protective layer to prevent further deterioration.

Lastly, intrinsically safe materials are preferred for electrolyte applications. Safety is one of the main advantages that solid-state electrolytes hold over liquid-state. Most of the liquid electrolytes in use in commercial batteries are salts dissolved in organic solvents. These solvents are highly flammable, meaning any leak may potentially be hazardous, especially inside moving vehicles. SSE, on the other hand, cannot leak by nature, requiring less safety casing, which allows for lighter battery packs and higher energy densities.

High ionic conductivity and negligible electronic conductivity are the two fundamental properties which define an electrolyte. Here, we will first discuss the thermodynamic principles behind ionic transport, before showing how they translate to anionic conductors and giving some examples of important F-electrolytes.

0.4.2. General conduction process

0.4.2.1. Atomic scale transport

Mobile charges diffusing through a crystal hop from one site to another. When they are in their sites, they reside in an energy well, which makes them stable. In order to move, they need to leave their well and overcome an energetic barrier E_m, as well as travel a certain distance α_0 to the next site. Depending on the crystal structure, the energy landscape (i.e. the barriers, wells and distance between sites) may be more or less favourable for diffusion. For instance, structures containing interstitial sites usually are more beneficial for conduction, as ions may hop from site to interstitial site, a shorter distance than site-site. The shape of these two paths are illustrated in **Figure 0.9**.

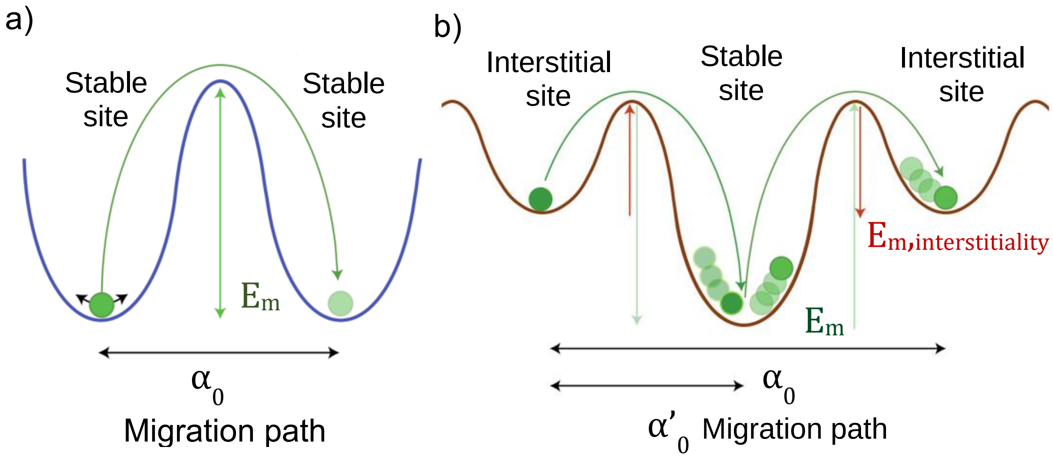

Figure 0.9. charge carrier hopping in a crystal a) without and b) with interstitial sites, adapted from ref.74

The link between ionic conductivity σ and these parameters is expressed in the following equation for direct, uncorrelated hopping:

$$\sigma = \sigma_0 \frac{1}{T} e^{\frac{-E_a}{k_B T}}$$

Where $$\sigma_0 \propto nq^2\alpha_0^2$$

Where n is the number of mobile charged species, q is the charge of the charge carriers, T the temperature, k_B the Boltzman constant, and E_a the activation energy of ionic conduction.

The conductivity is hence directly proportional to the number of mobile charge carriers. These "charge carriers" are defects or imperfections in the lattice, which, in the case of anion conductors, consist of anionic vacancies and interstitial anions, together known as Frenkel pairs.

For an ion to be mobile within a solid, the main requirements are a small size and a high polarizability, so as to be able to pass bottlenecks. Most ions that satisfy these conditions are cations: Ag^+, Li^+, Na^+… Anions, on the other hand, are generally bigger and less polarizable. O^{2-}, for instance, has the biggest ionic radius in many structures which are oxygen-conductors.[43] As a result, anionic conduction tends to be heavily reliant on pre-existing defects in the lattice.

Defects exist naturally in almost all crystals, as the energy barrier for their formation (which is a part of the ionic conduction activation energy E_a) is smaller than the thermal energy at room temperature. Thermally activated defects are intrinsic to each material.

In order to improve a material's conductivity, two routes may be taken: altering the energy landscape or increasing the number of charge carriers.

- **Modification of the energy landscape** is accomplished by the introduction of dopants in the material. Dopants generally replace one of the ions by sitting in the same lattice site as them. If the dopants have the same valence as the ion they are replacing, this process is called "isovalent doping". If not, it is then "aliovalent doping". For this substitution to be possible, both elements should have similar ionic radii. The degree of similarity required is variable and depends on each structure. The addition of dopants in a crystal structure induces local distortions in the lattice, which contracts or expands to accommodate the new species. The effect of structural disorder on the energy landscape is twofold: first, it modifies the distance α_0 between two charge carriers' sites. Second, it may also lower the migration energy barrier. This barrier is representative of the bottleneck charge carriers need to hop over. Warping of the lattice leads to deformed bottlenecks, which are easier to pass. This added disorder and geometric frustration has an effect akin to heating the material. This is particularly striking in fluorites, where doped materials exhibit conduction behaviours that would normally only be observed at high temperature.[44–46]

- **Aliovalent doping** is the replacement of an ion with one which has a different valence. For instance, in fluorites (general formula MF_2), the valence of M is +II. M(II) could be substituted for a monovalent M'(I) or a trivalent M''(III). In order to maintain charge neutrality, each of these substitutions is accompanied by the formation of a defect, either a vacancy (for undervalent dopants) or an interstitial (for supervalent dopants). These are called extrinsic defects. Extrinsic defects may participate in conduction as extra charge carriers, but tend to form clusters when present in too great numbers. Defect clusters then act as traps, impeding conduction. As a result, aliovalent doping is often only efficient when introducing a few mol% of dopant in a matrix. Circling back to the example of MF_2 fluorites, supervalent dopants may be Bi(III), rare earths Ln(III), Zr(IV), and Ni(III), while undervalent dopants may be K(I), Na(I), Li(I), or Ag(I). When added, they generally result in conductivity increases at temperatures where transport regime is dependent on defect number.[47–50]

0.4.2.2. Particle-scale transport

The processes described until this point all take place in crystal bulk. Batteries are however not made from single crystal electrolytes, but rather with polycrystalline powders. The grain boundaries between crystalline domains, and the interfaces between particles both also play a role in the overall conductivity.

Grain boundaries are areas of crystallographic mismatch, and carry a charge from the excess or depletion of a particular type of ions. To compensate for this charge, they attract opposite charge carriers, which create a space-charge zone. This zone and the grain boundary itself can either function as a trap for mobile ions/vacancies, or create fast-conducting pathways through repulsion. Whether the presence of grain boundaries is beneficial or detrimental is highly material-dependent.

In PbF_2 fluorite, for instance, they are thought to improve conductivity, thanks to a high concentration of defects in that region, which facilitates the vacancy-based ionic mobility.[51] On the other hand, Li conductor Li_3OCl was shown to have grain boundaries with both lower conductivity and higher activation energy than the bulk, thus severely impeding transport.[52]

Improvement of conduction properties on the microscopic scale may be achieved through modifications of the synthesis conditions. For instance, materials sintered at high temperatures usually have larger crystallite size (and therefore lower amounts of GB), and are denser, sign of better contact between particles, facilitating hops.[53]

0.4.3. Important solid electrolytes for FIB

There are several types of electrolytes suitable for fluoride-ion batteries. Most are solids, but some organic liquids, polymers or even aqueous electrolytes have been reported, though they are beyond the scope of this thesis.[21,54,55] There is a high number of materials that may be called "solid state fluoride electrolytes", split in various families, as shown on **Figure 0.10**.[56]

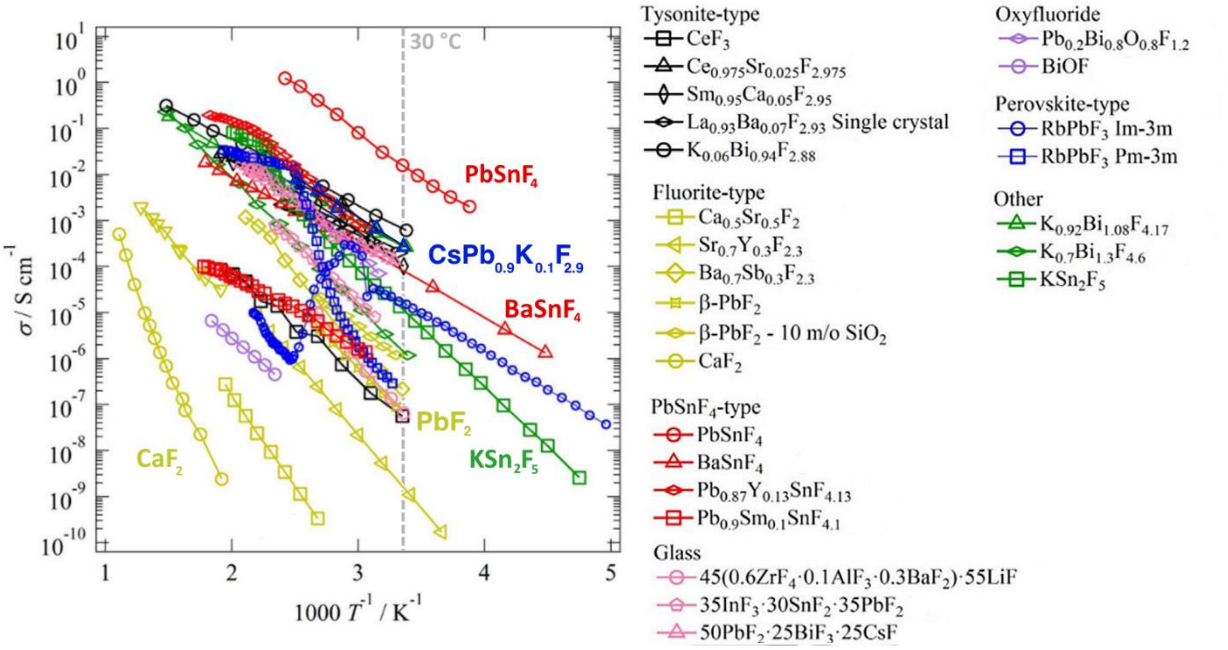

Figure 0.10 Ionic conductivities of solid-state fluoride ion conductors, adapted from ref. 56

Out of all these electrolytes, only 4 have been built in batteries: $La_{1-x}Ba_xF_{3-x}$, $PbSnF_4$, $BaSnF_4$ and $CsPb_{0.9}K_{0.1}F_{2.9}$, (introduced in **section 0.3.3**).

0.4.3.1. $La_{1-x}Ba_xF_{3-x}$ (LBF)

LBF is one of the most used solid electrolytes for FIBs. It is a doped LaF_3, which crystallizes in a tysonite structure, shown in **Figure 0.11**. Many similar $Ln_{1-x}M_xF_{3-x}$ have been investigated, with Ln = La, Ce, Sm, Er and M = Ba, Sr, Cd or Ca.[57,58] The addition of M(II) in Ln(III)F_3 causes the formation of F-vacancies. These vacancies are mainly localized in the *12g* sites. ^{19}F NMR studies highlighted that at lower temperatures, the main fluoride hops occur between *12g* sites. The introduction of vacancies facilitates this exchange, as well as the slower and more energetically costly *12g-4d/2a* jumps, thus improving conductivity by up to one order of magnitude.[59–61]

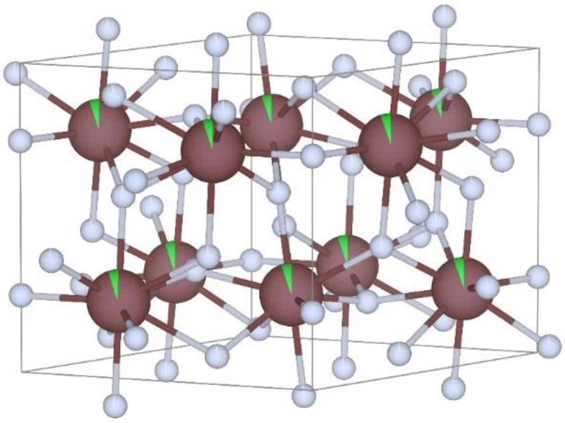

Figure 0.11 unit cell of $La_{0.95}Ba_{0.05}F_{2.95}$ (tysonite, spacegroup *P* -3 *c* 1). Brown La and green Ba are randomly distributed within the same *6f* site; while grey F

The highest conductivity value for polycrystalline $La_{1-x}Ba_xF_{3-x}$ was found to be $\sigma_{30°C}$ = 3.45 x10^{-5} S.cm^{-1} for x = 0.01.[62] This is not enough to enable room-temperature battery operation, which is why most LBF-containing systems, including the first reversibly cycled example, are operated at high temperature, usually around 150°C, as was for instance the previously mentioned first reversible FIB reported in 2011.

Despite this drawback, LBF is still a fairly ubiquitous FIB electrolyte, especially in thin-film batteries where the ionic conductivity is not as essential. Its popularity lies mainly with its high electrochemical stability window, though it was recently shown that many potential electrode materials are unstable towards it, rendering it less attractive for future use in FIBs.[63]

0.4.3.2. Sn-based $MSnF_4$ electrolytes

Structure

$BaSnF_4$ and its isomorph $PbSnF_4$ are currently the best and third best reported F-ion conductors, with respective conductivities at 30°C of 3.5×10^{-4} to 5×10^{-3} and 1.6×10^{-3} $S\cdot cm^{-1}$.[64–66] As both $MSnF_4$ (M = Pb, Ba) showcase impressive transport properties, their structure has been thoroughly studied, and after some debate was settled to be as is depicted in **Figure 0.12**.[67] These materials both crystallise in two polymorphic structures, a cubic fluorite phase which will be the subject of a subsequent chapter, and a tetragonal phase, which is the product of the ordering of the fluorite and the most conductive polymorph. This structure is a 2D material, consisting of successive layers of M and Sn, connected by fluoride ions. The layers sequence is the following: -Sn-Ba-Ba-Sn-. The Sn-

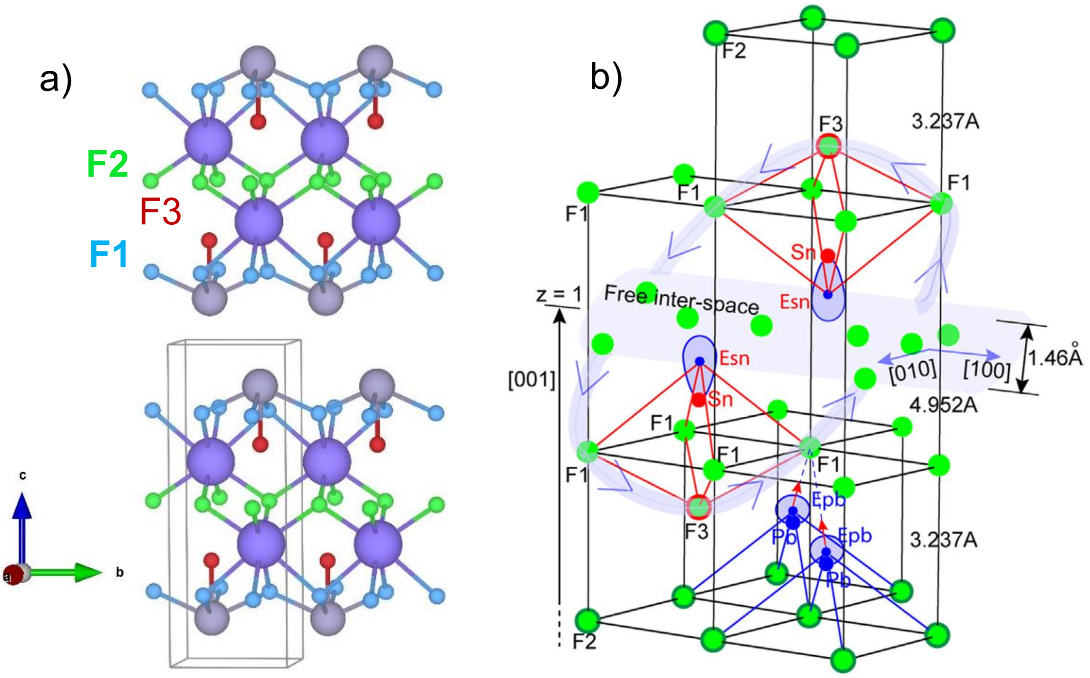

Figure 0.12. $MSnF_4$ a) structure, with purple = M (Ba, Pb), gray = tin, blue/red/green = the three fluoride sites, b) F conduction pathway in $PbSnF_4$,

Sn interlayer is void of any F-ion, as tin's 5s^2 electrons form a stereoactive lone pair, which takes up the space of a fluoride in the tin coordination sphere. All lone pairs point towards the c-direction, thus forming this interlayer.

As the tin lone pair is an essential feature of these materials, it is useful to understand its origin. A schematic of the interaction from which they arise is presented in **Figure 0.13**.

Lone pairs, or asymmetric electron densities, occur in heavier post-transition elements M, such as Pb, Sn, Bi, Ge, Sb, or Tl. In association with ligands L (O, S, F, Cl), they form crystal structures in which mixing may then take place between the M s- and L p-orbitals, giving rise to a bonding and an anti-bonding state. The anti-bonding orbital interacts with the empty p-orbitals of M through a second-order Jahn-Teller interaction (interaction between the valence and conduction band of a material, resulting in this case in structural modifications)[68], giving rise to a stabilising orbital occupied by an electron pair, which becomes stereoactive. In other words, asymmetric electron densities are the result of an indirect M s- and p- states mixing, mediated by the L p-orbital.[69,70]

Lone pairs often take the place of a ligand in the coordination sphere of the M, distorting it simultaneously through electron-L repulsion effects, as is the case in t-$BaSnF_4$ and

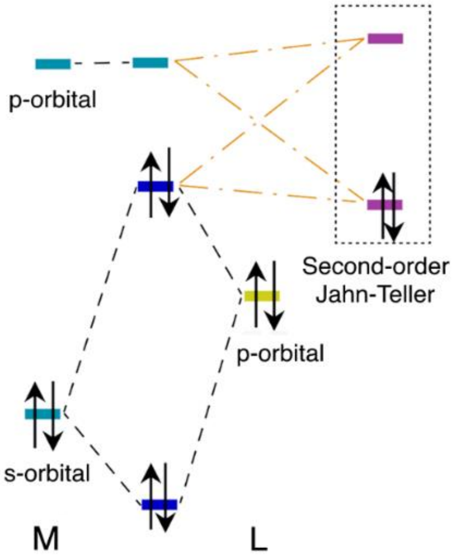

Figure 0.13 Interaction between M and L orbitals, giving rise to stereoactive lone pairs. Adapted from ref.69

t-$PbSnF_4$, where the lone pair is in the apical position of the Sn polyhedron, pushing the equatorial fluorides down. This results in a F1-F3 angle of 72.2(4)° against a theoretical 90° in an undistorted octahedron.

Structural impacts are also accompanied by repercussions on ionic transport mechanisms. For instance, significantly higher ionic conductivities are found in fluorite-structured materials that contain cations with stereoactive lone pairs, such as β-PbF_2 [71–73]. This effect has been suggested to be a possible consequence of the high polarisability of the cation facilitating diffusion of the mobile anions [71,73,74], or that the negative charge of the Pb lone pairs might electrostatically destabilise adjacent fluoride ions in tetrahedral sites, thereby promoting the formation of anti-Frenkel pairs[71]. Neutron diffraction data [75] and AIMD simulations [76] of β-PbF_2, however, show no evidence for octahedral site occupation by fluoride ions, bringing into question the hypothesis that the presence of stereoactive lone pairs in fluorite-structured materials promotes Frenkel pair formation.

Transport mechanism

The transport mechanism in $BaSnF_4$ and $PbSnF_4$ has been studied via a combination of 19F Nuclear Magnetic Resonance (NMR),[11,77–79] Molecular dynamics,[80] and Neutron diffraction.[12] All three techniques point towards the same results, summarized in **Figure 0.12**, panel b) :

- The conductivity primarily originates from F motion in the M-Sn layer (F1 and F3 exchange)
- There are some fast-moving interstitials in the Sn-Sn layer (well-demonstrated for t-$PbSnF_4$ but only speculated for t-$BaSnF_4$)
- The M-M layer is, at its root, a basic fluorite and therefore F2 ions are the least mobile here (conduction 6 to 7 orders of magnitude lower than in the M-Sn layer).[77] This makes t-$MSnF_4$ a 2-dimentional conductor. At higher temperatures, exchange within this layer is activated, and conduction becomes more 3D.
- t-$PbSnF_4$'s superior anionic transport arises from the Pb's electronic lone pair, which some authors describe as additional polarizability, an element well-known to

facilitate mobility.[81] This induces F2 hops, rendering the material more 3D than its Ba isomorph.

The conduction mechanisms in t-MSnF$_4$ are evidently well-understood.

Doping MSnF$_4$

To facilitate them and improve transport, many attempts were made to dope PbSnF$_4$, mostly using aliovalent rare earths such as supervalent Y, La, Nd, Eu, Gd, Sm,[82] d- and p-block metals Zr, Al, Ga, and In,[83] all forming anion-excess phases which were less conductive than the parent material at room temperature. On the other hand, undervalent alkaline metal doping was also undertaken, Li, K and Na all give in the best case very slight improvements.[83–85] Finally, isovalent doping utilizing elements like Ce or Ca did not generate any increase of conductivity.[86]

BaSnF$_4$ was also the subject of a few doping studies, all originated from the group of X. Wang (Xiangtan University) and all reporting marginally higher conductivities for the Eu, Sm, Nd and Mn-doped samples, though some of the data presented raises unanswered questions.[87–90]

One of the central questions one might ask relative to doping these t-MSnF$_4$ is “where does the dopant go?”. There are two possible sites, either in the M or in the Sn layer. As we have discussed, the M layers are the least conductive ones, so dopants inserted in the M layers would be most efficient. It was however shown in the cases of Al, Ga and Ca doping in PbSnF$_4$ that these cations preferentially sit on the Sn *2c* site, which was attributed to a close proximity in size between the tin and the dopants. This explains the failure in raising conductivity through the use of these elements as dopants. For other dopants, no information on their location was provided, but it can be inferred in the instances of M’(III) substitutions that, since the M-M layer ionic transport mechanism is fluorite-like (vacancy-based), the addition of interstitials would be of limited usefulness. On the other hand, M’(I) introduce vacancies, which justifies the marginal enhancement their presence generates.

As Sn cations precipitate most of the fluoride hops, it has also been attempted to obtain non-stoichiometric materials with an excess of tin, $M_{1-x}Sn_{1+x}F_4$. This was the most successful conductivity-enhancing strategy, both for $PbSnF_4$[91] and $BaSnF_4$[66], where it was shown that the excess tin sits in the M sites, thus boosting ionic transport in the M-M layer.

0.5. Scope of the thesis

Fluoride-ion batteries are a new high-energy density alternative to LIBs that recently started being considered. Partly because of the newer nature of this cell chemistry, most of the systems detailed in this introduction have significant flaws, though some very promising results were already reported, notably a state-of-the-art battery with a capacity of over 150 mAh.g^{-1}, and reversible through 100 cycles at room-temperature, which was partly enabled by the use of a performant solid-state electrolyte. In this work we will therefore focus on this key component of FIBs.

The most conductive F-electrolytes reported are arguably two Sn-based isomorphs solid electrolytes, $PbSnF_4$ and $BaSnF_4$. Despite the numerous studies describing synthesis routes, structures, conduction mechanisms and use in full batteries for both materials, some important properties related to their role as electrolytes remain understudied. In this thesis, we will attempt to fill some of these gaps:

- In **Chapter I.**, we examine the cubic polymorph c-$BaSnF_4$. We give a new, more accurate structural description of this material and show the impact of the lone pair of tin on both the structure and ionic transport.

- In **Chapter II.**, we focus on the tetragonal polymorph, t-$BaSnF_4$. Two new synthesis routes are investigated, and we underline differences in the resulting materials, trying to link the structural variations to changes in the ionic conductivity.

- In **Chapter III.**, we report the synthesis of a new isomorph to $BaSnF_4$ and $PbSnF_4$: $SrSnF_4$. We characterize this material, discussing its structural specificities compared to $BaSnF_4$, notably the distinct expression of the tin lone pair in both structures, before highlighting their impact on fluoride transport.

- In **Chapter IV.**, we evaluate the electrochemical properties of $BaSnF_4$ in order to demonstrate its potential as a solid electrolyte beyond its high conductivity. For this purpose, we establish its electrochemical stability window, test its stability under current, and study its decomposition pathway. We find its potential stability to be significantly higher than previously reported thanks to kinetic factors, enabling the use of $MSnF_4$ as an electrolyte in high-voltage batteries.

Finally, we detail some perspectives for fluoride-ion batteries and the $MSnF_4$ material family.

Chapter I

Dynamic Lone Pairs and Fluoride-Ion Disorder in Cubic-BaSnF$_4$

Table of Contents

Introduction 35
I.1.Methods 37
  I.1.1.1. Synthesis of Cubic BaSnF$_4$ 37
  I.1.2. Impedance Spectroscopy 37
  I.1.3. X-Ray Diffraction 37
  I.1.4. ^{119}Sn Mössbauer Spectroscopy 38
  I.1.5. ^{19}F Solid-State NMR 38
  I.1.6. Pair-Distribution Functions 38
  I.1.7. Molecular-Dynamics Simulations 39
I.2.Results and discussion 40
  I.2.1. The fluorite structure, cation disorder and stereoactive lone pairs 40
  I.2.2. Fluoride-ion dynamics 54
  I.2.3. Sn lone pair dynamics 57
Summary and Conclusions 62

The present chapter is an adaptation of the article "Dynamic Lone Pairs and Fluoride-Ion Disorder in Cubic-$BaSnF_4$" published in the *Journal of the American Chemical Society*. The authors are B. Mercadier, S. W. Coles (co-first author), M. Duttine, C. Legein, M. Body, O. Borkievicz, O. Lebedev, B. J. Morgan, C. Masquelier and D. Dambournet.

Introduction

The ability of solid electrolytes to allow ion transport in the solid state makes them useful for a range of applications, including fuel cells and solid-state batteries[38,81,92–94]. As a consequence, a considerable amount of research has focussed on understanding how the structure and chemical composition of particular solid electrolytes modulate their ionic conductivity[94–102]. In addition to providing insight into the atomic-scale mechanisms of ionic conductivity within specific families of solid electrolytes, this body of research has also produced various "design principles"—general conceptual models that seek to explain, and predict, trends in ionic conductivity across different families of solid electrolytes [97,101,103–108]. Many of these solid electrolyte design principles reflect how changes to the structure and composition of the host framework (set of non-diffusive ions within a solid electrolyte) modulate the potential energy surface for the mobile ions, and hence influence the overall ionic conductivity [95,100,105,108–110].

One such design principle arises from the observation that solid electrolytes with some form of host- framework disorder often have significantly higher ionic conductivities than related compounds with well-ordered host frameworks [99,104,111–119]. Framework-disordered solid electrolytes typically exhibit one of two classes of disorder: occupational disorder, where two or more distinct species occupy the same crystallographic positions [99,104,113,117,118,120–125]; or orientational disorder, where molecular or polyatomic subunits within the host framework have different disordered orientations [126–129]. Orientational disorder can be static, where each polyatomic sub-unit has a fixed average orientation over experimentally relevant timescales [130,131], or dynamic, where the polyatomic sub-units rotate and reorient[129,132,133]. In some solid electrolytes, this reorientational dynamics of the host framework is thought to be coupled to the diffusive dynamics of the mobile ion species, giving rise to a so-called “paddlewheel” effect [110,127,132,134].

While orientational disorder in solid electrolytes is usually discussed in the context of molecular or polyanion orientational degrees of freedom, materials that contain post transition metals with “stereoactive” lone pairs (such as Sn or Bi) may exhibit electronic orientational disorder [135]. These cations, when in an oxidation state two less than their formal maximum (e.g., Sn(II) for Sn(IV) and Bi(III) for Bi(V)), have a formal electron configuration with a filled s-orbital as their last valence shell. As explained in the previous chapter, s^2 states can mix with neighbouring-anion p states to form a bonding state and an antibonding state, and this antibonding state mixes with metal p states to form an asymmetric lone pair state, characterised by an acentric “stereoactive” charge density that directs the cation coordination geometry and typically results in distorted low-symmetry cation coordination environments [136,137].

In many materials that contain stereoactive lone pairs, the local distortions due to these lone pairs are correlated over long length scales. These materials are long-range ordered and their structures can be determined using average crystallographic techniques such as Bragg diffraction. In other materials, however, the disortions due to stereoactive lone-pairs are uncorrelated [135,138,139]. These materials are crystallographically disordered and average-structure crystallographic methods yield inaccurate high-symmetry structural models. Because the distortion around each cation depends on the relative orientation of the corresponding lone pair, this behaviour can be considered a form of orientational disorder, analogous to molecular or polyanionic orientational disorder as discussed above. These lone-pair effects may also be dynamic, showing fluctuations [135,140–142] or even rotations[143,144] of the lone-pair charge density, mirroring the dynamic orientational disorder of “paddlewheel” materials [110,127,134].

While the role of stereoactive lone-pairs in solid electrolytes has previously been discussed in the context of crystallographically ordered materials [71,145–148], a detailed understanding of lone-pair behaviour and its effect on ion transport in crystallographically disordered solid electrolytes is currently lacking [149–151].

I.1. Methods

I.1.1. Synthesis of Cubic $BaSnF_4$

Cubic $BaSnF_4$ was synthesized via a ball- milling process, using a planetary mill (Fritsch Pulverisette 6). Precursors (SnF_2, Sigma-Aldrich, 99 %; BaF_2, Sigma-Aldrich 99.99 %) were dried at 150°C under vacuum for 3 h, and stored under Ar inert atmosphere. The desired amounts of precursors were weighed and sealed in Zirconia milling jars in an argon-filled glove box, with a powder to ball ratio of 1:13. The balls were 10 mm in diameter and made out of zirconia. The precursors were then milled at 400 rotations/min for 12 hours, divided into 24 cycles. Each cycle consisted of 15 minutes of milling and 15 minutes of pause, which prevented overheating.

I.1.2. Impedance Spectroscopy

Electrochemical Impedance spectroscopy was performed on c-$BaSnF_4$ powder pressed into a 10 mm diameter pellet of 89% compacity. Gold was sputtered on both sides of the pellet to guarantee good electronic contact. A BioLogic MTZ-35 impedance analyser was used to collect data in a frequency range of $3.5\ 10^7$ Hz to 1 Hz, under Ar atmosphere. The temperature was varied at a rate of 1 $K.min^{-1}$ using a Biologic Intermediate Temperature System (ITS), and each temperature was held for 15 mn before measuring the impedance of the system. The resulting data were fitted using the equivalent circuit model proposed in Ref. [152].

I.1.3. X-Ray Diffraction

X-ray diffraction was performed using a Bruker D8 Advance powder diffractometer in θ-θ geometry, with a copper anti-cathode ($Cu–K_\alpha$ = 1.5418 Å). The powder XRD pattern was fitted using the Rietveld method as implemented in the Fullprof program[153], with a split–pseudo-Voigt function to model the peaks[154].

I.1.4. ^{119}Sn Mössbauer Spectroscopy

A lab-made constant acceleration Halder-type spectrometer operating in transmission geometry was used to carry out the Mössbauer analyses. The spectrometer was equipped with a radioactive source of ^{119}Sn (370 MBq) embedded in a $CaSnO_3$ matrix and maintained at room-temperature. Experiments were performed with 50 mg to 70 mg of sample ([Sn] = 5 mg.cm^{-2} to 8 mg.cm^{-2}) at room temperature (293 K) and 77 K using a liquid nitrogen bath cryostat. The Mössbauer hyperfine parameters (δ isomer shift, Δ quadrupole splitting, Γ signal linewidth, G_{11} Goldanskii–Karyagin factor and relative areas) were refined using the WinNormos software[155]. Isomer-shift values are reported relative to $CaSnO_3$ at room temperature.

I.1.5. ^{19}F Solid-State NMR

Quantitative ^{19}F Magic Angle Spinning (MAS) NMR spectra were recorded on Bruker Avance III spectrometers operating at B_0 = 7.0 T (^{19}F Larmor frequency of 282.4 MHz), using a 1.3 mm CP-MAS probe head, and, for variable temperature experiments, using a 2.5 mm double resonance (^{1}H/^{19}F–X) CP-MAS probe and a Bruker Cooling Unit (BCU-II). The ^{19}F MAS spectra were recorded using a Hahn echo sequence with an interpulse delay equal to one rotor period. The 90° pulse lengths were set to 1.25 µs (for SnF_2 and $BaSnF_4$) and 1.5 µs (BaF_2) and the recycle delays were set to 900 s (for SnF_2) and 300 s (for BaF_2 and $BaSnF_4$) using the 1.3 mm CP-MAS probe head. For the variable-temperature experiments, using the 2.5 mm CP-MAS probe head, the 90° pulse length was set to 2 µs and the recycle delay was set to 10 s. The temperature inside the rotor was estimated from the chemical shift and spin-lattice relaxation time (T1) of ^{79}Br in KBr powder[156]. ^{19}F spectra are referenced to $CFCl_3$ and were fitted using the Dmfit software[157].

I.1.6. Pair-Distribution Functions

Pair-distribution function (PDF) measurements were performed at the 11-ID-B beamline at the Advanced Photon Source at Argonne National Laboratory (USA). High-energy Synchrotron XRD (λ = 0.2128 Å) 2D total scattering data were collected and integrated into one-dimensional diffraction data using FIT2D[158]. The PDFgetX3 software was used to carry out Fourier transformation and correction of the PDFs. Refinements were performed using the software PDFgui[159].

I.1.7. Molecular-Dynamics Simulations

To model the equilibrium structure and dynamics of c-$BaSnF_4$, ab initio molecular dynamics (AIMD) was performed by our collaborators S. W. Coles and B. J. Morgan from the university of Bath, using the Vienna ab initio simulation package (VASP)[160–162]. We used the revised Perdew–Burke–Ernzerhof generalized gradient approximation PBEsol exchange-correlation function[163]. Interactions between core and valence electrons were described within the projector-augmented-wave (PAW) method[164], with cores of [Kr] $4d^{10}$ for Ba, [Kr] for Sn, and [He] for F. We simulated a 6x6x6 supercell, starting from a cation-disordered fluorite structure with a special-quasi-random configu ration of Ba and Sn over the Wyckoff *4a* cation sites, that we generated using the icet package[165]. This 6x6x6 special-quasi-random structure best approximates the Ba/Sn correlations for an infinite lattice with a fully-random arrangement of cations[166,167].

Our molecular dynamics simulation used a plane-wave cutoff of 350 eV with only the gamma point used for k-space sampling, and without spin-polarisation. The simulation was performed at 600 K and used a time-step of 2 fs. Before our production run, we obtained the 600 K equilibrium volume by running a preliminary series of simulations with different cell volumes for 8 ps each, and fitting the Birch–Murnaghan equation to the resulting energy–volume dataset. The simulation was run in the NVT ensemble using a Nosé–Hoover thermostat. Thermal equilibration was performed by running a 2 ps NVE run with temperature rescaling every 50 steps. The production run was 159 ps in length.

To calculate fluoride-ion site occupancies and site–site transition frequencies, at each simulation timestep we assigned every fluoride ion to a distinct tetrahedral or octahedral site by projecting the instantaneous fluoride-ion positions onto polyhedral “sites” defined by the Wyckoff *4a* positions as fixed vertex positions.

For structural analysis (calculation of radial distribution functions and cation–4a displacements) we extracted a set of “inherent” structures[168–170] from our simulation trajectory by performing a conjugate-gradient geometry optimisation on configurations selected every 50 timesteps. Each inherent structure represents a local minimum on the corresponding 3N-dimensional potential energy surface. To calculate an example electron localisation function (ELF)[171], and to calculate an example energy difference between a thermally equilibrated and relaxed structure and the reference cation-disordered fluorite starting structure, we performed full geometry optimisations with a cutoff of 500 eV with a minimum k-point spacing of 0.25 $Å^{-1}$, with atomic positions and cell parameters relaxed until all atomic forces were less than 2×10^{-2} eV $Å^{-1}$.

To obtain tin lone pair orientations, we calculated the set of maximally-localised Wannier functions[172] for structures sampled every 50 ps, using the Wannier90 code[173]. The net dipole on each tin atom is calculated by associating each Wannier center with the closest ion, and then, for each tin, summing over all associated Wannier-center displacement vectors[174]. We assume that tin polarisation is dominated by contributions from the lone pair states, and that our calculated polarisation vectors therefore characterise these lone pair orientations. Analysis of the simulation data was performed using the RevelsMD[175], site-analysis[176], ase[177], pymatgen[178], numpy[179], and scipy[180] codes. The time-average fluorine density (Fig. 6) was calculated using a linear combination of a conventional histogram with a triangular kernel and a force-extrapolated analogue, as described in Refs.[181–183].

I.2. Results and discussion

I.2.1. The fluorite structure, cation disorder and stereoactive lone pairs

The study of fluoride-ion–conducting fluorites has a long history, starting from Faraday's discovery of superionic β-PbF_2[184]. More recently, this family of materials has been the subject of renewed interest because of their potential use as electrolytes in solid-state fluoride-ion batteries[185–188].The MF_2 fluorite structure is comprised of a face-centered cubic (FCC) M cation lattice with anions occupying all of the tetrahedral interstices (**Figure I.1** a). The octahedral holes (4 per unit-cell) are vacant, and are usually considered as "interstitial" sites. An alternative structural description is obtained by considering the positions of cations within an anionic substructure (**Figure I.1** panel b):

from this perspective, the anions define a simple-cubic lattice, and the cations occupy half the cubic holes, giving 8-fold MX_8 cation coordination.

In conventional fluorites, such as CaF_2, anion transport requires the presence of thermally-generated point defects—vacancies and/or interstitials—within the anionic substructure. Fluorites are typically anti-Frenkel disordered: some fraction of anions occupy octahedral interstitial sites, leaving an equal number of tetrahedral sites vacant. While additional interstitials and vacancies can be introduced via aliovalent doping, the intrinsic defect concentration depends on the ease with which anti-Frenkel pairs can form, which, in turn, approximately depends on the relative energies of ions occupying the tetrahedral and octahedral anion sites within the FCC cationic host framework. In simple fluorites, the anti-Frenkel-pair formation energy is usually high: for CaF_2, anion Frenkel-pair formation energies have been calculated as 2.2 eV to 2.9 eV [189–191]. As a consequence, at low-to-moderate temperatures, these materials have low fluoride-ion defect concentrations and corresponding low ionic conductivities [71,72].

A second class of fluorite-structured materials that exhibit particularly high ionic conductivities are disordered mixed-cation systems, $M'_xM_{1-x}F_2$ [73,113,122,192–195]. The highest ionic conductivity materials in this class are those with different valence cations, such as $RbBiF_4$, where cation disorder induces high levels of anion disorder [193,196]. A significant increase in ionic conductivity compared to analogous single-cation fluorites is also observed for mixed-cation systems where both cations have a formal 2+ oxidation state,

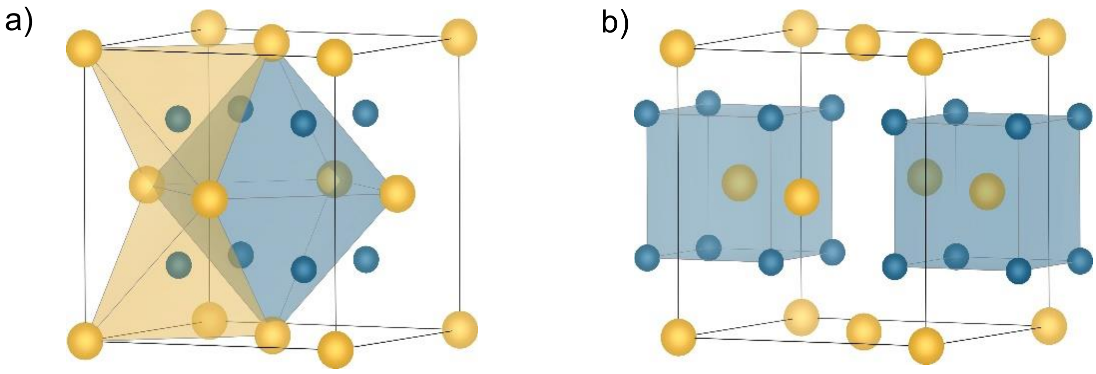

Figure I.1 Schematic of the MF_2 fluorite structure (space group $Fm\overline{3}m$), with the cations in yellow and fluorides in blue, highlighting a) tetrahedral (Wyckoff *8c*) and octahedral (interstitial; Wyckoff *4b*) anion sites and b) cubic cation sites such as $Ba_{1-x}Ca_{1+x}F_2$ [113,114,122]: again, the presence of cation disorder causes considerable fluoride disorder where fluoride ions are displaced significantly from their ideal crystallographic positions to form "pseudovacancies" [113].

Some fluorite materials exhibit both stereoactive lone pairs and cation mixing [150,196–199]. Of particular relevance to the present study is the work of Dénès et al. on $Ca_{1-x}Sn_xF_2$ ($x = 0.27$) [150,197]. For this system, X-ray diffraction (XRD) data show evidence of a cubic fluorite average structure, consistent with a solid solution of Ca and Sn distributed randomly over the cation positions. Additionnally, ^{119}Sn Mössbauer data show a large quadrupole doublet, characteristic of a stereoactive tin lone pair. The presence of a stereoactive tin lone pair requires an asymmetric tin coordination environment, which is inconsistent with the structural model implied by the diffraction data, in which Ca and Sn both have cubic MF_8 coordination (cf. **Fig. I.1** b). To reconcile these apparently contradictory data, Dénès and coworkers proposed a structural model wherein each tin is displaced towards one face of the enclosing $[F_8]$ cube to give square-pyramidal SnF_4E coordination, where E denotes the stereoactive lone pair, with this lone pair oriented towards the more distant $[F_8]$ cube face. These tin lone pairs then are assumed to orient randomly along each possible <100> direction to give an average structure with cubic symmetry, consistent with the experimental diffraction data.

The structural model proposed by Dénès et al. implies that $Ca_{1-x}Sn_xF_2$ exhibits both occupational cation disorder and Sn lone-pair orientational disorder, and similar behaviour might be expected in other mixed-cation fluorites where one cation species has a stereoactive lone pair [198,199]. Such materials are therefore particularly interesting to examine in the context of understanding how these distinct coexisting forms of host-framework disorder together modulate the structure and dynamics of the mobile anion species.

I.2.2. Structural characterisation of the fluorite c-$BaSnF_4$

Cubic $BaSnF_4$ was synthesised by mechanically milling BaF_2 and SnF_2 following the route described in Ref. [152] (see methods, **section I.1.1.**). The X-ray diffraction pattern **Figure I.2** a) indexes to a face-centered cubic structure from the $Fm\overline{3}m$ (225) space group, consistent with an average fluorite-structure. The X-ray pattern shows no visible peaks for the parent SnF_2 (*C*2/*c*) phase, and Energy Dispersive X-ray analysis (EDX-mapping) shows homogeneous distributions for both Sn and Ba. Quantitative analysis of the EDX-mapping data, shown in **Figure I.2** c), gives proportions of Ba and Sn of 49.6(7) % and 50.3(7) %, respectively, which is very close to the nominal 1:1 Ba:Sn stoichiometry.

As a further check on the synthesised compound, we performed electrochemical impedance spectroscopy, and obtained an ionic conductivity at 30 °C of 4.6 10^{-6} S cm^{-1}, with an activation energy of 0.56 eV in the temperature-range (-20 – 50°C) This ionic conductivity is consistent with previous literature values for c-$BaSnF_4$ [152], and is >10^3 higher than that of the fluorite-structured BaF_2 [113], illustrating the positive effect of cation mixing on fluoride-ion transport.

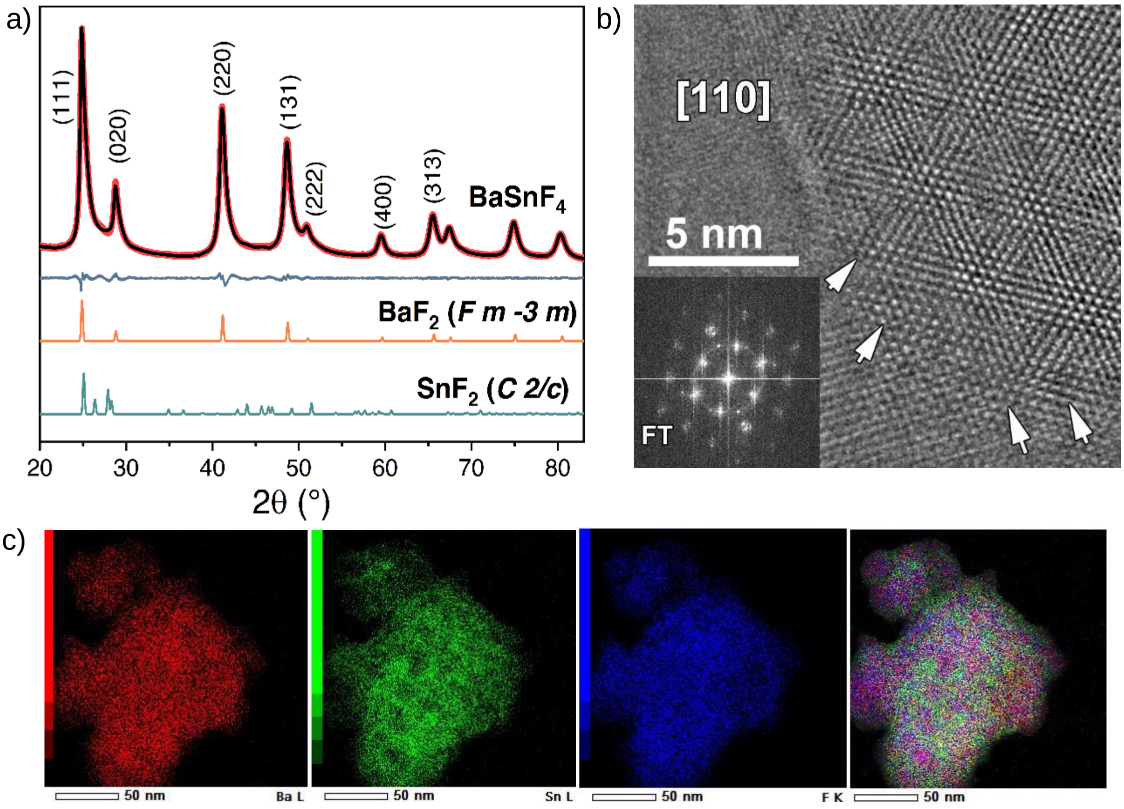

Figure I.2. a) Powder XRD pattern and Rietveld analysis of c-$BaSnF_4$. Reference patterns of the BaF_2 and SnF_2 precursors are presented at the bottom of the panel, b) HRTEM image of c-$BaSnF_4$ c) Distribution of barium (red), tin (green), and Fluoride (blue) within a c-$BaSnF_4$ particle

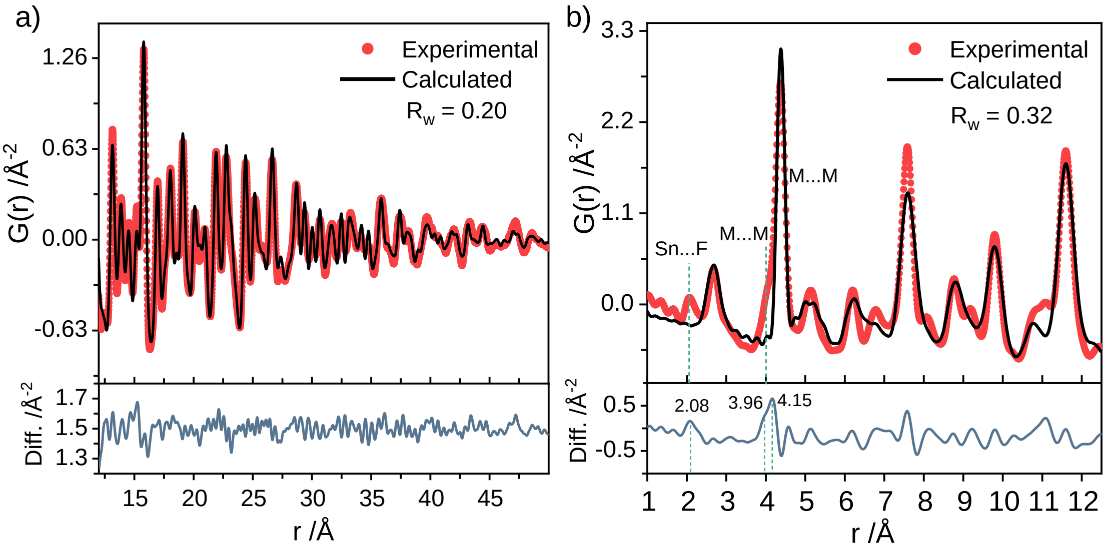

Figure I.3 PDF refinements obtained using a cubic model. a) long-range refinement, b) local-scale refinement, with the main model/experimental discrepancies labelled

Our XRD data show no superstructure reflections, indicating that Ba and Sn are disordered over the cation sites. From indexing the XRD data, we obtain a cell parameter of a = 6.1945(2) Å, which is close to the value for pristine BaF_2 of a = 6.1964(2) Å [200]. This result is somewhat unexpected, given the smaller ionic radius of Sn^{2+} compared to Ba^{2+}, and suggests the possibility of local distortions in the cation substructure. Düvel et al. reported similar excess-volume behaviour in $Ba_{1-x}Ca_xF_2$ solid solutions [113], where this was proposed as a contributing factor to enhanced fluoride-ion transport relative to the end-members. HRTEM data provide further evidence of local deviations from an ideal fluorite-type structure; these show visible changes in inter-reticular distances (**Fig. I.2** b, white arrows) that indicate regions of local strain.

Additional structural information is given by our X-ray total-scattering PDF data. For interatomic distances between 12 Å and 50 Å, the PDF data are relatively well described by a cubic fluorite using a $Fm\bar{3}m$ model (Rw = 20 %; see **Figure I.3** a). At short range, however (between 1 Å and 12 Å; **Figure I.3** b) this high-symmetry structural model gives a poor fit to the PDF data (Rw = 32 %), indicating that the local structure of c-$BaSnF_4$ deviates significantly from an ideal fluorite-type structure. The cubic model fails to predict the peak observed at r = 2.08 Å and the apparent splitting from r = 3.96 Å to

4.15 Å. In other materials containing Sn-F bonds, such as SnF_2 and SnF_4, short Sn–F distances are observed (e.g., 2.28 Å in tetragonal $BaSnF_4$[152], and as short as 2.03 Å in SnF_2 [201]). We therefore provisionally assign the peak at r = 2.08 Å to short Sn–F bonds, which requires that Sn or F, or both species, are displaced from their ideal fluorite positions. **Figure I.4** a) shows the room-temperature ^{119}Sn Mössbauer spectrum for our c-$BaSnF_4$ sample, fitted using parameters summarized in **Table I.1**. ^{119}Sn Mössbauer spectroscopy is a local probe, sensitive to changes in the electron density around the Sn nucleus, and as such, it can give valuable information about the local environment, the oxidation state and the coordination number of tin, as well as the lone-pair stereoactivity. The room-temperature ^{119}Sn Mössbauer spectrum of c-$BaSnF_4$ is displayed in Figure 5.

It features an apparent asymmetric quadrupole doublet with an isomer shift characteristic of divalent Sn, *i.e.*, around 3 mm/s, and large quadrupole splitting parameter ($\Delta > 1.5$ mm/s). The latter is strongly influenced by the electric field gradient at the tin nucleus and by the stereoactivity of the $5s^2$ lone pair, which is usually responsible of an increase of the quadrupole splitting parameter (Δ) value. To understand the origin of the significant doublet asymmetry, a low temperature (77K) measurement was performed (**Fig. I.4** b), which led to a significant decrease in dissymmetry. The asymmetry is hence most likely caused by the Goldanskii-Karyagin (G_{11}) effect, i.e., the anisotropic vibration of the tin nucleus caused by lone pair stereoactivity, which disappears at low temperature.[202] Nevertheless, due to the multiplicity of environments around Sn atoms, the doublet remains dissymmetric at 77 K.

The spectra were reconstructed using two quadrupole doublets with distinct values of isomer shift and quadrupole splitting parameters (**Table I.1**). We note here that the doublet is a convolution of many contributions, representing a wide variety of environments around the tin. It was initially attempted to fit the spectra using only one contribution, but the difference between calculated and experimental data was too great. Hence, the choice to reconstruct it using two contributions was made as it allowed us to extract more reliable information. However, each of these contributions does not account for only one Sn-environment but for a multitude, and is an average of them. The different values of the quadrupole splitting parameters for the two contributions suggest that the different Sn environments may have various degrees of distortion (mainly induced by the stereoactive lone pair).

To gain more insight into the origin of the quadrupole doublet, the ^{119}Sn Mossbauer spectra of the $BaSnF_4$ tetragonal phase and of α-SnF_2 were also recorded at room temperature (**Fig. I.4 c and d**). The contribution 1 hyperfine parameters are very similar to those of the $BaSnF_4$ tetragonal phase, hinting at the existence of similar environments for the tin atoms in the cubic phase i.e., SnF_5E.

The contribution 2 quadrupole doublet is characterized by hyperfine parameters close to those of monoclinic α-SnF_2 (Table 1) where tin occupies the general *8f* Wyckoff position with two possible environments: SnF_5E (square pyramid) and SnF_3E (trigonal pyramid).

The structural model for fluorite $Ca_{1-x}Sn_xF_2$ described in **section I.2.1.** was proposed by Dénès et al, on the basis of experimental XRD and Mössbauer data similar to those reported here[150,197]. This model was also later extended by the same group to c-$BaSnF_4$, though it was not accompanied by the synthesis or characterization of that material.[150] In this model, the presence of a tin stereoactive lone pair causes each tin cation to be displaced towards one face of its enclosing [F_8] cube, giving square-pyramidal SnF_4E coordination with a reduced nearest-neighbour Sn–F distance. This structural model at first appears to be consistent with our XRD and Mössbauer data and hence to provide an explanation for the deviation from the ideal fluorite structure evident in the short-range PDF data described above. The position of the first peak in our PDF data, however, at r = 2.08 Å, is too short to be explained by square-pyramidal SnF_4E coordination within an ideal cubic array of fluoride ions: the shortest possible Sn–F distance from this model is a 2/2 = 2.19 Å. We therefore interpret the PDF feature at r = 2.08 Å as indicative of a significant degree of distortion to the fluorine substructure away from the reference simple-cubic structure. The structural model of Dénès et al. also predicts equivalent SnF_4E coordination for all tin cations, which is inconsistent with the apparent variation in bonding and coordination geometry for tin cations evidenced by the Mössbauer data.

Table I.1 A table containing room temperature ^{119}Sn Mössbauer hyperfine parameters for the two resonances in c-$BaSnF_4$, t-$BaSnF_4$ and α-SnF_2. δ = isomer shift relative to the reference $CaSnO_3$ at RT, ΔEQ = quadrupole splitting, Γ = Lorentzian line split, G11 = Goldanskii-Karyagin factor

Samples	**δ (mm/s)**	**Relative area**	**Δ (mm/s)**	**Γ (mm/s)**	**G_{11}**
c-$BaSnF_4$ (293 K)	3.12(5)	59 %	1.77(5)	0.91(4)	1.27(4)
	3.44(5)	39 %	1.55(6)	0.85(3)	1.26(4)
t-$BaSnF_4$ (293K)	3.19(1)	-	1.65(1)	0.99(1)	1.24(2)
α-SnF_2 (293K)	3.43(1)	-	1.52(1)	0.82(1)	1.29(3)

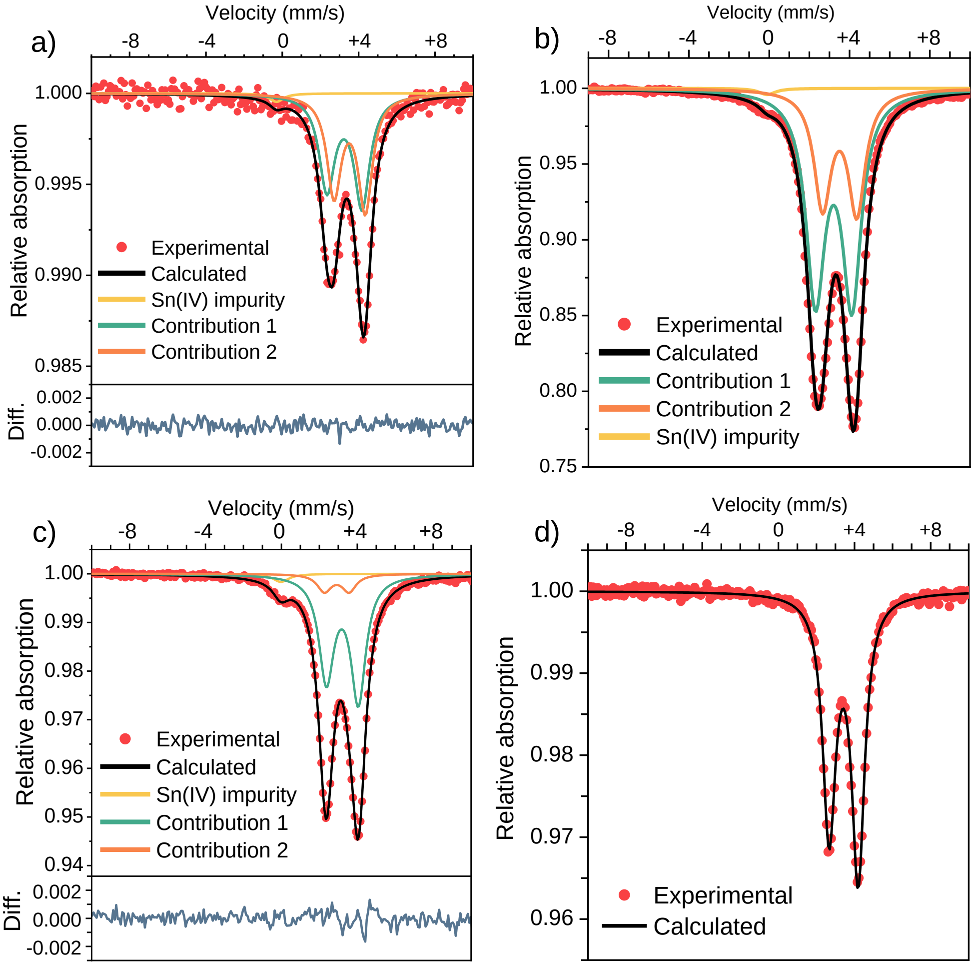

Figure I.4. Mössbauer spectroscopy a) of c-$BaSnF_4$ at 293 K, b) c-$BaSnF_4$ at 77 K, c) t-$BaSnF_4$ at 293 K, d) SnF_2 at 293 K

More detail about the local structure of c-$BaSnF_4$, including the behaviour of the Sn lone pair, is provided by analysing the structures obtained by “quenching” from an AIMD simulation. **Figure I.5** a) shows a (001) cross-section through the electron localisation function (ELF)[171], calculated for a quenched structure from our AIMD simulation. This cross-section intersects with the Wyckoff *4a* positions that are occupied by cations in the perfect fluoride structure. Atoms are visible as regions of non-zero ELF density, and each chemical species, Ba, Sn, and F, has a distinct appearance. Ba are visible as bright symmetric rings that are centered approximately on the *4a* positions, indicating that barium sits close to its ideal fluorite position. Sn appear as less bright rings, with a bright a-centric lobe that corresponds to the stereoactive lone pair. These lone pairs are generally oriented approximately along <100> directions. The Sn centers appear either to be close to the *4a* positions, or, where they are displaced, the displacement appears uncorrelated with the orientation of the lone pair.

We also observe ELF features due to fluoride ions, even though the (001) plane in the figure contains no tetrahedral *8c* sites, and therefore should contain no fluoride ions for a perfect fluorite structure. However, we observe a number of fluoride ions occupying either octahedral or tetrahedral-edge positions, showing a high degree of fluoride-ion disorder.

A more quantitative analysis of the c-$BaSnF_4$ structure is presented in **Figure I.5** c), which shows the probability distributions of cation distances from their closest *4a* site, P [r(M 4a)], for Ba and Sn. Both cation species are, on average, displaced from their corresponding ideal fluorite cation positions, indicating how the cation substructure is locally distorted from a perfect FCC lattice. On average, Sn is displaced further from the nearest *4a* position than Ba, which is consistent with the smaller size of Sn. In general, however, the two probability distribution functions have similar shapes, indicating no qualitative difference between Ba positions and Sn positions relative to their formal crystallographic sites.

Figure I.5 b) shows the radial distribution functions (RDFs), g(r) extracted from the simulated 6*6*6 cell. The RDF of each interatomic distance is weighed against the molecular weight of each atom involved in the pair, as a proxy for the atomic scattering factor. All RDFs are added, yielding an approximation of the PDF diagram of the simulated cell, which we can then compare with the experimental PDF data.

The two are somewhat similar, the main difference residing in peak width, much greater in the simulated PDF due to the small size of the 6*6*6 cell in comparison with the experimental sample, which amplifies the peak widening effect of the local disorder.

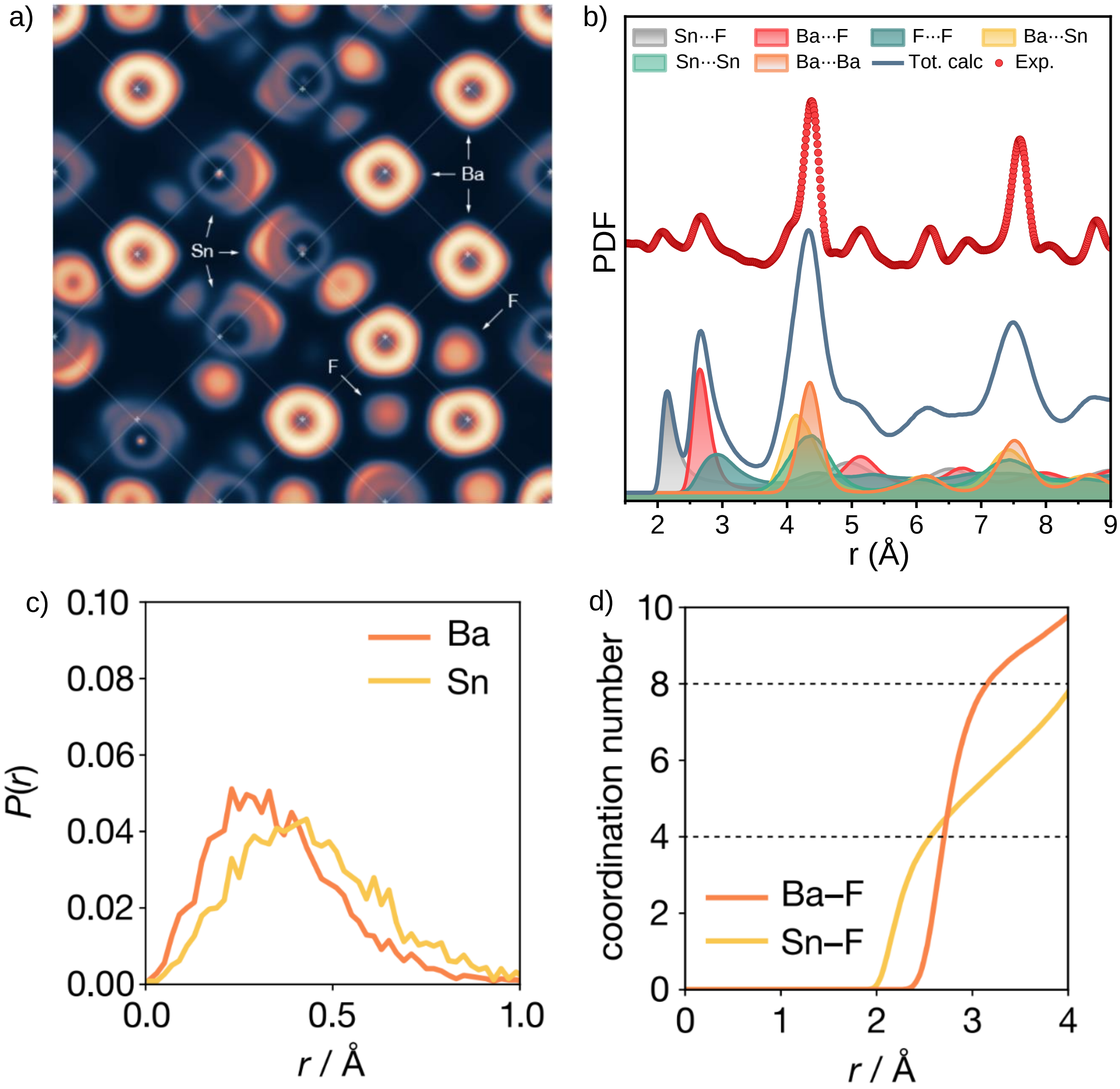

Figure I.5 a) (001) cross-section through the electron localisation function calculated for c-BaSnF$_4$ for a single structure quenched from AIMD simulations. Crosses show ideal cation positions ($F\,m\bar{3}m$ Wyckoff *4a*) for a fluorite ($F\,m\bar{3}m$) structure, b) comparison of the experimental PDF data with the G(r) derived from the AIMD calculations, c) displacement probability P(r) of Ba and Sn from the center of the 4a site, d) coordination number of Ba and Sn with regard to M-F distance

Nevertheless, the RDF shows the nearest neighbour M–F distance to be shorter for Sn (~ 2.1 Å) than for Ba (~ 2.7 Å), confirming our earlier assignment of the feature at 2.08 Å in our PDF. Integrating these RDFs gives cumulative coordination numbers, which are shown in **Figure I.5** d). The coordination number for Ba rises sharply to 8, which is the expected number for fluorite- like MF_8 cation coordination. The coordination number for Sn, however, initially only rises to 4, indicating that, on average, each Sn has only four neighbouring fluoride ions.

Dénès et al. have previously proposed that in $Ca_xSn_{1-x}F_2$, Sn is displaced from the ideal fluorite *4a* position towards one face of an enclsing $[F_8]$ cube, to accommodate the stereoactive Sn lone pair [150,197]. For c-$BaSnF_4$, if Sn were sitting off-center in a well-formed $[F_8]$ cube then the coordination number would show two distinct steps corresponding to [4+4] coordination. The calculated Sn–F coordination number, however, rises continuously after the first step, reaching 8 at 4 Å: the average coordination environment around Sn includes four neighbouring F that occupy *8c*-type positions, with four more F in some diffuse disordered arrangement at distances of 2.3 Å to 4.0 Å. Our data therefore suggest an alternative model for the Sn coordination environment, where the Sn lone pair is accommodated not by Sn being displaced significantly from the *4a* position, but instead by a significant disruption of the fluoride ions on the lone-pair–adjacent face of the nominal $[F_8]$ coordination environment, which presumably reduces the mutual electrostatic repulsion expected between these fluoride ions and the proximate lone pair. Additional evidence for significant disordering of fluoride ions comes from the F–F RDF (**Figure I.5** b), which shows a very weak second peak, more typical of an amorphous glassy phase than a regular crystalline array of atoms.

Figure I.6 shows a section through the time-average fluoride-ion density calculated from our AIMD simulation. The section is centered on a (001) plane of tetrahedral *8c* positions. The superimposed closed and open squares indicate the Ba and Sn atoms, respectively, that tetrahedrally coordinate these *8c* positions. The fluoride-ion density is highly heterogeneous and shows stark qualitative differences between Ba-rich regions and Sn-rich regions. In Ba-rich regions, the fluoride-ion density is well localised around the *8c*

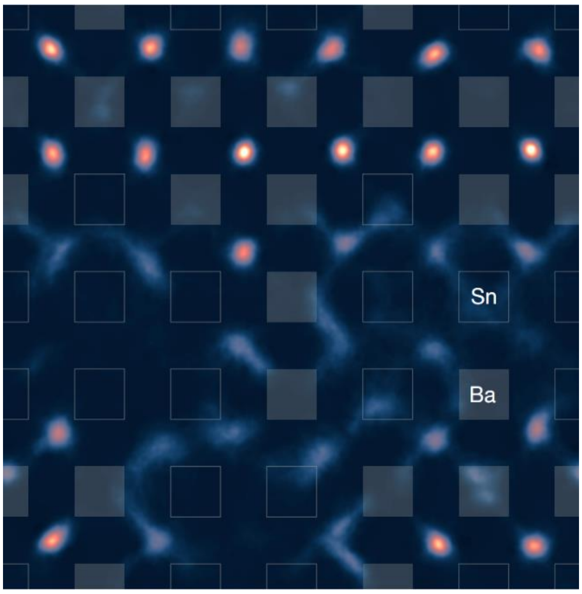

Figure I.6 (001)-projected slice through the time-average fluoride-ion density of c-BaSnF$_4$ from AIMD simulation at 600 K, showing a single plane of tetrahedral sites. Each tetrahedral site is coordinated by four cations (cf. **Fig.I.1** a), which have their projected positions marked by squares. Filled squares indicate Ba positions and empty squares indicate Sn positions.

positions, as expected for a conventional fluorite structure. In Sn-rich regions, however, the fluoride-ion density is highly diffuse, which is consistent with the proposal we mentioned previously, that Sn lone pairs are associated with significant disorder in the local fluoride substructure. These fluoride-ion density data also suggest that the dynamic behaviour of the fluoride ions is strongly dependent on the identity of the nearby cation species: fluoride ions in Ba-rich regions of c-BaSnF$_4$ appear to be relatively immobile, while fluoride ions in Sn- rich regions appear to be much more mobile, and we return to this point below.

To obtain another perspective on the degree of fluoride ion disorder, we project the instantaneous fluoride-ion positions from our AIMD simulation trajectory onto discrete tetrahedral or octahedral sites, defined by the set of Wyckoff *4a* sites that define their vertices. This site projection gives a remarkable 1/3 of fluoride ions occupying octahedral “interstitial” sites rather than conventional tetrahedral sites—i.e., individual octahedral sites are, on average, equally likely to be occupied by fluoride ions than individual tetrahedral sites. This degree of fluoride-ion site-disorder is even greater than the “massive disorder” found in $RbBiF_4$[203], where 1/4 of fluoride ions occupy nominally octahedral positions[204]. Furthermore, this disorder is not simply a large number of thermally generated anion “Frenkel pairs”: quenching from our AIMD simulation produces a 0 K structure with this same proportion of fluoride ions occupying octahedral sites, that is 16.7 meV/atom lower in energy than the corresponding optimised structure with all fluoride ions occupying tetrahedral positions. This extreme fluoride-ion disorder is therefore *intrinsic* to c-$BaSnF_4$.

Figure I.7 a), b), shows the probability distribution (number frequency) of tetrahedral and octahedral sites in our AIMD simulation, subclassified by the number of Ba and Sn cations that coordinate each site. These figures also show the proportion of time during

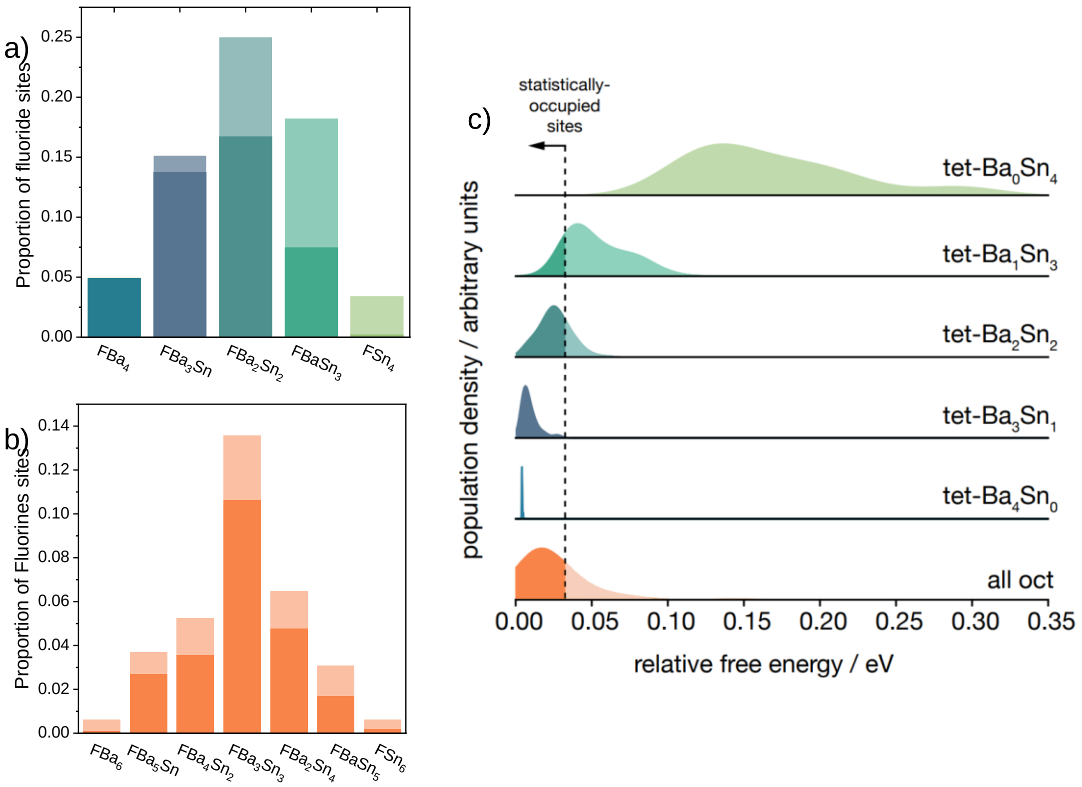

Figure I.7 a) and b) (lighter bars) probability distribution (number frequency) of tetrahedral and octahedral sites in the special-quasi-random AIMD simulation cell, subclassified by the number of Ba and Sn that coordinate each site; (darker bars) normalised probabilities that each site type is occupied by a fluoride ion, calculated from AIMD simulation. (c) Distributions of site-occupation relative free energies, calculated from AIMD, grouped by fluoride-ion site type. Octahedral sites are shown as a single distribution.

the simulation, or probability, that each type of site is occupied by a fluoride ion. For the tetrahedral sites, the occupation probability depends strongly on the identity of the coordinating cations: as the the number of coordinating Sn increases the probability of that site type being occupied by fluorine decreases. Comparing the limiting cases of exclusive Ba-coordination and exclusive Sn-coordination, Ba_4 coordinated sites are occupied nearly 100 % of the time, while Sn_4-coordinated sites are nearly always vacant. In contrast, for octahedral sites, the occupation probabilty depends much less strongly on the identity of the coordinating cations; each type of octahedral site is occupied approximately 2/3 of the time, although we do observe a weak preferential occupation of octahedral sites with equal numbers of coordinating Ba and Sn.

The probability of fluoride-ions occupying a given site can be interpreted as a relative free energy for that site. **Figure I.7** c) shows distributions of per-site relative free energies, calculated for each individual tetrahedral and octahedral site as$\Delta F_{site} = -kT\ln(P_{occ})$ where k is the Boltzmann constant, T is the simulation temperature, and P_{occ} is the probability of each site being occupied, calculated from the AIMD simulation. These distributions can be thought of as effective “densities-of-states” of the different tetrahedral and octahedral site types. In **Figure I.7** c), we also show a vertical line corresponding to the point where 2/3 of all available sites are statistically occupied, assuming that sites are preferentially occupied in order of increasing relative free energy.

In a conventional fluorite, the tetrahedral sites are low energy, and the octahedral “interstitial” sites are higher energy. Moving an anion from a tetrahedral site to an octahedral site increases the total system energy, and forming Frenkel pairs is therefore a thermally activated process. **Figure I.7** c) illustrates how this conceptual model breaks down in c-$BaSnF_4$, where the relative free energy of tetrahedral sites increases with increasing Sn coordination. For sites with two or more coordinating Sn, some proportion of these sites are spontaneously depopulated, with the corresponding fluoride ions instead preferentially occupying octahedral sites. For Ba_1Sn_3 and Sn_4 coordinated tetrahedral sites, this effect is large enough that these sites are nearly fully depopulated, contributing to the high octahedral-site occupation. This behaviour is consistent with a model where Sn lone pairs repel fluoride ions from adjacent tetrahedral sites, forcing these ions to instead occupy octahedral sites. The analysis presented here also indicates that this effect is additive; the more Sn cations coordinating a given tetrahedral site, the stronger the effective repulsion, and the greater the bias to spontaneously depopulate these sites.

I.2.2. Fluoride-ion dynamics

Having characterised the structure of c-$BaSnF_4$, we now consider the fluoride ion dynamics, and how this is affected by the structural features described above, first using ^{19}F MAS NMR spectroscopy, and second by further analysis of our AIMD simulations. In $M'_xM_{1-x}F_2$ mixed-cation fluorites with no stereoactive lone pair, such as $Ca_xBa_{1-x}F_2$, ^{19}F MAS NMR spectra show five distinct features corresponding to tetrahedral fluorine environments with different combinations of neighbouring cation species, i.e. $FM_{4-x}M'_x$ (x = {0, 1, 2, 3, 4}) [122,205,206]. The ^{19}F MAS NMR spectrum for c-$BaSnF_4$ instead shows only two distinct contributions at −14 ppm and −45 ppm (**Figure I.8** a). The first of these peaks has a δ_{iso} value close to that of BaF_2 (−14.2 ppm), where fluoride ions have occupied Ba_4 coordinated tetrahedral sites. The second peak aligns with the average δ_{iso} value of α-SnF_2 (−46 ppm) [207], in which fluorine is triply coordinated with short Sn–F distances [208]. Based on these comparisons, we assign these features at −14 ppm and −45 ppm to broadly Ba-rich and Sn-rich fluorine environments, respectively. The assignment of fluorine environments into broadly two types is qualitatively consistent with the computational fluoride-ion density data (**Figure I.7**), where we observe quite different fluoride-ion densities in Ba-rich versus Sn-rich regions of our simulation model.

Our XRD data presented in **Fig.2**. a), indicate that Ba and Sn are randomly distributed across the fluorite *4a* cation sites, and our AIMD simulations predict a complex fluorine sub structure. Both results imply that c-$BaSnF_4$ contains a rich variety of fluoride-ion environments, which might be expected to be observable in the experimental ^{19}F MAS NMR spectrum; and yet we observe only two peaks. This apparent contradiction can be reconciled with our expectation of a complex fluorine substructure if we consider fluorine exchange between different sites within the host framework. Fluorine exchange between Ba-rich sites can cause individual peaks associated with different Ba-rich environments to coalesce, giving a single observed resonance. The same reasoning applies to Sn-rich environments, suggesting that they too exhibit fluorine exchange on the NMR timescale.

A third type of fluorine exchange is that between Ba-rich and Sn-rich environments, which we probe using variable-temperature ^{19}F MAS NMR spectroscopy. **Figure I.8** b) shows spectra recorded at 40 °C, 65 °C and 90 °C. As the temperature increases, the relative intensity of the peak assigned to fluoride ions in Sn-rich environments also increases, from 54 % to 60 %, at the expense of the peak assigned to fluoride ions in Ba-rich environments, confirming some degree of fluoride-ion exchange between Ba-rich and Sn-rich environments. For a simple two-site exchange between Ba-rich and Sn-rich environments, increasing temperature would be expected to produce a broadening of the associated resonances before their coalescence into a single resonance with an intermediate chemical shift. We do not observe such behaviour, and instead the peaks assigned to Ba-rich and Sn-rich fluorine environments remain distinct across the investigated temperature range. This behaviour is consistent with only some fraction of fluoride ions in Ba-rich environments undergoing exchange with ions in Sn-rich sites, with this fraction gradually increasing with temperature, and with this Ba-rich–Sn-rich exchange process being slower than exchange between different Sn-rich

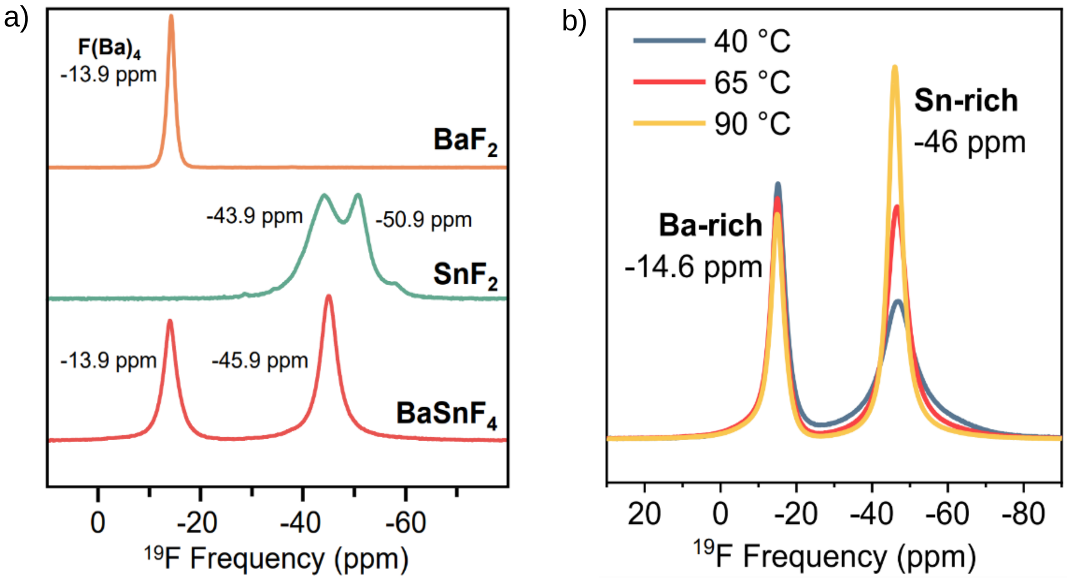

Figure I.8 a) ^{19}F MAS (64 kHz) NMR spectra of c-BaSnF$_4$ and its precursors BaF$_2$ and α-SnF$_2$. b) Variable-temperature ^{19}F MAS (30 kHz) of c-BaSnF$_4$ recorded at 40 °C, 65 °C and 90 °C.

environments[209]; i.e., on the same timescale of exchange between Ba-rich and Sn-rich environments, fluoride ions in Sn-rich environments undergo exchange between several different Sn-rich environments. The observation that fluoride ion exchange between Sn-rich environments is much faster than that between Ba-rich environments or between Ba-rich and Sn-rich environments is further supported by the observation of motional narrowing of the Sn-rich peak with increasing temperature, indicating that the so-called fast-exchange regime is reached. This picture of locally inhomogeneous fluoride-ion dynamics is also qualitatively consistent with the time-average fluoride-ion density obtained from AIMD (**Fig. I.6**), where Ba-coordinated regions show highly localised fluoride-ion density, indicative of significantly fewer mobile ions, while Sn-coordinated regions show diffuse interconnected fluoride-ion density, suggesting more facile fluoride-ion motion between these sites.

To validate this model of faster fluoride-ion motion in Sn-rich regions, we performed additional analysis of our AIMD data to calculate site–site transition frequencies for each

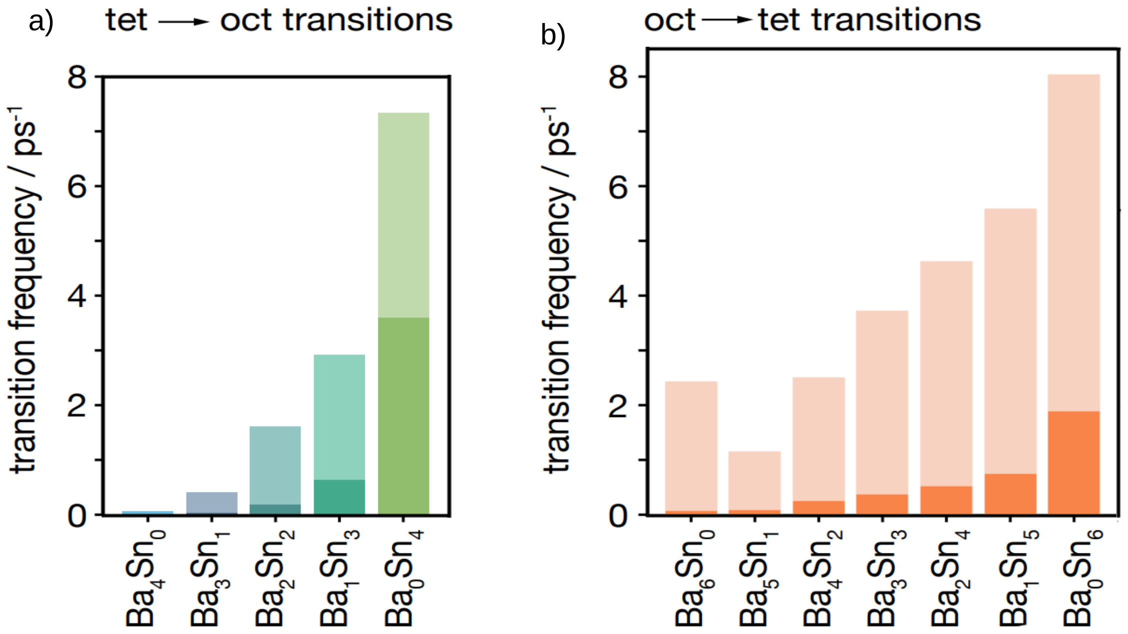

Figure I.9 Site–site transition frequencies for fluoride ions in a) tetrahedral sites, and b) octahedral sites, classified according to the cation nearest-neighbours. Transition frequencies are normalised with respect to their time-average occupations, giving frequencies that are equivalent to inverse average site occupation times. Lighter bars show data for all transitions and darker bars show data only for “non-returning” transitions, as described in the main text type of tetrahedral and octahedral site. To estimate the degree to which these fluoride-ion site–site transitions contribute to long-range diffusion, rather than simple back-and-forth motion between adjacent sites, we also calculated frequencies of “non-returning” transitions; these are transitions between two sites, 1 → 2, where the next transition made by the mobile ion takes it to a third site, 1 → 2 → 3, rather than returning it to the original site, 1 → 2 → 1.

The calculated site–site transition frequencies for tetrahedral and octahedral sites as a function of their Ba/Sn coordination are shown in **Figure I.9**, normalised by the proportion of time each site type is occupied—this normalisation gives transition frequencies that are equivalent to average inverse residence times; higher transition frequencies correspond to fluoride ions leaving a particular site more quickly. The calculated site–site transition frequencies for both tetrahedral and octahedral sites generally increase with increasing degree of Sn-coordination, with this effect being particularly strong for the tetrahedral sites. These data from AIMD simulation, therefore, are consistent with the model inferred from the variable-temperature NMR and fluoride-ion time-average density data (**Figs. I.6** & **I.8** b): fluoride ions in “Sn-rich” sites are, in general, more mobile than fluoride ions in “Ba-rich” sites.

I.2.3. Sn lone pair dynamics

The ^{19}F MAS NMR and AIMD data presented above show that the local mobility of fluoride ions in c-$BaSnF_4$ is strongly dependent on the local cation composition: fluoride ions in Sn-rich environments are significantly more mobile than those in Ba-rich environments. An obvious partial explanation for this behaviour is that the stereoactive lone pairs on tin cations somehow promote the motion of fluoride-ions in adjacent tetrahedral and octahedral sites. Our calculated time-average fluoride-ion density (**Figure I.6**) shows that the fluoride-ion substructure is highly diffuse in Sn-rich regions, which further suggests a possible direct interaction between the Sn lone pairs and the mobile fluoride ions.

To quantify the degree of spatial correlation between the Sn lone pairs and nearby fluoride ions, we have calculated the lone-pair–fluoride-ion polar spatial distribution

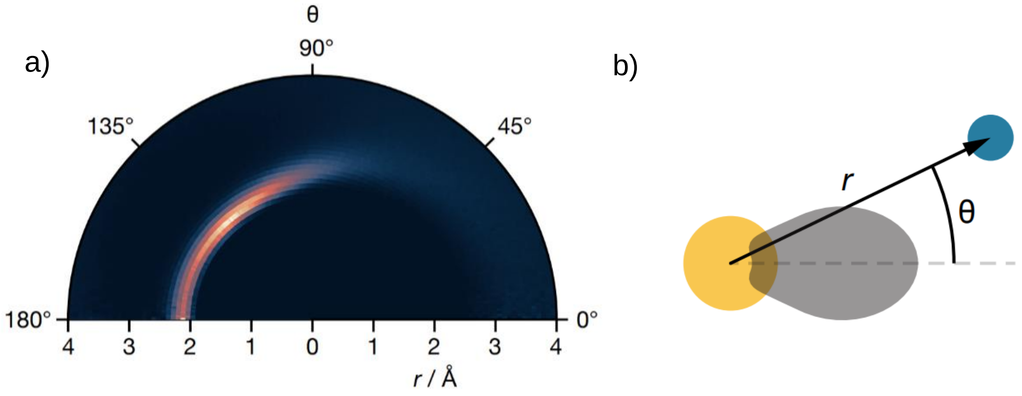

Figure I.10 Sn–lone-pair–fluoride-ion polar spatial distribution function, g(r, Θ), for c-$BaSnF_4$, calculated from AIMD simulation

function g(r, θ) (**Figure I.10**) This distribution function describes the time-average fluoride-ion coordination environment around tin, as a function of distance from the central tin cation, r, and the angle between the Sn–F vector and the lone-pair–orientation vector, θ. On the reverse side of the central tin from the lone-pair, there is a clear feature at r = 2.1 Å with maximum intensity at 135°, i.e., the position of the tetrahedral *8c* site if the lone pair is oriented towards the center of the opposite cube-face. On the lone-pair side, however, there is a distinct lack of structure, and fluoride density is instead smeared out in a broad region from r > 3 Å. This distribution function is consistent with the model proposed from inspection of the time-average fluoride-ion density plot (Fig. I.6): the Sn lone pair is preferentially oriented towards one face of the enclosing cubic site, and fluoride ions that would occupy the corners of this face in a perfect fluorite structure are repelled by the lone pair, which strongly disrupts the fluoride structure in the vicinity of the lone pair.

Another notable feature of the lone-pair–fluoride-ion patial distribution function is that the intense feature corresponding to fluoride ions occupying tetrahedral sites is angularly diffuse. While some of this effect can be attributed to movement of these fluoride ions within their tetrahedral sites, it would be surprising for such movement to preserve the Sn–F separation. An alternative process that provides an explanation for the angular form of this feature is that the tin lone pair is reorienting relative to the reference fluorite lattice on a simulation timescale. To quantify any lone-pair reorientation

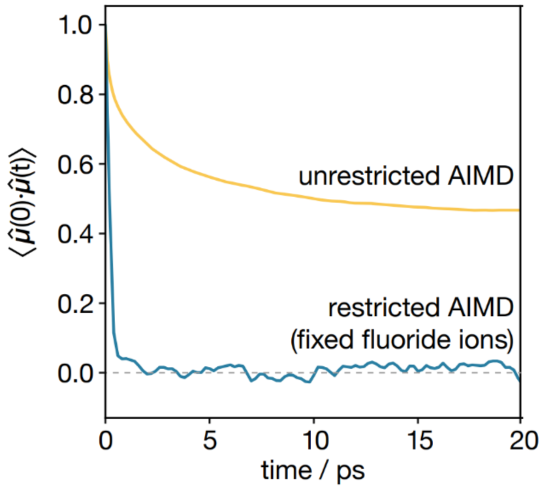

Figure I.11 Sn-dipole orientational autocorrelation function for c-$BaSnF_4$, for unrestricted AIMD, and for AIMD with fixed position fluoride ion

dynamics, we calculated the Sn-dipole orientational autocorrelation function$< \hat{\mu}(0) \cdot \hat{\mu}(t) >$, which describes the average change in relative orientation of the stereoactive lone pairs in time *t*. This autocorrelation function (**Figure I.11**) shows a clear decay on a picosecond timescale, showing that tin lone pairs in c-$BaSnF_4$ undergo dynamic reorientation.

The Sn-dipole orientational autocorrelation function does not decay to zero. Therefore, on average, the orientation of each tin lone pair is biased, with the lone pair more likely to point in one particular direction than in another. Plotting individual dipole-orientation autocorrelation functions for each lone pair (see the Supporting Information) shows that the strength of this bias varies significantly across tins, indicating that the degree of orientational bias is sensitive to the local tin environment.

To probe the degree to which the local tin environment directs the orientational bias for individual tin lone pairs, we calculated, for each lone pair, the proportion of time that this lone pair points towards each face of the enclosing cubic site. Each Sn has 12 cations nearest-neighbours arranged in a cuboctahedron (**Figure I.12** panel a). For a given <001> vector from the central Sn, four of these cations are infront of the central Sn, and coordinate the fluoride sites on the front-face of the Sn *4a* site, and four of these cations are behind the central Sn, and coordinate the fluoride sites on the back-face of the Sn *4a* site—the other four neighbouring cations occupy the same (001) plane as the central Sn.

Because the local fluorine environment depends on the arrangement of the nearby Sn and Ba cations, we consider the numbers of Ba and Sn cations coordinating the front-face and back-face of each tin as effective descriptors for the degree to which a particular tin has a symmetric or asymmetric local coordination environment

In **Figure I.12** b) we show the distribution of time a lone pair points towards a particular face of its cubic site, depending on the number of tins amongst next-nearest neighbours. These next-nearest neighbours are divided into two categories, depending on whether they coordinate the "front face" or "back-face" of the tin cubic site (see **Figure I.12** panel b).

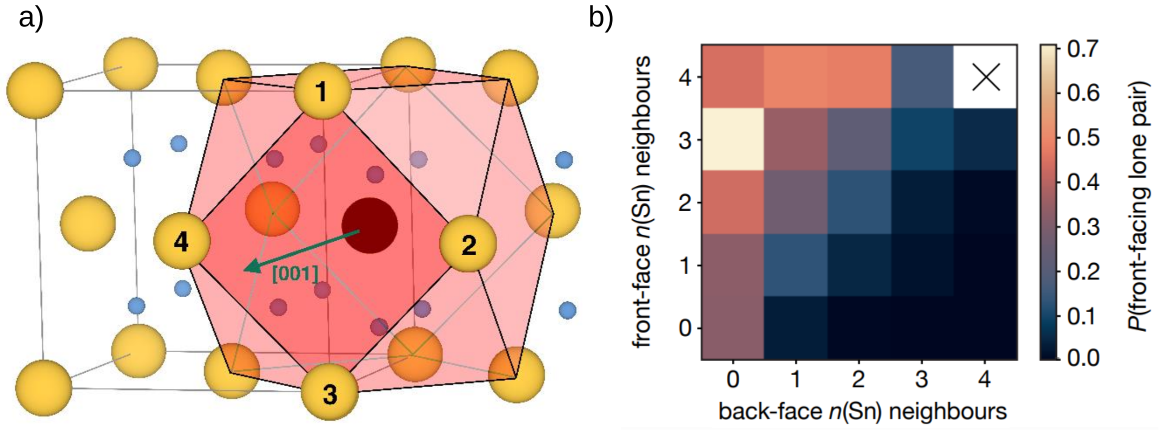

Figure I.12. a) octahedron formed by next-nearest cationic neighbours neighbours around the cationic *4a* sites b) Heat-map for the proportion of time that a Sn lone pair is oriented towards a particular face of the cubic cation site, as a function of the number of nearest-neighbour tins in the {001} plane adjacent to the front-face of the cubic site (with respect to the lone pair orientation) and the number of nearest-neighbour tins in the plane {001} plane adjacent to the back-face of the cubic site (with respect to the lone pair orientation)

Data on the diagonal where $n_{(Sn,)front} = n_{(Sn),back}$ correspond to lone pair orientations with symmetric front-face/back-face nearest-neighbour cation environments. These data all show relatively low values, indicating that lone pair orientations with balanced cation coordination are weakly or negligibly biased. In contrast, lone pair orientations with more front-face Sn neighbours than back-face Sn neighbours show a strong bias. As a consequence, the stereoactive Sn lone pairs in c-$BaSnF_4$, on average, tend to point towards other nearby tins. Clusters of Sn cations are therefore expected to have all their lone pairs preferentially oriented towards the interior of the cluster, giving a cooperative effect where these Sn lone pairs all disrupt any fluoride ion occupation of mutually coordinated tetrahedral sites. This model is consistent with the increasing tetrahedral site free energy with increasing Sn-coordination (**Figure I.7**) and provides an explanation for the extreme disruption of the fluoride substructure in Sn-rich regions, as observed in the fluoride-ion time-average density (**Figure I.6**).

The timescale for lone-pair reorientation is similar to the timescale of fluoride-ion site-site transitions, which suggests possible coupling between these two kinds of dynamics. To examine whether the fluoride ion dynamics and lone pair dynamics are, in fact, coupled, we performed an additional AIMD simulation with all fluoride ions fixed at their ideal fluorite positions, and calculated the corresponding Sn-dipole orientational auto-correlation function. With the fluoride ions fixed, the lone-pair orientational auto-correlation function decorrelates within a sub-picosecond timescale, decaying to a rotationally symmetric (unbiased) value of zero.

This rapid decay of the Sn-dipole orientational auto-correlation function when the fluoride positions are fixed suggests that fluoride-ion dynamics and lone pair dynamics are strongly coupled. When the fluoride ions are fixed to their *8c* lattice positions, the lone pair moves freely—no matter which direction it points in there is a strong lone-pair–fluoride repulsion. When the fluoride ions are free to move, however, a number of these fluo- ride ions move from unstable tetrahedral sites into more favourable octahedral sites, leaving vacant tetrahedral sites next to tin. The Sn lone pair then preferentially orients towards these vacant sites to minimise the lone-pair–fluoride repulsion. As fluoride ions move between sites, the Sn lone pairs dynamically reorient in response to the changing local fluoride ion configuration, giving strong coupling between the fluoride-ion dynamics and the lone-pair reorientation dynamics.

Summary and Conclusions

(M, Sn)F_2 fluorites have previously been proposed by Dénès et al. to exhibit two distinct forms of host-framework disorder : cation–site-occupation disorder, where the two cationic species are distributed randomly over the available sites; and Sn–lone-pair orientational disorder, where Sn exhibits stereoactive lone pairs with random orientations. This proposed coexistence of two distinct forms of host-framework disorder makes (M, Sn)F_2 fluorites an interesting focus of study in the context of understanding the possible interplay between disorder types, and how, together, they modulate ion transport.

Here, we have investigated the structure and fluoride-ion dynamics of the cation-disordered fluorite cubic (c-)$BaSnF_4$. Rietveld refinement of XRD data confirmed an average fluorite structure with (Ba,Sn) disorder. ^{119}Sn Mössbauer spectroscopy demonstrates the presence of stereoactive Sn(II) lone pairs, and total-scattering PDF data show clear deviations from the average fluorite structure at short range.

Using ab initio molecular dynamics (AIMD) simulations, we have shown that the fluorine substructure in c-$BaSnF_4$ is highly inhomogeneous and depends strongly on the local cationic composition. In Ba-rich regions, the fluoride ions occupy fluorite-like tetrahedral sites. In Sn-rich regions, in contrast, the fluoride-ion substructure is highly diffuse, with fluoride ions displaced from tetrahedral sites adjacent to tin into the octahedral interstitial sites.

We attribute the displacement of fluoride ions from tin-adjacent tetrahedral sites into octahedral interstitial sites to the presence of the stereoactive lone pair on the tin cations. The lone-pair destabilises fluoride ions occupying tetrahedral sites adjacent ton tins, in effect pushing these fluoride ions into octahedral sites, thereby strongly disrupting the fluoride-ion substructure. As a consequence of this Sn–lone-pair–fluoride-ion repulsion, c-$BaSnF_4$ exhibits a remarkable concentration of “interstitial” fluoride ions that occupy octahedral sites. In our simulations, 1/3 of fluoride ions occupy octahedral sites. This level of octahedral-site occupation exceeds that of previously reported “massively disordered” fluorites, such as $RbBiF_4$, where 1/4 of fluoride ions occupy octahedral sites.

We have also directly probed fluoride ion dynamics and the effect of cation disorder using variable-temperature ^{19}F MAS NMR experiments and additional analysis of our AIMD data. Our NMR data show that fluoride ions in c-$BaSnF_4$ can be broadly categorised as residing in either “Ba-rich” or “Sn-rich” environments, with fluoride ions in Sn-rich environments more mobile than fluoride ions in Ba-rich environments. This picture of cation environment–dependent fluoride-ion dynamics is corroborated by our AIMD simulations: calculated site–site transition frequencies are higher for sites with a higher proportion of coordinating tin, showing a direct relationship between the local cation configuration and local anion dynamics.

Our AIMD simulations also reveal that the tin lone pairs dynamically reorient on a picosecond timescale, and that this orientational dynamics is coupled to the dynamics of the nearby fluoride ions. This effect is modulated by the local cation arrangement: for tins with an asymmetric Sn/Ba nearest-neighbour configuration, the tin lone pair preferentially orients in the direction of other, nearby, tins. Hence, clusters of tin cations exhibit a cooperative effect where by the lone pairs on each tin tend to orient towards the interior of this cluster. This cooperative effect explains the dramatic disruption of the fluoride ion substructure in regions where several Sn cations are clustered together.

The results presented here demonstrate the complex interplay between two distinct forms of host-framework disorder (cationic site-occupation disorder and lone-pair orientational disorder) and the structure and dynamics of the mobile ion species within a fluoride-ion–conducting solid electrolyte. The complex nature of these interacting effects suggests that the resulting effect on mobile-ion dynamics is likely to be highly dependent on the exact composition and structure of the solid electrolyte, as will be explored in the next chapter.

Chapter II

Effect of the cation nature in $MSnF_4$ (M = Ba, Sr) on the stereoactivity of tin lone pairs and dynamics of the fluoride-ion sublattice

Introduction **67**

II.1. Comparative study: from c-$BaSnF_4$ to c-$SrSnF_4$ 68

- II.1.1. Synthesis route of c-$SrSnF_4$ 68
- II.1.2. Local structure study of c-$SrSnF_4$ 73
- II.1.3 Transport properties evolution with the substitution of barium for strontium in c-$MSnF_4$ 79

II.2. A perspective: introducing additional cationic disorder in the $Ba_{1-x}Sr_xSnF_4$ mixed cation solid solution 83

- II.2.1. Synthesis of cubic $Ba_{1-x}Sr_xSnF_4$ 83
- II.2.2. Conductivity in $Ba_{1-x}Sr_xSnF_4$ 85

Conclusion.. 87

Introduction

After characterizing and understanding the structure and conductivity mechanisms in c-$BaSnF_4$, we will now turn to a similar system (with M = Sr) and attempt to highlight similarities and differences. In c-$BaSnF_4$, we found that the tin lone pair stereactivity was at the center of both the local structure and the ionic transport mechansim. The electrons of this lone pair push 1/3rd of the F-ions into the octahedral interstitials sites, resulting in a material with both cationic and anionic disorder. Both tetrahedral and octahedral sites are also distorted, as Tin is displaced from the center of its *4a* site through repulsion between the lone pair and neighbouring fluorides. This facilitates the diffusion of F-ions through the bottlenecks (see **Figure II.1.**).

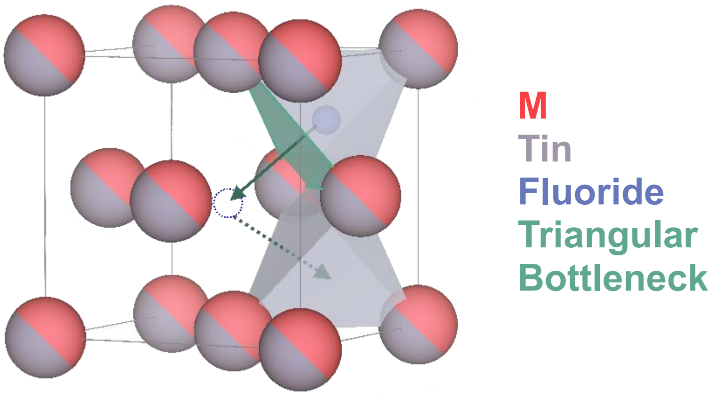

Figure II.1 Diffusion pathway of F-ion, jumping from tetrahedral site through the bottleneck to an octahedral interstice, and through a second bottleneck to an empty tetrahedral site. The immobile F-ions in this cell were removed for clarity. We note that F-ions do not necessarily pass through the centre of the Oct sites.

SrF_2 crystallizes in a fluorite structure, isostructural to BaF_2: Sr(II) cations are located in *4a* sites, while F-ions sit on the tetrahedral *8c* sites. The 11% size difference between Ba(II) (r = 1.42 Å) and Sr(II) (r = 1.26 Å) leads to a decrease in lattice volume of 17%, from V_{BaF2} = 237.91 Å^3 to V_{SrF2} = 195.06 Å^3.[210,211] The difference in size is expected to have a significant effect on the reactivity of MF_2 towards SnF_2, as there is a large size difference between Sr and Sn, which is generally considered a barrier to ionic substitution. Additionally, volumetric variations within similar structures are known to impact ionic conductivity. This expansion is also concomitant with an increase of the "host framework" (lattice formed by the immobile cations) polarizability, which, in fluorites, can facilitate ion transport.[212]

Hence, we will here study another member of the $MSnF_4$ structural family: $SrSnF_4$. We compare it to $BaSnF_4$ and discuss how the lattice contraction affects the tin lone pair, fluoride-ion lattice, and, by extension, transport properties.

II.1. Comparative study: from c-$BaSnF_4$ to c-$SrSnF_4$

As far as we are aware, the reactivity between SrF_2 and has only been reported on once, and the end product was a cubic phase with an impurity.[213] We therefore started our $SrSnF_4$ study by attempting to obtain the pure cubic phase c-$SrSnF_4$.

II.1.1. Synthesis route of c-$SrSnF_4$

The first synthesis attempts to obtain a strontium-based material isostructural to $BaSnF_4$ were made using the same milling parameters as those used for $BaSnF_4$ (ball:powder ratio of 13:1, 40 mL jars made from Zirconia, ball-milling cycles of 15:15 milling:pause for 12h). However, as displayed below **Figure II.2**, a), the resulting product had a significant amount of impurities, implying that the energy necessary for a complete reaction between BaF_2 and SnF_2 is lower than in the case of SrF_2 and SnF_2. This difference in reactivity could be related to both the smaller volume of SrF_2 and the lower polarizability of Sr compared to Ba,[214] which lead to a "harder" SrF_2 lattice.[215] Tin ions would then have more difficulties to replace the strontium in the cationic sites.

In order to obtain pure c-$SrSnF_4$, we modified the milling parameters, so that more energy would be transferred into the particles. This may be achieved through higher ball:powder (B:P) ratios, larger volume in ball-milling jars, higher ball-milling speeds or longer milling

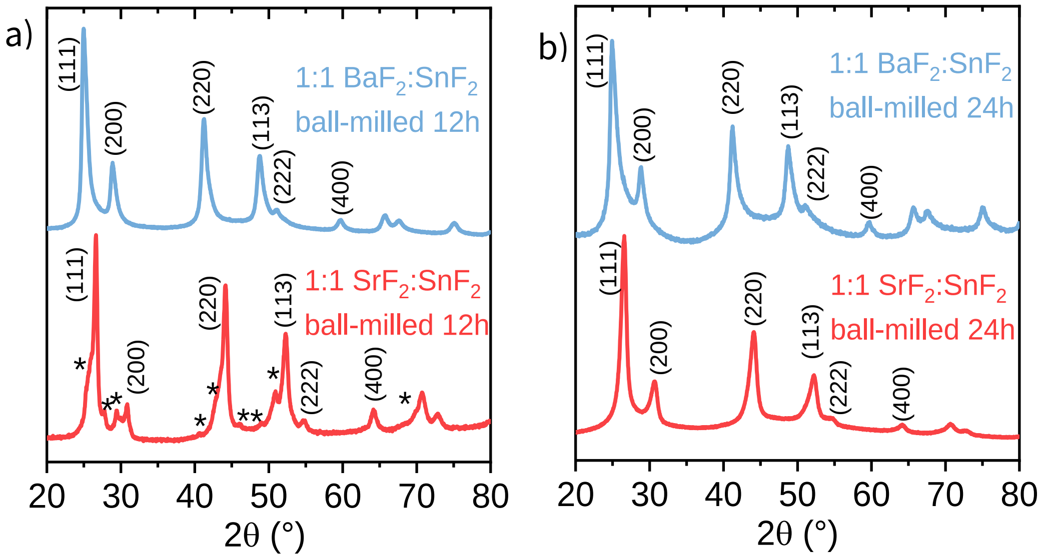

Figure II.2. Synthesis of the $Sr_{2-x}Sn_xF_4$ fluorite. a) XRD diagram of a 1:1 MF_2:SnF_2 global composition after using the c-$BaSnF_4$ ball-milling parameters (ball:powder ratio of 13:1, 40 mL jars made from Zirconia, ball-milling cycles of 15:15 milling:pause for 12h) b) with same ball-milling parameters, with longer milling of 24h.

times. Some tests were made varying these parameters, but, in most cases, the higher energy deployed during the synthesis caused the milled powder to turn orange and a black deposit was found on the sides of the jar. Only milling time changes did not cause the same issue, we therefore opted to increasing gradually the synthesis length. For each milling time, we recorded the XRD diagram of the product and determined the purity of the material by focusing on the (111) XRD peak. At this 2Θ, for uncomplete reactions, both the (111) fluorite peak and the (112) peak of unreacted SnF_2 (the most intense ones for each phase) are visible. We used this region as an indicator, fitting the (111) peak with either one or two phases. If the two-phase fit was significantly better, we deemed the reaction incomplete. An example is shown in **Figure II.3**. Finally, milling the 1:1 Sr:Sn mixture for 24h yielded to a single phase (**Figure II.2.**b).

It is interesting to compare this material with its isomorph c-$BaSnF_4$. In order to carry out this comparison between to materials as similar as possible, we applied the c-$SrSnF_4$ synthesis parameters to c-$BaSnF_4$.

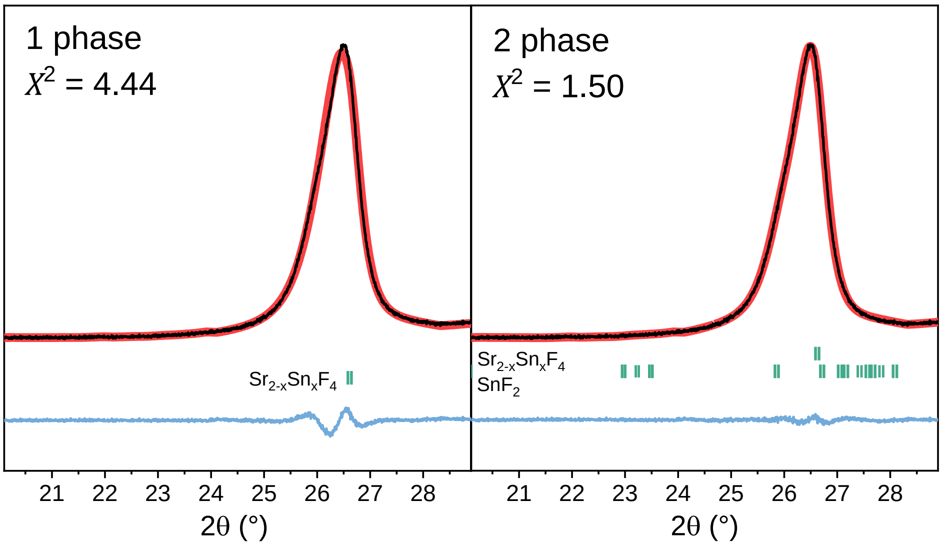

Figure II.3 fitting of the (111) peak with, on the right, one phase, FCC $Sr_{2-x}Sn_xF_4$, resulting in a visible discrepancy on the difference curve, and on the left, two phases, FCC $Sr_{2-x}Sn_xF_4$ and α-SnF_2, leading to a very flat difference curve.

For the same milling times, the barium-based fluorite showcases significantly wider peaks (**Figure II.4**), with strong and unusual asymmetry. Taking the (111) peak as an example, in $BaSnF_4$ the peak tail points to higher angles, whereas in $SrSnF_4$ it points towards the opposite direction. Asymmetry and peak width are usually linked to crystallite size and micro-strain effects. In this case, the peak features are likely to be related to both phenomena. For instance, in $BaSnF_4$, the bump in the background at ~47° strongly suggests there is an amorphization of the fluorite, which should come with smaller crystallite sizes, thus larger peaks. It is however difficult to explain why this amorphization should take place only in one of the two materials.

We first hypothesized that it could be related to differences in the fluorite precursors, however the crystallite domain sizes of both fluorite precursors were determined via Williamson-Hall diagrams to be similar, around 32 nm and 46 nm for BaF_2 and SrF_2 respectively. Alternatively, it is possible that the previously-described higher lattice softness of BaF_2 could be responsible for its higher tendency to amorphize upon milling.

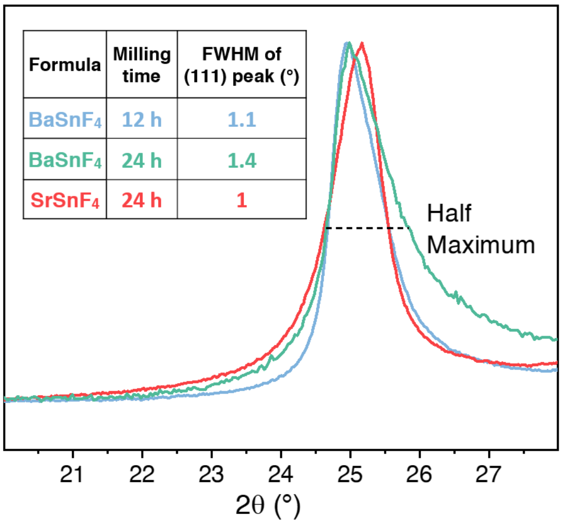

Formula	Milling time	FWHM of (111) peak (°)
$BaSnF_4$	12 h	1.1
$BaSnF_4$	24 h	1.4
$SrSnF_4$	24 h	1

Figure II.4 Comparison of the (111) Full Widths at Half Maximum (FWHM) of $BaSnF_4$ and $SrSnF_4$ at different milling times. We note that all peaks were shifted in 2Θ to facilitate the comparison

Similarly, the difference in asymmetry could also be related to the natures of both cations. Barium(II) has an ionic radius of r = 1.42 Å, leading to Ba-F distances of 2.68 Å. In the strontium fluorite, Sr-F distances are 2.51 Å. As Sn-F distances are usually smaller, the introduction of Sn in the structure may lead to more local deformations, such as the ones described in chapter I, in $BaSnF_4$, due to a larger gap between Ba-F and Sn-F distances. This increase in local strain would then be reflected in the XRD diagrams as asymmetry and larger peaks. Normally, strain and crystallite domain size would be determined through Williamson and Hall diagrams.[216] In these cubic phases, this method was not applicable as the obtained Williamson-Hall diagrams had distinctly negative slopes, which would lead to a negative strain value with no physical meaning. This phenomenon was reported before, and attributed to a combination of very small particle size and high strain, conditions which should both be fulfilled in these ball-milled materials.[217] Therefore, instead of using integral breadths and Williamson-Hall diagrams to compare quantitatively these materials, we used a more qualitative approach and instead opted to focus on the full width at half maximum of the (111) peaks.

As shown above in **Figure II.4**, for similar milling times, the full width at half maximum of the (111) peak for c-$BaSnF_4$ materials are significantly larger than they are for the strontium-based fluorites. It is then evident that barium-based c-$MSnF_4$ are significantly more strained and/or have smaller particles. Because both of these characteristics are generally considered to affect ionic diffusion,[51,218,219] we decided to compare a strontium and a barium tin fluorite with different milling times but similar full widths at half maximum when later investigating transport properties.

In addition to not fulfilling the conditions to be analysed through the Williamson and Hall method, the unusual peak shapes complicate the fitting of the XRD diagrams, and require the use of the function 'Split Pseudo-Voight' for Le Bail refinements. Under these circumstances, each peak is split in two in its middle and each half simulated via a

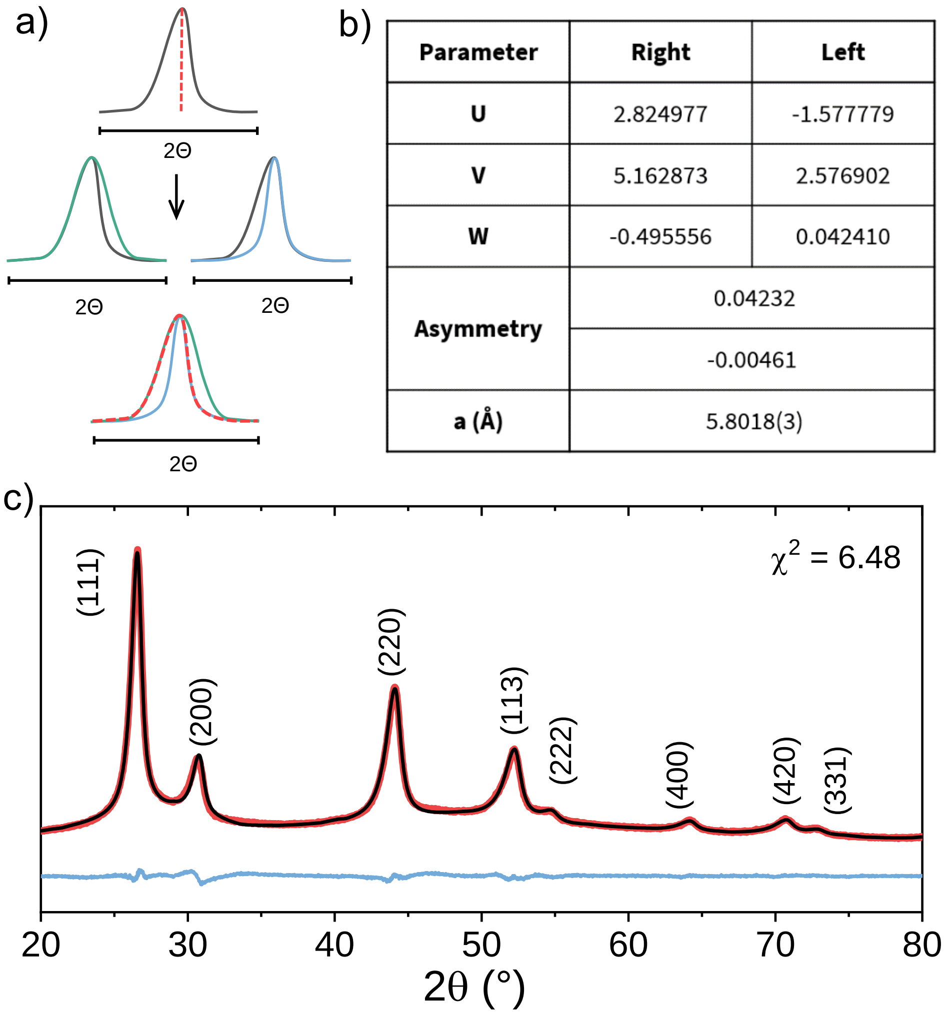

Parameter	Right	Left
U	2.824977	-1.577779
V	5.162873	2.576902
W	-0.495556	0.042410
Asymmetry	0.04232	
	-0.00461	
a (Å)	5.8018(3)	

Figure II.5 Profile-matching of the X-ray diffraction diagram of $SrSnF_4$, a) schematic showing how each half of a peak is modelled by a separate function under the Split-Pseudo-Voigt mode b) resulting fit parameters of $SrSnF_4$. U, V and W values are very high, as the peaks are unusually large c) XRD diagram with the corresponding simulated diagram and difference curve pseudo-Voigt function with separate U, V and W parameters. A schematic of the procedure is shown in **Figure II.5** a), with a fitting example along with the resulting parameters presented in panels b) and c). Thanks to this, we were able to study the impact of the introduction of tin on the SrF_2 structure. The extracted cell parameter for $SrSnF_4$ is 5.8018(3) Å. As observed for c-$BaSnF_4$ in **Chapter I**, there is very little cell variation in cell volume after the introduction of tin. This is all the more surprising when accounting for the size difference between tin and strontium, which is supposedly larger than that between tin and barium. We would then expect that the tin would cause significant distortion. As the size of tin is heavily dependent on the stereoactivity of the lone pair, we then moved to characterizing it, in the interest of gaining a better understanding of the local $SrSnF_4$ structure.

II.1.2. Local structure study of c-$SrSnF_4$

The Tin environment and the stereoactivity of its lone pair was characterized through ^{119}Sn Mössbauer spectroscopy, in collaboration with Mathieu Duttine, from the ICMCB (Bordeaux). An example of a resulting Mössbauer spectra is shown in Figure II.6, and the extracted parameters are presented in **Table II.1**. Several points of interest may be highlighted. Firstly, this spectrum is very similar to that of c-$BaSnF_4$, reproducing its most important feature: the peak splitting into a doublet, demonstrating the stereoactivity of the lone pair in all materials. Once again, the doublet was fitted using two contributions, reflecting the disorder present in these structures, and the great variety of environments the Sn(II) may find itself in.

Table II.1 Mössbauer hyperfine parameters of $MSnF_4$

		Isomer shift (mm/s)	**Δ quadrupole splitting (mm/s)**	**G_{11}**	**Relative Intensity (%)**
c-$BaSnF_4$	Contribution 1	3.26(5)	1.84(6)	1.29(4)	52(3)
	Contribution 2	3.53(4)	1.64(5)	1.25(4)	46(3)
	Sn(IV) impurity	0	0.6	-	2(3)
c-$SrSnF_4$	Contribution 1	3.22(3)	1.96(6)	1.36(4)	36(3)
	Contribution 2	3.36(3)	1.34(6)	1.31(4)	43(3)
	Sn(IV) impurity	-0.13(3)	0.53(8)	-	21(3)

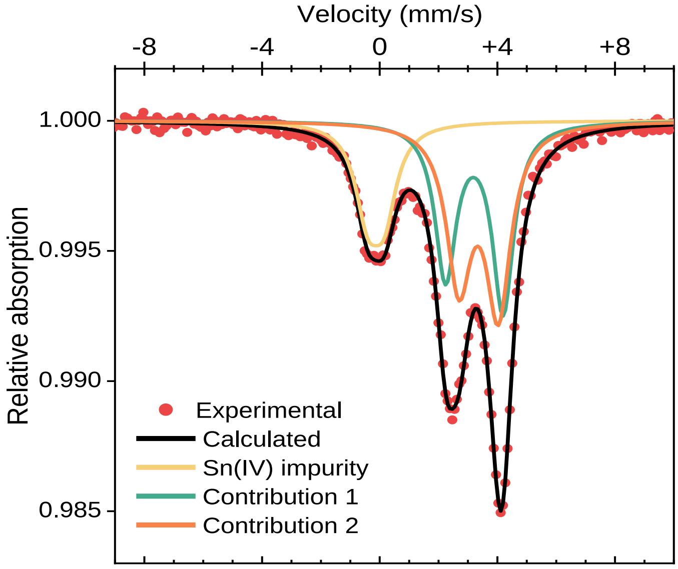

Figure II.6 Room-temperature Mössbauer spectra of $SrSnF_4$, fitted using two contributions to reflect the range of possible around the Sn.

Comparing the hyperfine parameters of each contribution in the different materials, it is visible that the isomeric shift is slightly lower in $SrSnF_4$.

Isomeric shifts are strongly related to the electronic density around the tin core, and thus to its oxidation state. The values we obtained are all in the range of what is anticipated for Sn(II), but reflect an increase in the Sn-F bond covalency in c-$SrSnF_4$, likely cause by the contraction of the lattice.[220]

Secondly, there appears to be a substantial amount (around 21(3)%) of Sn(IV) impurity in c-SrSnF4. This room-temperature value is, however, a large over-estimation, arising from the different Lamb-Mossbauer factors of Sn(II) and Sn(IV). The Lamb-Mössbauer factor is representative of the strength of the Mössbauer effect for a given temperature, and thus impacts peak intensity.[221] When approaching 0 K, this factor nears 1 for both Sn(II) and Sn(IV), permitting an accurate comparison of the relative intensities. Here, we could only reach 100 K, at which the (still over-estimated) percentage of impurity decreases to 7(3)%. Therefore, we do not anticipate significant interference of this impurity in future analysis. It is unclear why this material contains more oxidized tin compared to its barium counterpart, but it could be related to the longer ball-milling time.

The third point of interest to be emphasized is the variation in quadrupole splitting, which significantly decreases when switching from a Ba-based to a Sr-based fluorite. Quadrupole splitting in Mössbauer spectra originate from the electric field gradient around the tin. A more stereoactive lone pair yields a stronger gradient, and hence a larger splitting.[222] In c-$SrSnF_4$, the quadrupole splitting values for both contributions are not all lower than in the Barium Tin fluorite, but the average quadrupole splitting is significantly lower in the former (Δ = 1.27 mm/s) than the latter (Δ = 1.70 mm/s), implying that the lone pair in strontium fluorites is less stereoactive.[223]

This raises questions about the local arrangement of fluorides in the strontium-based fluorites: in c-$BaSnF_4$, we showed that the lone pair pushes fluorides out of their tetragonal sites and created large lattice distortions. Therefore, one may wonder whether this less stereoactive electron pair would have the same effect, and if so whether it would be as strong. To probe the local structure, we turn to Pair Distribution Function (PDF).

The PDF diagram of $SrSnF_4$ was measured at room-temperature, in a Kapton capillary sealed under Argon, in the 11-1D-B beamline at the Argonne National Laboratory Advanced Photon Source, in the same conditions as $BaSnF_4$, as described in the methods

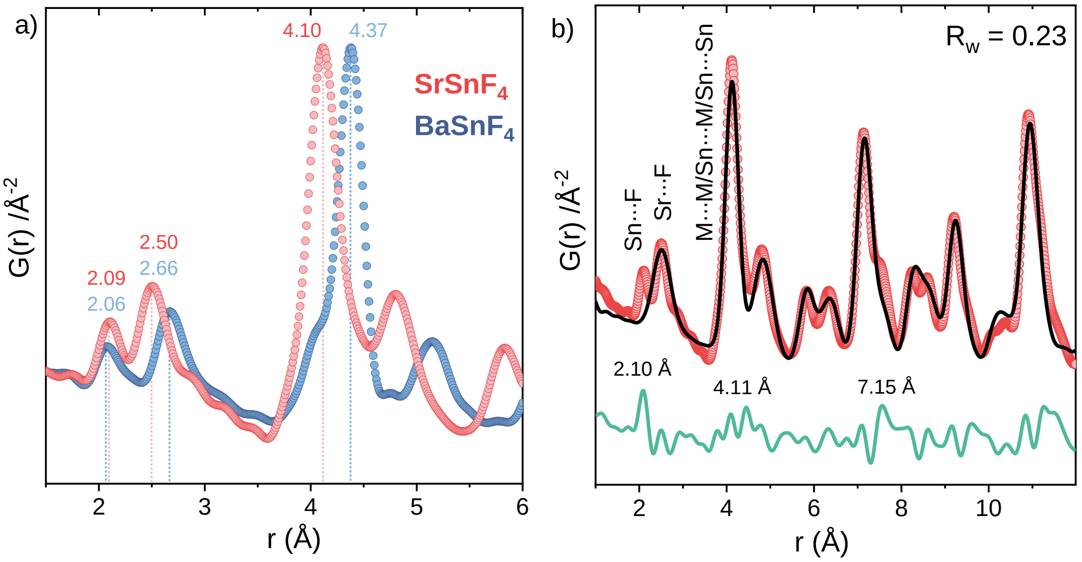

Figure II.7 Pair Distribution function a) comparison of $BaSnF_4$ and $SrSnF_4$ b) short-range fit of $SrSnF_4$, using an average fluorite structure model part of chapter I. The resulting data is shown juxtaposed to that of $BaSnF_4$ in **Figure II.7**, panel a). Peaks are heavily shifted, illustrating the contraction of the fluorite when switching from barium to strontium, with a notable exception in the first peak, Sn-F, which appears around the same r for both materials. It then comes that, while the fluorite cell size influences the lone pair stereoactivity, as shown though Mössbauer spectroscopy, it does not dictate the Sn-F bond length. Further insight could be obtained through the fitting of the $SrSnF_4$ diagram, which was performed following the same procedure as for c-$BaSnF_4$, and is displayed in **Figure II.7**, panel b).

The same general conclusions could be drawn, with slight deviations. The long-range fit is satisfactory, as it approaches the average model structure. The short-range fit, on the other hand, highlights significant discrepancies between said model and the actual atomic ordering, originating from the tin off-centre displacements and resulting F-disorder. In $BaSnF_4$, these effects are very visible in the form of peaks on the difference curve, which lead to an overly high reliability factor. Here, for $SrSnF_4$, the difference curve is very similar to that of $BaSnF_4$, with peaks at 2.10 (Sn-F), 4.11 (M/Sn-M/Sn) and 7.15 (M/Sn-M/Sn) Å. The reliability factor is however significantly better: 0.23 for $SrSnF_4$ vs 0.32 for $BaSnF_4$. This may be caused by the contraction of the cell when switching from BaF_2 to SrF_2. Sr-F and Sr-Sr distances are shorter than their Ba-F and Ba-Ba counterparts, and thus closer to the small Sn-F and Sn-Sn distances. Adding this element to the less stereoactive lone pairs in the strontium phases, it appears that the local distortion of the M sites is lower. The F-disorder, however, appears to remain the same, as illustrated by the unfitted peak at 2.10 Å.

In order to gain more insight on these structures, Ab Initio Molecular Dynamics and Density Functional Theory calculations were performed by our collaborators, Dr. S. W. Coles and Dr. B. J. Morgan of the University of Bath. We first tried to compare the tin lone pair stereoactivity in the Ba and Sr systems. We initially attempted to compare the volumes of the Sn(II) ions in each structure but it was not as straightforwardly feasible as anticipated. Instead, we opted to examine the tin dipole lengths as a proxy for stereoactivity, in each simulated material. An example is presented in **Figure II.8**.

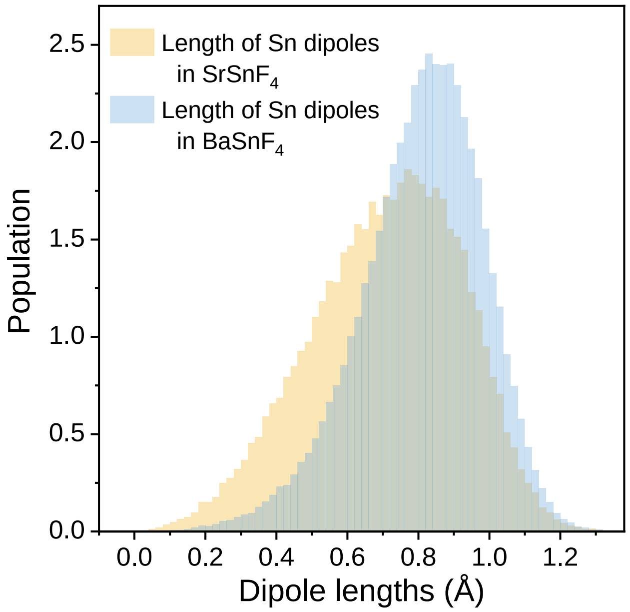

Figure II.8 Dipole lengths of tin in DFT-simulated BaSnF$_4$ and SrSnF$_4$.

Both dipole lengths are plotted as populations, as the tin lone pair is dynamic (see **Ch.I**) and thus may adopt various configurations, changing with time. Results show the lone pair is, on average, smaller in the simulated Sr-based fluorite. Interestingly, the shape of both distributions varies, as dipole lengths are more spread out in SrSnF$_4$. This could be related to the higher chemical pressure applied on the tin in this smaller-volume structure, which would cause the lone pair to be both more delocalized around the nuclei and more distorted, resulting in a higher number of populated states but smaller average dipole length.

As it was done for BaSnF$_4$, we moved to investigate the localisation of fluorides within SrSnF$_4$, as shown in **Figure II.9**. There are some key differences in the site occupancies between the barium and the strontium tin fluorites. Firstly, there is a change in the occupancy of the Oct. sites: in BaSnF$_4$, 35% of F$^-$ ions are in these interstitial holes, in SrSnF$_4$ this number drops to 27%. This corresponds to a 23% occupancy decrease. Additionally, the M-rich tetrahedral sites, M$_4$ and M$_3$Sn, have lower occupation in the strontium structures. In turn, the fluoride population is higher in the Sn-rich tetrahedral sites in SrSnF$_4$ compared to BaSnF$_4$, which hints to F-sites in the neighbourhood of tins being more stable in strontium fluorites.

We may attribute both of these effects to the lower stereoactivity of the tin lone pair: in $BaSnF_4$, it pushes the F-ions out of the Tet. into interstitial Oct. sites, which leads to very low populations in the tin-rich sites. Here, the "compressed" lone pair may not be large enough to do so as effectively. Additionally, the contraction of the strontium-based cell leads to smaller, more difficult to pass bottlenecks for the F-ion, which then cannot access the Sr-rich octahedral sites easily.

The variations in site population with the change of M may have a sizeable impact on transport properties, as tin-rich and Oct. sites were shown to be responsible for a great part of the conductivity in c-$BaSnF_4$. Hence, we now move to characterize the F-ion transport within these materials.

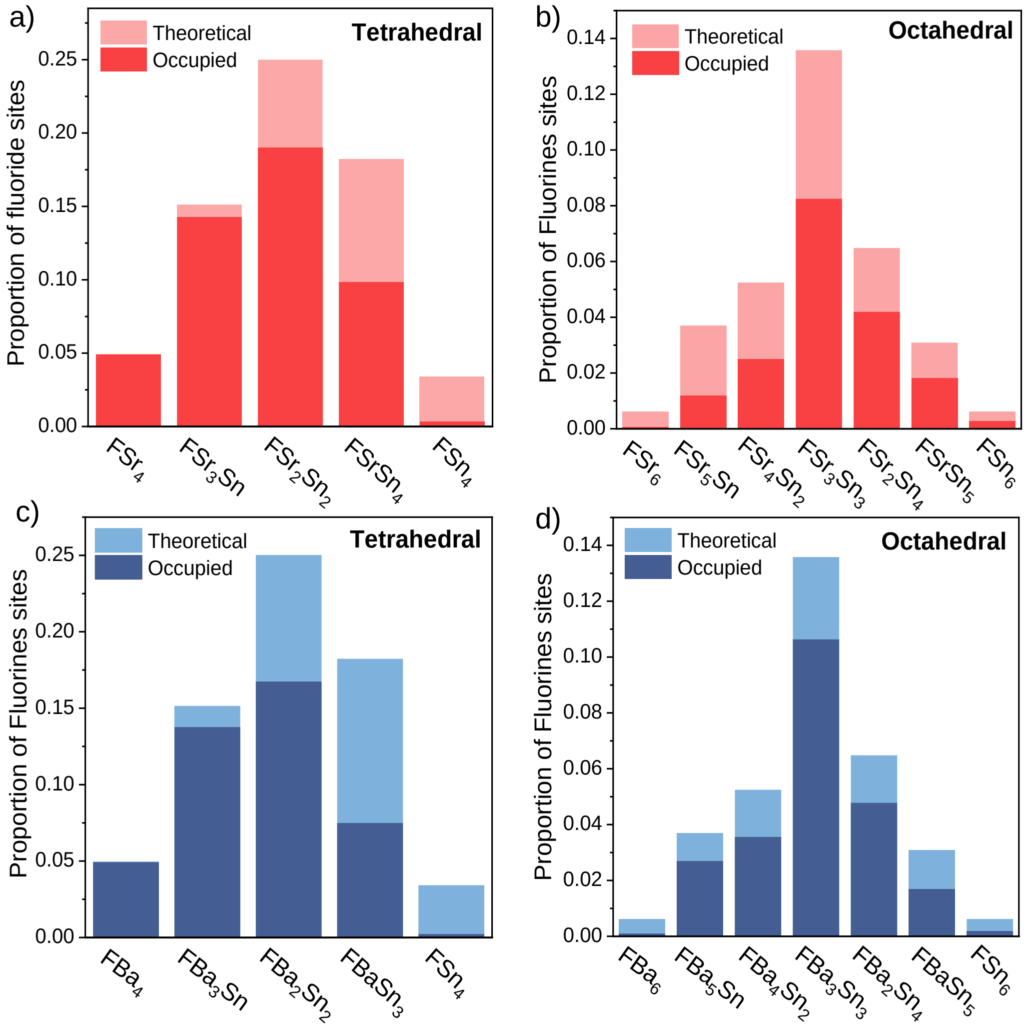

Figure II.9 F-site distribution (light colors) and occupation (darker colors), a) Tetrahedral sites in $SrSnF_4$, b) Octahedral sites in $SrSnF_4$, c) Tetrahedral sites in $BaSnF_4$, d) Octahedral sites in $BaSnF_4$

II.1.3 Transport properties evolution with the substitution of barium for strontium in c-$MSnF_4$

$SrSnF_4$ and $BaSnF_4$ have been shown to be of very similar structures, albeit with slight differences in the sites that fluorides occupy. We will now compare directly the F-mobility in both materials, first through Electrochemical Impedance Spectroscopy (EIS). Pellets were made by pressing 250 mg of powder in a 10mm die with 4 t uniaxial pressure in a glovebox. A layer of gold was sputtered on both sides. The pellet shown on subsequent figures had a compacity of 92.7%, which is higher than that of c-$BaSnF_4$. We therefore keep in mind when comparing both materials that the conductivity of the latter is underestimated with regards to the former.

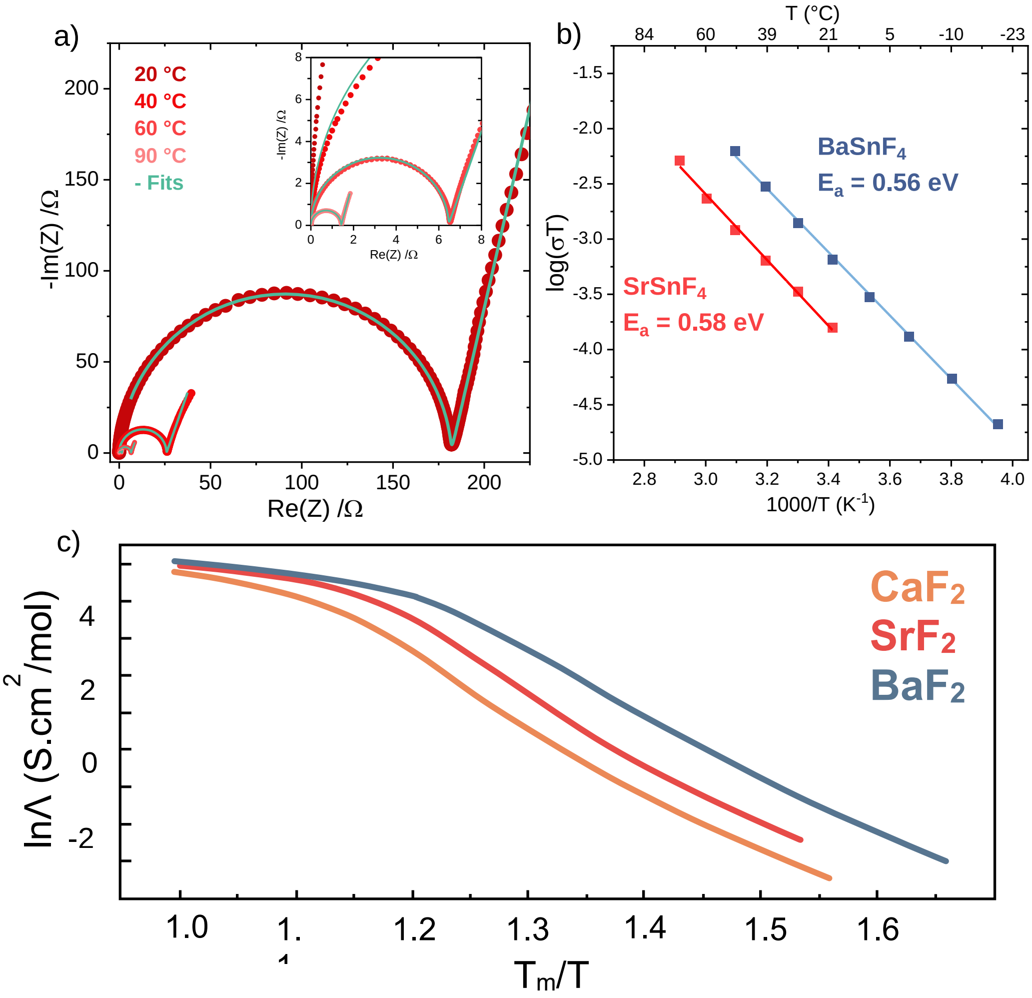

Figure II.10 Effect of M substitution on conductivity, a) Nyquist plots at different temperatures for $SrSnF_4$, b) Arrhenius plot comparison of $BaSnF_4$ and $SrSnF_4$, c) molar ionic conductivity in MF_2, reproduced from ref. 224

At 30°C, both materials have a low ionic conductivity, in the order of 10^{-6} S.cm^{-1}, but that of $BaSnF_4$ is 4 times higher, reaching 4.6 10^{-6} S.cm^{-1} versus 1.1 10^{-6} for $SrSnF_4$. From the Nyquist representations shown in **Figure II.10**, panel a), we determine the conductivity at different temperatures and us Arrhenius plots (panel b) to find activation energies of 0.56 and 0.58 eV for $BaSnF_4$ and $SrSnF_4$, respectively. This trend follows that of the conductivity of the pure MF_2 (see **Figure II.10** c). It has been shown by Voronin et al. that in fluorites, the size of the cation, and, by extension, the volume of the structure, is the most influential factor for ionic transport, as it governs the bottleneck size.[224]

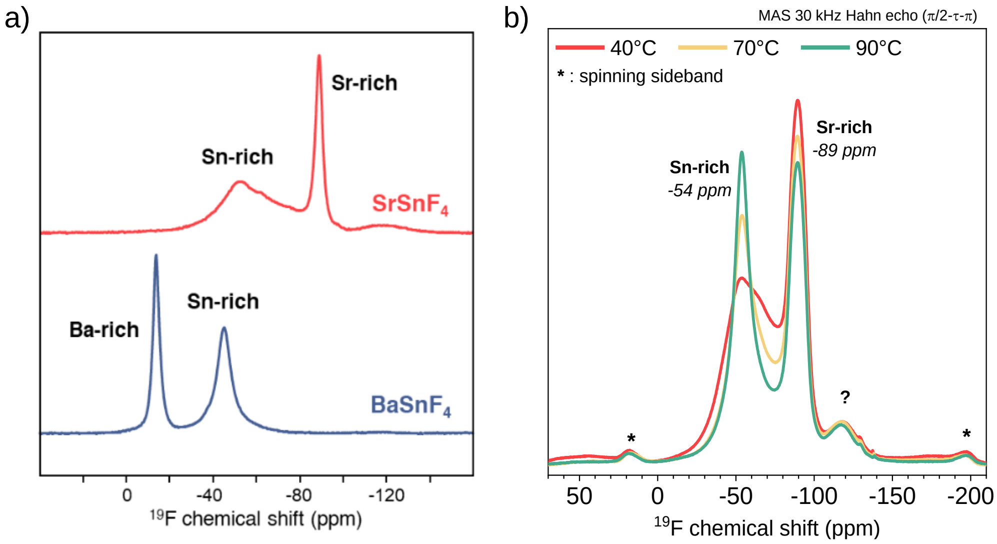

Figure II.11 a) ^{19}F MAS NMR spectra of c-$BaSnF_4$ and c-$SrSnF_4$ at 44 kHz, c) temperature-dependant ^{19}F MAS NMR of c-$SrSnF_4$

Hence, $r_{Ca2+} < r_{Sr2+} < r_{Ba2+}$ leads to $V_{CaF2} < V_{SrF2} < V_{BaF2}$ leads to $\sigma_{CaF2} < \sigma_{SrF2} < \sigma_{BaF2}$, and this trend is seemingly conserved through the addition of tin in the structure, though with a jump in conductivity (and only for barium and strontium, as we never succeeded to obtain c-$CaSnF_4$). This change in bottleneck size might also impact transport mechanisms, motivating the study of F-ion dynamics in this material, through ^{19}F Magic Angle Spinning Nuclear Magnetic Resonance (^{19}F MAS NMR). Displayed in **Figure II.11**, panel a) is the comparison between $BaSnF_4$ and $SrSnF_4$ spectra. In **Chapter I.**, we found that the two peaks in $BaSnF_4$ NMR spectra were representative for the two types of F-exchanges within the structure, i.e. exchanges in Sn-rich environments around -46 ppm and in Ba-rich environments around -13 ppm. We had hypothesized that all exchanges could not be seen due to their high speed. The example of $SrSnF_4$ appears to support this theory: in this less-conductive material, more peaks are visible between the Sn-rich peak around -54 ppm and the Sr-rich peak at -89 ppm.[225] These peaks may appear because of the slow exchanges between mixed F-environments, as shown for other materials.[60] Most interestingly, there is an additional peak at -119 ppm in $SrSnF_4$. We speculate that this peak could originate from F-ions located in the octahedral sites, as this chemical shift is characteristic of over-coordinated fluorides, in $F(Sr)_5$ environments.

At higher temperatures (**Figure II.11**, panel b), the two most intense peaks evolve as the exchanges get faster. The intensity of the Sn-rich peak increases, as it did in the barium tin fluorite, which we once again attribute to the higher mobility of fluorides in the vicinity of tins. The experimental data appears to point to a conduction mechanism similar to that of cubic $BaSnF_4$, but slower, which we tentatively attribute to the volumetric difference between these structures.

In order to further explore this possibility, we turn to Density Functional Theory (DFT) and Ab Initio Molecular Dynamics (AIMD) once again. Around one hundred cells of various sizes were generated and relaxed via DFT at 0 K. No ordering was observed, therefore the

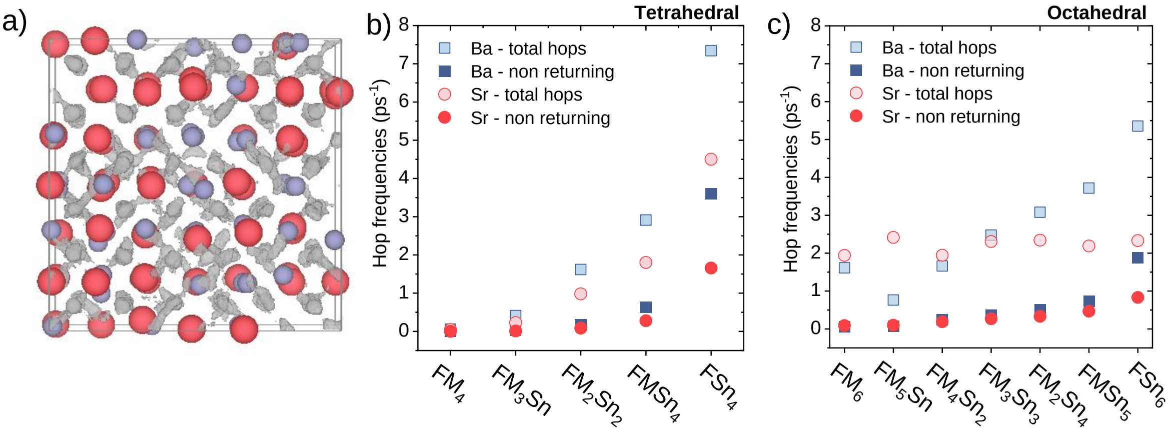

Figure II.12 AIMD analysis a) localisation of the fluoride-ions in Strontium (red) tin (dark grey) fluoride (light grey) throughout the 60 ps simulation, b) comparison of the hopping frequencies in tetrahedral environments in c-$BaSnF_4$ (blue) and c-$SrSnF_4$ (yellow). The light dots are the total number of jumps, the dark dots are the non-returning jumps, c) hopping frequencies in the octahedral sites (same legend) subsequently generated $SrSnF_4$ supercell was given a quasi-random atomic arrangement. AIMD was run on that supercell at 600 K for a timeframe of 60 ps. We followed the F-ion localization during the duration of the simulation using an electron localization function, as shown in **Figure II.12**, panel a). Fluorides in Sr_4 or Sr-rich environments sit in their tetrahedral sites, while in tin-rich zones, they are delocalized, matching the conclusions of NMR regarding the higher F-mobility in these environments.

We look into the F-conduction in each environment in **Figure II.12**, panels b) and c). These panels show the hop frequencies for each tetragonal an octahedral site, normalized by its population (see **Figure II.9**). We separate the total number of hops from the non-returning hops, from which the long-range transport properties originate. In tetrahedral environments, the behaviour of F-ions is similar in $BaSnF_4$ and $SrSnF_4$: hop frequencies increase with the number of neighbouring tins, with the majority of the non-returning hops originating from the FSn_4 sites. In $BaSnF_4$, we observed that the conduction pathways for F-ions were largely Tetrahedral -> Octahedral -> Tetrahedral (see **Figure II.1**). We also showed that in both the Sr- and the Ba- based tin fluorites, the lone pair pushes the F-ion into neighbouring Oct. sites. The same reasoning may be applied here : tin-rich sites are the most conductive, as more lone pairs are more effective at pushing F-ions out of the Tet. site into a closeby (also logically tin-rich) Oct. site. We note however that there is an overall lower number of jump attemps in the strontium material, which is expected, as its lower volume yields smaller bottlenecks, more difficult for the F-ions to pass, as is also reflected in the higher activation energy of $SrSnF_4$. The overall trend of F hopping in the tetrahedral sites still remains very similar. In the octahedral intersticials, however, F-behaviour varies significantly when substituting the barium for strontium, as seen in **Figure II.12** panel c). While in c-$BaSnF_4$ we once again observed a strong correlation between hop frequencies and number of tins around the site, in c-$SrSnF_4$ this tendency is much less pronounced, and even dissapears if looking at the overall number of jumps. We hypothetize that this could be once again related to the diminished stereoactivity of the tin lone pair, as F-ions in the center of Oct. sites are further away from cations compared to those in Tet. sites. In $BaSnF_4$, the lone pair is large enough that it can still impact intersticial fluorides, but in $SrSnF_4$ it does not appear to be the case, leading to these similar hop frequencies regardeless of tin content around the site.

We can then propose a dual effect of the contraction of the cell on ionic transport: the smaller bottlenecks lead to less jump attempts, and the reduced stereoactivity of the tin lone pair prevents it from affecting fluoride ions in interstitial positions as much.

II.2. A perspective: introducing additional cationic disorder in the $Ba_{1-x}Sr_xSnF_4$ mixed cation solid solution

We have now shown that the variation in conductivity in $MSnF_4$ is related to M-induced volumetric changes. In this next part, we wish to see whether this reasonning applies in $Ba_{1-x}Sr_xSnF_4$ fluorites, in which we expected to observe two effects that would influence the conductivity in an opposite manner : more cationic disorder is introduced in the structure, and in parrallel the fluorite volume is modified. We wished to see whether there would be an effect from the added disorder on the transport properties, or if the volumetric variations alone will be sufficient to explain the changes.

II.2.1. Synthesis of cubic $Ba_{1-x}Sr_xSnF_4$

It is known from the litterature that the BaF_2-CaF_2 system is a complete solid solition, *i.e.* these two phased are “miscible” in all proportions. Since we were however unsuccessful in our efforts to obtain c-$CaSnF_4$ (see Annexe 1), we moved to the BaF_2-SrF_2 system, which should also be a complete solid solution.[226]

This experimental work was in majority performed by Jeaniero Ralaitsizafy, during his master internship, and Sandrine Leclerc at Phenix Laboratory in Paris.

The first synthesis attempts were made by mixing the three precursors (BaF_2, SrF_2, SnF_2) in ball-milling jars under inert atmosphere and milling. Even for long milling times, the synthesis was incomplete and some unreacted precursors were visible on the XRD diagrams. Another route was therefore chosen, with two separate steps of ball-milling. First, BaF_2 and SrF_2 were milled together to form $Ba_{1-x}Sr_xF_2$. This product was pure for high Sr content, but below xSr = 0.5, a subsequent heat treatment at 300 °C overnight was necessary for the reaction to be completed. Below xSr = 0.3, we could not obtain a pure product and therefore did not proceed with the rest of the synthesis. The resulting pure $Ba_{1-x}Sr_xF_2$ were then milled with SnF_2 for 16h. Both steps had a ball:powder ratio of 17:1 and utilized 10mm diameter yttrium-stabilized zirconia balls and a 20 mL jar made from the same material.

An example of an XRD diagram of a product after both steps is shown in **Figure II.13**, panel a). The peak shift is very visible. Panel b) summarizes the evolution of the cell parameter with the increase of xSr. The tin-less fluorite follows Vegard's law, as the cell parameter decreases linearly when Sr is introduced in the structure.[227] This solid solution then behaves similarly to BaF_2 and SnF_2, in that the addition of tin does not incur any change in lattice volume. All structural characterizations, including PDF, point to these fluorites being very similar to the end members of the solid solution in terms of local order, with a random distribution of Ba, Sr and Sn on the cationic *4a* site.

These structures are therefore expected to be even more disordered than the end-members. In fluorites, cationic disorder has been shown to be beneficial to conductivity, with some studies finding the BaF_2-CaF_2 solid solution to be more conductive than either

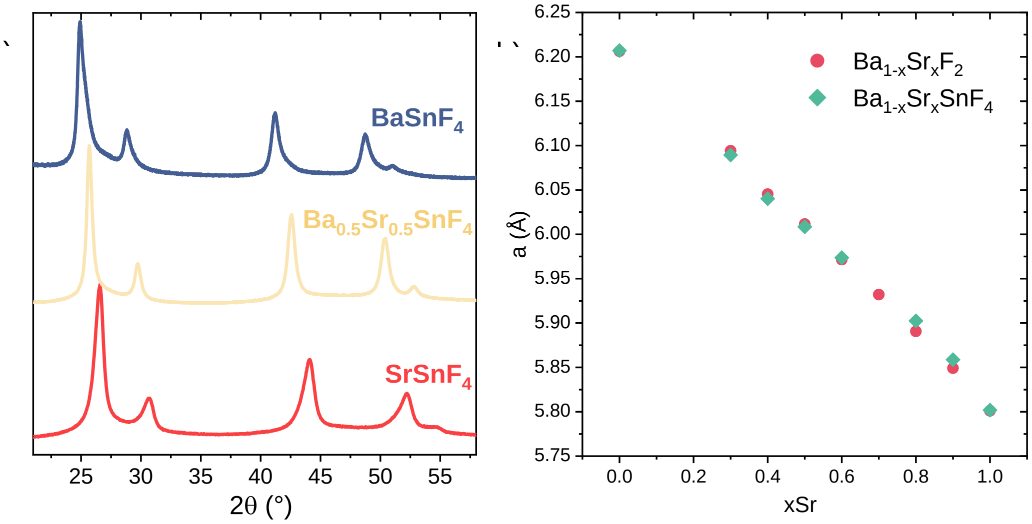

Figure II.13 X-Ray diffraction analysis of $Ba_{1-x}Sr_xSnF_4$, a) comparison with $SrSnF_4$ and $BaSnF_4$, b) cell parameter evolution with xSr, the tin-less fluorite is in red and the tin-containing structure in green

BaF_2 or CaF_2, which was attributed to “free volume” introduced by the local lattice disorder,[45] facilitating the fluoride diffusion through interstitial sites.[228] Here, the tin-containing structures are already very disordered, so it is interesting to see whether this effect will be present as well or if the conductivity of the solid solution will be governed by its cell volume.

II.2.2. Conductivity in $Ba_{1-x}Sr_xSnF_4$

To start with, the ionic conductivity was evaluated through Electrochemical Impedance Spectroscopy. Pellets were made by pressing 250 mg of powder at 4 t in a uniaxial press, and a layer of gold was deposited by Chemical Vapor Deposition. Typical compacities

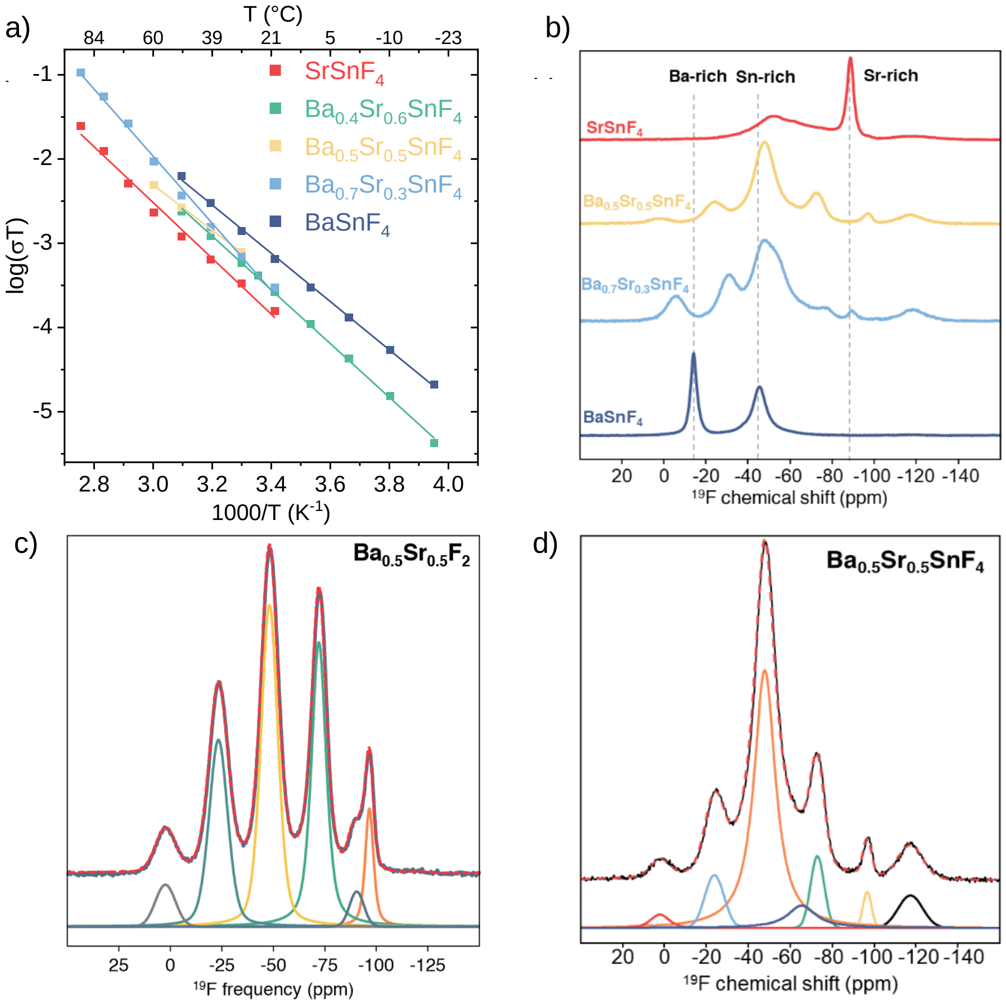

Figure II.14 F-transport properties of $Ba_{1-x}Sr_xSnF_4$, a) EIS-derived Arrhenius plot, b) ^{19}F MAS NMR spectra across the solid solution, c) fit of Sn-less $Ba_{0.5}Sr_{0.5}F_4$, d) fit of the corresponding tin-containing $Ba_{0.5}Sr_{0.5}SnF_4$

were between 85-90%. A comparison of the Arrhenius plots of materials with various xSr is shown in **Figure II.14**, panel a).

Neither the evolution of the conductivity, nor that of the activation energy appear to be correlated with the evolution of xSr, and, interestingly, all the measured $Ba_{1-x}Sr_xSnF_4$ compositions had very similar room-temperature conductivity (see **Table II.2**), which is below that of c-$BaSnF_4$ but higher than that of $SrSnF_4$.

Table II.2 Conduction properties of the solid solution of $Ba_{1-x}Sr_xSnF_4$

xSr	**$\sigma_{30°C}$ ($S.cm^{-1}$)**	**E_a (eV)**
100	$1.10\ 10^{-6}$	0.67
60	$1.93\ 10^{-6}$	0.63
50	$2.60\ 10^{-6}$	0.53
30	$2.30\ 10^{-6}$	0.79
0	$1.19\ 10^{-5}$	0.56

It therefore appears that the transport properties in these materials is not completely dependent on volume, as all the investigated $Ba_{1-x}Sr_xSnF_4$ compositions have a different cell parameter, and also not completely controlled by disorder, as the most “disordered” material, $Ba_{0.5}Sr_{0.5}SnF_4$, did not have better ionic conduction than the other compositions. For further informations, we turned to ^{19}F MAS NMR, as seen in panel b. The spectra of the $Ba_{1-x}Sr_xSnF_4$ samples appear significantly more complex than those previously studied. In $BaSnF_4$, there were only two peaks, one for F-jumps in Sn-rich environments and one for jumps in Ba-rich environments. There was only one type of Ba-rich environment, FBa_4, hence the simplicity of the spectra. In the $Ba_{1-x}Sr_xF_2$ solid solution however, there is a distribution of FMM’ environments, as shown in **Figure II.14** panel c), which result in a similar distribution post tin addition, see panel d). We will now discuss the important parameters that could be extracted from the fit of these spectra, shown below in **Table II.3**. The ***d_{iso}*** obtained for $Ba_{0.5}Sr_{0.5}F_4$ matches with reported literature, and the intensities are close to the calculated intensities based on a random distribution model, though Sr-rich site peaks are slightly more intense than predicted while Ba-rich site peaks are less intense. [225] This might be related to the different F-dynamics in each environment, but is difficult to confirm without further experiments.

Table II.3. Fit results of the ^{19}F MAS NMR spectra of $Ba_{0.5}Sr_{0.5}F_4$ and $Ba_{0.5}Sr_{0.5}SnF_4$. Peaks at -90.46 ppm in $Ba_{0.5}Sr_{0.5}F_4$ and -117.4 ppm in $Ba_{0.5}Sr_{0.5}SnF_4$ are impurities. **d_{iso}** is the ^{19}F shift, **I_{exp}** the peak intensity derived from the fit, and **I_{th}** the theoretical intensity based on a random cationic distribution. **I_{th}** is not given for $Ba_{0.5}Sr_{0.5}SnF_4$ as we know from previous experiments that the intensity of peaks in tin-containing phases is largely dependant on F-hopping rather that the relative abundance of each environment.

$Ba_{0.5}Sr_{0.5}F_4$				**$Ba_{0.5}Sr_{0.5}SnF_4$**	
d_{iso} (ppm)	**I_{exp} (%)**	**Assignment**	**I_{th} (%)**	**d_{iso} (ppm)**	**I (%)**
-90.46	2.79	-	-	-117.4	5
-96.59	6.95	FSr_4	6.25	-96.7	1.9
-72.08	28.93	FSr_3Ba	25	-72.9	8.3
-48.1	34.84	FSr_2Ba_2	37.5	-65.4	7.5
				-47.8	66.9
-23.34	21.91	$FSrBa_3$	25	-23.8	8.1
2.4	4.58	FBa_4	6.25	2.3	2.3

In $Ba_{0.5}Sr_{0.5}SnF_4$, we find peaks at the same frequencies as $Ba_{0.5}Sr_{0.5}F_4$ (except for the impurity at -90.46 ppm which disappeared, as a different $Ba_{0.5}Sr_{0.5}F_4$ sample was used in the synthesis of this $Ba_{0.5}Sr_{0.5}SnF_4$). The peak at -47.8 ppm has a significantly higher intensity, which originates from the merging of the FSr_2Ba_2 and Sn-rich peaks. Only one Sn-related peak is observed, which suggests Sn environments are more conducive to F-mobility in these materials as well. We may also deduce from the absence of intermediary Sn-containing environments that the FSr_xBa_y sites are more conductive than FSr_4, as in $SrSnF_4$ the slow dynamics gave rise to these additional FSr_xSn_y peaks.

Overall, though the addition of a third cation in the structure yields FSr_xBa_y sites, which might be more conductive than FBa_4 and FSr_4, the F-dynamics are still dominated by tin-rich sites. There appears to be an interplay between the cell contraction as more Sr is added and the increase cationic disorder it brings (up to xSr = 0.5), as the variation of conductivity across the $Ba_{1-x}Sr_xSnF_4$ solid solution is not linear.

Conclusion

In this chapter, we were interested in studying the effects of cationic substitution in the c-$MSnF_4$ structure.

To do so, we started by synthesizing a new c-$MSnF_4$, where M = Sr. We showed through several structural probes that this was an isomorph of $BaSnF_4$ with similar local-scale disorder, originating from the stereoactivity of the tin lone pair. The smaller size of strontium however leads to some structural differences between the two isomorphs, the most important of which is the contraction of the unit cell. This contraction induced a higher chemical pressure on the tin, which resulted in a lower stereoactivity of its lone pair, observed both experimentally and through computational simulations, the latter of which highlighted interesting repercussions on the F-ion sublattice: tin-rich sites being more readily occupied in the strontium tin-fluorite, as well as a significantly lower occupation of the octahedral interstitial sites.

The impact of these differences on the conduction mechanism was then examined. As expected, a decrease in ionic conductivity came with the substitution of barium for strontium, which we attribute in majority to the smaller cell volume that leads to the narrowing of bottlenecks. Through Ab Initio Molecular Dynamics, we also brought to light the more minor role played by octahedral interstitial in the ionic transport, which we ascribe to the decrease in lone pair stereoactivity that may prevent interaction between it and the F-interstitials.

Finally, we attempted to discuss the combination of volume and disorder effect through a new solid solution: $Ba_{1-x}Sr_xSnF_4$. We designed a synthesis route for these materials, which were demonstrated to be structurally similar to $BaSnF_4$ and $SrSnF_4$. It was however complicated to draw definitive conclusions on the presence or lack of benefits arising from the addition of disorder in these fluorites. More experiments, such as temperature ^{19}F MAS NMR, would give helpful insight on this topic.

Chapter III

Synthesis-originated structural variations in t-$BaSnF_4$

Table of Contents

Introduction **91**
III.1. Revisiting the Ball-milling/high temperature route... 92

III.1.1. Methods.. 92

III.1.2. Results and discussion 93

III.2. A new route to produce $BaSnF_4$: Spark “Plasma” Sintering............................. 95

III.2.1 SPS working principle.. 96

III.2.2 Methodology of the SPS synthesis 97

III.2.3. SPS synthesis 97

III.2.3.1 Synthesis of a pure t-BaSnF4 phase through SPS 97

III.2.3.2 Influence of synthesis temperature on the microstructure of $BaSnF_4$ 99

III.2.3.3 Optimization of synthesis parameters for reaching high conductivity . 105

III.2.3.4 Structural analysis of SPS-synthetized t-$BaSnF_4$: Attempt to correlate the ionic conductivity to unit cell parameters. 109

III.2.3.5 Neutron diffraction : characterization of stacking faults and interticial fluorides within the structure.. 111

Conclusions.. 119

Introduction

The tetragonal polymorph of $BaSnF_4$ is, as described in the introductive chapter, significantly more conductive than its cubic counterpart. The first reported synthesis of t-$BaSnF_4$ dates back to 1984 and is a solid-state synthesis, where a stoichiometric amount of BaF_2 and SnF_2 precursors were ground and heated to 500°C in a sealed copper tube under N_2. The authors identified the space group of this tetragonal phase, and showed its close relation to fluorite.[229]

Subsequently, a number of routes were reported, ranging from coprecipitation[87,230,231] to high temperature,[11,231] and finally a combination of mechanosynthesis and heat treatment.[36,66,231,232]

Interestingly, the reported unit-cell parameters tend to vary dramatically from one synthesis to another. **Table III.1** is a summary of $BaSnF_4$ cell parameters for each synthesis that reported them. The same phenomenon is observed for the $PbSnF_4$ isomorph, with the c parameter varying from 11.415 Å to 11.744(32) Å.[233,234] Authors seldom remark on differences between their findings.

Table III.1 Literature survey of reported cell parameters and phase purity for t-$BaSnF_4$. BM = ball-milling, HT = heat treatment

Synthesis method	**a (Å)**	**c (Å)**	**V (Å^3)**	**Phase purity**	**Reference**
BM+HT	4.345(1)	11.228(1)	211.97	Cubic 7.6wt%	232
BM+HT	~4.3375	~11.238	~211.43		66
BM + HT	4.35	11.28	213.44	Cubic impurity	231
HT	4.3564(6)	11.289(2)	214.2(1)	unreported	229
Coprecipitation	4.348 (5)	11.243 (3)	212.6	Cubic impurity	231
Coprecipitation + HT	4.3538(2)	11.3752(9)	215.62(2)	pure	87

Another important variation in materials from one synthesis to another is the purity. Oftentimes, the final product is not pure tetragonal $BaSnF_4$ but consist of a mix of t-$BaSnF_4$ with a cubic impurity, present in most of the Ball-milling/Heat treatment syntheses. Its structure is similar to that of BaF_2, but its composition is unknown, as, like previously described in chapter I., Sn may be introduced in BaF_2 fluorite without causing cell expansion or contraction.

Here, we will try to improve the BM/HT synthesis route so that it may yield pure t-$BaSnF_4$, as well as study the impact of the synthesis parameters on conductivity.

III.1. Revisiting the Ball-milling/high temperature route

III.1.1. Methods

Synthesis. For the initial ball-milling step, adequate amounts of BaF_2 (Sigma-Aldrich 99.99%) and SnF_2 (Sigma-Aldrich, 99%) precursors were weighed in a glovebox under Ar atmosphere, and transferred to Ball-milling jars. The jars and balls were made of zirconia, the volume of the jar was 80mL, the balls were 9mm in diameter and the ball:powder ratio was 13:1. Ball-milling was performed using a Pulverisette (Fitsch), at 300 RPM, in cycles which generally consisted of 15mn of milling, followed by 5mn of rest to allow the material to cool down. The product was then retrieved in a glovebox.

Heat treatments proceeded differently depending on whether they took place in PHENIX or LRCS, as both labs have different apparatus. In PHENIX Laboratory (Paris), samples were placed in an alumina boat and heated under vacuum in a tubular furnace. It was not possible to transfer materials from the glovebox to the furnace without them being exposed to air for a few minutes. The resulting powders tended to have a slight ochre colouration (though no impurity was ever observed through XRD). In LRCS Laboratory (Amiens), samples were placed in an alumina crucible inside an autoclave in the glovebox, which was sealed under argon before being placed in a muffle furnace. The resulting powders were whiter.

Electrochemical impedance spectroscopy. EIS was recorded using a BioLogic MTZ-35 impedance analyser, in combination with a Controlled-Environment Sample Holder, which kept the samples under inert atmosphere.

Powders were first pressed into pellets using the following procedure: in the glovebox, 250 mg of sample were added to 2-core 10mm diameter dies, and compressed with 4 tons of uniaxial pressure. After 5 minutes, the pellet was taken out. Pellets were very fragile and stuck to the sides of the dies, often breaking when being pushed out. To maximize the chances of obtaining a pellet of good quality, we found that exercising downwards pressure with one hand on the upper piston while pushing the lower piston and pellet up (using the press) was very effective. Gold was then sputtered on each side.

III.1.2. Results and discussion

Following the pioneer work of Ahmad et al, t-$BaSnF_4$ was synthetized via a two steps processes consisting in ball-milling a stochiometric amount of BaF_2 and SnF_2 precursors. The mixture was then heat treated at 300 °C for 4 h. The resulting XRD pattern consists of t-$BaSnF_4$ with a cubic phase as an impurity, as commonly observed in the literature. The composition of this impurity being unknown, we worked towards developing an alternative route using the same synthesis tools.

Synthesis. The route developed consists of 4 steps: a short ball-milling step, followed by a heat treatment, another ball-milling step, and finally, a heat treatment. Typical XRD diagrams of the obtained materials after each step are visible in **Figure III.1.** The first ball-milling step is significantly longer than what was described in chapter I., where c-$BaSnF_4$ was obtained after 24 milling cycles. Here, the precursors were milled for 99 cycles, lasting in total 33h. Shorter milling times (24, 40 cycles) were explored but resulted in unsuccessful synthesis. After annealing 3h at 300°C, a mix of c- and t-$BaSnF_4$ was obtained. Rietveld refinement points to 20.9(6) wt% of cubic phase and 79.1(1.2) wt% of t-$BaSnF_4$. The second ball-milling step was significantly longer, i.e. 185 cycles. Shorter millings were attempted as well (24, 40 cycles), and produced impure end materials. The last annealing, identical to the first one, produced a pure t-$BaSnF_4$ phase, whose specificities will be discussed later.

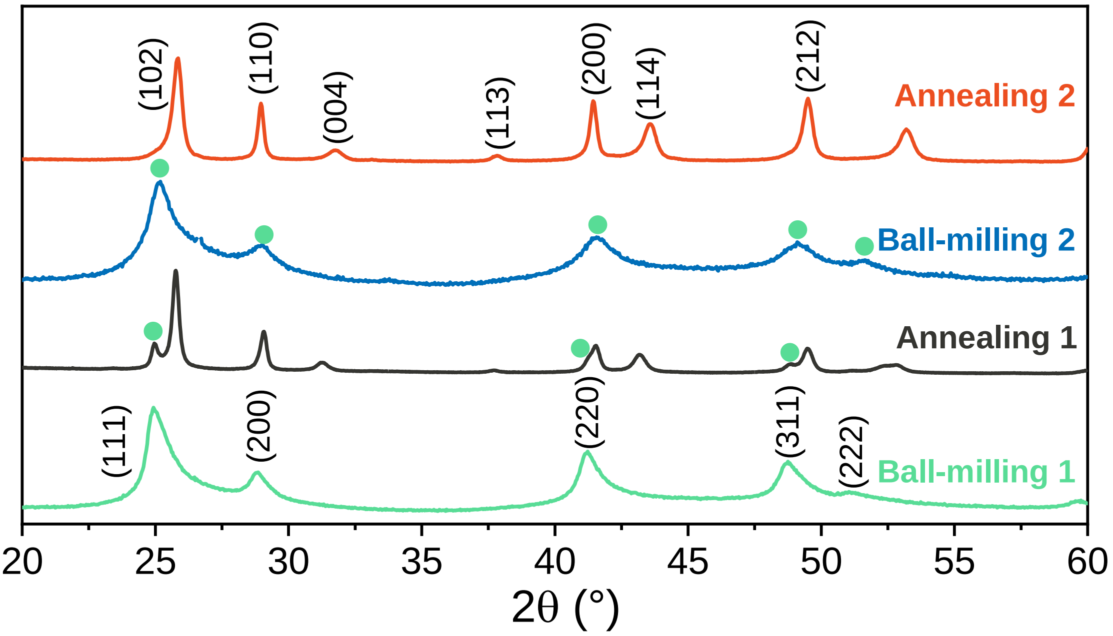

Figure III.1 XRD diagrams measured after each step of the newly developed synthesis route, indexed with FCC *F m*-3*m* c-$BaSnF_4$ after the first and second ball-milling steps, and tetragonal *P* 4/*nmm* t-$BaSnF_4$ after both annealing steps (with a cubic impurity after the first heat treatment)

Other trials were made, with varying ball:powder ratios, numbers of cycles, furnace temperatures, holding times, with only one ball-milling step and two heat treatment, etc... Only the described procedure consistently yielded a pure phase. It was obtained a few times through other routes as well, but these results could not be reproduced.

The ionic conductivity of the resulting sample was evaluated through electrochemical impedance spectroscopy. A pellet was made by adding 250 mg of powder in a 10mm diameter die and putting it under uniaxial pressure of 4t in a glovebox. Gold was then sputtered on either side of the pellet. A low compacity of 77.8% was calculated. The conductivity predictably increased with temperature (**Figure III.2**), but was significantly lower than what could be found in the literature for t-$BaSnF_4$ which still had cubic impurities. The activation energy was also higher. The synthesis pathway we described included long ball-milling, which generally introduces a lot of defects such as dislocations in the material. Although mechanosynthesis was previously shown to improve conductivity in fluorites,[51,218] it appears not to be the case for this structure. We hypothesize that this could be due to the 2D nature of t-BaSnF$_4$, which makes ion transport more sensitive to defects in the ionic pathways.

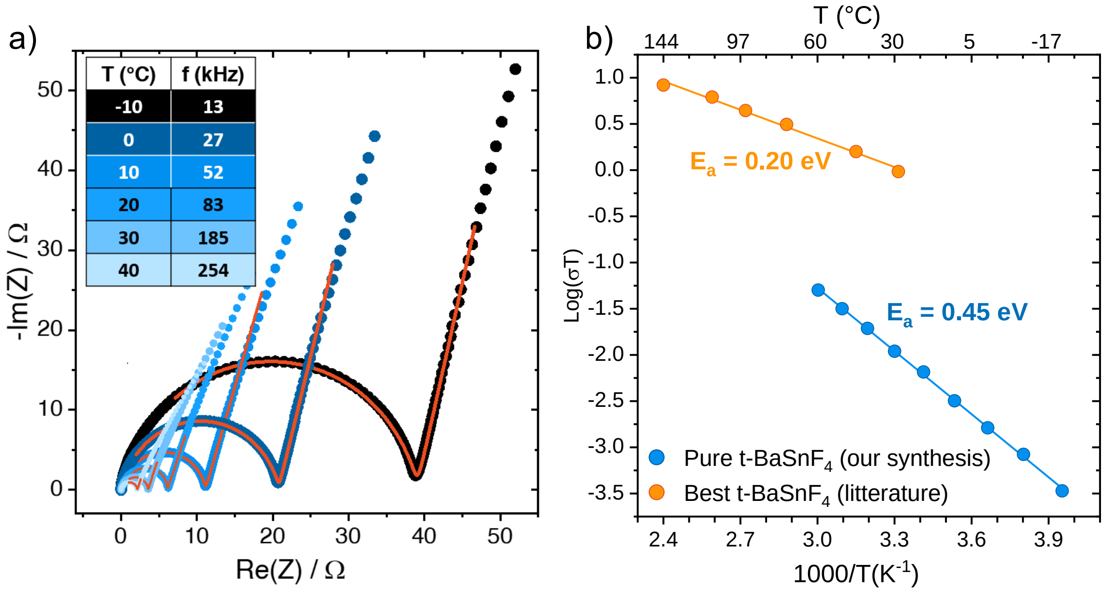

Figure III.2 EIS of the pure t-BaSnF$_4$ phase a) Nyquist plots recorded at increasing temperatures, with the characteristic frequencies of each semi-circle explicated in the table b) Arrhenius plot comparing our product with the (impure) t-BaSnF$_4$ from the literature with the highest reported conductivity (ref 66). The compacity of the highly conductive pellet was not given.

The low compacity of our pellet may also be a factor of poor conductivity. Both of these considerations are motivation to explore other synthesis methods.

III.2. A new route to produce BaSnF$_4$: Spark “Plasma” Sintering

Though the Ball-milling/annealing/ball-milling/annealing method is effective and produces a pure material, it is a fairly long process. Additionally, it yields a powder which is difficult to transform into compact pellets. We therefore decided to explore a different route, which allowed us to obtain a pellet with less difficulties, shortening the synthesis time and facilitating the subsequent EIS characterization.

III.2.1 SPS working principle

"Spark Plasma Sintering" (SPS) is a pressure and electric current assisted sintering/synthesis technique. DC current millisecond pulses are sent through powders, heating it via Joule effect, while it is kept under uniaxial pressure. A schematic of the SPS apparatus is presented in **Figure III.3**.

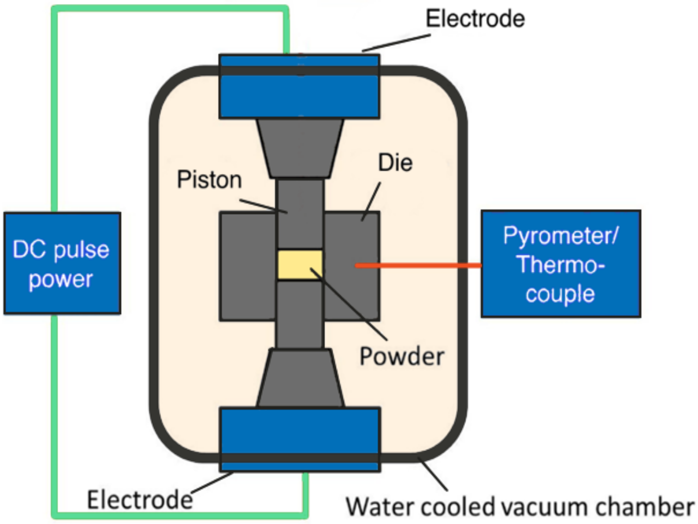

Figure III.3 Working schematic of an SPS apparatus, adapted from ref. 236

It is akin to a hot press, though heat originates from the current, which is thought to provide additional benefits in terms of sintering kinetics. The combination of current and pressure allows for efficient sintering, often at temperatures between 200°C and 500°C, i.e. lower than what would be required by regular high-temperature process. The sintering times are also significantly shorter.[235] One of the attractive features of SPS is its high heating and cooling rates, reaching up to 1000 K.min^{-1} and 150 K.min^{-1} respectively.

The exact working principle of SPS is still unclear, especially about the presence or absence of actual plasma during heating, which is why SPS is sometimes called "pulsed electric current sintering". Here, we will be calling this technique SPS, as it is the most used denomination.

III.2.2 Methodology of the SPS synthesis

At first, the synthesis was attempted using the protocol previously developed in LRCS for other materials.[236,237] SPS dies were lined with carbon paper (Papyex) and dried in the oven at 70 °C for a few hours. Inside the glovebox, around 450mg of precursor powder were added to the die and pressed into pellets using a uniaxial press. Dried Papyex discs were then added to both sides of the pellet and this stack was once again pressed, before being placed in the SPS apparatus.

After the synthesis, the pellets were removed from the dies and polished until their surface was even using 2000 and 5000 grit polishing paper. The papyex discs mostly adhered to the materials and were therefore kept as semi-blocking electrodes for Electrochemical impedance Spectroscopy measurements, before being polished off for XRD measurements. The pellets were very fragile and tended to fall apart upon removal of the papyex. This stack yielded intact pellets a couple of times, which had very promising conductivities. Unfortunately, the great majority of subsequent attempts lead to stack adhesion to the upper piston, and removal resulted in the disintegration of the pellet, which could not be salvaged for EIS or XRD. A new stack was therefore developed which consisted of the electrolyte pellet, with two papyex discs pressed into it on each side, and a thin layer of carbon powder added after pressing on both sides of the stack. The two papyex discs instead of one facilitated the polishing of the pellet, while the carbon layer prevented unwanted adhesion.

Note that Carbon diffusion inside the material is sometimes an issue when using SPS but was not observed here, as the pellets remained pure white.

III.2.3. SPS synthesis

III.2.3.1 Synthesis of a pure t-$BaSnF_4$ phase through SPS

The first synthesis attempts were made by holding the sample for 30 minutes at 300°C, as it is the temperature previously used for ordinary heat treatments. There was a small amount of cubic impurity left, enough for the most intense peak of this phase to be visible but not for it to be accurately quantified by Rietveld refinement. In order to improve the purity, we first tried changing the holding time. Increasing it to 45mn or 1h and decreasing it to 15 and later 5mn did not prevent the appearance of the (111) cubic impurity peak. Interestingly, the material held for only 5mn at 300°C had a similar purity as the others. Faster and slower ramps were also tested and did not influence the purity. All resulting pellets were characterized using X-Ray Diffraction, and indexed to t-$BaSnF_4$. Le Bail refinements of resulting diagrams showed they all had different cell parameters, with some significant variations of the c-parameter, though the variation did not follow any trend with regards to holding time.

It should be noted here that SPS is known for being user-dependent and difficult to reproduce. Although general trends and patterns can be deduced from these experiments, there are a lot of variations which cannot be explained in a straightforward way. Generally, the presence or absence of cubic impurity was reproducible, but the cell parameters varied slightly even when replicating the same experiment.

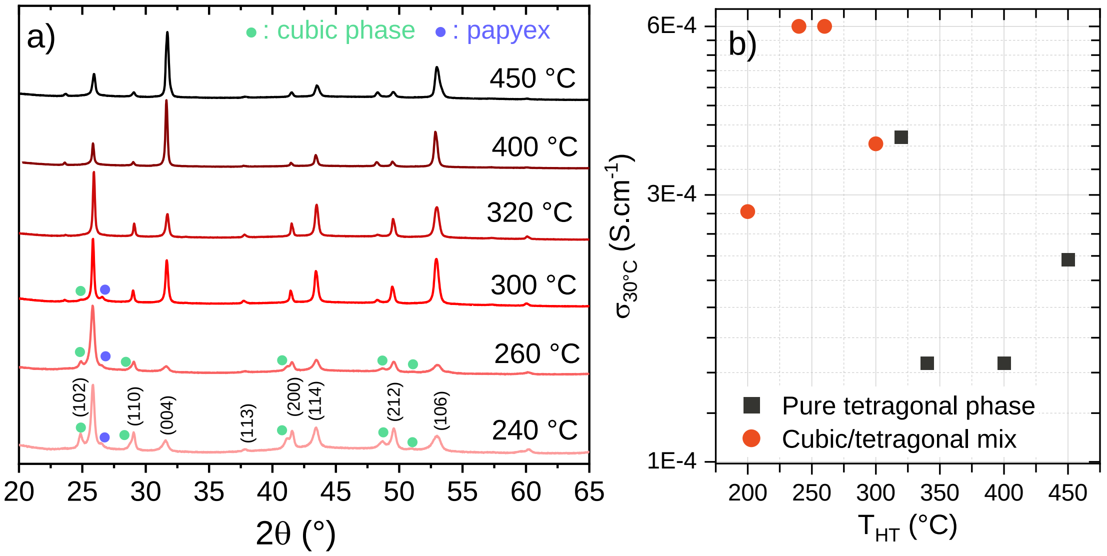

Figure III.4 Effect of the SPS synthesis temperature on a) the X-ray diffractometers of pellets obtained from different SPS temperatures. The blue stars mark the presence of carbon paper (papyex) that was not be polished off completely because of the high pellet fragility, b) the room-temperature conductivity

The greatest impact on the final purity of the sample was obtained by varying the synthesis temperature, as shown in **Figure III.4** panel a). The weight percent of cubic phase was determined through Rietveld analysis for each sample, going from 18.4(9)% for the 240°C synthesis down to 5.8(3)% at 260°C, reaching unquantifiable quantities from 300°C to 360°C and completely disappearing from 400°C on. When investigating the transport properties of these materials, however, it was found that higher purity did not necessarily result in higher conductivity. As seen in **Figure III.4** panel b), the best conductivity for this series of experiments was obtained for mixed cubic/tetragonal phases. We did not expect it to be so, given the higher bulk conductivity of the tetragonal phase compared to any tin-containing $Ba_xSn_{1-x}F_4$ fluorites.[56] Additionally, in most ceramics, higher sintering temperatures generally result in lower porosity, and hence better global ion transport. Here, the measured conductivity mostly decreases when the annealing temperature increases.

III.2.3.2 Influence of synthesis temperature on the microstructure of $BaSnF_4$

In order to find a possible explanation for the conductivity variation as a function of annealing temperature, we further characterized the microstructure variations firstly through compacity measurements. Compacity is defined as the ratio of the experimental density over the theoretical density. The theoretical density was calculated specifically for each pellet in order to account for the various amounts of cubic phase impurity, as well as for the slight variations in cell parameters. For many ceramics, sintering temperature has a dramatic effect on pellet compacity and as a result, on the final conductivity. We could however not link higher compacity with higher synthesis temperatures. Compacities ranged from 84% to 94%, but higher compacities were surprisingly not systematically synonymous with higher conductivities in this case.

Similarly, synthesis temperatures normally impact crystallinity, which should in turn influence conductivity. We therefore evaluated the crystallite domain sizes using Williamson-Hall diagrams, based on the Scherrer formula:

$$\beta cos\Theta = \lambda/L + 4\varepsilon \, sin\Theta$$

where β is the integral breadth of the peak, Θ the diffraction angle (in radian), λ the diffractometer radiation, L the crystallite size, and ε the rate of microstrain ($\varepsilon = \Delta d/d$, with d the interplanar distance and Δd the local variations introduced in the material by distortions). The integral breadth β of a peak is different from its Full Width at Half Maximum (FWHM), though that is sometimes used as a proxy. β is defined as the width of a rectangle which as the same height and surface as the peak, and is obtained through refinement of the XRD diagram.

It should be noted that diffractograms measured on either side of a same pellet often displayed slight differences. In order to accurately evaluate the impact of various synthesis parameters on the microstructure, we tried as much as possible to measure both sides, though it was not always feasible due to the fragility of the pellets. Usually, the top side, which was exposed to the current first, had more anisotropic crystallites and had stronger preferential orientations.

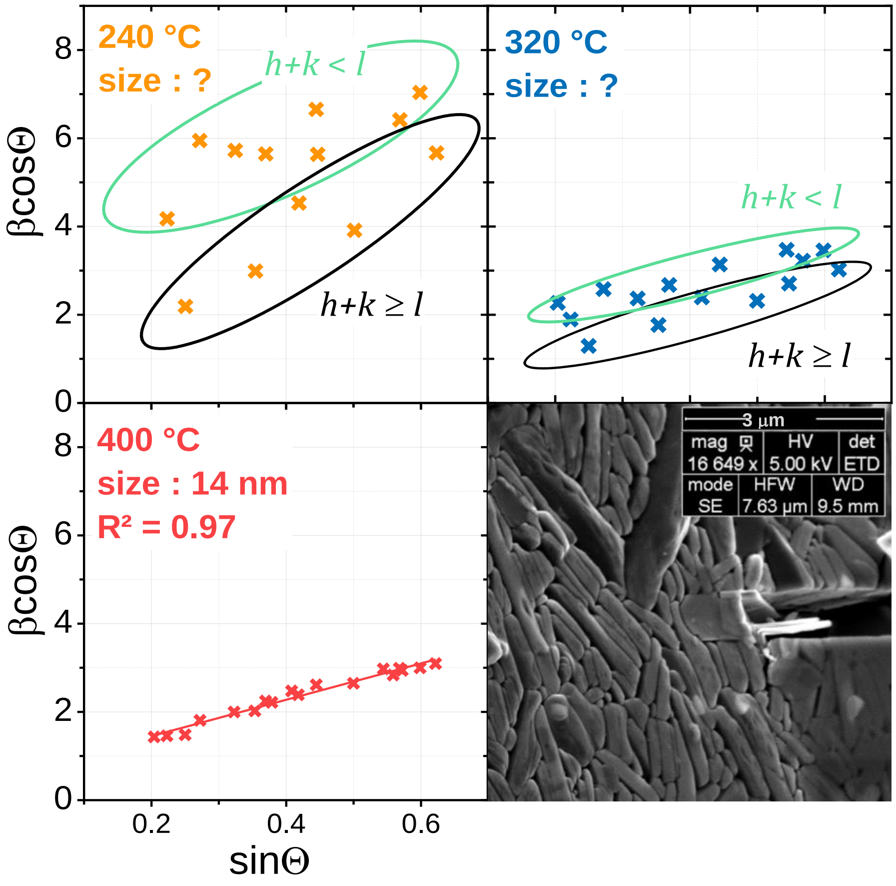

Figure III.5 Williamson-Hall diagrams of samples treated at different temperatures. The black circles encompass planes where $h+k \geq l$, the purple circles planes where $h+k < l$, the last panel is a SEM image of a pellet piece after SPS synthesis at 320 °C, where the layered structure is visible

Generally, the peaks get progressively wider as 2Θ increases, and the product of the integral breadth and the cosine of the angle forms a line, from which the crystallite size and the microstrain may be deduced.

As shown in **Fig III.5**, this behaviour is indeed observed for samples synthetized at high temperature (T_{SPS}>380 °C). As the synthesis temperature lowers however, the relationship is no longer linear. The distribution of points in the Williamson-Hall diagrams of these materials becomes cloud-like, where the bottom points are associated with (*hkl*) peaks where $h+k \geq l$, and top points with peaks where $h+k < l$. Even with this separation it was not possible to estimate the strain or crystallite size in either direction, as the R^2 of the linear fits were too low (e.g for 240°C, 0.79 for the bottom part and 0.43 for the top).

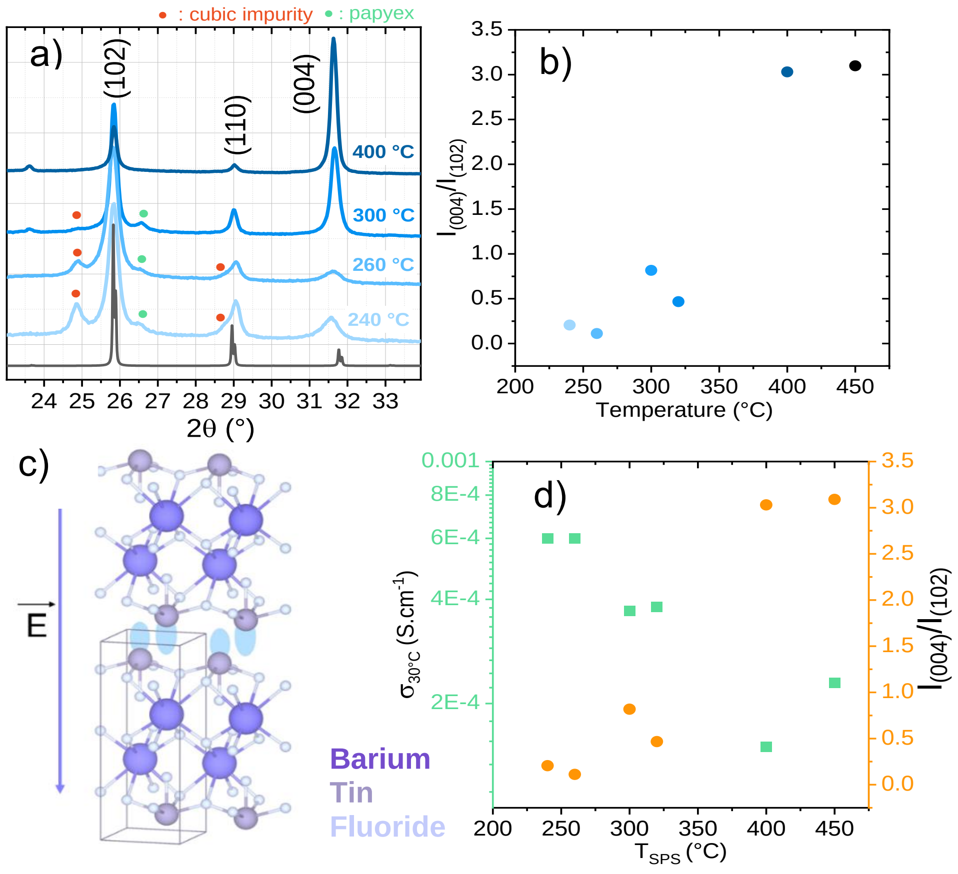

Figure III.6 Preferential growth in SPS-synthetized t-BaSnF$_4$, a) evolution of XRD diagrams intensities at low angles, the black diagram at the bottom is the theoretical diagram b) quantification of the increase of the I(004)/I(102) ratio with increasing SPS temperatures, c) schematic of the preferred orientation along the c-axis, the tin lone pairs are represented in light blue d) variation of the ionic conductivity and preferential growth with regards to synthesis temperature

Overall, the trend seems to point to larger and more strained crystallites in high [hk] directions. This anisotropy is also visible at a higher scale: as shown in the last panel of **Figure III.5**, crystallites assemble in particles with sheet-like shapes. Higher temperature yielded less anisotropic and somewhat smaller crystallites: 14nm for 400°C and 8nm for 450°C. Previous Differential Scanning Calorimetry measurements suggested that BaSnF4 might decompose at these high temperatures. We therefore used faster cooling rates, which in turn may be responsible for the smaller crystallite sizes.

Another feature of the XRD diagrams which evolves with temperature is the relative peak intensities. The theoretical diagram of t-$BaSnF_4$ gives the (102) reflection as the most intense. The (004) peak has a theoretical intensity of $I_{(004)} = 0.13 \text{ x } I_{(102)}$. As seen **Figure III.4** and **Figure III.6**, relative peak intensities shift dramatically with temperature, to the point where (004) becomes the most intense reflection of the diagram. The intensity of its harmonic, (002), also grows significantly. In general, all peaks originated from $h+k<l$ planes expand. This is strong evidence for the presence of preferential growth of the crystallites. This phenomenon has already been observed for other materials synthesized with SPS, such as Sb_2Te_3[238], Bi_2Te_3[239], and Ti_3SiC_2 [240]. For the latter, oriented crystallite growth has been linked with the presence of pressure and high heating rates, but for some materials there may also be an electronic effect induced by lone pairs,

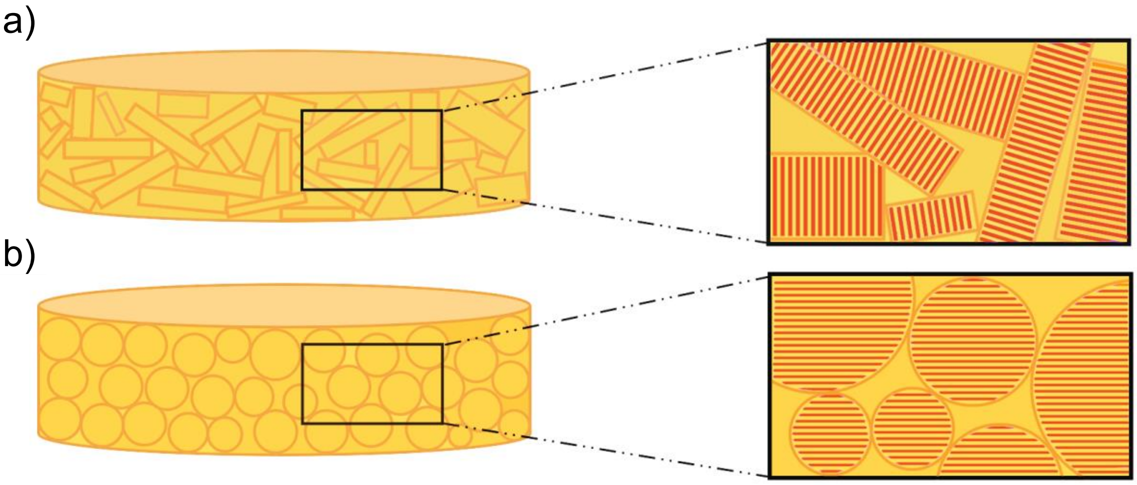

Figure III.7. particle morphology and plane orientation in a pellet sintered in SPS at a) lower temperature b) higher temperature present on Sb and Bi ions in the previously cited examples. In our case as well, the tin electronic lone pair may be responsible for the preferential growth, as it aligns with the SPS electric field, as shown in **Figure III.6**, panel c). Lone pairs are known to rotate to align with electric fields in other materials as well (ferroelectric switching).[241]

It is interesting to note that the degree of crystallographic orientation is here inverse to the degree of anisotropy of the crystallites. At low synthesis temperature, the crystallographic domains are not oriented (within the pellet) but particles are strongly anisotropic, forming platelets (**Figure III.7.** a). At higher temperatures, the domains become smaller and isotropic, but the crystallographic planes are highly aligned from one particle to the other (**Figure III.7** b)

This preferential orientation affects the transport properties of the pellet. As previously explained, t-$BaSnF_4$ is a 2D conductor, with the Ba-Ba layer largely preventing ion diffusion in the c-direction.[77] The high-temperature-induced orientation is such that F-ions diffusing vertically from one side of a pellet to the other must cross more Ba-Ba layers than they would in a randomly oriented material. Since the ionic conductivities measured via Electrochemical Impedance Spectroscopy (EIS) probe transport in this precise direction, it is no surprise that the conductivity would decrease as the preferential orientations become more and more prominent, as shown in **Figure III.6**, panel d).

In order to confirm this hypothesis, we designed an experiment which allowed us to measure conductivities in two opposite directions. A very thick pellet was therefore prepared, and heated via SPS at 400°C in order to favour orientations of planes along (00*l*). EIS was measured, as well as XRD which confirmed the orientation. The pellet was then cut, and a slice was polished to be as round as possible, as physical models used to interpret EIS data are only valid for this shape. A thin gold layer was sputtered on the polished slice and its ionic conductivity once again measured. A schematic of the experiment and its main results are visible in **Figure III.8.**

As shown in panel b), XRD confirmed the presence of preferential (004) orientations of the pellet's face (004). The slice we obtained from the pellet was in turn oriented with rectangular facets perpendicular to [110]. However, the slice exhibited only a slight

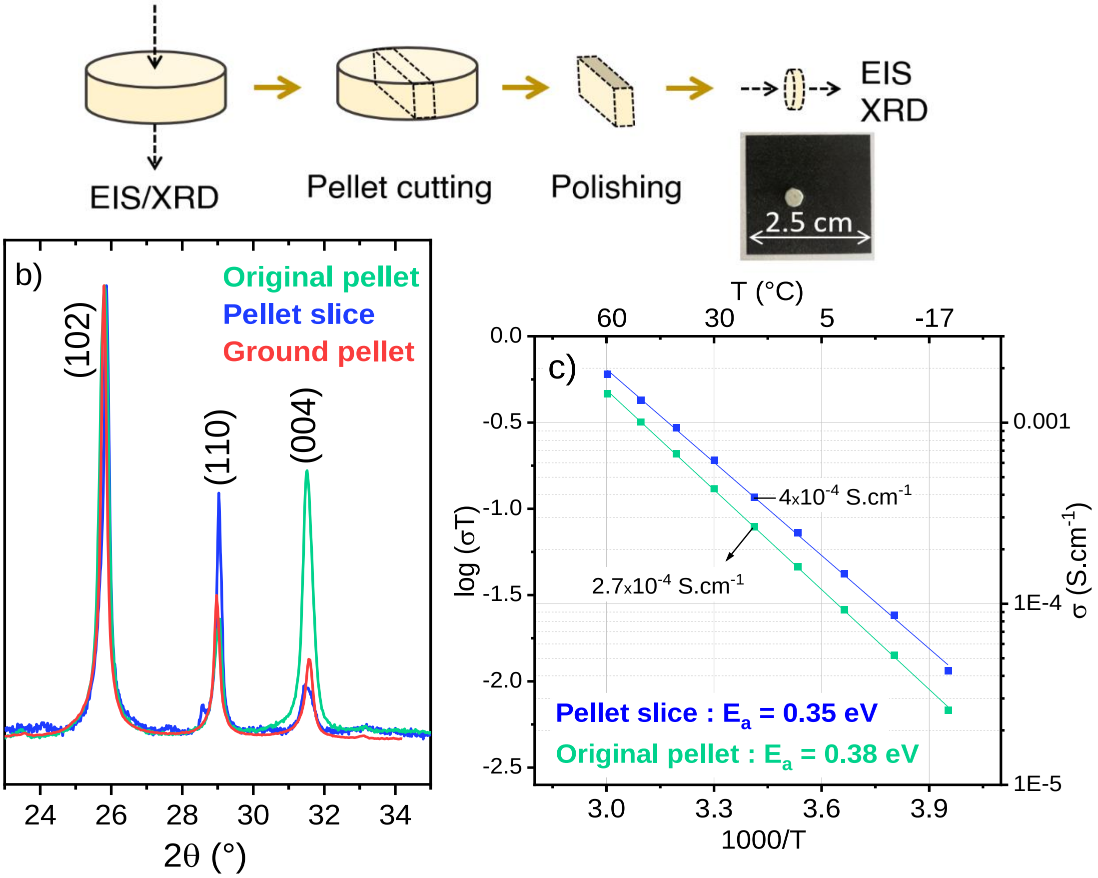

Figure III.8 pellet slicing experiment a) process, b) XRD diagrams of the ground pellet as reference (red), pristine pellet (green), and pellet slice (blue). For the latter, the background was removed in order to be able to compare the three c) Arrhenius plots extracted from EIS measurements of the pristine and cut pellet

improvement in conductivity compared to the whole pellet (panel c)). This could stem from the difficulty in accurately assessing the area of the slice, which would then lead to an under-estimation of its conductivity. It is therefore difficult to give a definitive conclusion regarding the impact of preferential orientations from this experiment alone.

The combination of this experiment and the evolutions of transport properties versus the relative intensity of the (004) (**Figure III.6** d) peak does however strongly suggest that there is a correlation. We then focused on evaluating the impact of various synthesis parameters on the orientation degree of the pellet and on its ionic transport properties.

III.2.3.3 Optimization of synthesis parameters for reaching high conductivity

In an attempt to optimize the ionic conductivity of the pellets, different parameters were tuned: the SPS pressure during synthesis, the milling time of the two precursors (BaF_2 and SnF_2) before pelletization, the uniaxial pressure applied prior to the synthesis ("cold pressure"), and the stack composition. Each parameter was studied independently from the others.

Overall, the stack pressure during synthesis (**Figure III.9** panel b)) had little effect on either conductivity or preferential orientation of the crystallographic planes. It was expected, based on literature reports,[242] that the pressure should impact crystallite size and anisotropy, but Williamson-Hall diagrams did not reflect this, as all domains were between 10 and 12 nm large.

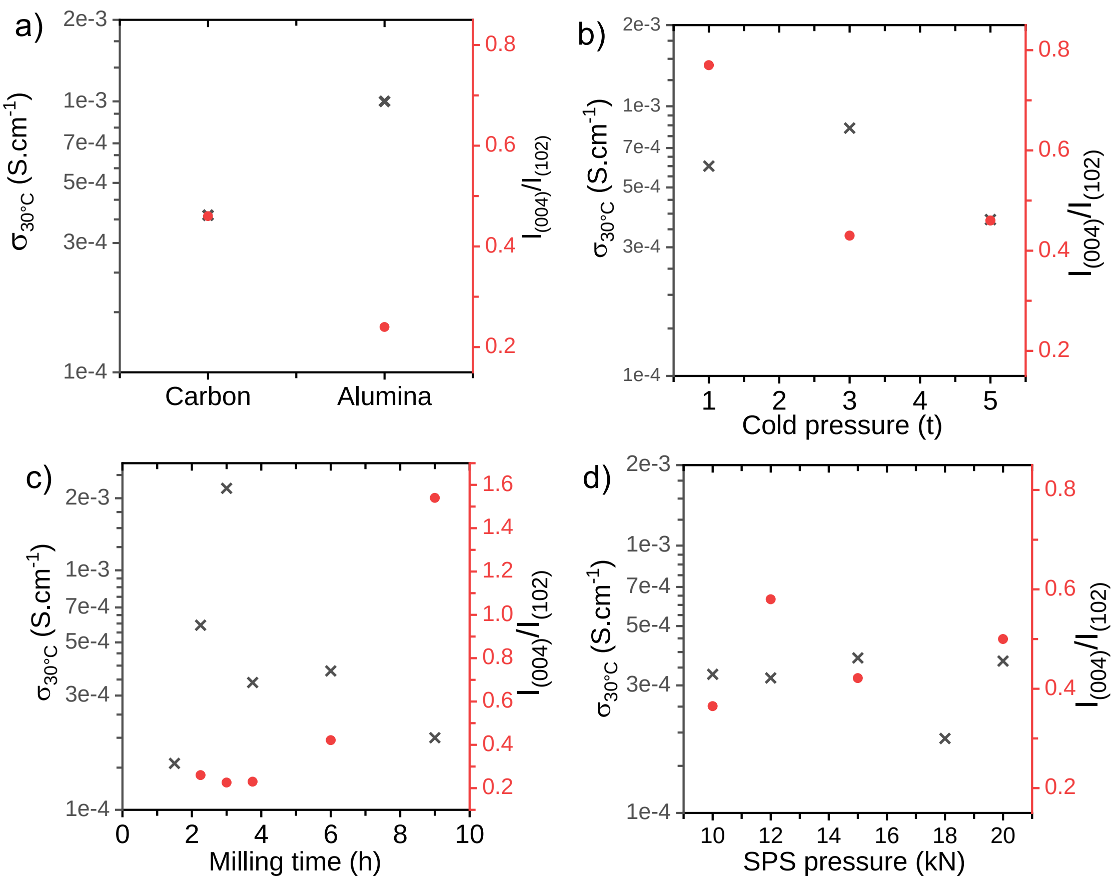

Figure III.9 Effect of parameter variations on conductivity and preferential orientations, a) effect of pressure during synthesis, b) effect of milling time, c) effect of pre-synthesis pressure, d) effect of stack composition

The precursor milling time, on the other hand, had a dramatic and reproducible effect, with a conductivity maximum observed for 3 hours of ball-milling time, as seen **Figure III.9** panel c). After 3h of milling, the product is not the pure cubic phase described in chapter I., but a mix of $Ba_{1-x}Sn_xF_4$ and yet unreacted SnF_2. Milling time has seemingly no influence on the product in terms of crystallite size, shape or orientation, nor in terms of purity (all samples still contain some cubic phase) or compacity.

Likewise, the pressure applied to the sample to make it into a pellet before the SPS step has a substantial impact on the conductivity, which could not be linked to any microstructural variation.

Lastly, two stack compositions were compared, which both impacted current diffusion in the sample differently. The first stack is the one which was used in all previous experiments, i.e. carbon powder / 2 graphite discs / sample / 2 graphite discs / carbon powder. Both the carbon powder and graphite discs are electronic conductors, which allows the current to flow vertically through the sample, favouring c-direction crystallite orientations, as previously discussed. For the second stack, the carbon powder was replaced with alumina, an electronic insulator, which prevents vertical flow and forces

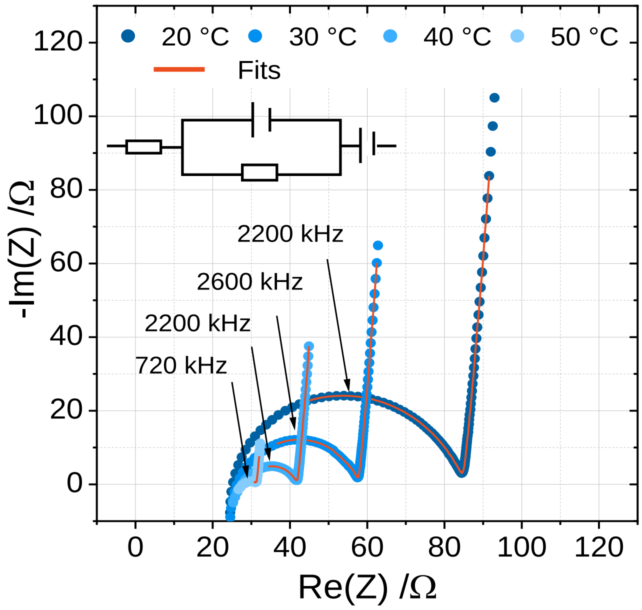

Figure III.10 temperature-dependant Electrochemical Impedance Spectroscopy of the most conductive sample synthetized via SPS and data fitting. The equivalent circuit used for fitting is shown under the legend.

the current to pass through the sides of the pellet, making current lines more isotropic. The resulting pellets were significantly more conductive and preferential plane orientations were decreased by half, as seen in **Figure III.9** panel a). This change however does not impact crystallite shape, which remains highly anisotropic for this temperature. As a 2D material, t-BaSnF$_4$ tends to grow as platelets, regardless of the synthesis method.

For the route described in III.1.2, SEM also showed this to be true and authors reporting on coprecipitation syntheses have observed this as well.[231] Finally, optimal synthesis parameters were combined: 3h of precursor milling, 3 tons of cold-pressure, 12 kN of pressure and 280°C during sintering within an alumina-containing stack. The resulting pellet had an ionic conductivity of 2.20 x 10^{-3} S.cm^{-1} at 20°C and an activation energy of 0.55 eV. The highest conductivity that we obtained was for a sample synthesized with global same conditions, but at 340°C, yielding a record value of 5 x 10^{-3} S.cm^{-1} at 20°C, with an activation energy of 0.63 eV. The temperature-dependant EIS and corresponding fits are shown in **Figure III.10**.

Both these activation energies are higher than what is usually reported (≈0.3 eV) for t-BaSnF$_4$. This is surprising, as normally high activation energies render ionic diffusion more difficult, lowering conductivities, as per the well-known equation:

$$\sigma = \sigma_0 \exp\left(\frac{-E_a}{kT}\right)$$

where σ is the ionic conductivity, σ_0 the prefactor, E_a the activation energy, k the Boltzmann constant and T the temperature. An increase of both σ and E_a suggests a change in the value of the prefactor, which itself is dependent on various factors:

$$\sigma_0 = z\frac{n_c q^2}{k}\exp\left(\frac{\Delta S_m}{k}\right)\alpha_0^2 \upsilon_0$$

with z a geometric factor, n_c the concentration of mobile species, q their charge, ΔSm the entropy of migration, α_0 the jump distance and υ_0 the jump attempt frequency.

Using Broadband Dielectric Spectroscopy, it is possible to evaluate both the jump attempt frequency and the prefactor, which allows for the calculation of the charge carrier density. This technique is very similar to Electrochemical Impedance Spectroscopy (EIS), with two key differences: their frequency ranges and the types of perturbations used. EIS probes phenomena in the mHz to MHz range, while dielectric spectroscopy can reach up to THz, hence potentially accessing very fast relaxations. Both methods are based on the same principle: a small perturbation is sent through the system and its response is measured. For EIS, the perturbation is a sinusoidal potential variation, and we record the current response (changes in phase and amplitude of the wave) at each frequency. From this information, the impedance, or complex resistivity, is deduced. For dielectric spectroscopy, the collected response is slightly different, as both fluctuations in current density and dipole moment are recorded, simultaneously giving access to complex permittivity and complex conductivity.

In collaboration with O. Dubrunfault and J-C Badot (LGEP), we performed temperature-dependant dielectric spectroscopy measurements of a pellet synthetized via SPS, and compared the results with those of Ahmad et al., who measured the dielectric properties of a t-$BaSnF_4$ sample synthesized through ball-milling and subsequent annealing (which contained 7.6% of cubic secondary phase).[232] A summary of the results is given in **Table III.1**. The SPS-synthetized pellet is over 20 times more conductive at 30°C than the other sample, while having a significantly higher activation energy. The increase in conductivity appears to be directly linked to the increase of the number of charge carriers, which is 23 times higher for the SPS sample. We hypothesize that the ball-milling steps introduces a large quantity of defects in the material, which may act as traps to the mobile ions. The higher conductivity of SPS-synthetized samples could then be tentatively assigned to a lower number of defects, which results in a higher proportion of mobile ions.

The activation energy is, as explained in the introduction chapter, highly dependent on the energy landscape of a material, which is itself determined in part by structure. We therefore turn to structural characterizations to better understand the impact of synthesis parameters on the transport properties of t-$BaSnF_4$.

Table III.1 : comparison of the dielectric properties of t-BaSnF$_4$, from two different synthesis routes

	Ball-milling/annealing synthesis (ref 6)	**SPS synthesis**
$\sigma_{30°C}$ (S.cm^{-1})	1 x10^{-4}	2.2 x10^{-3}
E_a	0.34	0.47
υ_0 (Hz)	5.6 x10^{10}	2 x10^{10}
n_c (cm^{-3})	3.13 x10^{21}	7.14 x10^{22}

III.2.3.4 Structural analysis of SPS-synthetized t-BaSnF$_4$: Attempt to correlate the ionic conductivity to unit cell parameters.

Globally, we prepared many materials through SPS which were all analysed by XRD so as to extract unit-cell parameters, microstructures and preferential orientations. Cell parameters were obtained through Le Bail refinements, using the Fullprof software. One noteworthy specificity of these refinements is the use of a Thompson-Cox-Hastings function (NPR = 7) to model the peaks.[243] This function accounts for microstructure, and as such we were able to more accurately fit the diagrams of heavily oriented samples which had platelet-shaped crystallites. An example of one such fit is presented in **Figure III.11**, panel b).

The resulting cell parameters were plotted against room-temperature conductivity, probing for potential correlations. Firstly, the evolution of the conductivity with the cell volume is shown (**Figure III.11** panel a)). It appears that there is a faint connection between these, with a lower unit-cell volume generally leading to a higher conductivity. This seems counter-intuitive, as generally a smaller volume leads to smaller bottlenecks, which increases the activation energy. As previously discussed, the most conductive samples indeed had higher activation energies, the structural data appears therefore consistent with the Electrochemical Impedance Spectroscopy results.

The unit-cell volume being calculated from the two cell parameters, a and c, we deconvoluted the effect of each parameter, as seen in panels c) and d). The a-parameter does not vary much, and no correlation can be made. On the other hand, the c-parameter fluctuates by as much as 0.8 Å, a very significant deviation. There also appears to be more of a correlation between the c-parameter and conductivity, with once again lower c leading to better transport properties.

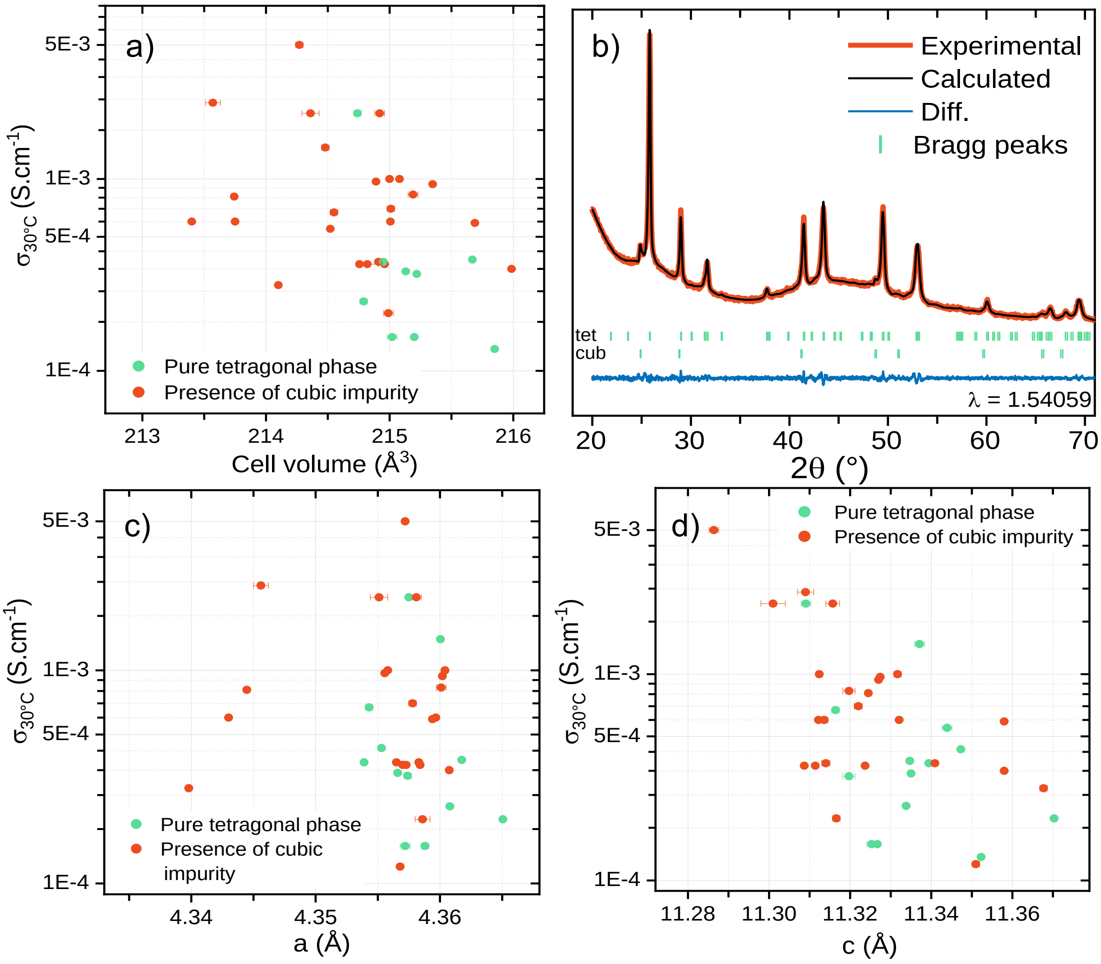

Figure III.11 Structural variations of SPS-synthetized t-$BaSnF_4$, a) evolution of the conductivity with volume change, b) example of a Le Bail refinement using NPR = 7 for the sample with the largest error bars (the bumps in the background are caused by the sample holder, c) and d) effect of a and c-parameters on conductivity

These large variations along one particular axis are a sign of possible stacking faults in the material, which can increase lattice parameters, as well as cause asymmetry and broadening of the XRD peaks, as seen for the (00*l*) reflections for t-$BaSnF_4$, shown in **Figure III.12.**[244] Faults are generally visible via TEM, however in this case the platelet shape of the particles favoured their flat deposition on the copper grid, only exposing non-faulted ($hk0$) directions to the beam.

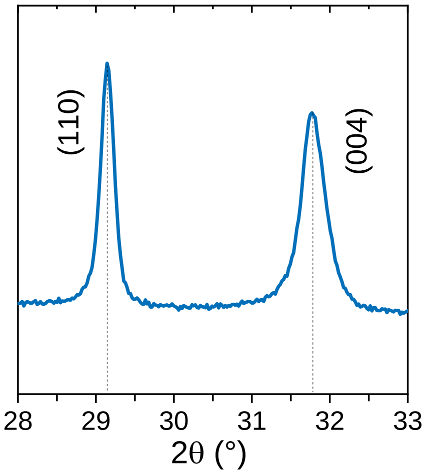

Figure III.12 XRD diagram of SPS-synthetized t-$BaSnF_4$ (V = 215.34(1) Å), the (004) peak is significantly larger and more asymmetric than the (110)

In order to gain further insight on the structure, we turned to neutron diffraction.

III.2.3.5 Neutron diffraction: characterization of stacking faults and interstitial fluorides within the structure

To have points of comparison, we measured neutron diffraction on three different samples:

- The product of the ball-milling/annealing/ball-milling/annealing synthesis described ealier was analysed using neutron diffraction, in collaboration with Dr. E. Suard at the Institut Laue-Langevin, Grenoble, France.

- A sample synthetized via SPS, which had a large c-parameter of c = 11.3813(4) Å, which we will refer to as “Hc”, measured at the Reactor Institute of Delft in collaboration with Dr T. Famprikis.

- A second sample synthetized via SPS with a lower c-parameter, c = 11.3382(7) Å, referred to as “Lc”, measured at the Reactor Institute of Delft in collaboration with Dr T. Famprikis.

We will now detail the Rietveld fitting process of these samples, and what insight we gained at each step while discussing the refinement procedure. The initial result, obtained from using a regular Pseudo-Voigt function to model the peaks (with the Fullprof Software)[245] is shown in **Figure III.13**.

Several points draw attention. Firstly, the (002) peak, magnified in the zoomed in window, is extremely asymmetric, especially compared to others. This is consistent with the XRD data previously discussed. The fitting of this peak is also unsatisfactory, the calculated curve being not well aligned with the center of the experimental peak, which suggests that the c-parameter obtained through the fit is incorrect. As this reflection only contains contribution related to c, we can directly deduce the value of c based on its position, using Bragg's law. The results of this calculation for the (002) and (003) reflections, as well as the Rietveld-determined parameter are summarized below in **Table III.3**.

Table III.2 c-parameters determined through the fit of the neutron data shown in **fig. III.13**, as well as directly from the (00l) peak positions

c determination method	**Higher-c**	**Lower-c**	**Ball-milling/annealing**
(002) neutron diffraction	11.608 Å	11.554 Å	11.4 Å
(003) neutron diffraction	11.481 Å	11.409 Å	11.274 Å
Rietveld refinement (neutron diffraction)	11.350(4) Å	11.311(6) Å	11.287(3)

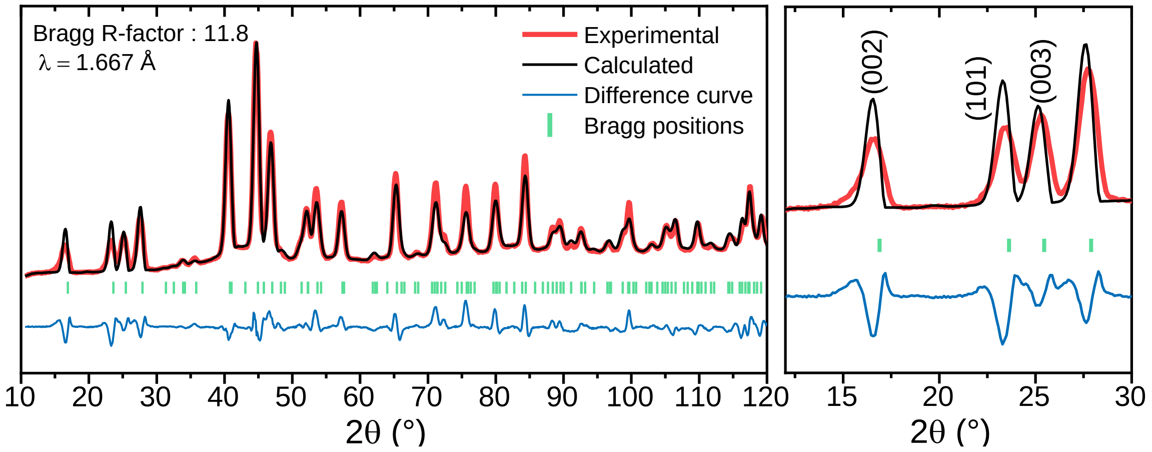

Figure III.13. Initial fit of the Hc sample neutron data, with a zoom on the first 4 peaks

The c-parameters vary wildly, from one sample to another but also for the same sample, depending on the determination method. The neutron refinement also leads to values lower than the previously given XRD-extracted parameters (c_{Lc} = 11.3382(7) Å, c_{Hc} = 11.3813(4) Å). All parameters follow the same trend: highest for the (002) reflection determination, decreasing when calculated through (003), and the lowest value is obtained through Rietveld refinement.

In face-centered cubic structures, it has been shown that the presence of stacking faults causes a 2θ shift for the reflections in the impacted directions. The shift is related to the reflection *hkl* values though the following equation[244] :

$$\Delta 2\theta_{(hkl)} = \frac{90\sqrt{3} * \alpha * tan\theta}{\pi^2 h_0^2 (u + b)} \sum_b L_0$$

where α is the deformation fault probability, $h_0 = h^2 + k^2 + l^2$, u is the number of unbroadened components (for which $L_0 = 3N$), b is the number of broadened components ($L_0 = 3N \pm 1$), and $L_0 = h + k + l$. It then comes that as the l-value increases, the 2Θ shift decreases, which is exactly what we observe. As t-$BaSnF_4$ is not face-centered cubic, this equation cannot be used to determine the deformation fault probability (though if we did apply it, we would find that about 1 layer in 16 appears faulted along c, which is as expected very high). It does however appear that it is closely related enough to it to exhibit similar shifting behaviours.

We note that the *Ball-milling/annealing/ball-milling-annealing* sample has the lowest unit-cell parameter, suggesting it contains the least number of faults. This is fairly surprising, as that sample has wide diffraction peaks (e.g. $FWHM_{(102)}$ = 0.71 °), associated with small crystallite size but also lattice defects. Perhaps the defects introduced by the ball-milling steps do not include stacking faults, or perhaps these dissipate during the annealing step. The annealing and cooling times are indeed significantly longer for this synthesis (3h of temperature hold + overnight cooling) than they are for the SPS synthesis (30mn temperature hold, 15mn cooling).

This brings about the question of accurate determination of the c lattice parameter. It is reasonable to assume that most, if not all our syntheses, as well as the syntheses reported in the literature yield samples containing various amounts of stacking faults.

Some Density Functional Theory calculations were performed on t-BaSnF$_4$, but the resulting c-parameter was 11.2388 Å,[80] which is higher than what has been reported by Ahmad et al. for their synthesis,[232] in other words the DFT value may be overestimated. In our group, a machine-learning model was built by Xiliang LIAN to simulate this structure (to be published), and it produced a c-parameter of 10.90 Å, an a-parameter of 4.33 Å, and hence a volume of 204.93 Å^3. This appears to be very small, but the a-parameter is fairly consistent with the experimental data, indicating a fault-less material could indeed have a much smaller cell than previously imagined.

The heavy presence of stacking faults in t-BaSnF$_4$, leading to increases of the c-parameters, provides the beginning of an explanation for the conductivity increases, observed concurrent to the c-shrinkage. Lower amounts of stacking faults would incur lower c-parameters, but also less defects in the crystal, which should facilitate ionic diffusion.

It is complicated to properly fit the neutron data while accounting for stacking faults. As a way to improve the fitting of the shifted peaks, we refined an additional parameter, the

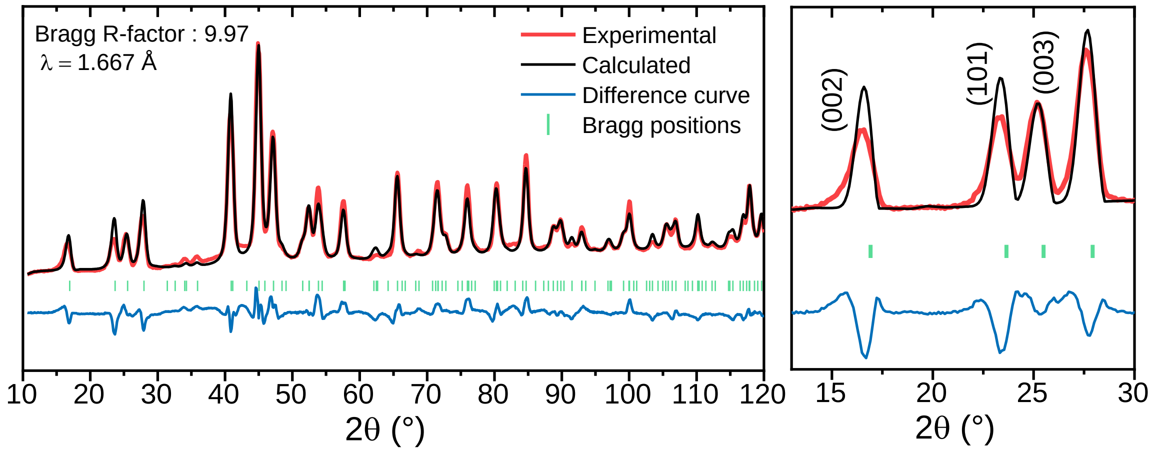

Figure III.14 Fit of the neutron diffraction data using Sysin parameter to account for stacking faults. The overall fit is improved, especially the c-dependent peaks (zoom on the left), where while the asymmetric peak width are not well calculated, the 2Θ of the calculated and experimental diagrams align well.

sin(2Θ)-dependant systematic shift (Sysin). This parameter normally accounts for peaks shift that have an instrumental origin. We know however that apparatus is not the cause for the shifting in our diagrams, as the Sisyn values obtained for the two samples measured on the same instrument were significantly different : -0.10(1)° for Lc and -0.20(1)° for Hc. The new fit (**Figure III.14**) is substantially better, and the new c-parameters are closer to those previously determined via XRD ($c_{Lc, sysin}$ = 11.332 (3) Å, $c_{Hc, sysin}$ = 11.374 (4) Å). The asymmetry of the low-angle peaks could however not be fitted properly. Other authors have presented neutron diffraction data on this structure, but had significantly less difficulties to obtain satisfactory fits.[66] In particular, the first peaks, at 23.21°, 25.11°, and 27.63°, did not appear differently shaped compared to the rest. As Mori et al. report a low c = 11.2273(10) Å ($c_{Lc, sysin}$ = 11.332 (3) Å), it is possible that our samples contain more stacking faults, making the fitting more complicated.

In addition to shifts and assymetry on specific peaks, some of the calculated intensities are incorrect. Peak intensity is related to electron density in the plane, [246] having intensity missing is then sometimes an indicator of the presence of interstitial ions. It is possible to visualize where in the cell there is electron density missing or in excess through Fourier maps calculated from the difference curve of the fit. One such map is shown in **Figure**

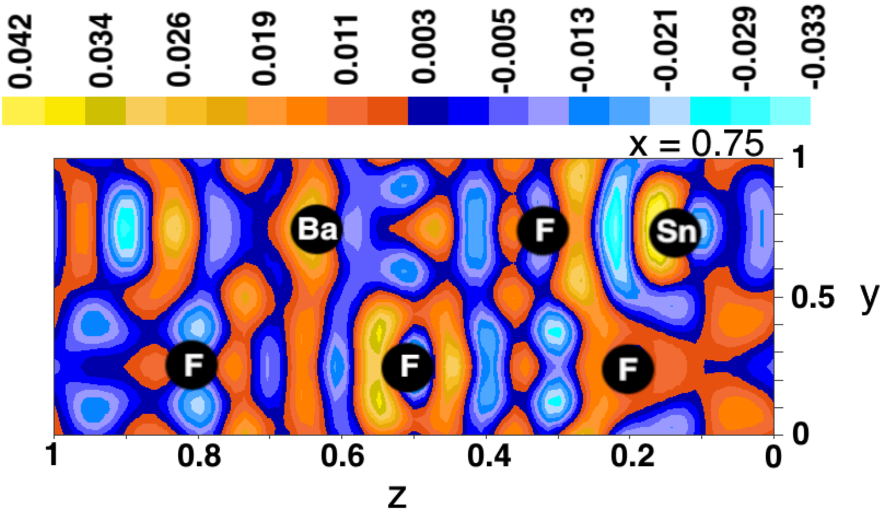

Figure III.15 slice at x=0.75 of the Fourier difference map, showing missing (cold colors) and excess (warm colors) electron densities in the Lc sample fitted using the sysin parameter.

III.15. Possible intersticial sites are signalled by a high missing electron density. The two main electronic deficits visible on the x=0.75 slice (which mirrors the x = 0.25 slice) are at y = 0.75, z = 0.25 (Sn site : lone pair related) and at y = 0.75, z = 0.9 (empty site). As explained in the introduction, the t-$BaSnF_4$ phase is a deformation of the cubic c-$BaSnF_4$ fluorite structure. This second site corresponds to where an octahedral interstice would be (**Figure III.16**).

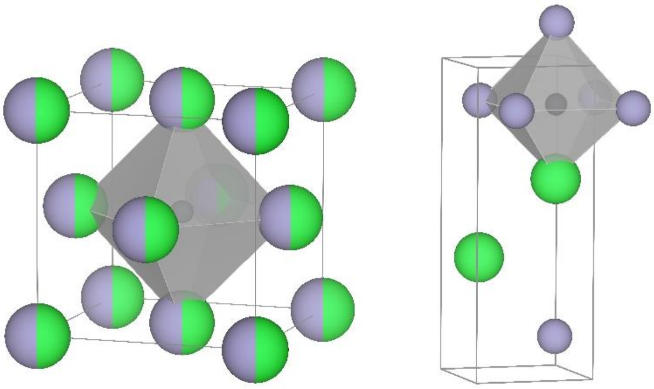

Figure III.16 Octahedral interstice in the cubic fluorite structure (right), and in its tetragonal distortion t-$BaSnF_4$ (left) Bariums are green, tins grey, and interstitial fluorides are black. The non-interstitial fluorides were omitted for clarity.

In c-$BaSnF_4$, we showed that tin-rich Oct sites were not only occupied, but also one of the most conductive environments. It therefore appears reasonable that these sites would be occupied in t-$BaSnF_4$ as well, especially since the existence of such interstitials has been proven in the isomorph t-$PbSnF_4$,[80] and Chaudhuri et al. suggested that the conduction mechanism of t-$BaSnF_4$ may involve anion hops to these Oct. sites.[77]

Hence, we proceeded with fitting the neutron diffraction data with a structure containing an additional fluoride site : x = 0.25, y = 0.25, z = 0.1. The occupancy of this $F_{interstitial}$ as well as the two neighbouring fluorides, F1 and F3, were refined in addition to the $z_{interstitial}$. The resulting fit is displayed **Figure III.17**, panel a), and we will now discuss several noteworthy informations extracted from that refinement, including final parameters summarized in **Table III.4**.

Table III.3 Summary of the Rietveld refinement fit parameters obtained for the Lc and Hc samples. The β are multiplied by 1000.

Lc a = 4.3589(4) Å, c = 11.335(3) Å, V = 215.36(6) Å^3					
Atom (Wyckoff site)	**z**	**β_{11}**	**β_{22}**	**β_{33}**	**Occ**
Ba (*2c*)	0.3686(12)	0.16e3 (2)	0.16e3 (2)	42 (9)	2
Sn (*2c*)	0.8686(9)	345.2	345.2	31.9	2
F1 (*4f*)	0.1920(9)	0.85e3 (9)	0.502e3 (8)	96 (15)	3.38 (7)
F2 (*2b*)	0.5	99 (30)	99 (30)	71 (12)	2
F3 (*2c*)	0.6902(12)	1.35e3 (9)	1.35e3 (90)	38 (1)	1.92(3)
$F_{interstitial}$ (*2c*)	0.106(6)	6.8e3 (447)	6.8e3 (447)	87 (40)	0.72(9)
Hc a = 4.3585(6) Å, c = 11.365(3) Å, V = 215.90(8) Å^3					
Atom (Wyckoff site)	**z**	**β_{11}**	**β_{22}**	**β_{33}**	**Occ**
Ba (*2c*)	0.36842	122.0	122.0	122.0	2
Sn (*2c*)	0.86925	338.6	338.6	33.3	2
F1 (*4f*)	0.19248	682.8	496.9	135.7	3.42(3)
F2 (*2b*)	0.5	171.9	171.9	90.9	2
F3 (*2c*)	0.68867	1424.3	1424.3	66.6	2
$F_{interstitial}$ (*2c*)	0.104 (3)	5221.5	5221.5	232.7	0.83(3)

Ba(0.25, 0.25, z); Sn(0.25, 0.25, z), F1(0.75, 0.25, z), F2(0.75, 0.25, 0.5), F3(0.25, 0.25, z), F4(0.25, 0.25, z)

The final occupation of interstitial sites was 1/3rd, which is high but similar to that of c-$BaSnF_4$. The great majority of interstitial originated from the F1 4*f* position. Both SPS-synthetized samples had similar occupation of the interstitial positions, but for the material obtained through the other synthesis route (ball-milling/annealing), the introduction of these atoms did not improve the fit. We attribute this to the lower quality of the data, which is due to the small crystallite size of that material.

While the Bragg-R factor only improved marginally in Lc and Hc after the inclusion of interstitial fluorides (for Lc, 9.97 → 8.98); other reliability factors seemed more affected, X^2 for instance was halved (though it remained high, around 33). Both the difference curve and the Fourier difference map (panel b) also suggest a slight betterment of the fit, but overall there is little improvement after interstitial addition, we therefore cannot reach a definitive conclusion on the presence or absence in t-$BaSnF_4$.

Finally, we refined the atomic displacement factors β as anisotropic entities, which allowed us to draw the structure with the displacement ellipsoid of each atom (**Figure III.17** panel d). The interstitial fluorides appear to be extremely delocalised within their site, though only in the (110) plane, possibly due to the fact that tin lone pairs from the above Sn layer are pointed towards them, preventing displacements in the c direction. These ellipsoids are also representative of anionic conduction pathways, which once again are mainly in-plane, as expected of a 2D conductor.

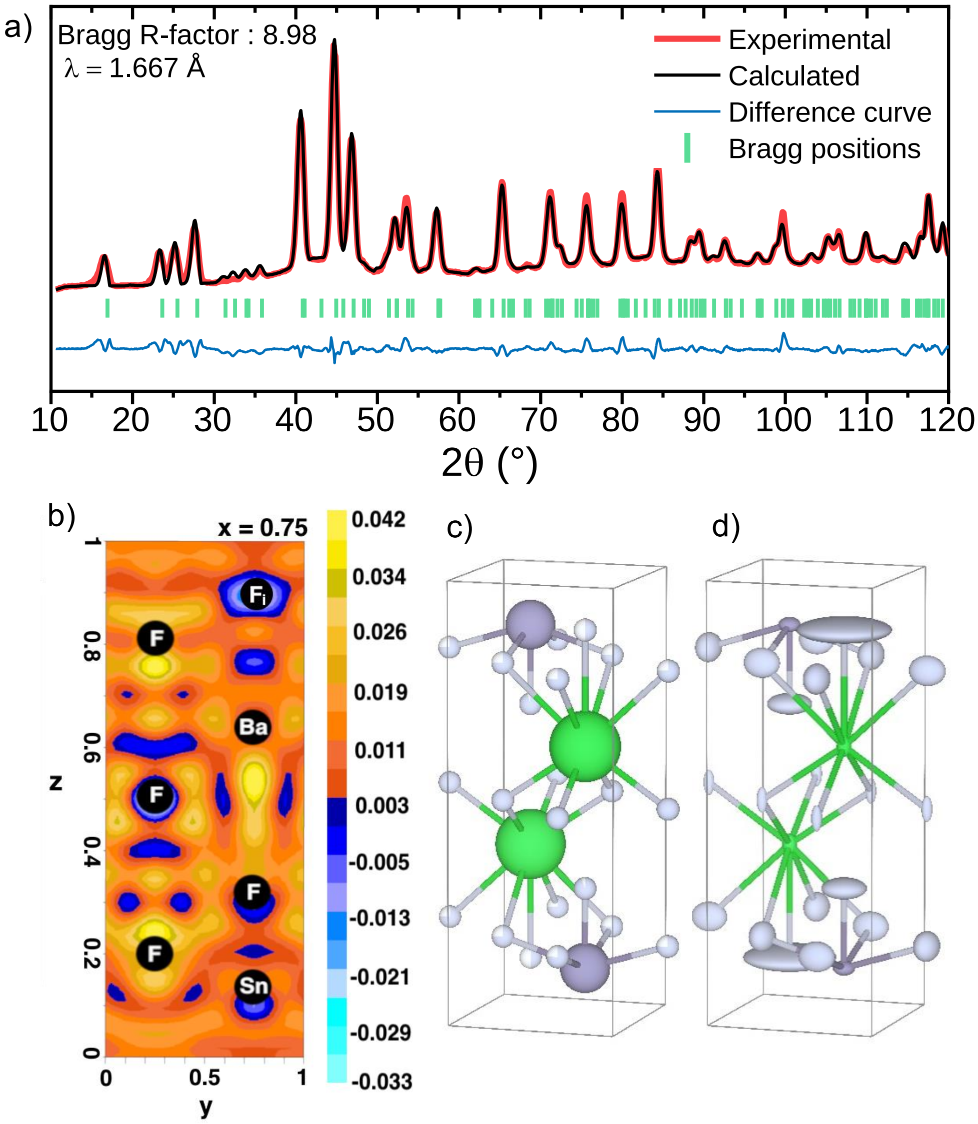

Figure III.17 Final fit of the Lc sample neutron diffraction diagram, a) Rietveld refinement with an additional intersticial fluoride ion, b) Fourier map calculated from the difference curve of the refinment c) resulting structure with green barium, dark grey tin and light grey fluoride, d) displacement ellipsoids of each atom

Neutron diffraction has now provided several avenues for reflection on the structure of t-$BaSnF_4$. Overall, it was difficult to confirm some of the conjectures we made to explain the discrepancies between calculated and experimental diagrams, it would therefore be interesting to perform additional experiments. Further computational simulations could also help shed light on the diffusion mechanism and fluoride localization, as it did in the cubic phase.

Conclusions

Most syntheses routes for t-$BaSnF_4$ reported in the literature yield a mix of phases, with large variations in the cell parameters of the tetragonal lattice. In this chapter, we attempted to both search for new pathways leading to a pure phase, and explore possible explanations for the reported cell expansions/contractions.

The first route was a continuation of the work of Ahmad et al., who proposed the use of mechanosynthesis followed by heat treatment, which yielded a final material with around 7% of impurities. Expanding on this, we showed that an additional long ball-milling step and subsequent annealing produced a pure product. This product however had poor ionic transport properties, as the lengthy milling step introduced additional defects in the structure, trapping the diffusing F-ions.

We therefore turned to a different and new synthesis method, Spark Plasma Sintering, though which a pure phase could be procured. We studied the impact of some SPS parameters on the microstructure and conductivity, thereby highlighting the two main microstructural effects: crystallite anisotropy, which occurs at lower synthesis temperature, and preferential orientation of the crystallites along the high-l lattice planes at high temperatures, which we believe to be the main driving force behind most of the conductivity variation we observed. High conductivities could be achieved through this method, reaching up to 5.10^{-3} $S.cm^{-1}$ at 30 °C.

After characterizing the microstructure, we focused on the lattice itself, pointing out the large variations in cell parameters of the products obtained throughout all synthesis routes. Through successive refinements of our neutron diffraction data, these volumetric variations are tentatively attributed to stacking faults along the c-axis. We also suggested that there could be a significant number of interstitial F-ions in the structure, although it was not possible to find definite proof of this. The tetragonal phase then still requires more studies, especially regarding the anionic sublattice, which appears to be less ordered than initially thought.

Overall, the new SPS route seems to be promising: it yields compact pellets, with somewhat tunable properties and provides the highest conductivities reported for a fluoride-ion conductor. In the future, SPS could also be used to make all-solid-state batteries in one step, as it was previously accomplished in LRCS (for Na-ion batteries).[237]

There are however some significant downsides. SPS is very user-dependant, and, despite the care put into our experiments, they sometimes yielded surprising or seemingly unreliable results. We did attempt to reproduce several of the experiments, and while the resulting transport properties were similar, there were still some slight (+/- 0.03 Å) variations in cell parameters. Additionally, not all materials are SPS-compatible. For example, we made SPS synthesis attempts for the majority of Sn-based materials mentioned in this thesis, which all failed except for $BaSnF_4$.

Chapter IV

Electrochemical properties of Sn-based solid electrolytes

Table of contents

Introduction 123
IV.1. Testing of possible reference electrodes through symmetrical cells 124
  IV.1.1. Using tin as a reference electrode in symmetrical cells 125
  IV.1.2. Using Lithium as a reference electrode in symmetrical cells 129
IV.2. Electrochemical Stability Window (ESW) of $MSnF_4$ 133
  IV.2.1. Prediction of the ESW through thermodynamics 133
  IV.2.2. Experimental ESW 134
    IV.2.2.1. Methods 134
    IV.2.2.2. ESW of $BaSnF_4$ 136
    IV.2.2.3. Degradation mechanism (s) 138
    IV.2.2.4. Electrochemical stability at higher temperatures 141
    IV.2.2.5. ESW of $SrSnF_4$ and $Ba_xSr_{1-x}SnF_4$ 143
Conclusions and Perspectives 146
  Perspective : FIB reference electrode in the litterature 146

Introduction

As explained in the introductive chapter, one of the key desirable properties of solid electrolytes is a high electrochemical stability, which would enable high power- or energy-density devices. This electrochemical stability is quantified through the electrochemical stability window (ESW), and the critical current density. The evaluation of these characteristics may be performed using different methods.

Potentiostatic methods, such as Linear Sweep Voltammetry and Cyclic voltammetry are commonly used to determine the ESW. Both methods consist of incrementally varying the potential of a cell and measuring the current response. For Linear Sweep Voltammetry, the potential only varies in one direction, whereas for Cyclic voltammetry, it circles between two set values. In both cases, an onset of current indicates the limit of the ESW. For Li-ion electrolytes, these experiments are ideally conducted on cells with a Li/Electrolyte/inert electrode architecture. Li plays the role of reference and counter electrode. The inert electrode should have a similar contact area with the electrolyte as it would in a full battery, in order to better replicate future working conditions in these systems. Notably, lower surface contact leads to larger overpotential and therefore an overestimation of the ESW, as shown in **Figure IV.1**.[247,248] A composite of carbon and solid electrolyte may be used as an inert electrode.[249]

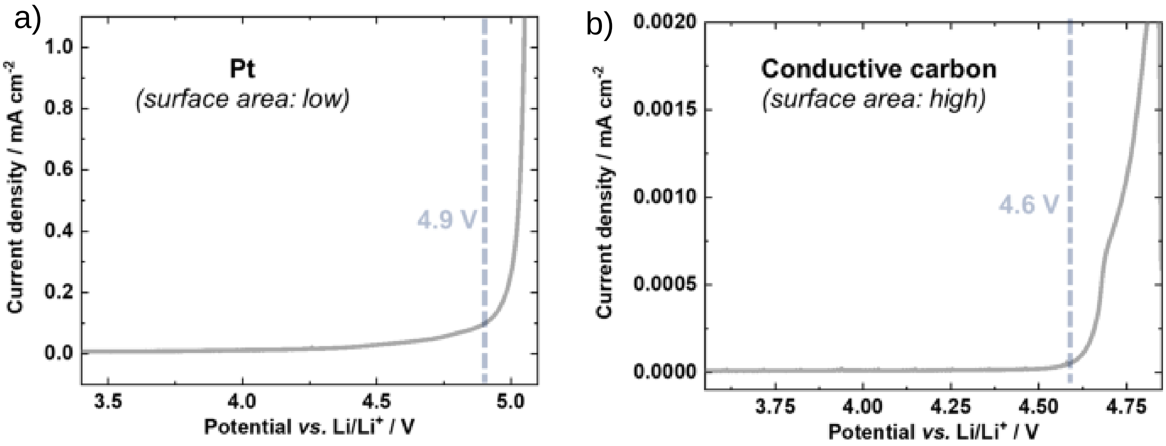

Figure IV.1 Example of ESW determination of a polyethylene oxide electrolyte, using Linear Sweep Voltammetry, at a scan rate of 0.1 mV.s^{-1}, a) with a small surface area, b) with a large surface area, from ref. 1.

Other experimental parameters also play an important role in the accurate determination of the ESW: the potential scanning speed, for instance, influences which phenomena are observable on the current vs. potential plot. Solid electrolyte decomposition kinetics tend to be sluggish, and therefore, at high scan rates, it is more difficult to observe.[250]

To circumvent these issues, galvanostatic methods may be used to determine the ESW instead.[251] Instead of a potential ramp, a set current is imposed on the system (which may consist of the same cell configuration), and the potential response is recorded. From these experiments, the potential can be plotted against the capacity delivered by the system. Any capacity therefore directly originates from electrolyte decomposition. In these experiments, the ESW is determined with respect to a reference electrode, which allows to place it in a potential scale and compare it with other materials to determine their compatibility. For Fluoride-ion batteries, however, it is complicated to perform similar tests, as there is no widely accepted reference electrode. A reference electrode is an electrode which has a stable and known potential during cell operation, i.e., that is not polarizable.[252] Some attempts were made to find suitable reference electrodes, and lithium metal was used for this purpose, as it provided good contact and stable potential when used to evaluate the ESW of $La_{0.9}Ba_{0.1}F_{3.9}$.[253] Here, we wish to test another potential reference electrode, as well as to explore the use of the Li reference in conjunction with the $MSnF_4$ electrolyte family.

IV.1. Testing of possible reference electrodes through symmetrical cells

In this part, we will study the interactions under electric current of $BaSnF_4$ and different electrodes, with two goals in mind: finding an appropriate reference electrode for this system, and determining the critical current density of $BaSnF_4$. To do so, we built symmetrical cells using our two reference electrode candidates, lithium and tin metal.

IV.1.1. Using tin as a reference electrode in symmetrical cells

We study the stability of materials at different current densities using symmetric cells. Typically, for Li of Na All-Solid-State Batteries (ASSBs), the electrolyte is sandwiched between two lithium or sodium metal discs, so that there is ample charge carriers quantity and to guarantee good contact, as Li and Na metal are soft.

Here, we decided to first test the current density stability using tin metal electrodes, under the assumption that Sn-containing electrolytes would be stable against it and that its relative softness would ensure a proper contact with the electrolytes. The symmetric cells constructed were then Sn|t-$BaSnF_4$|Sn.

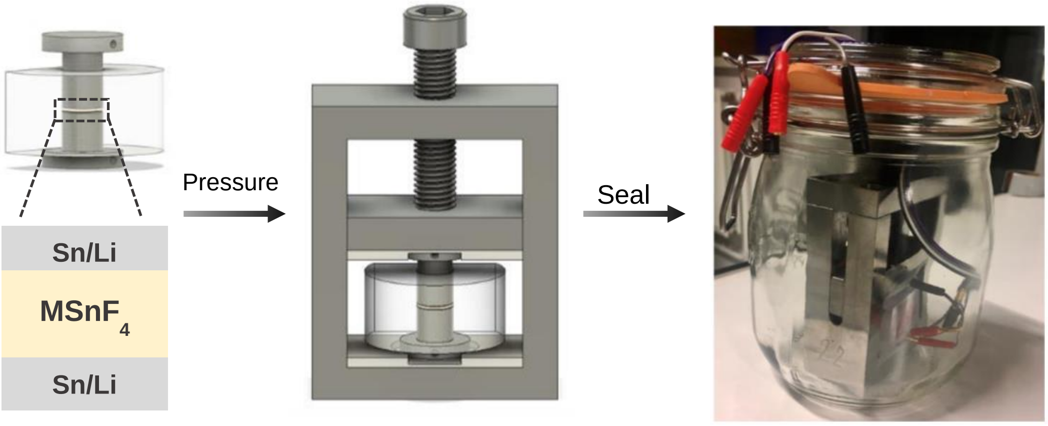

Figure IV.2 Assembly process of symmetrical cells, allowing for electrochemical cycling under pressure and inert atmosphere. Schematics were made by Mickael Bolmont from LRCS

The cells were constructed using an in-house setup, shown in **Figure IV.2**. (adapted from [254]), which allows for electrochemical operation under constant pressure and inert atmosphere. In a glovebox, 120mg (optimized amount) of solid electrolyte was pressed in a 10mm diameter PMMA matrix at 1.5 tons for 5mn. Afterwards, about 100mg of tin metallic beads were added on each side of the electrolyte pellet, and the stack was put under pressure, either 10 or 20 kN. The cells were cycled at 25°C, under argon. The open circuit voltages were of a few mV. In this setup, the M used provides good contact, and the actual electrodes where the reactions take place are the interfaces formed between the M and the electrolyte, as illustrated in **Figure IV.3**, panel a). The actual interface composition is discussed later, in **section IV.2.2.3.**

These cells were polarized under increasing current densities held for 15 minutes, followed by 10 minutes of rest, followed by 15 minutes of reverse polarization (e.g. for 10 μA.cm^{-2}, -10 μA.cm^{-2}). This cycle was repeated 50 times for each current density. The results of these experiments are presented in **Figure IV.3**, panel b).

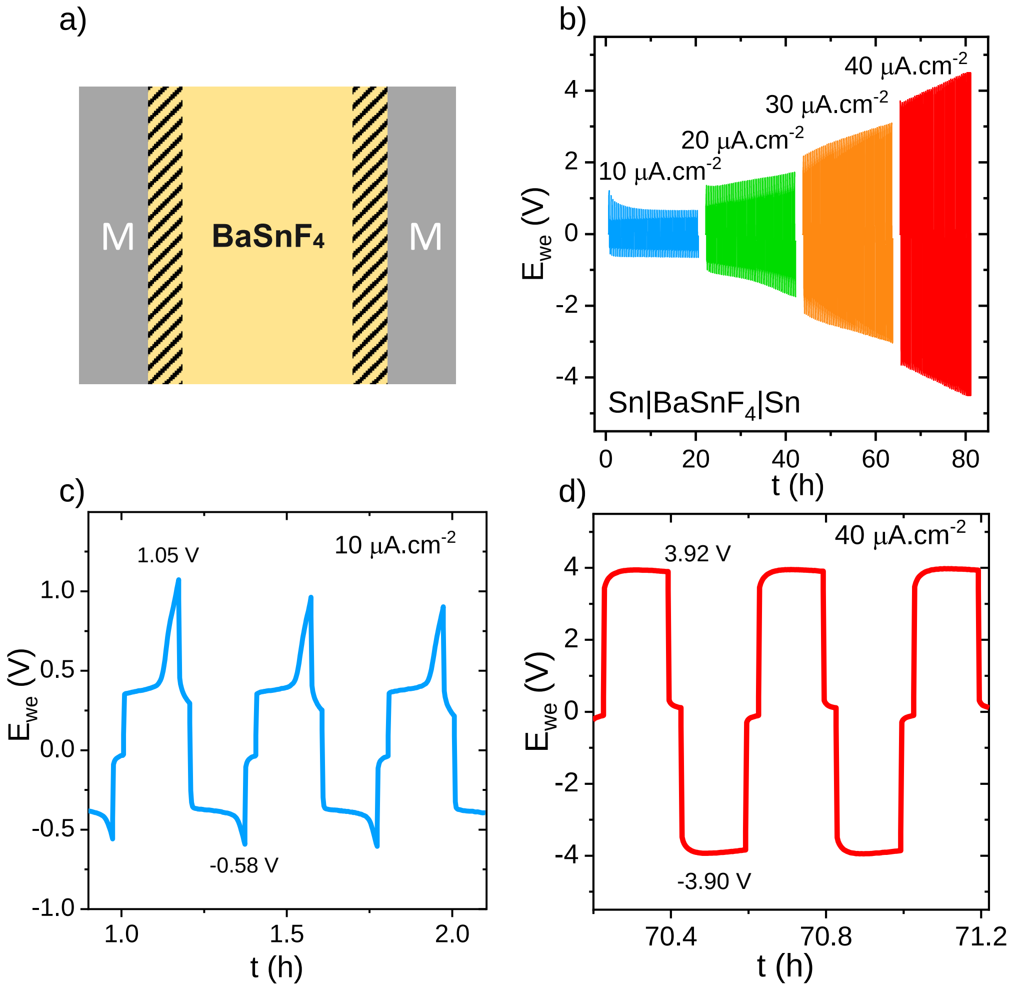

Figure IV.3 polarization of a Sn|BaSnF_4|Sn symmetric cell a) schematic of the cell, with the formed interfaces between BaSnF_4 and the metal acting as electrodes, b) increase of current densities c) shape of the polarization curve at 10μA.cm^{-2} . The asymmetry of the profile under positive or negative polarization could possibly be related to an inhomogeneity or to a mechanical defect in the electrodes, d) shape of the polarization curve at 40 μA.cm^{-2}

The polarization of the cell initially decreases at the very beginning of the 10 μA.cm^{-2} current density step, before stabilizing. The formation shape of the polarization curves also evolves during the experiment, (**Figure IV.3**, c). Peaks (sharp increase in E vs. t) are visible at the beginning of the 10 μA.cm^{-2} step. In other systems, such as Li-ion batteries with lithium metal anodes, similar phenomena have been observed and associated with poor contact between the electrolyte and the metal during cycling, which gives rise to local increase of the current density, reflected on the E vs t curves as peaks.[255,256]

These peaks subside gradually during the course of the experiment, until complete disappearance (**Figure IV.3**, d). This may be related to the formation of a solid-electrolyte interface (SEI) under current between Sn and t-BaSnF. If we assume the most straightforward degradation reaction: $BaSnF_4 \rightarrow BaF_2 + SnF_2$, we find a volume increase of 7%. In Lithium-ion batteries, this variation would be considered small, as it is lower than that of graphite during lithiation and delithiation,[257] but in solid-state batteries, changes of this order were previously shown to be significant.[258] In our case, the added volume could create additional pressure within the cell, bettering the contact as the interface grows. The growth of this layer is visible through the cell polarization, which increases continuously when current densities surpass 20 μA.cm^{-2}.

In an attempt to mitigate contact issues at the beginning of the experiment, we built another Sn|t-BaSnF$_4$|Sn symmetrical cell, using a stack pressure of 20 kN (twice that of the cell from **Figure IV.3**). It produced much lower polarization at all current densities, but the cell resistance was still very large, as seen through Electrochemical Impedance Spectroscopy (EIS), recorded before and after each polarization step, presented in **Figure IV.4.** panels a) and b). In the initial state (measured a few minutes after the assembly of the cell), the resistance is around 25000 Ω, and the characteristic frequency of the (convoluted) semicircle is around 1400 Hz. This semicircle hence cannot be attributed to t-BaSnF$_4$, which has a resistance 100 folds lower, and a bulk characteristic frequency of 90000 Hz. The first semi-circle grows only during the first two polarization steps, while its characteristic frequency stays relatively similar. Starting from 20 μA.cm^{-2}, a second semi-circle (also a convolution of several contributions) appears in the EIS spectra at lower frequencies, as seenin **Figure IV.4**. a) and b). The appearance of this circle is concomitant with a very large increase of the overall cell resistance, and could be ascribed to SEI layer growth.

To better understand the interface formation between $BaSnF_4$ and metallic tin, we monitored the evolution of the resistivity of the cell in the absence of current. As depicted in **Figure IV.4** c), the semi-circle previously attributed to the interfacial resistance grows with time. It then appears that this interface forms spontaneously as soon as $BaSnF_4$ and Sn are in contact.

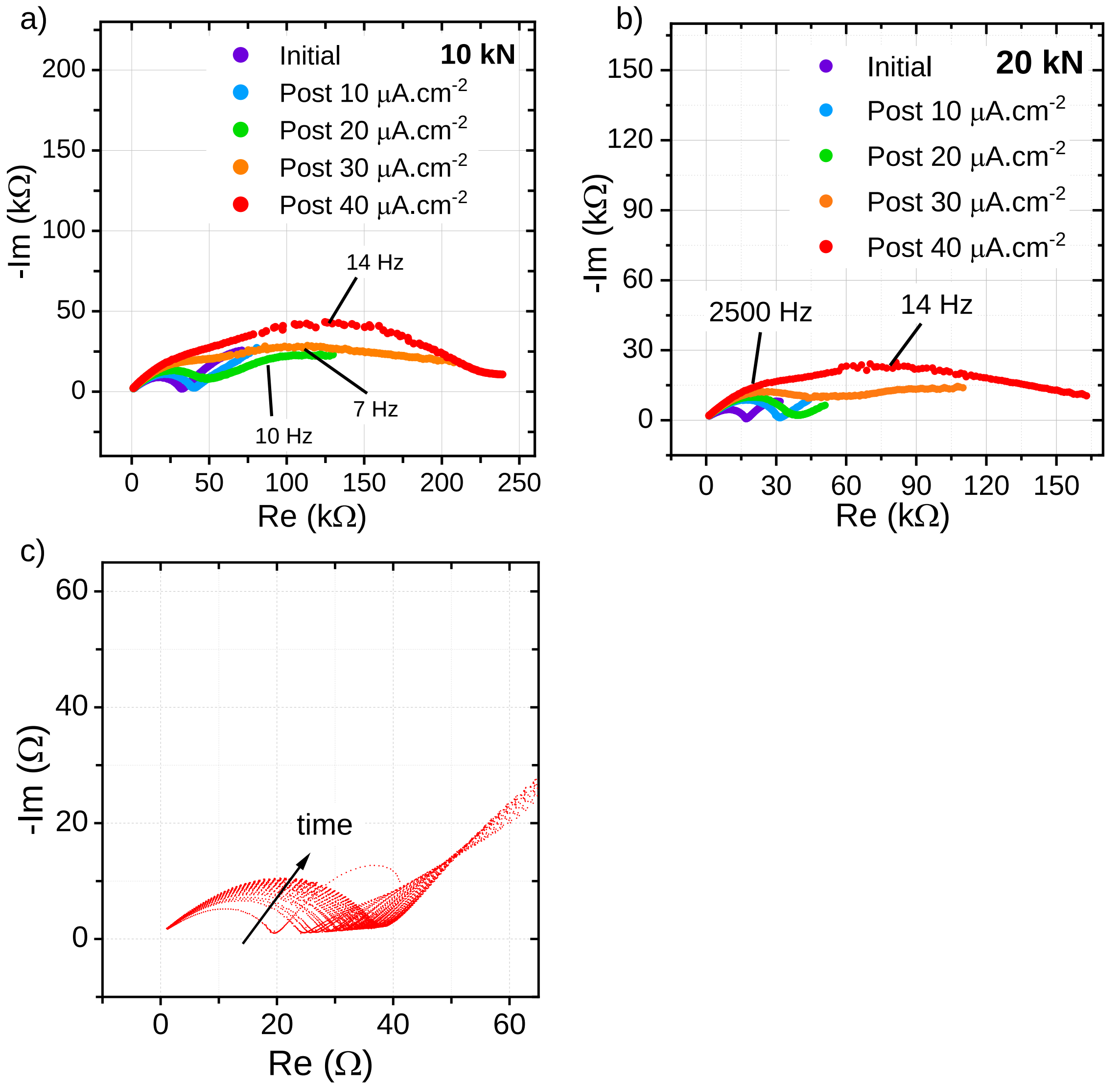

Figure IV.4 EIS study of Sn|$BaSnF_4$|Sn cells, a) EIS recorded after polarization at different current densities, b) repeat of panel a) with a higher stack pressure of 20 kN c) evolution of EIS with time, in the absence of current

It was unfortunately not possible to peel the tin layer and retrieve the electrolyte pellet for analysis, so in order to investigate the composition of the interface, $BaSnF_4$ and tin powder were mixed directly in a mortar. Interestingly, there were no major changes observable in the XRD diagram of the resulting powder. Both $BaSnF_4$ and metallic tin were present, but no new peak was visible. More attempts were made, heating tin powder and $BaSnF_4$ to 150°C after mixing, pressing the mixed powders, etc.. but we could not see anything indicating that a reaction had taken place. The XRD pattern does showcase a slight bump, which could be an indication that an amorphous compound might have been formed. It is difficult to otherwise explain the increase of interfacial resistance measured in all $Sn|BaSnF_4|Sn$ symmetrical cells. Regardless, the $Sn|BaSnF_4$ interface is resistive and unstable. As a result, other options must be tested.

In summary, $Sn|BaSnF_4|Sn$ symmetrical cells were built. The metal/electrolyte contact was poor before polarization, but improved upon formation of a degradation layer under current. The degradation layer developed even at very low current densities, suggesting poor stability of $BaSnF_4$ towards tin. This layer was highly resistive, and its growth caused very large cell polarization, reaching 4.5 V at only 40 $\mu A.cm^{-2}$. Tin metal therefore does not appear to be a suitable reference electrode for this system. Consequently, we opted to explore other options that would provide better contact and, ideally, less resistive SEI.

IV.1.2. Using lithium as a reference electrode in symmetrical cells

Lithium metal is routinely used in symmetrical cells as electrodes when determining critical current densities of solid electrolytes in Lithium-ion batteries. Such cells may also help with the investigations of chemical stability of the SE vs Li metal, and dendrite formation. Here, the aim is a bit different since it is impossible to have dendrite formation in our setup. Nevertheless, if the interface between Li and our electrolytes is stable and not too resistive, we will be able to use Li as a reference electrode in subsequent testing, and determine the critical current density accurately.

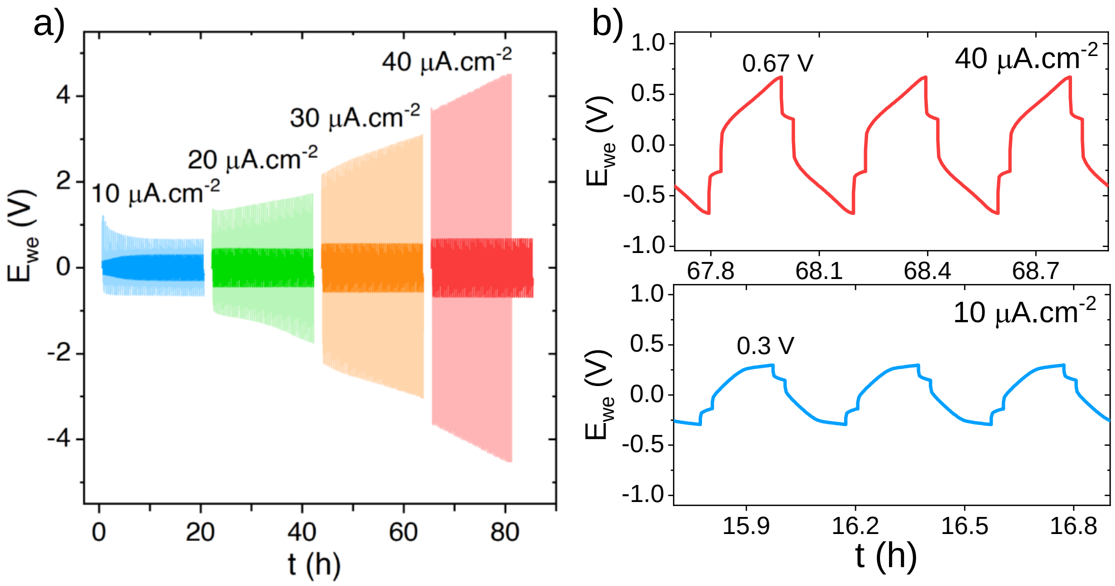

Figure IV.5. potential response of Li|BaSnF$_4$|Li cell under different current densities a) complete experiment, with Li cell in dark, compared with the Sn symmetrical cell in light. The Li cell runs for longer as it did not short circuit, b) zooms of different regions of graph a)

Cells were assembled using the protocol described in **section IV.1.1**., replacing the Sn with a disc of lithium of around 300μm in thickness. The stack pressure was maintained at 9 kN, as higher values always lead to short circuits. Experiments were repeated twice and yielded similar results.

The potential response under different current densities is displayed in **Figure IV.5**, panel a), and compared with that of the Sn symmetrical cell. The lithium cells showcased much lower polarization at all points, and there were no visible polarisation peaks at low current (though the shape is not completely square) suggesting there was little amounts of degradation. At higher currents, the shapes become more uneven as seen in **Figure IV.5**, panel b), while there is no evolution in the overall polarization of the cell over the course of the cycling. We then can hypothesize that there is some electrolyte degradation that increases with current density, yielding seemingly ionically conductive products. This idea is also supported by the EIS data (**Figure IV.6** panel a) as there is no increase in the overall cell resistance over the course of the experiment. Nevertheless, at 10 μA.cm^{-2}, the first few polarization profiles have different shapes and are accompanied by an initial increase of polarization, suggesting that even at this low density, the lithium and BaSnF$_4$ react to form an interface (which composition we investigate later). Interestingly, the EIS shows a decrease in cell resistance upon interface formation. This could possibly be due to a bettering of electrolyte-lithium contact during the growth.

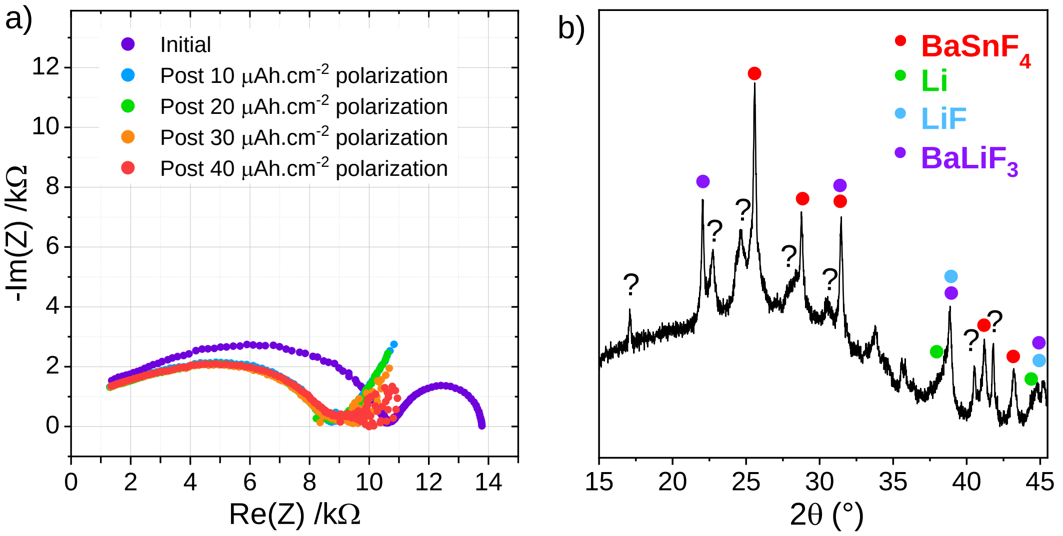

Figure IV.6. $BaSnF_4$|Li interface a) evolution of the EIS during GCPL cycling of a symmetrical cell (the presence of a low frequency semi-circle was recorded at the beginning of all experiments and disappeared after the rest period, before current was applied to the cell), b) XRD diagram of hand-ground $BaSnF_4$ and Li metal

Following these findings, the interface composition was investigated by grinding Lithium metal and $BaSnF_4$ in an agate mortar in a glovebox. The reaction was seemingly highly exothermal, as a red-orange glow appeared under the pestle. The resulting XRD diagram of the (now black) powder is shown in **Figure IV.6**, panel b. Many new products are formed, most of which could not be identified, despite searching several database (ICSD, ICDD, Material Project)[259,260]. The two easily indexable phases were the two precursors. Two potential products were identified, LiF and $BaLiF_3$, though this should be considered a tentative affectation, given the low number of peaks for each of these phases and the impossibility to confirm their presence through Full-pattern matching. If both of these products are indeed present, the reaction between $BaSnF_4$ and Li would then be:

$$2Li + BaSnF_4 \rightarrow LiF + BaLiF_3 + Sn^0 + D$$

Followed by

$$xSn + yLi \rightarrow Sn_xLi_y$$

where D is an additional degradation product, responsible for the not-indexed peaks on the XRD diagram. Tin would be reduced to its metallic state under these conditions, possibly in the form of nanoparticles, which spontaneously react with lithium to form Sn_xLi_y alloys, which can be amorphous.[261] This would explain both the black colour of the powder after reaction, the bump in the background (**fig IV.6** b) and the absence of Sn-containing products on the diagram.

The products appear to be stable under current and not ionically blocking, as visible in **Figure IV.6,** a). The value of the initial interfacial resistance, extrapolated from the first semi-circle, is around 14 kΩ. We note the change in the shape of the EIS spectra between the initial measurement (recorded soon after cell assembly) and after polarization. This could be related to the lithium surface state, which despite being scraped has always some amount of impurity layer. After the first polarizations, the interfacial resistance decreases to 8.5 kΩ and is stable throughout the rest of the GCPLs until 40 $\mu A.cm^{-2}$.

Similar experiments were completed for t-$SrSnF_4$ which also reacted with Li upon contact. Because of the significantly lower conductivity of the strontium-based phase, the polarization was very high, even at low currents. At high current, the polarization immediately reached the limits of the range measurable by the potentiostat. This is expected, as the measured interfacial resistance is around 300 kΩ. At a current density of 40 $\mu A.cm^{-2}$, per Ohm's law, the polarization would then be 15.4 V.

In summary, $BaSnF_4$ and $SrSnF_4$ both react upon contact with Li metal, to form non-blocking interfaces which are fairly stable at all measured current densities, though degradation was lowest at a current density of 10 $\mu A.cm^{-2}$. This is an extremely small value, especially when compared to Li-ion conductors which can stay stable at current densities reaching hundreds of $\mu A.cm^{-2}$ (sometimes with the help of coatings).[262,263] This inability of $MSnF_4$ electrolytes to withstand high current densities may later force the use of small C-rates in the FIB utilizing them, which is a substantial downside. It can however be noted that in the case of Li, though there is some degradation happening, the polarization stays stable, which allows for the use of slightly higher current densities. Therefore, the final C-rate would depend on each particular set of electrodes.

The Li|$BaSnF_4$ interface hence appears significantly better suited than the previously studied Sn|$BaSnF_4$ for our next purpose: measuring the electrochemical stability window (ESW) of $MSnF_4$.

IV.2. Electrochemical Stability Window (ESW) of $MSnF_4$

ESWs are a critical part of assessing the usability of a material as a battery electrolyte. Knowing the ESW is essential when deciding on which electrodes to use, as without this information, irreversible degradation could take place even before electrochemical operation. Additionally, the ESW provides with an estimate of what the maximum potential of a full battery build with that electrolyte would be, which is a determining factor in reaching high energy densities.

IV.2.1. Prediction of the ESW through thermodynamics

The chemical stability of a material may be evaluated through thermodynamic calculations, by tracing a phase diagram of all possible decomposition products, assuming a general degradation reaction such as:

$$Electrolyte + xF^- \rightarrow D1 + D2 + \cdots$$

with D1 and D2 being the decomposition products. Potential decomposition products usually include all possible compounds formed by the electrolytes' components (solids), which are found in databases, such as the Inorganic Crystal Structure Database (ICSD) or the Materials Project.[260] Phase equilibria and decomposition reaction energies are calculated, and potential phase diagrams are then constructed.[250,264,265] This has been done for $BaSnF_4$ (**Figure IV.7**)[36], a small stability windows of 0.45 V is found.

While both of these methods provide insight on a material's stability and can serve as relevant first approaches, they are exclusively reliant on thermodynamics, not accounting for kinetic factors. As a result, the predicted ESW tend to be significantly smaller than what is measured through experimental means.

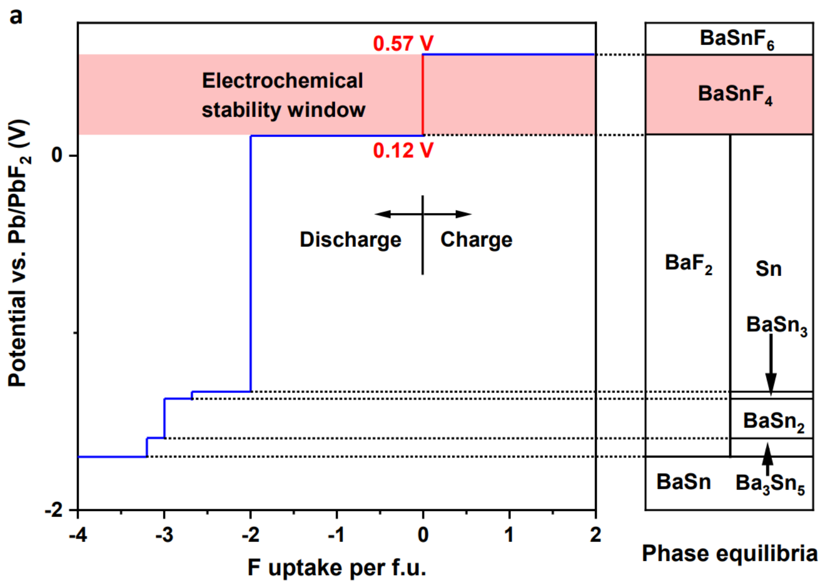

Figure IV.7 Calculated thermodynamic equilibrium voltage profiles and phase equilibria of $BaSnF_4$

IV.2.2. Experimental ESW

ESW can be evaluated through various means. The most common one is Cyclic Voltammetry (CV), in which one sweeps through a potential window, measuring the current for each step. Even at small step sizes, this method exposes the material to a specific potential only for a short amount of time, which, in combination with sluggish decomposition kinetics, may not be enough for the reactions to take place. In order to circumvent this issue, we mainly used galvanostatic charging and discharging of cells which utilized the electrolyte as their active material. It was then possible to observe oxidation and reduction behaviours while staying in equilibrium conditions.[266]

IV.2.2.1. Methods

Measurements were performed using the in-house setup described earlier, but this time with a different stack. First, 120mg of $MSnF_4$ were pressed at 1.5 tons in the PMMA matrix. For the electrodes, $MSnF_4$/VGCF composites were prepared by grinding (with a mortar and a pestle) 30 mg of $MSnF_4$ with 10 mg of VGCF. 20 mg of this composite was then added to the electrolyte pellet and pressed again at 1.5 tons. This is a rather high amount of composite, which was chosen in order to be able to perform XRD measurements on the cycled electrodes. Some experiments were conducted with 10 mg instead and both yielded comparable results.

A sheet of lithium, of around 300 μm in thickness, was scraped and cut using a 10mm diameter puncher. The disc of Lithium was then added on the other side of the electrolyte pellet, and the stack was put under a pressure of 9 kN, and sealed under Argon atmosphere. Higher stack pressures or thicker Li discs resulted in short circuits.

The lithium electrode acts as a reference. For FIB, the lack of reference electrode is a major issue. Most of the other batteries may simply use the elemental form of their charge carriers as electrodes, but this is of course not possible for fluorides. Previous work has shown that Lithium behaves as a pseudo reference, as it can form a stable LiF layer upon contact with electrolytes.[31] Based on this work and our experiments detailed in **section IV.1.2.**, Li appears to be a good choice to test the ESW of our materials. All potentials below are given vs Li/LiF (0.36 V vs Li). For each experiment, 2 cells were assembled, one to probe stability towards reduction and one towards oxidation. The "reduction" cells were cycled between the OCV (usually 1.1-1.2 V vs Li/LiF) and 0 V vs Li/LiF, and the oxidation resistance was measured by galvanostatic charging and discharging between the OCV and various maximum potentials depending on the material. The cycling consisted of GCPL, starting with negative polarization of + or - 10 μA.cm^{-2} respectively, until the set potential limit was reached, followed by a rest and an inversion of polarization to revert back to the OCV. This cycle was repeated several times, to probe the stability of decomposition products. PEIS was measured at the beginning and end of experiments.

The derivative d(Q-Q$_0$)/dE was calculated using the software EC-Lab and plotted vs E (vs Li/LiF), resulting in a kind of pseudo-CV measured in equilibrium conditions. Some actual cyclic voltammograms were also recorded for future reference and comparison, using the same cell geometry and assembly procedure.

IV.2.2.2. ESW of $BaSnF_4$

The pseudo-CV obtained for tetragonal $BaSnF_4$ is displayed in **Figure IV.8**. Decomposition takes place during the first cycle, with peaks at 2.3 V, 3.3 V and 3.86 V, as well as a reduction onset at 0.6 V. In order to estimate the amount of decomposition taking place in the first cycle, we calculate the theoretical capacity of $BaSnF_4$ and compare it with the capacity exchanged during that cycle. If we consider a two-electron

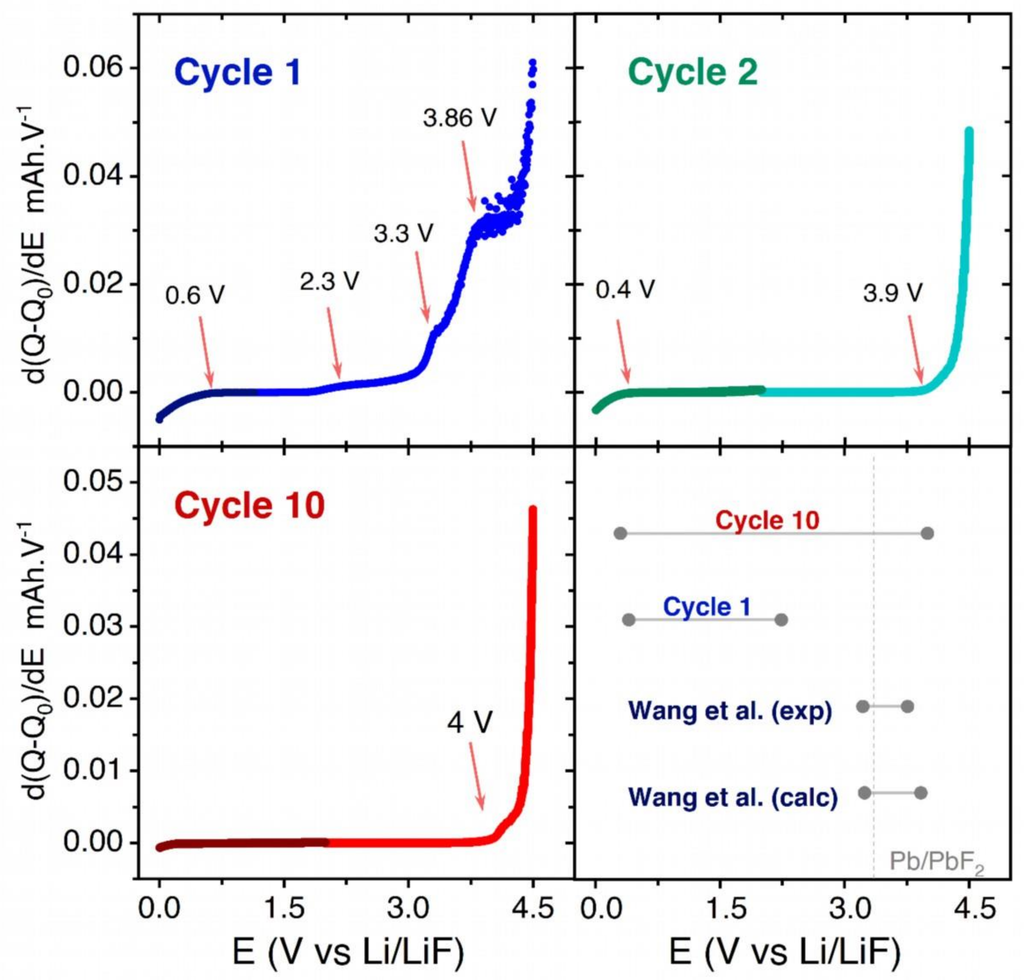

Figure IV.8 Pseudo CV obtained through polarization of Li|$BaSnF_4$|$BaSnF_4$/VGCF cells. The bottom right pannel is a comparison of ESWs, from the first cycle, the 10th cycle, and litterature, experimental and calculated from the thermodynamic equilibrium voltage profile. The experimental ESW was determined by Wang et al (ref.35) using a Pb/PbF_2 reference electrode, discussed in more details in the conclusion of the chapter decomposition pathway (justified by additional experiments described in **section IV.2.2.3**):

$$Q_{th} = \frac{Fn_{e-}}{3.6 * M}$$

With Q_{th} the theoretical capacity, F the Faraday constant, n_{e-} the number of electrons exchanged in the reaction and M the molar mass of the active material (here, $BaSnF_4$). We find a theoretical capacity of 161 mAh.g^{-1}. The capacity exchanged during the first cycle is 2.57 mAh.g^{-1}, which corresponds to 1.6 % of electrolyte decomposing. From the second cycle on, none of the oxidative peaks are visible, and the oxidation onset moved to 3.9 V, while the reduction onset shifts closer to 0 V. In the first cycle, the ESW can be evaluated to 1.2 V (or 2.7 V given the size of the 2.3 peak), later reaching 3.75 V in the 10th cycle. This is significantly larger than both the thermodynamic and (potentiostatic) experimental windows previously reported implying that kinetic factors play an important role in this case.

The hypothesis of kinetic limitations is corroborated by cyclic voltammetry, which is shown in **Figure IV.9**. The general appearance of the i-V profiles is similar to that obtained

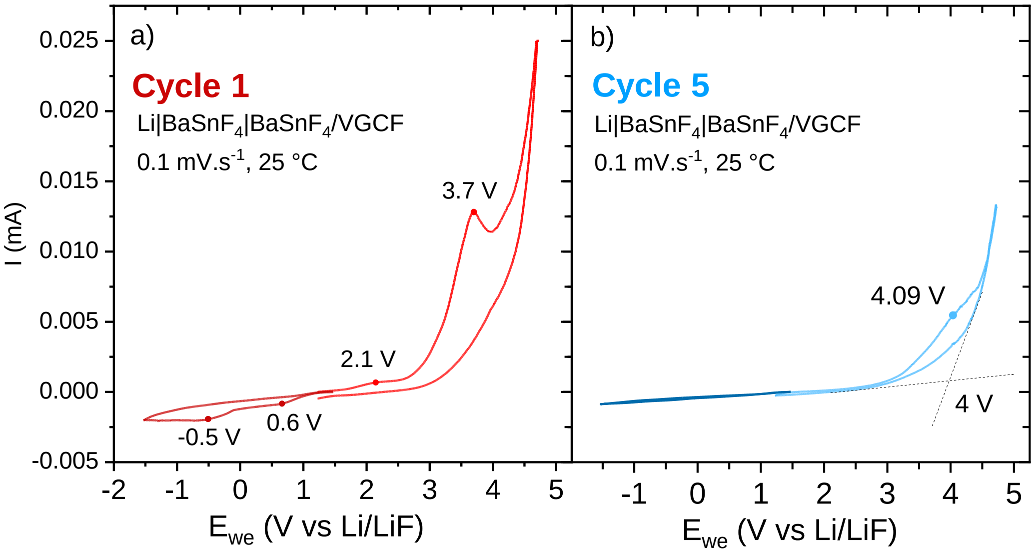

Figure IV.9 Cyclic voltammograms of Li|BaSnF4|BaSnF4/VGCF cells,at a scan rate of 0.1mV/s, a) first cycle (cathodic scan in light red and anodic scan in dark red), b) 5th cycle (cathodic scan in light blue, anodic scan in dark blue) by the derivation of the GCPL, with peak positions shifted towards slightly lower currents, which is a bit counter-intuitive as one would expect kinetics to cause a shift in the other direction. Nevertheless, one of the peaks is missing from the first voltammogram, at 3.3 V (or it has shifted to 3.7 V). This suggests that the kinetics of the reaction happening at this potential are sluggish, and therefore not visible even at low scan rates.

The behaviour upon subsequent cycling is similar to that of galvanostatic cells, with little electrochemical activity, suggesting once again that the decomposition products formed during the first cycles are stable.

IV.2.2.3. Degradation mechanism (s)

The decomposition mechanism was investigated as well. The XRD diagrams of the composite electrodes were systematically measured after the galvanostatic experiments. The lithium discs could not be measured as they stuck to the electrolyte pellets and current collectors. It was possible to detach the disc only once and it was measured under inert atmosphere, but only Lithium could be seen.

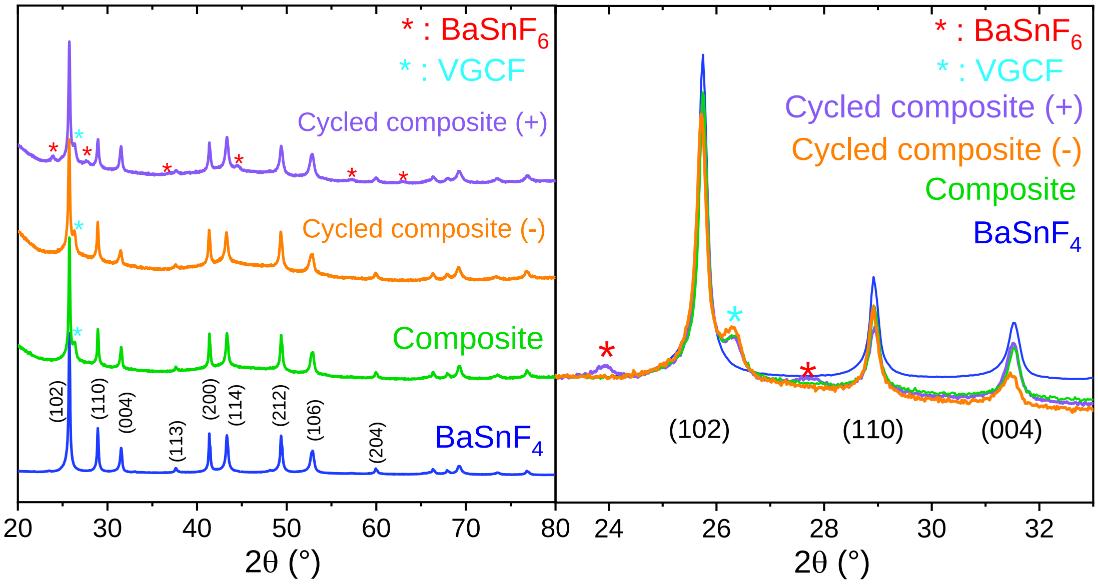

Figure IV.10 XRD patterns of the electrodes before (green) and after (orange/purple) cycling. The bumps in the background in the composites is attributed to the carbon additive

The composite electrodes after a simple galvanostatic charge or discharge did not showcase any detectable change. A battery was then positively polarized until it reached 4 V, and it was held at this potential for 50h. Another cell was negatively polarized until it reached 0 V, and held for 100h (the experiment was first attempted with a 50h hold, yielding similar results). The XRD diagrams of the composite electrodes before and after these experiments are visible in **Figure IV.10**.

After the 50 h hold at 4 V, we find 51 mAh.g^{-1} of capacity has been exchanged (32% of electrolyte decomposition), and a new phase appears on the XRD diagram, identified as $BaSnF_6$. It follows that the tin degree of oxidation increased from +II to +IV (hence justifying the 2-electron exchange used for calculating the theoretical capacity of $BaSnF_4$ earlier). We also attempted to hold batteries for the same amount of time at 2.3 and 3.3 V to see what reactions caused the peaks on the pseudo-CV at these potentials (**Figure IV.8**)For both of these experiments, post-cycling XRD patterns were similar to the pristine electrode, which suggests that the oxidation of $BaSnF_4$ only takes place at around 4V. The electrode held at reductive potentials showed no phase modification, even after 100h at 0 V, as shown in **Figure IV.10**. There is little to no reduction taking place at this potential. Other tests were made, exposing the cell to very low potentials, up to -10 V, but no reduction peak was observed even then. This result is surprising, because although fluorites are known to have high electrochemical stability, Sn is normally easily reduced from Sn(II) to Sn^0, so the reduction of $BaSnF_4$ should be observable.

We hypothesize that the presence of an oxidation peak coupled with the absence of observable reduction could be related to our use of Li as a reference electrode, and to the decomposition layer it forms when in contact with $BaSnF_4$. In **section IV.1.2**, we suggested that this layer could contain the following products: $BaLiF_3$, LiF, and Sn_xLi_y (in addition to other unknown product(s)). This layer is acting as an electrode in the cell, which means it is involved in the electrochemical reactions.

When the current sent through the cell is <0, only a very small peak is visible on the reduction curve on the CV, and barely any peak is observed from the galvanostatic experiment. We suggest that this could be due to a reduction reaction taking place in the ⊕ electrode, but being quickly stunted. This would be possible if the reduction reaction is $BaSnF_4 + 2e^- \rightarrow BaF_2 + Sn + 2F^-$. BaF_2 is a very poor ionic and electronic conductor ($\sigma_{RT} \approx 10^{-9}$ S.cm^{-1})[45]. During the reduction, a thin layer of BaF_2 (and Sn) would form at the surface of $BaSnF_4$ particles, blocking F-ions from diffusing out, and therefore stopping the reaction.

i > 0	
Electrode ⊖ 1) $BaSnF_4 + 2e^- \longrightarrow BaF_2 + Sn + 2F^-$ 2) $LiF + 2e^- \longrightarrow Li + 2F^-$	Electrode ⊕ $BaSnF_4 + 2F^- \longrightarrow BaSnF_6 + 2e^-$
i < 0	
Electrode ⊖ $BaSnF_4 + 2F^- \longrightarrow BaSnF_6 + 2e^-$	Electrode ⊕ ~~$BaSnF_4 + 2e^- \longrightarrow BaF_2 + Sn + 2F^-$~~

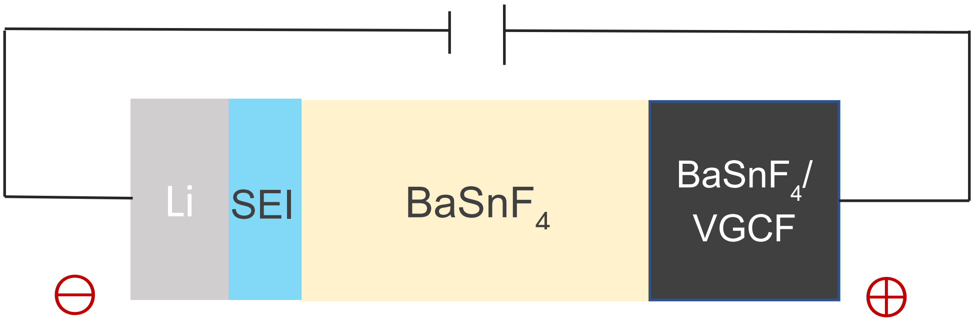

Figure IV.11. schematic of the system used for galvanostatic experiments and cell reactions under current

When the current sent through the cell is >0, we form $BaSnF_6$ in the ⊕ electrode, as confirmed via XRD ($BaSnF_4 + 2F^- \rightarrow BaSnF_6 + 2e^-$). On the other side of the cell, at the ⊖ electrode, we hypothesize that, at first, $BaSnF_4 + 2e^- \rightarrow BaF_2 + Sn + 2F^-$ takes place. As explained before, this reaction drives the formation of an insulating BaF_2 layer at the surface of $BaSnF_4$ particles. However, the electrode where the reduction takes place is different, it also contains the lithiated products of the reaction between $BaSnF_4$ and Li. Once the first reaction cannot take place anymore due to the BaF_2 layer, another reaction could take place instead, which we believe could be either $2\ LiF + 2\ e^- \rightarrow 2\ Li + 2F^-$, or $BaLiF_3 + e^- \rightarrow BaF_2 + Li + F^-$. In both cases, this half reaction would enable the oxidation at the $\oplus$ electrode to take place by providing F-ions. A summary of the cell reactions is displayed in **Figure IV.11**.

The cell oxidation is then enabled by the existence of lithiated products at the $\ominus$ electrode, which are involved in the redox reactions. This poses an issue with the use of Li metal as a reference electrode: the potential of a reference electrode is meant to be constant and known. Here, however the counter electrode is the decomposition layer, we do not know its potential, or at which potential the reactions involving LiF and $BaLiF_3$ occur. As a result, we measure an electrochemical stability window for $BaSnF_4$ but we cannot situate it on the potential scale. Additionally, it is likely that this counter electrode gets very polarized, which would artificially expand the ESW. Regardless, $BaSnF_6$, formed after oxidation in the $BaSnF_4$/VGCF electrode, appears to form a stable layer on the electrolyte particles, which widens the ESW in subsequent cycles.

IV.2.2.4. Electrochemical stability at higher temperatures

Another possible explanation for the enlarged potential window after the first cycle is related to the low ionic conductivity of decomposition products in our experiments. After electrochemical cycling of the Li|$BaSnF_4$|$BaSnF_4$/VGCF cells, the recorded impedance had increased by an order of magnitude (**Figure IV.12**. c). This increase in resistivity due to electrolyte decomposition in the first cycle may hinder ionic and electronic transfer within the electrodes, preventing further decomposition and artificially extending the ESW.

To improve the conductivity in the electrode, hereby maximizing the chances of observing degradation after the first cycle, polarization experiments were repeated at higher temperatures, up to 80°C, which is the maximum temperature our setup could sustain. The results are displayed in **Figure IV.12**. Panel a) showcases the pseudo-CV of $BaSnF_4$ at 80°C, it is fairly different from its 25°C counterpart. The peak at 2.3 V disappeared, a peak at 0.48 V appeared, and most importantly the scale of the degradation is much larger, with about 18% of electrolyte decomposing in the first cycle based on the capacity calculated using the decomposition pathway previously

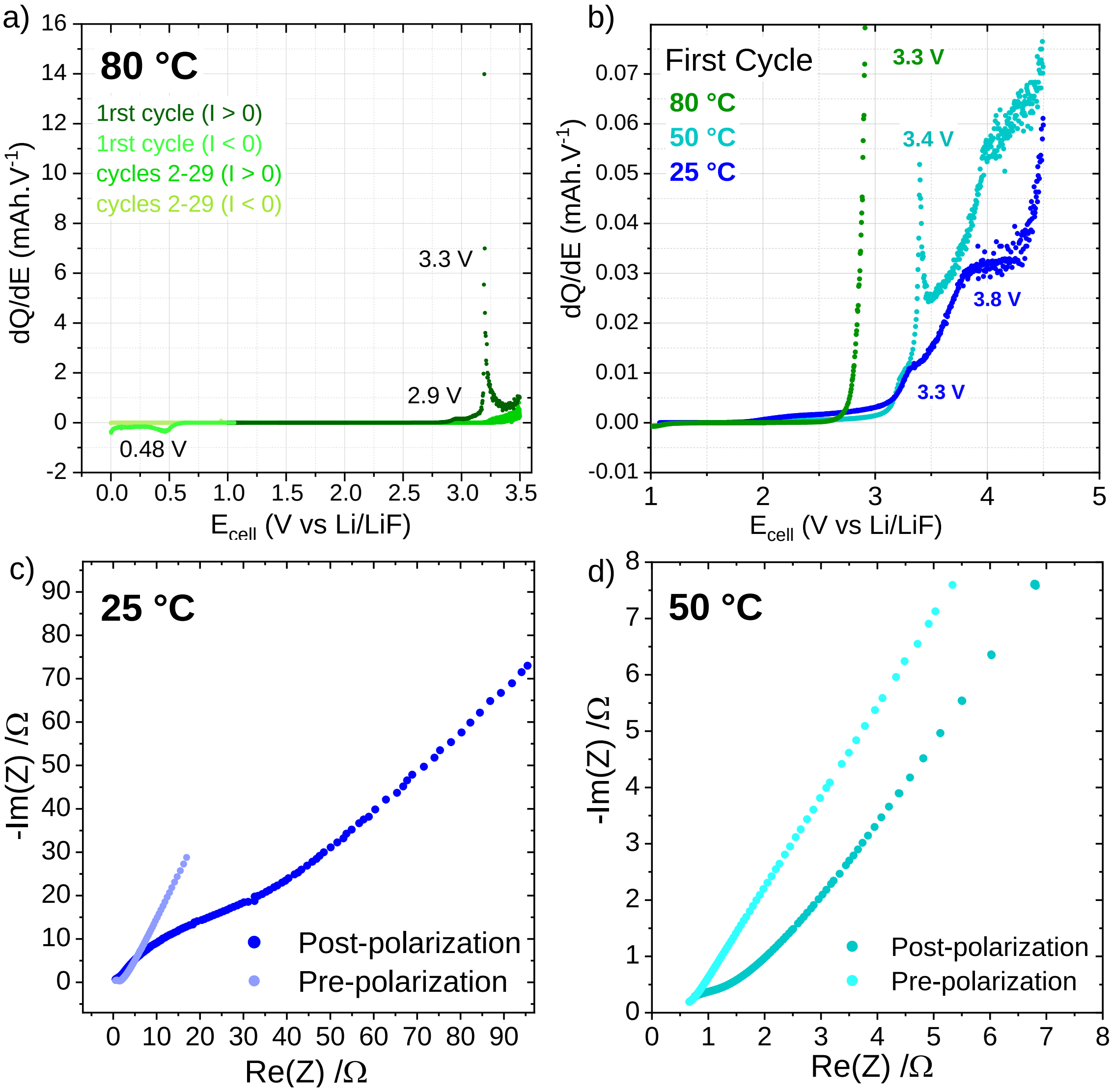

Figure IV.12 study of the electrochemical stability window evolution with temperature, a) pseudo-CV derived from GCPL experiments at 80°C, b) comparison of the first pseudo-CV cycles at 3 temperatures. We note that for the 80°C curve, the 3.3V peak is not visible because of the scale, much smaller than in the first panel, c) EIS of the $Li|BaSnF_4|BaSnF_4$/VGCF before and after polarization at 25°C, d) EIS of the $Li|BaSnF_4|BaSnF_4$/VGCF before and after polarization at 50°C described. The following cycles, however, once again suggest there is no degradation anymore.

Impedance measurements show a significant temperature-related improvement of the conductivity both before and after degradation (see **Figure IV.12** panels c and d), which supports the theory that the absence of degradation upon subsequent cycles is then correlated with high stability rather than low conductivity. These temperature experiments are also interesting for future battery investigations using this electrolyte, as FIB tend to be operated at high temperature in order to boost ionic transport inside the active material particles as a means to increase effective capacity.

In summary, we showed that $BaSnF_4$ appears a significantly wider ESW than expected, reaching 1.2V at 25°C, likely due the use of Li as a reference electrode, which artificially extended said window. The decomposition products were studied, and served as a basis for a proposed decomposition pathway. This pathway involved lithiated phases at the Li | $BaSnF_4$ interface. The potential at which these reactions occur is unknown but differs from that of Li/LiF, which implies that there is a variation of potential at what is meant to act as a reference electrode, invalidating the use of lithium metal in that role.

IV.2.2.5. ESW of $SrSnF_4$ and $Ba_xSr_{1-x}SnF_4$

We now have established that the use of Li as a reference leads to erroneous results and potentially overestimated ESW, however it might still be useful for qualitative comparison between similar materials.

Using the setup described in section 2.2.1., we also studied the stability window of the other t-$MSnF_4$ which we had synthetized. The cubic phases were not considered here, as their low conductivity makes them lesser candidates for battery applications.

Firstly, the stability of tetragonal $SrSnF_4$ at room-temperature was investigated. Similar to $BaSnF_4$, an interface was formed upon contact with Li. We could follow its formation through EIS measurements, which showed the increase of the cell resistance with time. After the impedance had stabilized, GCPL was started, the dQ/dV curve of which is shown in **Figure IV.13**, panel a). We note that no data could be obtained below 1.2-1.5 V. We did perform several measurements between 0 and 1.2 V, but the cell immediately reached the minimum set potential upon negative polarization, which meant no point could be recorded in that range. It also strongly suggests no redox reaction took place.

Just as for $BaSnF_4$, some small peaks are visible in the first cycles, and the material appears to be more stable during subsequent cycles. The current exchanged is however

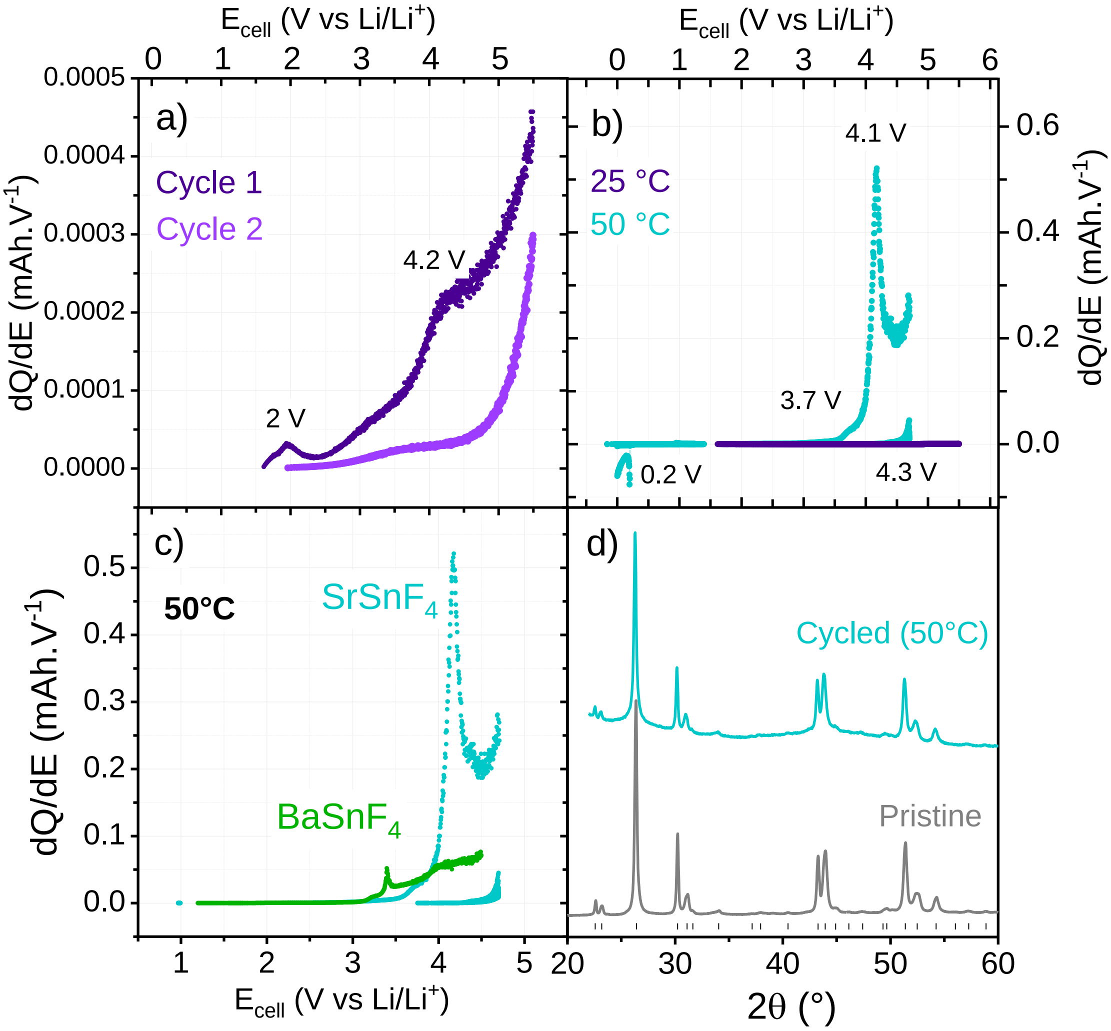

Figure IV.13 Stability study of t-$SrSnF_4$. a) pseudo-CV of a Li|$SrSnF_4$|$SrSnF_4$/VGCF cell, polarized at 10 µA.cm^{-2} and 25°C, with the first galvanic polarization in dark purple and second in light purple, b) comparison of the first scans at 25°C (purple) and 50 °C (blue), c) comparison of the 50°C stabilities of $SrSnF_4$ (blue) and $BaSnF_4$ (green), d) XRD diagrams of the pristine (grey) and cycled at 50°C (blue) $SrSnF_4$ composite electrodes, the indexed Bragg peaks are marked below the pristine diffractogram.

significantly smaller than it is for the barium phase, which could hint towards a larger window of stability for $SrSnF_4$. Nevertheless, the extremely high impedance of the cell (>250 kΩ) may also be at the root of this result, as the passage of a small current causes a fast increase of the potential under Ohm's law, quickly reaching the set limit.

In order to lower the impedance of the cell and more accurately probe the stability of $SrSnF_4$, GCPL experiments were performed at 50°C. The EIS shows the cell impedance to be comparable to that of $BaSnF_4$ at room temperature, which is consistent with the EIS values of the electrolyte pellets previously measured on their own (σ_{SrSnF4} = 2.46 x10^{-5} S.cm^{-1} at 50°C and σ_{BaSnF4} = 4.03 x10^{-5} S.cm^{-1} at 20°C). A comparison of the 25°C and 50°C pseudo-CV is shown in **Figure IV.13**, panel b). The material gets degraded significantly in the first cycle, but interestingly, as shown in panel d), there is no visible degradation product on the XRD diagram. It is then more complicated to accurately estimate the percentage of electrolyte degraded, as we do not know the number of electrons exchanged. If we assume that somehow tin is once again oxidized from Sn(II) to Sn(IV) and that the strontium stays at a D.O of +II, this two-electron exchange yields 8% degradation in the first cycle, which is above the limit normally visible via XRD. It is possible that the products could be amorphous.

After the first cycle, even at high temperatures, there is very little further decomposition, suggesting as for $BaSnF_4$ that the degradation products are stable. Compared to $BaSnF_4$, $SrSnF_4$ is more stable until 3.89 V, and becomes significantly less stable afterwards, as shown in **Figure IV.13** panel c).

In summary, $SrSnF_4$ appears more stable than $BaSnF_4$ at room temperature, however we demonstrate this to be an artefact caused by its low conductivity. Comparing both $MSnF_4$ at temperatures at which they have similar conductivities, the degradation of $SrSnF_4$ is largely superior. With low room-temperature ionic conductivity and low electrochemical stability, $SrSnF_4$ emerges as a poor choice of electrolyte for FIB.

Some attempts to characterize $Ba_xSr_{1-x}SnF_4$'s stabilities were made but repeatedly resulted in short-circuits for unknown reasons. It would be expected that their ESW would lie somewhere between that of $BaSnF_4$ and $SrSnF_4$, but given the subpar conductivities of these materials, we did not investigate further.

Conclusions and Perspectives

In this chapter, we attempted to find a suitable reference which would allow us to evaluate our electrolytes electrochemical properties, namely their critical current densities and electrochemical windows of stability.

Tin was tested first, but it led to very high polarizations and an unstable interface with $BaSnF_4$, both of which made it unsuitable for use as a reference electrode. We then turned to Lithium, which formed a non-blocking interface with $BaSnF_4$. This led us to perform ESW measurements using a Li | $BaSnF_4$ | $BaSnF_4$/VGCF cell configuration, but the results suggested that the Li | $BaSnF_4$ interface interfered with the decomposition, and, more importantly, that the potential at this interface was unknown, which meant the potential of the "reference" electrode was unknown, Li can therefore not be considered a reference electrode either when appraising the electrochemical properties of $MSnF_4$.

Nevertheless, we may qualitatively compare the stability of $BaSnF_4$ and $SrSnF_4$. Though $SrSnF_4$ appears more stable at room-temperature, galvanostatic cycling at higher temperature showed this to be an artefact caused by its lower ionic conductivity.

Perspective: FIB reference electrode in the litterature

So far, only one other research group attempted to characterize the ESW of $BaSnF_4$, doing so by assembling $MSnF_4$/MWCNTs|$MSnF_4$|PK10|Pb/PbF_2/MWCNTs (MWCNT = Multi-Walled Carbon NanoTubes, PK10 = solid electrolyte $CsPb_{0.9}K_{0.1}F_{2.9}$) cells and performing CV experiments on them, shown in **Figure IV.14** and from which they deduce the ESW of 0.24 V.[36]

The reference electrode (and counter electrode) in this cell architecture is Pb/PbF_2. A reference electrode is, by definition, supposed to have a stable potential in the measurement conditions, which should be the case here, as the fluorination / defluorination of Pb is a biphasic reaction and should therefore take place at a fixed potential.

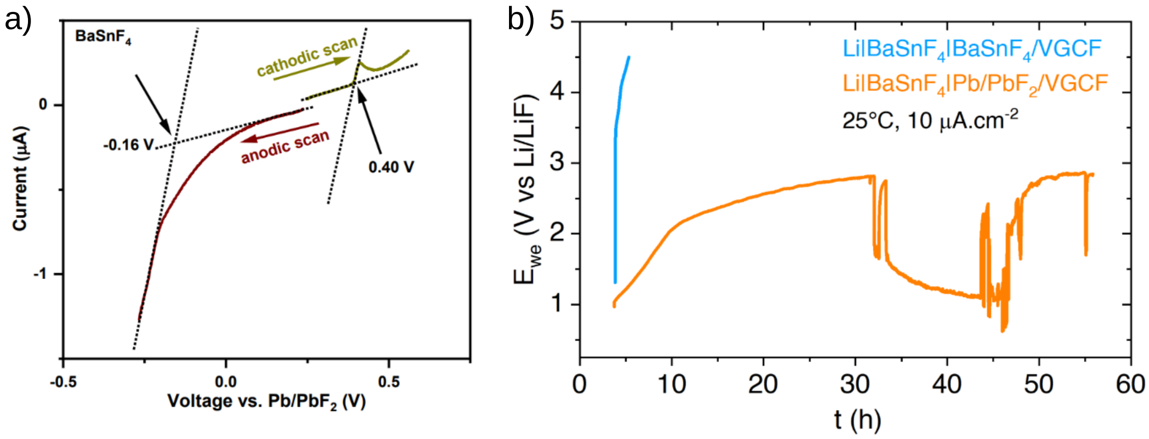

Figure IV.14 testing of Pb/PbF_2 as a reference electrode a) Linear sweep voltammetry of a $BaSnF_4$/MWCNTs|$MSnF_4$|PK10|Pb/PbF_2/MWCNTs, at a 0.1mV/s scan rate, extracted from reference 35. We note that the limits of the ESW are chosen based on very small onsets of current, b) galvanostatic charge of Li | $BaSnF_4$ | Pb/PbF_2/VGCF, at 25 °C and 10 μA.cm^{-2}

As an additional test of the Li reference electrode, we assembled Li | $BaSnF_4$ | Pb/PbF_2/VGCF cells following the same procedure as for the symmetrical cells but with one of the electrodes being 10 mg of a Pb/PbF_2/VGCF composite, in a 45:45:10 weight ratio, as reported by Wang et al.

Galvanostatic testing was then used instead of linear sweep voltammetry, in order to avoid kinetic-related issues. The potential response of this cell under positive current is shown in **Figure IV.14**, panel b). The potential rises throughout the charge, which has to originate from the Li|$BaSnF_4$ interface, as the potential of the Pb/PbF_2 electrode is stable.

This is more definite evidence that the “reference” electrode in our Li | $BaSnF_4$ | $BaSnF_4$/VGCF systems has both an unknown and changing potential.

While Pb/PbF_2 appears to be a better choice of reference, it should be noted that the experiments performed by Wang et al to determine the ESW are also lacking: the potential sweep only covers a very small range as the current onset chosen is small, only Potentiostatic experiments are made (which may not allow the observation of slower reactions), and only one scan in cathodic and anodic direction is made.

To obtain a more reliable assessment of $BaSnF_4$ (and $SrSnF_4$) ESW, we would need to build Pb/PbF_2/VGCF | $BaSnF_4$ | $BaSnF_4$/VGCF cells, and galvanostatically charge and discharge them.

Conclusions and perspectives

The work detailed in this thesis has been centered around Sn-based solid electrolytes for fluoride ion batteries, with the aim of describing the structure and ion transport mechanisms in several of the $MSnF_4$ (M = Ba, Sr) polymorphs. These studies highlighted the central role of tin and more specifically, its lone pair.

In the study of cubic c-$BaSnF_4$, we used a combination of experimental and computational methods, which allowed us to gain a more complete picture of this material on the local scale. We first characterized the disorder though local probes, using Pair Distribution Function and Mössbauer spectroscopy to highlight the stereoactivity of the Sn^{2+} lone pair and its impact on both the cationic and anionic framework of the fluorite structure. Using Density Functional Theory, we demonstrated how the lone pair creates disorder in both the cationic and anionic sublattice, pushing neighbouring fluoride-ions into interstitial sites, which are normally unoccupied in the fluorite structure. As interstitials are well-known to impact diffusion pathways, we then moved to characterize conductivity within this material. ^{19}F MAS NMR showed ionic mobility to be enabled by the presence of tin in fluoride environments. Using Ab Initio Molecular Dynamics, this experimental result was reproduced, and explained as the lone pair was shown to be dynamic, seemingly impacting F-ion jumps through a paddlewheel-like mechanism. As a result, fluorides in the vicinity of tins are extremely mobile, accounting for the majority of the conductive hopping within the structure. Through experimental, as well as computational means, we show that the presence of two types of disorder in a textbook structure like fluorite yields complex ionic mobility behaviours which cannot be described using simplistic models.

We investigated further the c-$MSnF_4$ structure by substituting the starting fluorite, BaF_2, with one of smaller volume: SrF_2. The addition of tin in this structure once again did not cause any change in the lattice parameter, which, through Mössbauer Spectroscopy, we linked to variations in the stereoactivity of the lone pair, notably a shrinkage of the doublet as the fluorite contracts. This decrease in lone pair expression is concomitant with a lower occupation of the octahedral interstices found through Ab Initio Molecular

Dynamics simulations, but, like in $BaSnF_4$, tin-rich environments were still the most favourable to F-ion transport. This study additionally reinforced our prior findings, as the slower ionic transport allowed for a more conclusive ^{19}F NMR analysis, confirming the existence of conductive mixed M/Sn environments and interstitial fluorides. In the tetragonal t-$Ba_{1-x}Sr_xSnF_4$ ($x \in [0,1]$), we likewise observe a similar volume effect (see annex 1).

The majority of our work on the tetragonal phase however, was focused on its synthesis. We proposed two new synthesis routes, including one using Spark "Plasma" Sintering, through which the ionic conductivity of electrolyte pellets was drastically improved. We used XRD to characterize the evolution of the microstructure with synthesis parameter variation, and link it with the fluctuations in F-transport, which allowed us to optimize the material for conductivity. Effects on the structure itself were studied as well through Neutron diffraction, from which we inferred the possible presence of stacking faults and interstitial fluorides in the structure, mirroring the effects of the tin lone pair in the cubic phase. Additional simulation work to shed light on lone pair dynamics and local structure is ongoing.

Furthermore, given the impressive transport properties that the tin lone pair confers to $MSnF_4$, it would be interesting to continue to direct material discovery efforts in this direction. We have also explored more materials than described in the experimental chapters, a summary of which is shown below. The syntheses are described in Annexe 1, along with some additional characterizations. These yielded interesting results, but require more in-depth studies than time allowed.

These structures are prospective electrolyte materials, thanks to their high ionic conductivity. We therefore undertook the characterization of the electrochemical properties of the most conductive phase, t-$BaSnF_4$, and searched for an appropriate reference electrode to do so, showing the inadequacy of both lithium and tin metal in combination with this family of electrolyte. A lot of experiments are still to be made to gain a good understanding of how these materials behave under current. Initial results did suggest a low critical current density, which would impede their use in fast-charging batteries, but these flaws may be overcome, for instance through the use of coatings. This was already done by Reddy et al, who coated $BaSnF_4$ with another electrolyte with higher stability, resulting in an improvement of overall cyclability.[267] As some suitable electrolytes have been found, we believe FIB now mainly need a stronger focus on the electrode composites and battery architecture, which go largely un-noticed, even in articles which focus on full-batteries. For other all-solid-state batteries, a lot of characterizations allowed for a good understanding of the important factors which improve the cyclability of a battery. These remain to be applied in FIB, where parameters such as cell pressure or active material particle size are often not accounted for, yielding unreliable results.

On the whole, as FIB are a very "young" system, an immense amount of work remains to be accomplished. In this light, the present thesis work hoped to provide additional tools on the solid electrolyte side of the battery, improving our understanding of transport in the best F-ion conductors and contributing new synthesis methods.

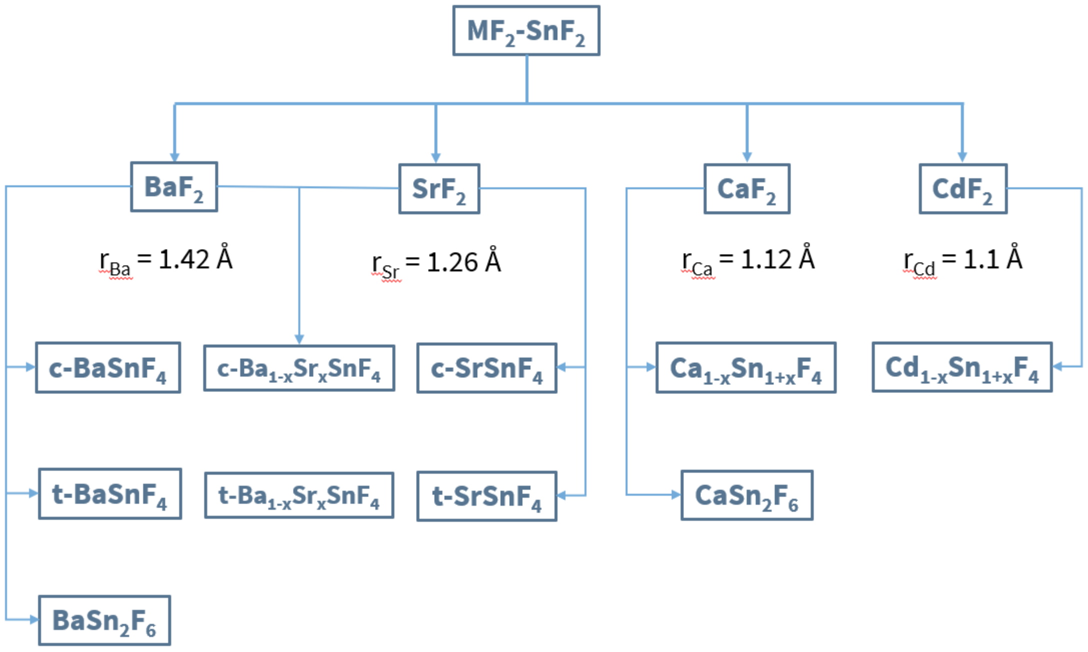

Annexe 1

Some work that was carried out has yielded promising results, but we did not integrate them in an experimental chapter, as it lacked in depth and more time would have been needed to investigate the results fully. We will nevertheless give a brief description of new Sn-based materials which were synthesized, along with an account of unsuccessful synthesis attempts for other materials, as a perspective for future work.

Synthesis of t-$Ba_{1-x}Sr_xSnF_4$

The synthesis and transport properties of c-$Ba_{1-x}Sr_xSnF_4$ are described in chapter II. Similar investigations were made on the corresponding tetragonal phases, t-$Ba_{1-x}Sr_xSnF_4$, which were obtained through a heat treatment of the cubic polymorphs at 300°C, under argon, for 3h. We note that even small amounts of oxygen in the atmosphere during synthesis resulted in tin oxide impurities in the final product.

Volumes increased linearly with the amount of barium in the structure, and so did the ionic conductivity, as shown in **Figure A.1.** Like in the cubic phase (chapter II), the introduction of additional disorder in these materials does not lead to an increase of ionic conductivity.

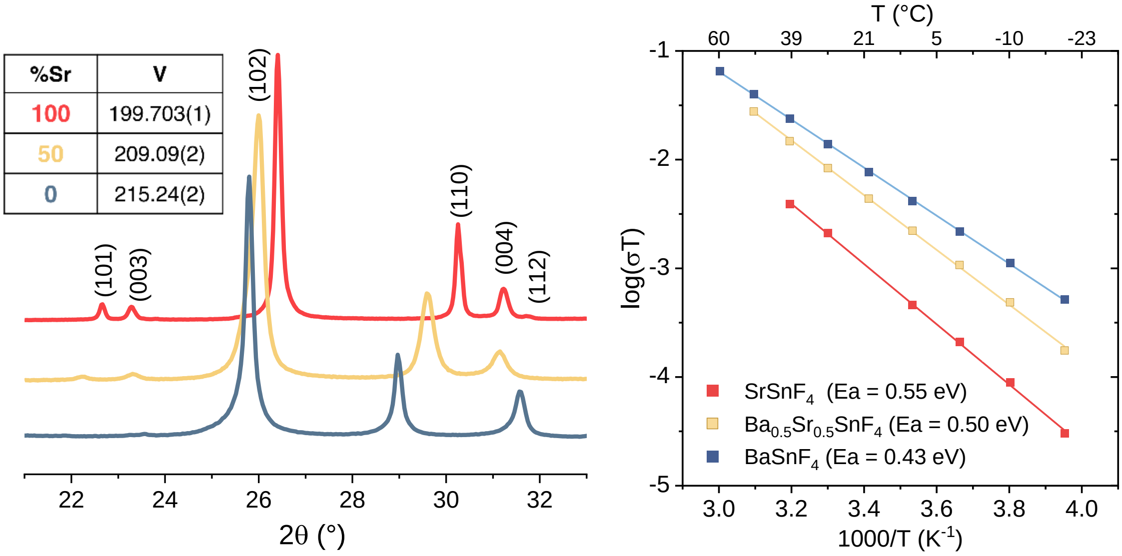

%Sr	V
100	199.703(1)
50	209.09(2)
0	215.24(2)

Figure A.1 a) XRD b) Arrhenius plot of t-$Ba_{1-x}Sr_xSnF_4$ solid solutions

Synthesis of $Cd_{2-x}Sn_xF_4$

Ball-milling of CdF_2 and SnF_2 ratio and subsequent heat treatment at 200 °C lead to the formation of a new compound, seemingly a cubic phase of the *F m-3m* spacegroup like CdF_2, but with a larger cell parameter (**Figure A.2**): 5.9400(2) Å for the new fluorite vs 5.393(3) for CdF_2. It then appears that in this new material, the cell parameter is not dictated by the radii of the Cadmium but by the tin itself. We verified that the lone pair is stereoactive in this new fluorite as well.

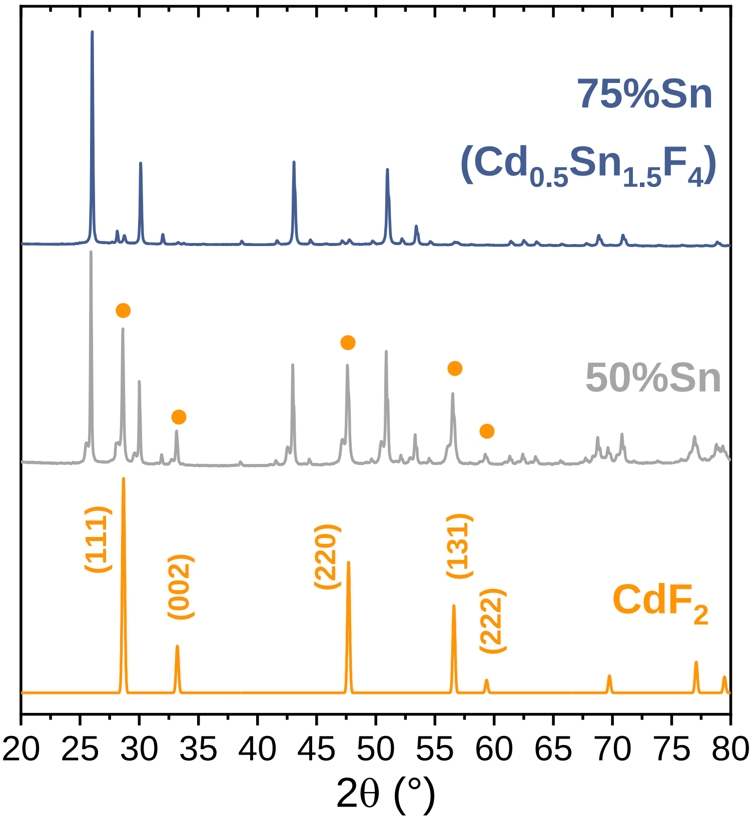

Figure A.2. XRD diagrams of the CdF_2:SnF_2 after ball-milling and heat treatment

Interestingly, this new material only accommodates a set amount of tin, unlike $BaSnF_4$ and $SrSnF_4$, which could exist at different stoichiometry, such as $Ba_{1.25}Sn_{0.75}F_4$ or $Sr_{1.25}Sn_{0.75}F_4$, the cadmium tin fluorite always exists as $Cd_{0.5}Sn_{1.5}F_4$, as adding more of either tin or cadmium in the precursor mix always resulted in additional CdF_2 or SnF_2 on the final XRD diagrams.

This new material could however never be obtained pure (see small peaks on **fig. A.2**, attributed to an impurity). It also had a low 4. 10^{-8} $S.cm^{-1}$ ionic conductivity at 30°C.

Reactivity of CaF_2 and SnF_2

The reactivity of CaF_2 and SnF_2 was fairly intensely studied, with the hopes of obtaining $CaSnF_4$, either a cubic or tetragonal phase, as for the other polymorphs.

We first attempted ball-milling of the two precursors, CaF_2 and SnF_2. Using the same synthesis parameters as for c-$BaSnF_4$, we obtained a material that appeared to be a mix of CaF_2 and a new phase. We used the software dicvol[268] to index the cell, but ultimately could not discriminate between the proposed spacegroups, as the XRD diagram peaks were larger than what the software we used for structure solving (FOX) was able to handle. From the small number of peaks, we hypothesized the spacegroup would be either cubic or tetragonal. The peak intensities would also be consistent with a FCC *F m* -3 *m* spacegroup, like the other c-$MSnF_4$ but, interestingly, a cell parameter significantly bigger than that of the parent fluorite CaF_2. This system then appears to bear similarities

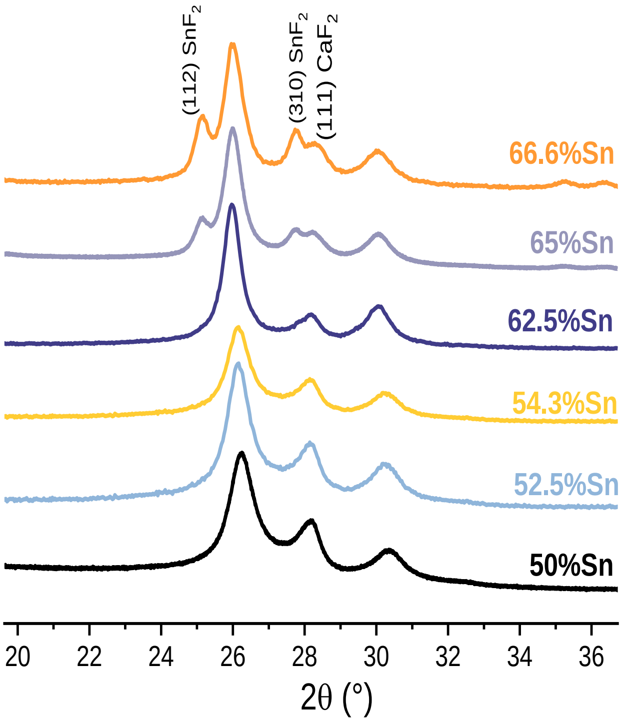

Figure A.3 XRD diagrams of CaF_2:SnF_2 after ball-milling, with increasing amounts of Sn.

with the Cd-based system, possibly due to their close ionic radii ($r_{Ca(VIII)}$ = 1.12 Å, $r_{Cd(VIII)}$ = 1.1 Å).

As there was leftover CaF_2 after ball-milling, we first thought that the reaction could necessitate more energy. We therefore tried to increase milling time, increase the ball:powder ratio, increase the jar volume, and finally made some trials with a higher-energy ball-milling machine, but all of these attempts resulted in failures. The amount of leftover CaF_2 could still be lessened, albeit only to a degree. This suggested that the newly formed phase was perhaps Sn-rich and that the stoichiometry of 1:1 was not providing sufficient amounts of tin. The next attempts were hence centered around different compositions, and are summarized in **Fig. A.3**.

Initially, the addition of tin is concomitant with the decrease in intensity of the (111) CaF_2 peak, suggesting the new $Ca_{2-x}Sn_xF_4$ phase is indeed Sn-rich. However, materials containing more than 62.5%Sn still had CaF_2 peaks present on their XRD diagrams, even though SnF_2 peaks appeared, which would imply that all CaF_2 has reacted. Even after 75h of milling, neither SnF_2 nor CaF_2 peaks subsided.

It might be possible to obtain a pure $Ca_{2-x}Sn_xF_4$ phase with more experiments.

The ball-milled materials were then heated to 200°C, which yielded in all cases the previously-reported $CaSn_2F_6$, a monoclinic phase (spacegroup *P* -1, a = 4.4231(2) Å, b = 7.1949(3) Å, c = 9.8462(6) Å, α = 98.690(6) °, β = 102.008(4) °, γ = 92.593(5) °) and electronic conductor.[269,270] This assignment was confirmed through Rietveld refinement. It was interesting that all Ca:Sn ratios, including 1:1, recrystallized into a *P* -1 phase which has a 1:2 ratio, despite the very large Sn deficiency. However, EDX mapping showed these materials to be inhomogeneous, with some Sn-rich and some Ca-rich zones, suggesting that two phase form during heat treatment: the monoclinic $CaSn_2F_6$, phase, and a Calcium-rich amorphous phase.

The Ca-based tin fluorides were not investigated further due to their consequent electronic conductivities, which barred them from being used as electrolytes. A battery was made with $CaSn_2F_6$ as a cathode material to check its whether it had any electrochemical activity, but none was detected.

References

(1) Armand, M.; Tarascon, J.-M. Building Better Batteries. *Nature* **2008**, *451* (7179), 652–657. https://doi.org/10.1038/451652a.

(2) *CATL launches condensed battery with an energy density of up to 500 Wh/kg, enables electrification of passenger aircrafts*. https://www.catl.com/en/news/6015.html (accessed 2023-06-13).

(3) Tarascon, J.-M. Is Lithium the New Gold? *Nature Chem* **2010**, *2* (6), 510–510. https://doi.org/10.1038/nchem.680.

(4) Placke, T.; Kloepsch, R.; Dühnen, S.; Winter, M. Lithium Ion, Lithium Metal, and Alternative Rechargeable Battery Technologies: The Odyssey for High Energy Density. *J Solid State Electrochem* **2017**, *21* (7), 1939–1964. https://doi.org/10.1007/s10008-017-3610-7.

(5) Nowroozi, M. A.; Mohammad, I.; Molaiyan, P.; Wissel, K.; Munnangi, A. R.; Clemens, O. Fluoride Ion Batteries – Past, Present, and Future. *J. Mater. Chem. A* **2021**, *9*, 5980–6012. https://doi.org/10.1039/D0TA11656D.

(6) Lorenz, R.; Kaufler, F. *Elektrochemie geschmolzener Salze*; Leipzig, 1909.

(7) Rose, B. A.; Davis, G. J.; Ellingham, H. J. T. Studies in the Thermodynamics of Metallurgical Reduction Processes by Electrochemical Methods. *Discuss. Faraday Soc.* **1948**, *4*, 154. https://doi.org/10.1039/df9480400154.

(8) Kessler, J. R.; Monberg, E.; Nicol, M. Studies of Fluorite and Related Divalent Fluoride Systems at High Pressure by Raman Spectroscopy. *The Journal of Chemical Physics* **1974**, *60* (12), 5057–5065. https://doi.org/10.1063/1.1681022.

(9) Lucat, C. Etude Des Propriétés de Conductivité Ionique de Quelques Fluorures de Structure Fluorine, Bordeau I, 1976.

(10) Danto, Y.; Poujade, G.; Pistré, J. D.; Lucat, C.; Salardenne, J. A Pb|PbF2|BiF3|Bi Thin Solid Film Reversible Galvanic Cell. *Thin Solid Films* **1978**, *55* (3), 347–354. https://doi.org/10.1016/0040-6090(78)90151-7.

(11) Chaudhuri, S.; Castiglione, M.; Wang, F.; Wilson, M.; Madden, P. A.; Grey, C. P. Study of Fluoride Ion Motions in PbSnF4 and BaSnF4 Compounds With Molecular Dynamics Simulation and Solid State NMR Techniques. *Mat. Res. Soc. Symp. Proc.* **2001**, *658*. https://doi.org/10.1557/PROC-658-GG10.9.

(12) Castiglione, M.; Madden, P. A.; Berastegui, P.; Hull, S. The Crystal Structure of α-PbSnF$_4$ and Its Anion Diffusion Mechanism. *J. Phys.: Condens. Matter* **2005**, *17* (6), 845–861. https://doi.org/10.1088/0953-8984/17/6/006.

(13) Matar, S.; Réau, J. M.; Demazeau, G.; Lucat, C.; Portier, J.; Hagenmuller, P. Influence de la pression sur les proprietes electriques de PbSnF4. *Solid State Communications* **1980**, *35* (9), 681–684. https://doi.org/10.1016/0038-1098(80)90873-X.

(14) Reddy, M. A.; Fichtner, M. Batteries Based on Fluoride Shuttle. *Journal of Materials Chemistry* **2011**, *21* (43), 17059–17062. https://doi.org/10.1039/C1JM13535J.

(15) Gschwind, F.; Rodriguez-Garcia, G.; Sandbeck, D. J. S.; Gross, A.; Weil, M.; Fichtner, M.; Hörmann, N. Fluoride Ion Batteries: Theoretical Performance, Safety, Toxicity, and a Combinatorial Screening of New Electrodes. *Journal of Fluorine Chemistry* **2016**, *182*, 76–90. https://doi.org/10.1016/j.jfluchem.2015.12.002.

(16) Grenier, A. Development of Solid-State Fluoride-Ion Batteries : Cell Design, Electrolyte Characterization and Electrochemical Mechanisms, Université Pierre et Marie Curie, 2016. https://tel.archives-ouvertes.fr/tel-01395108.

(17) Cabana, J.; Monconduit, L.; Larcher, D.; Palacín, M. R. Beyond Intercalation-Based Li-Ion Batteries: The State of the Art and Challenges of Electrode Materials Reacting Through Conversion Reactions. *Advanced Materials* **2010**, *22* (35), E170–E192. https://doi.org/10.1002/adma.201000717.

(18) Fawey, M. H.; Chakravadhanula, V. S. K.; Munnangi, A. R.; Rongeat, C.; Hahn, H.; Fichtner, M.; Kübel, C. First Results from in Situ Transmission Electron Microscopy Studies of All-Solid-State Fluoride Ion Batteries. *Journal of Power Sources* **2020**, *466*, 228283. https://doi.org/10.1016/j.jpowsour.2020.228283.

(19) Nakano, H.; Matsunaga, T.; Mori, T.; Nakanishi, K.; Morita, Y.; Ide, K.; Okazaki, K.; Orikasa, Y.; Minato, T.; Yamamoto, K.; Ogumi, Z.; Uchimoto, Y. Fluoride-Ion Shuttle Battery with High Volumetric Energy Density. *Chem. Mater.* **2021**, *33* (1), 459–466. https://doi.org/10.1021/acs.chemmater.0c04570.

(20) Zhang, D.; Yamamoto, K.; Ochi, A.; Wang, Y.; Yoshinari, T.; Nakanishi, K.; Nakano, H.; Miki, H.; Nakanishi, S.; Iba, H.; Uchiyama, T.; Watanabe, T.; Amezawa, K.; Uchimoto, Y. Understanding the Reaction Mechanism and Performances of 3d Transition Metal Cathodes for All-Solid-State Fluoride Ion Batteries. *J. Mater. Chem. A* **2021**, *9* (1), 406–412. https://doi.org/10.1039/D0TA08824B.

(21) Davis, V. K.; Bates, C. M.; Omichi, K.; Savoie, B. M.; Momčilović, N.; Xu, Q.; Wolf, W. J.; Webb, M. A.; Billings, K. J.; Chou, N. H.; Alayoglu, S.; McKenney, R. K.; Darolles, I. M.; Nair, N. G.; Hightower, A.; Rosenberg, D.; Ahmed, M.; Brooks, C. J.; Miller, T. F.; Grubbs, R. H.; Jones, S. C. Room-Temperature Cycling of Metal Fluoride Electrodes: Liquid Electrolytes for High-Energy Fluoride Ion Cells. *Science* **2018**, *362* (6419), 1144–1148. https://doi.org/10.1126/science.aat7070.

(22) Yoshinari, T.; Zhang, D.; Yamamoto, K.; Kitaguchi, Y.; Ochi, A.; Nakanishi, K.; Miki, H.; Nakanishi, S.; Iba, H.; Uchiyama, T.; Watanabe, T.; Matsunaga, T.; Amezawa, K.; Uchimoto, Y. Kinetic Analysis and Alloy Designs for Metal/Metal Fluorides toward High Rate Capability for All-Solid-State Fluoride-Ion Batteries. *J. Mater. Chem. A* **2021**, *9* (11), 7018–7024. https://doi.org/10.1039/D0TA12055C.

(23) Zhang, D.; Nakano, H.; Yamamoto, K.; Tanaka, K.; Yahara, T.; Imai, K.; Mori, T.; Miki, H.; Nakanishi, S.; Iba, H.; Watanabe, T.; Uchiyama, T.; Amezawa, K.; Uchimoto, Y. Rate-Determining Process at Electrode/Electrolyte Interfaces for All-Solid-State Fluoride-Ion Batteries. *ACS Appl. Mater. Interfaces* **2021**, *13* (25), 30198–30204. https://doi.org/10.1021/acsami.1c06947.

(24) Rongeat, C. Development of New Anode Composite Materials for Fluoride Ion Batteries. *Journal of Materials Chemistry A* **2014**, 12.

(25) Nowroozi, M. A.; Wissel, K.; Rohrer, J.; Munnangi, A. R.; Clemens, O. $LaSrMnO_4$: Reversible Electrochemical Intercalation of Fluoride Ions in the Context of Fluoride Ion Batteries. *Chem. Mater.* **2017**, *29* (8), 3441–3453. https://doi.org/10.1021/acs.chemmater.6b05075.

(26) Wissel, K.; Dasgupta, S.; Benes, A.; Schoch, R.; Bauer, M.; Witte, R.; Fortes, A. D.; Erdem, E.; Rohrer, J.; Clemens, O. Developing Intercalation Based Anode Materials for Fluoride-Ion Batteries: Topochemical Reduction of $Sr_2TiO_3F_2$ *via* a Hydride Based Defluorination Process. *J. Mater. Chem. A* **2018**, *6* (44), 22013–22026. https://doi.org/10.1039/C8TA01012A.

(27) Wissel, K.; Schoch, R.; Vogel, T.; Donzelli, M.; Matveeva, G.; Kolb, U.; Bauer, M.; Slater, P. R.; Clemens, O. Electrochemical Reduction and Oxidation of Ruddlesden–Popper-Type $La_2NiO_3F_2$ within Fluoride-Ion Batteries. *Chem. Mater.* **2021**, *33* (2), 499–512. https://doi.org/10.1021/acs.chemmater.0c01762.

(28) Nowroozi, M. A.; Ivlev, S.; Rohrer, J.; Clemens, O. La2CoO4 : A New Intercalation Based Cathode Material for Fluoride Ion Batteries with Improved Cycling Stability. *J. Mater. Chem. A* **2018**, *6* (11), 4658–4669. https://doi.org/10.1039/C7TA09427B.

(29) Zhang, W.-J. Structure and Performance of LiFePO4 Cathode Materials: A Review. *Journal of Power Sources* **2011**, *196* (6), 2962–2970. https://doi.org/10.1016/j.jpowsour.2010.11.113.

(30) Nowroozi, M. A.; Wissel, K.; Donzelli, M.; Hosseinpourkahvaz, N.; Plana-Ruiz, S.; Kolb, U.; Schoch, R.; Bauer, M.; Malik, A. M.; Rohrer, J.; Ivlev, S.; Kraus, F.; Clemens, O. High Cycle Life All-Solid-State Fluoride Ion Battery with La2NiO4+d High Voltage Cathode. *Commun Mater* **2020**, *1* (1), 27. https://doi.org/10.1038/s43246-020-0030-5.

(31) Grenier, A.; Porras-Gutierrez, A. G.; Body, M.; Legein, C.; Chrétien, F.; Raymundo-Piñero, E.; Dollé, M.; Groult, H.; Dambournet, D. Solid Fluoride Electrolytes and Their Composite with Carbon: Issues and Challenges for Rechargeable Solid State Fluoride-Ion Batteries. *J. Phys. Chem. C* **2017**, *121* (45), 24962–24970. https://doi.org/10.1021/acs.jpcc.7b07988.

(32) Clemens, O.; McTaggart, D.; Warren, S. C. *Reconsidering Anode Materials for Fluoride-Ion Batteries – The Unexpected Roles of Carbide Formation*; preprint; Chemistry, 2022. https://doi.org/10.26434/chemrxiv-2022-fww5l.

(33) Zhang, D.; Yamamoto, K.; Wang, Y.; Gao, S.; Uchiyama, T.; Watanabe, T.; Takami, T.; Matsunaga, T.; Nakanishi, K.; Miki, H.; Iba, H.; Amezawa, K.; Maeda, K.; Kageyama, H.; Uchimoto, Y. Reversible and Fast (De)Fluorination of High-Capacity Cu2O Cathode: One Step Toward Practically Applicable All-Solid-State Fluoride-Ion Battery. *Advanced Energy Materials* *n/a* (n/a), 2102285. https://doi.org/10.1002/aenm.202102285.

(34) Andrews, J.; McClure, E.; Jew, K.; Preefer, M.; Irshad, A.; Lertola, M.; Robertson, D.; Salamat, C.; Brady, M.; Piper, L.; Tolbert, S.; Nelson Weker, J.; Chmelka, B.; Dunn, B.; Narayan, S.; West, W.; Melot, B. *Room Temperature Electrochemical Fluoride (De)Insertion into the Defect Pyrochlore CsMnFeF6*; preprint; Chemistry, 2022. https://doi.org/10.26434/chemrxiv-2022-0w3lp.

(35) Wang, J.; Ma, C. Superior Room-Temperature Cycling Stability of Fluoride-Ion Batteries Enabled by Solid Electrolytes Synthesized by the Solid-State Reaction. *SCIENCE CHINA Materials* **2022**, *65* (11).

(36) Wang, J.; Hao, J.; Duan, C.; Wang, X.; Wang, K.; Ma, C. A Fluoride-Ion-Conducting Solid Electrolyte with Both High Conductivity and Excellent Electrochemical Stability. *Small* **2022**, *18* (5), 2104508. https://doi.org/10.1002/smll.202104508.

(37) Yamane, Y.; Yamada, K.; Inoue, K. Mechanochemical Synthesis and Order–Disorder Phase Transition in Fluoride Ion Conductor RbPbF3. *Solid State Ionics* **2008**, *179* (17), 605–610. https://doi.org/10.1016/j.ssi.2008.04.022.

(38) Janek, J.; Zeier, W. G. A Solid Future for Battery Development. *Nat Energy* **2016**, *1* (9), 1–4. https://doi.org/10.1038/nenergy.2016.141.

(39) Zhang, Z.; Nazar, L. F. Exploiting the Paddle-Wheel Mechanism for the Design of Fast Ion Conductors. *Nat Rev Mater* **2022**, *7* (5), 389–405. https://doi.org/10.1038/s41578-021-00401-0.

(40) Imre, Á. W.; Staesche, H.; Voss, S.; Ingram, M. D.; Funke, K.; Mehrer, H. Pressure-Dependent Diffusion Coefficients and Haven Ratios in Cation-Conducting Glasses. *J. Phys. Chem. B* **2007**, *111* (19), 5301–5307. https://doi.org/10.1021/jp070478q.

(41) Richards, W. D.; Miara, L. J.; Wang, Y.; Kim, J. C.; Ceder, G. Interface Stability in Solid-State Batteries. *Chem. Mater.* **2016**, *28* (1), 266–273. https://doi.org/10.1021/acs.chemmater.5b04082.

(42) Porz, L.; Swamy, T.; Sheldon, B. W.; Rettenwander, D.; Frömling, T.; Thaman, H. L.; Berendts, S.; Uecker, R.; Carter, W. C.; Chiang, Y.-M. Mechanism of Lithium Metal Penetration through Inorganic Solid Electrolytes. *Advanced Energy Materials* **2017**, *7* (20), 1701003. https://doi.org/10.1002/aenm.201701003.

(43) Skinner, S. J.; Kilner, J. A. Oxygen Ion Conductors. *Materials Today* **2003**, *6* (3), 30–37. https://doi.org/10.1016/S1369-7021(03)00332-8.

(44) Hull, S. Superionics: Crystal Structures and Conduction Processes. *Rep. Prog. Phys.* **2004**, *67* (7), 1233–1314. https://doi.org/10.1088/0034-4885/67/7/R05.

(45) Düvel, A.; Heitjans, P.; Fedorov, P.; Scholz, G.; Cibin, G.; Chadwick, A. V.; Pickup, D. M.; Ramos, S.; Sayle, L. W. L.; Sayle, E. K. L.; Sayle, T. X. T.; Sayle, D. C. Is Geometric Frustration-Induced Disorder a Recipe for High Ionic Conductivity? *J. Am. Chem. Soc.* **2017**, *139* (16), 5842–5848. https://doi.org/10.1021/jacs.7b00502.

(46) Annamareddy, V. A.; Nandi, P. K.; Mei, X.; Eapen, J. Waxing and Waning of Dynamical Heterogeneity in the Superionic State. *Phys. Rev. E* **2014**, *89* (1), 010301. https://doi.org/10.1103/PhysRevE.89.010301.

(47) Kennedy, J. H.; Miles, R. C. Ionic Conductivity of Doped Beta-Lead Fluoride. *J. Electrochem. Soc.* **1976**, *123* (1), 47–51. https://doi.org/10.1149/1.2132763.

(48) Ure, R. W. Ionic Conductivity of Calcium Fluoride Crystals. **1956**, 11.

(49) Bollmann, W.; Görlich, P.; Hauk, W.; Mothes, H. Ionic Conduction of Pure and Doped CaF2 and SrF2 Crystals. *physica status solidi (a)* **1970**, *2* (1), 157–170. https://doi.org/10.1002/pssa.19700020120.

(50) Gervais, A.; Jacquet, M.; Bathier, M. POINT DEFECTS, INTERACTION.DEFECT ASSOCIATION IN SrCl2 DOPED WITH Na+, K+, Rb+ OR Gd3+. *J. Phys. Colloques* **1976**, *37* (C7), C7-285. https://doi.org/10.1051/jphyscol:1976768.

(51) Scheiber, T.; Gombotz, M.; Hogrefe, K.; Wilkening, H. M. R. Fluoride Ion Dynamics in Nanocrystalline α-PbF2: On the Tremendous Impact of Structural Disorder on F− Anion Hopping in Poor Ion Conductors. *Solid State Ionics* **2022**, *387*, 116077. https://doi.org/10.1016/j.ssi.2022.116077.

(52) Dawson, J. A.; Canepa, P.; Famprikis, T.; Masquelier, C.; Islam, M. S. Atomic-Scale Influence of Grain Boundaries on Li-Ion Conduction in Solid Electrolytes for All-Solid-State Batteries. *J. Am. Chem. Soc.* **2018**, *140* (1), 362–368. https://doi.org/10.1021/jacs.7b10593.

(53) Chen, X. J.; Khor, K. A.; Chan, S. H.; Yu, L. G. Influence of Microstructure on the Ionic Conductivity of Yttria-Stabilized Zirconia Electrolyte. *Materials Science and Engineering: A* **2002**, *335* (1), 246–252. https://doi.org/10.1016/S0921-5093(01)01935-9.

(54) Gschwind, F.; Zao-Karger, Z.; Fichtner, M. A Fluoride-Doped PEG Matrix as an Electrolyte for Anion Transportation in a Room-Temperature Fluoride Ion Battery. *Journal of Materials Chemistry A* **2014**, *2* (5), 1214–1218. https://doi.org/10.1039/C3TA13881J.

(55) Li, X.; Tang, Y.; Zhu, J.; Lv, H.; Xu, Y.; Wang, W.; Zhi, C.; Li, H. Initiating a Room-Temperature Rechargeable Aqueous Fluoride-Ion Battery with Long Lifespan through a Rational Buffering Phase Design. *Advanced Energy Materials n/a* (n/a), 2003714. https://doi.org/10.1002/aenm.202003714.

(56) Motohashi, K.; Nakamura, T.; Kimura, Y.; Uchimoto, Y.; Amezawa, K. Influence of Microstructures on Conductivity in Tysonite-Type Fluoride Ion Conductors. *Solid State Ionics* **2019**, *338*, 113–120. https://doi.org/10.1016/j.ssi.2019.05.023.

(57) Dieudonné, B.; Chable, J.; Body, M.; Legein, C.; Durand, E.; Mauvy, F.; Fourcade, S.; Leblanc, M.; Maisonneuve, V.; Demourgues, A. The Key Role of the Composition and Structural Features in Fluoride Ion Conductivity in Tysonite Ce1−xSrxF3−x Solid Solutions. *Dalton Trans.* **2017**, *46* (11), 3761–3769. https://doi.org/10.1039/C6DT04714A.

(58) Sorokin, N. I.; Sobolev, B. P. Frequency Response of the Low-Temperature Ionic Conductivity of Single Crystals R1 − yMyF3 − y(R = La-Er; M = Ca, Sr, Ba, Cd). *Phys. Solid State* **2008**, *50* (3), 416–421. https://doi.org/10.1134/S1063783408030037.

(59) Roos, A.; van de Pol, F. C. M.; Keim, R.; Schoonman, J. Ionic Conductivity in Tysonite-Type Solid Solutions La1−xBaxF3−x. *Solid State Ionics* **1984**, *13* (3), 191–203. https://doi.org/10.1016/0167-2738(84)90030-4.

(60) Wang, F.; Grey, C. P. Probing the Mechanism of Fluoride-Ion Conduction in LaF_3 and Strontium-Doped LaF_3 with High-Resolution ^{19}F MAS NMR. *Chem. Mater.* **1997**, *9* (5), 1068–1070. https://doi.org/10.1021/cm970044f.

(61) Chable, J.; Dieudonné, B.; Body, M.; Legein, C.; Crosnier-Lopez, M.-P.; Galven, C.; Mauvy, F.; Durand, E.; Fourcade, S.; Sheptyakov, D.; Leblanc, M.; Maisonneuve, V.; Demourgues, A. Fluoride Solid Electrolytes: Investigation of the Tysonite-Type Solid Solutions La1−xBaxF3−x (x < 0.15). *Dalton Trans.* **2015**, *44* (45), 19625–19635. https://doi.org/10.1039/C5DT02321A.

(62) Rongeat, C.; Anji Reddy, M.; Witter, R.; Fichtner, M. Solid Electrolytes for Fluoride Ion Batteries: Ionic Conductivity in Polycrystalline Tysonite-Type Fluorides. *ACS Appl. Mater. Interfaces* **2014**, *6* (3), 2103–2110. https://doi.org/10.1021/am4052188.

(63) Gombotz, M.; Pregartner, V.; Hanzu, I.; Wilkening, H. M. R. Fluoride-Ion Batteries: On the Electrochemical Stability of Nanocrystalline La0.9Ba0.1F2.9 against Metal Electrodes. *Nanomaterials* **2019**, *9* (11), 1517. https://doi.org/10.3390/nano9111517.

(64) Fujisaki, F.; Mori, K.; Yonemura, M.; Ishikawa, Y.; Kamiyama, T.; Otomo, T.; Matsubara, E.; Fukunaga, T. Mechanical Synthesis and Structural Properties of the Fast Fluoride-Ion Conductor PbSnF4. *Journal of Solid State Chemistry* **2017**, *253*, 287–293. https://doi.org/10.1016/j.jssc.2017.06.007.

(65) Mohammad, I.; Witter, R.; Fichtner, M.; Anji Reddy, M. Room-Temperature, Rechargeable Solid-State Fluoride-Ion Batteries. *ACS Appl. Energy Mater.* **2018**, *1* (9), 4766–4775. https://doi.org/10.1021/acsaem.8b00864.

(66) Mori, K.; Mineshige, A.; Emoto, T.; Sugiura, M.; Saito, T.; Namba, K.; Otomo, T.; Abe, T.; Fukunaga, T. Electrochemical, Thermal, and Structural Features of BaF_2 –SnF_2

Fluoride-Ion Electrolytes. *J. Phys. Chem. C* **2021**, acs.jpcc.1c03326. https://doi.org/10.1021/acs.jpcc.1c03326.

(67) Birchall, T.; Dénès, G.; Ruebenbauer, K.; Pannetier, J. A Neutron Diffraction and119Sn Mössbauer Study of PbSnF4 and BaSnF4. *Hyperfine Interact* **1986**, *29* (1), 1331–1334. https://doi.org/10.1007/BF02399479.

(68) Pearson, R. G. The Second-Order Jahn-Teller Effect. *Journal of Molecular Structure: THEOCHEM* **1983**, *103*, 25–34. https://doi.org/10.1016/0166-1280(83)85006-4.

(69) Payne, D. J.; Egdell, R. G.; Walsh, A.; Watson, G. W.; Guo, J.; Glans, P.-A.; Learmonth, T.; Smith, K. E. Electronic Origins of Structural Distortions in Post-Transition Metal Oxides: Experimental and Theoretical Evidence for a Revision of the Lone Pair Model. *Phys. Rev. Lett.* **2006**, *96* (15), 157403. https://doi.org/10.1103/PhysRevLett.96.157403.

(70) Fu, Y.; Jin, S.; Zhu, X.-Y. Stereochemical Expression of Ns2 Electron Pairs in Metal Halide Perovskites. *Nat Rev Chem* **2021**, *5* (12), 838–852. https://doi.org/10.1038/s41570-021-00335-9.

(71) Portier, J.; Reau, J. M.; Matar, S.; Soubeyroux, J. L.; Hagenmuller, P. Advances on Fluorine Ion Conductors, Basic and Applied Research. *Solid State Ionics* **1983**, *11* (1), 83–90. https://doi.org/10.1016/0167-2738(83)90067-X.

(72) Patro, L. N.; Hariharan, K. Fast Fluoride Ion Conducting Materials in Solid State Ionics: An Overview. *Solid State Ionics* **2013**, *239*, 41–49. https://doi.org/10.1016/j.ssi.2013.03.009.

(73) Hagenmuller, P.; Réau, J.-M.; Lucat, C.; Matar, S.; Villeneuve, G. Ionic Conductivity of Fluorite-Type Fluorides. *Solid State Ionics* **1981**, *3–4*, 341–345. https://doi.org/10.1016/0167-2738(81)90110-7.

(74) Castiglione, M. J.; Wilson, M.; Madden, P. A. Polarization Effects in the Simulation of Lead (II) Fluoride. *J. Phys.: Condens. Matter* **1999**, *11* (46), 9009. https://doi.org/10.1088/0953-8984/11/46/304.

(75) Dickens, M. H.; Hayes, W.; Hutchings, M. T.; Smith, C. Investigation of Anion Disorder in PbF2 at High Temperatures by Neutron Diffraction. *J. Phys. C: Solid State Phys.* **1982**, *15* (19), 4043. https://doi.org/10.1088/0022-3719/15/19/006.

(76) Mohn, C. E.; Krynski, M.; Kob, W.; Allan, N. L. Cooperative Excitations in Superionic PbF2. *Philosophical Transactions of the Royal Society A: Mathematical, Physical and Engineering Sciences* **2021**, *379* (2211), 20190455. https://doi.org/10.1098/rsta.2019.0455.

(77) Chaudhuri, S.; Wang, F.; Grey, C. P. Resolving the Different Dynamics of the Fluorine Sublattices in the Anionic Conductor BaSnF4 by Using High-Resolution MAS NMR Techniques. *J. Am. Chem. Soc.* **2002**, *124* (39), 11746–11757. https://doi.org/10.1021/ja026155j.

(78) Murray, E.; Brougham, D. F.; Stankovic, J.; Abrahams, I. Conductivity and Fluoride Ion Dynamics in α-$PbSnF_4$; ^{19}F Field-Cycling NMR and Diffraction Studies. *J. Phys. Chem. C* **2008**, *112* (14), 5672–5678. https://doi.org/10.1021/jp7108708.

(79) Villeneuve, G.; Echegut, P.; Lucat, C.; Reau, J.-M.; Hagenmuller, P. Mobilité de l'ion fluor dans PbSnF4. *phys. stat. sol. (b)* **1980**, *97* (1), 295–301. https://doi.org/10.1002/pssb.2220970134.

(80) Matar, S. F.; Galy, J. Lone Electron Pair (E) Role on the Crystal Structures and the Mechanism of High Ionic Conductivity of PbSnF4E2. Stereochemical and Ab Initio Investigations. *Solid State Sciences* **2016**, *52*, 29–36. https://doi.org/10.1016/j.solidstatesciences.2015.11.011.

(81) Theodosios Famprikis; Pieremanuele Canepa; James A Dawson; M Saiful Islam; Christian Masquelier. Fundamentals of Inorganic Solid-State Electrolytes for Batteries | Nature Materials. *Nature* **2019**, *18*, 1278–1291.

(82) Pogorenko, Yu. V.; Pshenychnyi, R. M.; Omelchuk, A. O.; Trachevskyi, V. V. Conductivity of Aliovalent Substitution Solid Solutions Pb1-xRxSnF4+x (R = Y, La, Ce, Nd, Sm, Gd) with β-PbSnF4 Structure. *Solid State Ionics* **2019**, *338*, 80–86. https://doi.org/10.1016/j.ssi.2019.05.001.

(83) Kanno, R.; Nakamura, S.; Kawamoto, Y. Ionic Conductivity of Tetragonal PbSnF4 Substituted by Aliovalent Cations Zr4+, Al3+, Ga3+, In3+ and Na+. *Solid State Ionics* **1992**, *51* (1), 53–59. https://doi.org/10.1016/0167-2738(92)90343-N.

(84) Podgorbunsky, A. B.; Sinebryukhov, S. L.; Gnedenkov, S. V. Comparison of Superionic Phases for Some Fluorine Conducting Materials. *Physics Procedia* **2012**, *23*, 94–97. https://doi.org/10.1016/j.phpro.2012.01.024.

(85) Kavun, V. Ya.; Ryabov, A. I.; Telin, I. A.; Podgorbunskii, A. B.; Sinebryukhov, S. L.; Gnedenkov, S. V.; Goncharuk, V. K. NMR and Impedance Spectroscopy Data on the Ionic Mobility and Conductivity in PbSnF4 Doped with Alkali Metal Fluoride. *J Struct Chem* **2012**, *53* (2), 290–294. https://doi.org/10.1134/S0022476612020126.

(86) Kavun, V. Ya.; Uvarov, N. F.; Telin, I. A.; Polyantsev, M. M.; Podgorbunskii, A. B.; Brovkina, O. V.; Goncharuk, B. K. Ionic Mobility and Conductivity in PbSnF4 Doped with CaF2 from the NMR and Impedance Spectroscopy Data. *J Struct Chem* **2016**, *57* (2), 330–337. https://doi.org/10.1134/S002247661602013X.

(87) Zang, Z.; Liu, L.; Yang, L.; Luo, K.; Zou, C.; Chen, X.; Tao, X.; Luo, Z.; Chang, B.; Wang, X. Preparation and Performance of Eu^{3+}-Doped $BaSnF_4$-Based Solid-State Electrolytes for Room-Temperature Fluoride-Ion Batteries. *ACS Sustainable Chem. Eng.* **2021**, acssuschemeng.1c04523. https://doi.org/10.1021/acssuschemeng.1c04523.

(88) Liu, L.; Yang, L.; Shao, D.; Luo, K.; Zou, C.; Luo, Z.; Wang, X. Nd3+ Doped BaSnF4 Solid Electrolyte for Advanced Room-Temperature Solid-State Fluoride Ion Batteries.

Ceramics International **2020**, *46* (12), 20521–20528. https://doi.org/10.1016/j.ceramint.2020.05.161.

(89) Xiong, L.; Wen, P.; Zhang, Y.; Liu, X.; Ning, J.; Wang, X.; Wang, H.; Yang, Z. Exploring Efficient Solid Electrolyte Based on Nd Doped BaSnF4 for Fluoride-Ion Batteries at Atomic Scale. *Journal of Power Sources* **2022**, *518*, 230718. https://doi.org/10.1016/j.jpowsour.2021.230718.

(90) Zang, Z.; Liu, J.; Tao, X.; Zou, C.; Chen, X.; Yi, L.; Chang, B.; Wang, X. Mn2+ Doped BaSnF4-Based Solid State Electrolyte for Room-Temperature Fluoride Ion Batteries. *Journal of Electroanalytical Chemistry* **2023**, *930*, 117145. https://doi.org/10.1016/j.jelechem.2023.117145.

(91) Molaiyan, P.; Witter, R. Crystal Phase and Surface Defect Driven Synthesis of Pb1−xSnxF2 Solid Solution Electrolyte for Fluoride Ion Batteries. *Journal of Electroanalytical Chemistry* **2019**, *845*, 154–159. https://doi.org/10.1016/j.jelechem.2019.04.063.

(92) Yamamoto, O. Solid Oxide Fuel Cells: Fundamental Aspects and Prospects. *Electrochimica Acta* **2000**, *45* (15), 2423–2435. https://doi.org/10.1016/S0013-4686(00)00330-3.

(93) Goodenough, J. B.; Singh, P. Review—Solid Electrolytes in Rechargeable Electrochemical Cells. *J. Electrochem. Soc.* **2015**, *162* (14), A2387. https://doi.org/10.1149/2.0021514jes.

(94) Bachman, J. C.; Muy, S.; Grimaud, A.; Chang, H.-H.; Pour, N.; Lux, S. F.; Paschos, O.; Maglia, F.; Lupart, S.; Lamp, P.; Giordano, L.; Shao-Horn, Y. Inorganic Solid-State Electrolytes for Lithium Batteries: Mechanisms and Properties Governing Ion Conduction. *Chem. Rev.* **2016**, *116* (1), 140–162. https://doi.org/10.1021/acs.chemrev.5b00563.

(95) Culver, S. P.; Squires, A. G.; Minafra, N.; Armstrong, C. W. F.; Krauskopf, T.; Böcher, F.; Li, C.; Morgan, B. J.; Zeier, W. G. Evidence for a Solid-Electrolyte Inductive Effect in the Superionic Conductor Li10Ge1–xSnxP2S12. *J. Am. Chem. Soc.* **2020**, *142* (50), 21210–21219. https://doi.org/10.1021/jacs.0c10735.

(96) Kraft, M. A.; Ohno, S.; Zinkevich, T.; Koerver, R.; Culver, S. P.; Fuchs, T.; Senyshyn, A.; Indris, S.; Morgan, B. J.; Zeier, W. G. Inducing High Ionic Conductivity in the Lithium Superionic Argyrodites Li6+xP1–xGexS5I for All-Solid-State Batteries. *J. Am. Chem. Soc.* **2018**, *140* (47), 16330–16339. https://doi.org/10.1021/jacs.8b10282.

(97) He, X.; Zhu, Y.; Mo, Y. Origin of Fast Ion Diffusion in Super-Ionic Conductors. *Nat Commun* **2017**, *8* (1), 15893. https://doi.org/10.1038/ncomms15893.

(98) Burbano, M.; Carlier, D.; Boucher, F.; Morgan, B. J.; Salanne, M. Sparse Cyclic Excitations Explain the Low Ionic Conductivity of Stoichiometric ${\mathrm{Li}}_{7}{\mathrm{La}}_{3}{\mathrm{Zr}}_{2}{\mathrm{O}}_{12}$. *Phys. Rev. Lett.* **2016**, *116* (13), 135901. https://doi.org/10.1103/PhysRevLett.116.135901.

(99) Morgan, B. J. Mechanistic Origin of Superionic Lithium Diffusion in Anion-Disordered Li6PS5X Argyrodites. *Chem. Mater.* **2021**, *33* (6), 2004–2018. https://doi.org/10.1021/acs.chemmater.0c03738.

(100) Kim, K.; Siegel, D. J. Correlating Lattice Distortions, Ion Migration Barriers, and Stability in Solid Electrolytes. *J. Mater. Chem. A* **2019**, *7* (7), 3216–3227. https://doi.org/10.1039/C8TA10989C.

(101) Xiao, Y.; Jun, K.; Wang, Y.; Miara, L. J.; Tu, Q.; Ceder, G. Lithium Oxide Superionic Conductors Inspired by Garnet and NASICON Structures. *Advanced Energy Materials* **2021**, *11* (37), 2101437. https://doi.org/10.1002/aenm.202101437.

(102) Morgan, B. J. Understanding Fast-Ion Conduction in Solid Electrolytes. *Philosophical Transactions of the Royal Society A: Mathematical, Physical and Engineering Sciences* **2021**, *379* (2211), 20190451. https://doi.org/10.1098/rsta.2019.0451.

(103) Wood, B. C.; Varley, J. B.; Kweon, K. E.; Shea, P.; Hall, A. T.; Grieder, A.; Ward, M.; Aguirre, V. P.; Rigling, D.; Lopez Ventura, E.; Stancill, C.; Adelstein, N. Paradigms of Frustration in Superionic Solid Electrolytes. *Philosophical Transactions of the Royal Society A: Mathematical, Physical and Engineering Sciences* **2021**, *379* (2211), 20190467. https://doi.org/10.1098/rsta.2019.0467.

(104) Zeng, Y.; Ouyang, B.; Liu, J.; Byeon, Y.-W.; Cai, Z.; Miara, L. J.; Wang, Y.; Ceder, G. High-Entropy Mechanism to Boost Ionic Conductivity. *Science* **2022**, *378* (6626), 1320–1324. https://doi.org/10.1126/science.abq1346.

(105) Wang, S.; Liu, Y.; Mo, Y. Frustration in Super-Ionic Conductors Unraveled by the Density of Atomistic States. *Angewandte Chemie* **2023**, *135* (15), e202215544. https://doi.org/10.1002/ange.202215544.

(106) Di Stefano, D.; Miglio, A.; Robeyns, K.; Filinchuk, Y.; Lechartier, M.; Senyshyn, A.; Ishida, H.; Spannenberger, S.; Prutsch, D.; Lunghammer, S.; Rettenwander, D.; Wilkening, M.; Roling, B.; Kato, Y.; Hautier, G. Superionic Diffusion through Frustrated Energy Landscape. *Chem* **2019**, *5* (9), 2450–2460. https://doi.org/10.1016/j.chempr.2019.07.001.

(107) Jun, K.; Sun, Y.; Xiao, Y.; Zeng, Y.; Kim, R.; Kim, H.; Miara, L. J.; Im, D.; Wang, Y.; Ceder, G. Lithium Superionic Conductors with Corner-Sharing Frameworks. *Nat. Mater.* **2022**, *21* (8), 924–931. https://doi.org/10.1038/s41563-022-01222-4.

(108) Wang, Y.; Richards, W. D.; Ong, S. P.; Miara, L. J.; Kim, J. C.; Mo, Y.; Ceder, G. Design Principles for Solid-State Lithium Superionic Conductors. *Nature Mater* **2015**, *14* (10), 1026–1031. https://doi.org/10.1038/nmat4369.

(109) He, X.; Bai, Q.; Liu, Y.; Nolan, A. M.; Ling, C.; Mo, Y. Crystal Structural Framework of Lithium Super-Ionic Conductors. *Advanced Energy Materials* **2019**, *9* (43), 1902078. https://doi.org/10.1002/aenm.201902078.

(110) Zhang, Z.; Li, H.; Kaup, K.; Zhou, L.; Roy, P.-N.; Nazar, L. F. Targeting Superionic Conductivity by Turning on Anion Rotation at Room Temperature in Fast Ion Conductors. *Matter* **2020**, *2* (6), 1667–1684. https://doi.org/10.1016/j.matt.2020.04.027.

(111) Hull, S.; Keen, D. A.; Madden, P. A.; Wilson, M. Ionic Diffusion within the A* and β Phases of Ag3SI. *J. Phys.: Condens. Matter* **2007**, *19* (40), 406214. https://doi.org/10.1088/0953-8984/19/40/406214.

(112) Zhang, Y.; Zhao, Y.; Chen, C. Ab Initio Study of the Stabilities of and Mechanism of Superionic Transport in Lithium-Rich Antiperovskites. *Phys. Rev. B* **2013**, *87* (13), 134303. https://doi.org/10.1103/PhysRevB.87.134303.

(113) Düvel, A.; Heitjans, P.; Fedorov, P.; Scholz, G.; Cibin, G.; Chadwick, A. V.; Pickup, D. M.; Ramos, S.; Sayle, L. W. L.; Sayle, E. K. L.; Sayle, T. X. T.; Sayle, D. C. Is Geometric Frustration-Induced Disorder a Recipe for High Ionic Conductivity? *J. Am. Chem. Soc.* **2017**, *139* (16), 5842–5848. https://doi.org/10.1021/jacs.7b00502.

(114) Breuer, S.; Wilkening, M. Mismatch in Cation Size Causes Rapid Anion Dynamics in Solid Electrolytes: The Role of the Arrhenius Pre-Factor. *Dalton Trans.* **2018**, *47* (12), 4105–4117. https://doi.org/10.1039/C7DT04487A.

(115) Schlem, R.; Muy, S.; Prinz, N.; Banik, A.; Shao-Horn, Y.; Zobel, M.; Zeier, W. G. Mechanochemical Synthesis: A Tool to Tune Cation Site Disorder and Ionic Transport Properties of Li3MCl6 (M = Y, Er) Superionic Conductors. *Advanced Energy Materials* **2020**, *10* (6), 1903719. https://doi.org/10.1002/aenm.201903719.

(116) Gautam, A.; Sadowski, M.; Ghidiu, M.; Minafra, N.; Senyshyn, A.; Albe, K.; Zeier, W. G. Engineering the Site-Disorder and Lithium Distribution in the Lithium Superionic Argyrodite Li6PS5Br. *Advanced Energy Materials* **2021**, *11* (5), 2003369. https://doi.org/10.1002/aenm.202003369.

(117) Minafra, N.; Kraft, M. A.; Bernges, T.; Li, C.; Schlem, R.; Morgan, B. J.; Zeier, W. G. Local Charge Inhomogeneity and Lithium Distribution in the Superionic Argyrodites Li6PS5X (X = Cl, Br, I). *Inorg. Chem.* **2020**, *59* (15), 11009–11019. https://doi.org/10.1021/acs.inorgchem.0c01504.

(118) Gombotz, M.; Hanghofer, I.; Eisbacher-Lubensky, S.; Wilkening, H. M. R. Ionic and Electronic Transport in the Fast Ag+ Conductor A*-Ag3SI. *Solid State Sciences* **2021**, *118*, 106680. https://doi.org/10.1016/j.solidstatesciences.2021.106680.

(119) Zheng, J.; Fang, H.; Fan, L.; Ren, Y.; Jena, P.; Wu, Y. Antiperovskite K3OI for K-Ion Solid State Electrolyte. *J. Phys. Chem. Lett.* **2021**, *12* (30), 7120–7126. https://doi.org/10.1021/acs.jpclett.1c01807.

(120) Symington, A. R.; Purton, J.; Statham, J.; Molinari, M.; Islam, M. S.; Parker, S. C. Quantifying the Impact of Disorder on Li-Ion and Na-Ion Transport in Perovskite Titanate Solid Electrolytes for Solid-State Batteries. *J. Mater. Chem. A* **2020**, *8* (37), 19603–19611. https://doi.org/10.1039/D0TA05343K.

(121) Gautam, A.; Sadowski, M.; Prinz, N.; Eickhoff, H.; Minafra, N.; Ghidiu, M.; Culver, S. P.; Albe, K.; Fässler, T. F.; Zobel, M.; Zeier, W. G. Rapid Crystallization and Kinetic Freezing of Site-Disorder in the Lithium Superionic Argyrodite Li6PS5Br. *Chem. Mater.* **2019**, *31* (24), 10178–10185. https://doi.org/10.1021/acs.chemmater.9b03852.

(122) Düvel, A.; Ruprecht, B.; Heitjans, P.; Wilkening, M. Mixed Alkaline-Earth Effect in the Metastable Anion Conductor Ba1–xCaxF2 ($0 \leq x \leq 1$): Correlating Long-Range Ion Transport with Local Structures Revealed by Ultrafast 19F MAS NMR. *J. Phys. Chem. C* **2011**, *115* (48), 23784–23789. https://doi.org/10.1021/jp208472f.

(123) Haarmann, L.; Albe, K. From Ionic to Superionic Conductivity: The Influence of Cation Order on Sodium Diffusion in Na3Zr2Si2PO12. *Solid State Ionics* **2021**, *363*, 115604. https://doi.org/10.1016/j.ssi.2021.115604.

(124) Hogrefe, K.; Minafra, N.; Hanghofer, I.; Banik, A.; Zeier, W. G.; Wilkening, H. M. R. Opening Diffusion Pathways through Site Disorder: The Interplay of Local Structure and Ion Dynamics in the Solid Electrolyte Li6+xP1–xGexS5I as Probed by Neutron Diffraction and NMR. *J. Am. Chem. Soc.* **2022**, *144* (4), 1795–1812. https://doi.org/10.1021/jacs.1c11571.

(125) Hanghofer, I.; Brinek, M.; Eisbacher, S. L.; Bitschnau, B.; Volck, M.; Hennige, V.; Hanzu, I.; Rettenwander, D.; Wilkening, H. M. R. Substitutional Disorder: Structure and Ion Dynamics of the Argyrodites Li6PS5Cl, Li6PS5Br and Li6PS5I. *Phys. Chem. Chem. Phys.* **2019**, *21* (16), 8489–8507. https://doi.org/10.1039/C9CP00664H.

(126) Maughan, A. E.; Ha, Y.; Pekarek, R. T.; Schulze, M. C. Lowering the Activation Barriers for Lithium-Ion Conductivity through Orientational Disorder in the Cyanide Argyrodite Li6PS5CN. *Chem. Mater.* **2021**, *33* (13), 5127–5136. https://doi.org/10.1021/acs.chemmater.1c01170.

(127) Wang, F.; Evans, H. A.; Kim, K.; Yin, L.; Li, Y.; Tsai, P.-C.; Liu, J.; Lapidus, S. H.; Brown, C. M.; Siegel, D. J.; Chiang, Y.-M. Dynamics of Hydroxyl Anions Promotes Lithium Ion Conduction in Antiperovskite Li2OHCl. *Chem. Mater.* **2020**, *32* (19), 8481–8491. https://doi.org/10.1021/acs.chemmater.0c02602.

(128) Zhang, Z.; Nazar, L. F. Exploiting the Paddle-Wheel Mechanism for the Design of Fast Ion Conductors. *Nat Rev Mater* **2022**, *7* (5), 389–405. https://doi.org/10.1038/s41578-021-00401-0.

(129) Scholz, T.; Schneider, C.; Terban, M. W.; Deng, Z.; Eger, R.; Etter, M.; Dinnebier, R. E.; Canepa, P.; Lotsch, B. V. Superionic Conduction in the Plastic Crystal Polymorph of Na4P2S6. *ACS Energy Lett.* **2022**, *7* (4), 1403–1411. https://doi.org/10.1021/acsenergylett.1c02815.

(130) Smith, J. G.; Siegel, D. J. Ion Migration Mechanisms in the Sodium Sulfide Solid Electrolyte Na3–xSb1–xWxS4. *Chem. Mater.* **2022**, *34* (9), 4166–4171. https://doi.org/10.1021/acs.chemmater.2c00526.

(131) Gupta, M. K.; Ding, J.; Osti, N. C.; Abernathy, D. L.; Arnold, W.; Wang, H.; Hood, Z.; Delaire, O. Fast Na Diffusion and Anharmonic Phonon Dynamics in Superionic Na3PS4. *Energy Environ. Sci.* **2021**, *14* (12), 6554–6563. https://doi.org/10.1039/D1EE01509E.

(132) Tsai, P.-C.; Mair, S.; Smith, J.; Halat, D. M.; Chien, P.-H.; Kim, K.; Zhang, D.; Li, Y.; Yin, L.; Liu, J.; Lapidus, S. H.; Reimer, J. A.; Balsara, N. P.; Siegel, D. J.; Chiang, Y.-M. Double Paddle-Wheel Enhanced Sodium Ion Conduction in an Antiperovskite Solid Electrolyte. *Advanced Energy Materials* **2023**, *13* (7), 2203284. https://doi.org/10.1002/aenm.202203284.

(133) Jørgensen, M.; Shea, P. T.; Tomich, A. W.; Varley, J. B.; Bercx, M.; Lovera, S.; Černý, R.; Zhou, W.; Udovic, T. J.; Lavallo, V.; Jensen, T. R.; Wood, B. C.; Stavila, V. Understanding Superionic Conductivity in Lithium and Sodium Salts of Weakly Coordinating Closo-Hexahalocarbaborate Anions. *Chem. Mater.* **2020**, *32* (4), 1475–1487. https://doi.org/10.1021/acs.chemmater.9b04383.

(134) Zhang, Z.; Roy, P.-N.; Li, H.; Avdeev, M.; Nazar, L. F. Coupled Cation–Anion Dynamics Enhances Cation Mobility in Room-Temperature Superionic Solid-State Electrolytes. *J. Am. Chem. Soc.* **2019**, *141* (49), 19360–19372. https://doi.org/10.1021/jacs.9b09343.

(135) Laurita, G.; Seshadri, R. Chemistry, Structure, and Function of Lone Pairs in Extended Solids. *Acc. Chem. Res.* **2022**, *55* (7), 1004–1014. https://doi.org/10.1021/acs.accounts.1c00741.

(136) Waghmare, U. V.; Spaldin, N. A.; Kandpal, H. C.; Seshadri, R. First-Principles Indicators of Metallicity and Cation off-Centricity in the IV-VI Rocksalt Chalcogenides of Divalent Ge, Sn, and Pb. *Phys. Rev. B* **2003**, *67* (12), 125111. https://doi.org/10.1103/PhysRevB.67.125111.

(137) Walsh, A.; Payne, D. J.; Egdell, R. G.; Watson, G. W. Stereochemistry of Post-Transition Metal Oxides: Revision of the Classical Lone Pair Model. *Chem. Soc. Rev.* **2011**, *40* (9), 4455–4463. https://doi.org/10.1039/C1CS15098G.

(138) Avdeev, M.; Haas, M. K.; Jorgensen, J. D.; Cava, R. J. Static Disorder from Lone-Pair Electrons in Bi2−xMxRu2O7−y(M=Cu,Co;X=0,0.4) Pyrochlores. *Journal of Solid State Chemistry* **2002**, *169* (1), 24–34. https://doi.org/10.1016/S0022-4596(02)00007-5.

(139) Seshadri, R. Lone Pairs in Insulating Pyrochlores: Ice Rules and High-k Behavior. *Solid State Sciences* **2006**, *8* (3), 259–266. https://doi.org/10.1016/j.solidstatesciences.2006.02.020.

(140) Fabini, D. H.; Laurita, G.; Bechtel, J. S.; Stoumpos, C. C.; Evans, H. A.; Kontos, A. G.; Raptis, Y. S.; Falaras, P.; Van der Ven, A.; Kanatzidis, M. G.; Seshadri, R. Dynamic Stereochemical Activity of the Sn2+ Lone Pair in Perovskite CsSnBr3. *J. Am. Chem. Soc.* **2016**, *138* (36), 11820–11832. https://doi.org/10.1021/jacs.6b06287.

(141)Zhang, J.; Ishikawa, D.; Koza, M. M.; Nishibori, E.; Song, L.; Baron, A. Q. R.; Iversen, B. B. Dynamic Lone Pair Expression as Chemical Bonding Origin of Giant Phonon Anharmonicity in Thermoelectric InTe. *Angewandte Chemie International Edition* **2023**, *62* (13), e202218458. https://doi.org/10.1002/anie.202218458.

(142)Fabini, D. H.; Seshadri, R.; Kanatzidis, M. G. The Underappreciated Lone Pair in Halide Perovskites Underpins Their Unusual Properties. *MRS Bulletin* **2020**, *45* (6), 467–477. https://doi.org/10.1557/mrs.2020.142.

(143)Remsing, R. C.; Klein, M. L. A New Perspective on Lone Pair Dynamics in Halide Perovskites. *APL Materials* **2020**, *8* (5), 050902. https://doi.org/10.1063/5.0001908.

(144)Carnevali, V.; Mukherjee, S.; Voneshen, D. J.; Maji, K.; Guilmeau, E.; Powell, A. V.; Vaqueiro, P.; Fornari, M. Lone Pair Rotation and Bond Heterogeneity Leading to Ultralow Thermal Conductivity in Aikinite. *J. Am. Chem. Soc.* **2023**, *145* (16), 9313–9325. https://doi.org/10.1021/jacs.3c02536.

(145)Mairesse, G. Bismuth-Based Oxide Conductors Novel Structural and Electrical Features. In *Fast Ion Transport in Solids*; Scrosati, B., Magistris, A., Mari, C. M., Mariotto, G., Eds.; NATO ASI Series; Springer Netherlands: Dordrecht, 1993; pp 271–290. https://doi.org/10.1007/978-94-011-1916-0_15.

(146)Chaudhuri, S.; Castiglione, M.; Wang, F.; Wilson, M.; Madden, P. A.; Grey, C. P. Study of Fluoride Ion Motions in PbSnF4 and BaSnF4 Compounds With Molecular Dynamics Simulation and Solid State NMR Techniques. *MRS Online Proceedings Library* **2001**, *658* (1), 109. https://doi.org/10.1557/PROC-658-GG10.9.

(147)Castiglione, M. J.; Madden, P. A. Fluoride Ion Disorder and Clustering in Superionic PbF2. *J. Phys.: Condens. Matter* **2001**, *13* (44), 9963. https://doi.org/10.1088/0953-8984/13/44/311.

(148)Chaudhuri, S.; Wang, F.; Grey, C. P. Resolving the Different Dynamics of the Fluorine Sublattices in the Anionic Conductor BaSnF4 by Using High-Resolution MAS NMR Techniques. *J. Am. Chem. Soc.* **2002**, *124* (39), 11746–11757. https://doi.org/10.1021/ja026155j.

(149)Dénès, G.; Madamba, M. C.; Muntasar, A.; Peroutka, A.; Tam, K.; Zhu, Z. Fluoride-Ion Conductors Derived from the Fluorite Type. In *Mössbauer Spectroscopy in Materials Science*; Miglierini, M., Petridis, D., Eds.; NATO Science Series; Springer Netherlands: Dordrecht, 1999; pp 25–38. https://doi.org/10.1007/978-94-011-4548-0_3.

(150)Dénès, G.; Madamba, M. C.; Merazig, H.; Muntasar, A.; Zhu, Z. Site Distortions Created by the Stereoactive Lone Pair of Tin(II) in Highly Symmetric Structures. *AIP Conference Proceedings* **2016**, *1781* (1), 020006. https://doi.org/10.1063/1.4966002.

(151)Mohammad, I.; Chable, J.; Witter, R.; Fichtner, M.; Reddy, M. A. Synthesis of Fast Fluoride-Ion-Conductive Fluorite-Type Ba1−xSbxF2+x (0.1 ≤ x ≤ 0.4): A Potential Solid Electrolyte for Fluoride-Ion Batteries. *ACS Appl. Mater. Interfaces* **2018**, *10* (20), 17249–17256. https://doi.org/10.1021/acsami.8b04108.

(152) Ahmad, M. M.; Yamane, Y.; Yamada, K. Structure, Ionic Conduction, and Giant Dielectric Properties of Mechanochemically Synthesized BaSnF4. *Journal of Applied Physics* **2009**, *106* (7), 074106. https://doi.org/10.1063/1.3234393.

(153) Juan Rodríguez-Carvajal. Recent Advances in Magnetic Structure Determination by Neutron Powder Diffraction. *Physica B : Condensed Matter* **1993**, *1–2* (192), 55–69. https://doi.org/10.1016/0921-4526(93)90108-I.

(154) Thompson, P.; Cox, D. E.; Hastings, J. B. Rietveld Refinement of Debye–Scherrer Synchrotron X-Ray Data from Al2O3. *Journal of Applied Crystallography* **1987**, *20* (2), 79–83. https://doi.org/10.1107/S0021889887087090.

(155) Wissenschaftliche Elektronik GmbH - WinNormos for Igor. http://www.wissel-gmbh.de/index.php?option=com_content&task=view&id=55&Itemid=116 (accessed 2023-08-16).

(156) Thurber, K. R.; Tycko, R. Measurement of Sample Temperatures under Magic-Angle Spinning from the Chemical Shift and Spin-Lattice Relaxation Rate of 79Br in KBr Powder. *Journal of Magnetic Resonance* **2009**, *196* (1), 84–87. https://doi.org/10.1016/j.jmr.2008.09.019.

(157) Massiot, D.; Fayon, F.; Capron, M.; King, I.; Le Calvé, S.; Alonso, B.; Durand, J.-O.; Bujoli, B.; Gan, Z.; Hoatson, G. Modelling One- and Two-Dimensional Solid-State NMR Spectra. *Magnetic Resonance in Chemistry* **2002**, *40* (1), 70–76. https://doi.org/10.1002/mrc.984.

(158) FIT2D: An Introduction and Overview. https://www.esrf.fr/computing/scientific/FIT2D/FIT2D_INTRO/fit2d.html (accessed 2023-08-16).

(159) Farrow, C. L.; Juhas, P.; Liu, J. W.; Bryndin, D.; Božin, E. S.; Bloch, J.; Proffen, T.; Billinge, S. J. L. PDFfit2 and PDFgui: Computer Programs for Studying Nanostructure in Crystals. *J. Phys.: Condens. Matter* **2007**, *19* (33), 335219. https://doi.org/10.1088/0953-8984/19/33/335219.

(160) Kresse, G.; Furthmüller, J. Efficiency of Ab-Initio Total Energy Calculations for Metals and Semiconductors Using a Plane-Wave Basis Set. *Computational Materials Science* **1996**, *6* (1), 15–50. https://doi.org/10.1016/0927-0256(96)00008-0.

(161) Kresse, G.; Furthmüller, J. Efficient Iterative Schemes for Ab Initio Total-Energy Calculations Using a Plane-Wave Basis Set. *Phys. Rev. B* **1996**, *54* (16), 11169–11186. https://doi.org/10.1103/PhysRevB.54.11169.

(162) Kresse, G.; Joubert, D. From Ultrasoft Pseudopotentials to the Projector Augmented-Wave Method. *Phys. Rev. B* **1999**, *59* (3), 1758–1775. https://doi.org/10.1103/PhysRevB.59.1758.

(163) Perdew, J. P.; Ruzsinszky, A.; Csonka, G. I.; Vydrov, O. A.; Scuseria, G. E.; Constantin, L. A.; Zhou, X.; Burke, K. Restoring the Density-Gradient Expansion for Exchange in

Solids and Surfaces. *Phys. Rev. Lett.* **2008**, *100* (13), 136406. https://doi.org/10.1103/PhysRevLett.100.136406.

(164)Blöchl, P. E. Projector Augmented-Wave Method. *Phys. Rev. B* **1994**, *50* (24), 17953–17979. https://doi.org/10.1103/PhysRevB.50.17953.

(165)Ångqvist, M.; Muñoz, W. A.; Rahm, J. M.; Fransson, E.; Durniak, C.; Rozyczko, P.; Rod, T. H.; Erhart, P. ICET – A Python Library for Constructing and Sampling Alloy Cluster Expansions. *Advanced Theory and Simulations* **2019**, *2* (7), 1900015. https://doi.org/10.1002/adts.201900015.

(166)Zunger, A.; Wei, S.-H.; Ferreira, L. G.; Bernard, J. E. Special Quasirandom Structures. *Phys. Rev. Lett.* **1990**, *65* (3), 353–356. https://doi.org/10.1103/PhysRevLett.65.353.

(167)Wei, S.-H.; Ferreira, L. G.; Bernard, J. E.; Zunger, A. Electronic Properties of Random Alloys: Special Quasirandom Structures. *Phys. Rev. B* **1990**, *42* (15), 9622–9649. https://doi.org/10.1103/PhysRevB.42.9622.

(168)Keys, A. S.; Hedges, L. O.; Garrahan, J. P.; Glotzer, S. C.; Chandler, D. Excitations Are Localized and Relaxation Is Hierarchical in Glass-Forming Liquids. *Phys. Rev. X* **2011**, *1* (2), 021013. https://doi.org/10.1103/PhysRevX.1.021013.

(169)Stillinger, F. H.; Weber, T. A. Packing Structures and Transitions in Liquids and Solids. *Science* **1984**, *225* (4666), 983–989. https://doi.org/10.1126/science.225.4666.983.

(170)Heuer, A. Exploring the Potential Energy Landscape of Glass-Forming Systems: From Inherent Structures via Metabasins to Macroscopic Transport. *J. Phys.: Condens. Matter* **2008**, *20* (37), 373101. https://doi.org/10.1088/0953-8984/20/37/373101.

(171)Silvi, B.; Savin, A. Classification of Chemical Bonds Based on Topological Analysis of Electron Localization Functions. *Nature* **1994**, *371* (6499), 683–686. https://doi.org/10.1038/371683a0.

(172)Marzari, N.; Mostofi, A. A.; Yates, J. R.; Souza, I.; Vanderbilt, D. Maximally Localized Wannier Functions: Theory and Applications. *Rev. Mod. Phys.* **2012**, *84* (4), 1419–1475. https://doi.org/10.1103/RevModPhys.84.1419.

(173)Pizzi, G.; Vitale, V.; Arita, R.; Blügel, S.; Freimuth, F.; Géranton, G.; Gibertini, M.; Gresch, D.; Johnson, C.; Koretsune, T.; Ibañez-Azpiroz, J.; Lee, H.; Lihm, J.-M.; Marchand, D.; Marrazzo, A.; Mokrousov, Y.; Mustafa, J. I.; Nohara, Y.; Nomura, Y.; Paulatto, L.; Poncé, S.; Ponweiser, T.; Qiao, J.; Thöle, F.; Tsirkin, S. S.; Wierzbowska, M.; Marzari, N.; Vanderbilt, D.; Souza, I.; Mostofi, A. A.; Yates, J. R. Wannier90 as a Community Code: New Features and Applications. *J. Phys.: Condens. Matter* **2020**, *32* (16), 165902. https://doi.org/10.1088/1361-648X/ab51ff.

(174)Bernasconi, L.; Wilson, M.; Madden, P. A. Cation Polarizability from First-Principles: Sn2+. *Computational Materials Science* **2001**, *22* (1), 94–98. https://doi.org/10.1016/S0927-0256(01)00173-2.

(175)Coles, S. RevelsMD, 2023. https://github.com/user200000/revelsmd (accessed 2023-08-16).

(176)Morgan, B. Site-Analysis, 2021. https://github.com/bjmorgan/site-analysis (accessed 2022-07-15).

(177)Larsen, A. H.; Mortensen, J. J.; Blomqvist, J.; Castelli, I. E.; Christensen, R.; Du\lak, M.; Friis, J.; Groves, M. N.; Hammer, B.; Hargus, C.; Hermes, E. D.; Jennings, P. C.; Jensen, P. B.; Kermode, J.; Kitchin, J. R.; Kolsbjerg, E. L.; Kubal, J.; Kaasbjerg, K.; Lysgaard, S.; Maronsson, J. B.; Maxson, T.; Olsen, T.; Pastewka, L.; Peterson, A.; Rostgaard, C.; Schiøtz, J.; Schütt, O.; Strange, M.; Thygesen, K. S.; Vegge, T.; Vilhelmsen, L.; Walter, M.; Zeng, Z.; Jacobsen, K. W. The Atomic Simulation Environment—a Python Library for Working with Atoms. *J. Phys.: Condens. Matter* **2017**, *29* (27), 273002. https://doi.org/10.1088/1361-648X/aa680e.

(178)Ong, S. P.; Richards, W. D.; Jain, A.; Hautier, G.; Kocher, M.; Cholia, S.; Gunter, D.; Chevrier, V. L.; Persson, K. A.; Ceder, G. Python Materials Genomics (Pymatgen): A Robust, Open-Source Python Library for Materials Analysis. *Computational Materials Science* **2013**, *68*, 314–319. https://doi.org/10.1016/j.commatsci.2012.10.028.

(179)Harris, C. R.; Millman, K. J.; van der Walt, S. J.; Gommers, R.; Virtanen, P.; Cournapeau, D.; Wieser, E.; Taylor, J.; Berg, S.; Smith, N. J.; Kern, R.; Picus, M.; Hoyer, S.; van Kerkwijk, M. H.; Brett, M.; Haldane, A.; del Río, J. F.; Wiebe, M.; Peterson, P.; Gérard-Marchant, P.; Sheppard, K.; Reddy, T.; Weckesser, W.; Abbasi, H.; Gohlke, C.; Oliphant, T. E. Array Programming with NumPy. *Nature* **2020**, *585* (7825), 357–362. https://doi.org/10.1038/s41586-020-2649-2.

(180)Virtanen, P.; Gommers, R.; Oliphant, T. E.; Haberland, M.; Reddy, T.; Cournapeau, D.; Burovski, E.; Peterson, P.; Weckesser, W.; Bright, J.; van der Walt, S. J.; Brett, M.; Wilson, J.; Millman, K. J.; Mayorov, N.; Nelson, A. R. J.; Jones, E.; Kern, R.; Larson, E.; Carey, C. J.; Polat, İ.; Feng, Y.; Moore, E. W.; VanderPlas, J.; Laxalde, D.; Perktold, J.; Cimrman, R.; Henriksen, I.; Quintero, E. A.; Harris, C. R.; Archibald, A. M.; Ribeiro, A. H.; Pedregosa, F.; van Mulbregt, P. SciPy 1.0: Fundamental Algorithms for Scientific Computing in Python. *Nat Methods* **2020**, *17* (3), 261–272. https://doi.org/10.1038/s41592-019-0686-2.

(181)Borgis, D.; Assaraf, R.; Rotenberg, B.; Vuilleumier, R. Computation of Pair Distribution Functions and Three-Dimensional Densities with a Reduced Variance Principle. *Molecular Physics* **2013**, *111* (22–23), 3486–3492. https://doi.org/10.1080/00268976.2013.838316.

(182)Coles, S. W.; Borgis, D.; Vuilleumier, R.; Rotenberg, B. Computing Three-Dimensional Densities from Force Densities Improves Statistical Efficiency. *J. Chem. Phys.* **2019**, *151* (6), 064124. https://doi.org/10.1063/1.5111697.

(183)Coles, S. W.; Mangaud, E.; Frenkel, D.; Rotenberg, B. Reduced Variance Analysis of Molecular Dynamics Simulations by Linear Combination of Estimators. *J. Chem. Phys.* **2021**, *154* (19), 191101. https://doi.org/10.1063/5.0053737.

(184) Faraday, M. Experimental Researches in Electricity. —Fifteenth Series. *Phil. Trans. R. Soc.* **1838**, *129* (129), 1–12. https://doi.org/10.1098/rstl.1839.0002.

(185) Reddy, M. A.; Fichtner, M. Batteries Based on Fluoride Shuttle. *Journal of Materials Chemistry* **2011**, *21* (43), 17059–17062. https://doi.org/10.1039/C1JM13535J.

(186) Rongeat, C.; Reddy, M. A.; Witter, R.; Fichtner, M. Nanostructured Fluorite-Type Fluorides As Electrolytes for Fluoride Ion Batteries. *J. Phys. Chem. C* **2013**, *117* (10), 4943–4950. https://doi.org/10.1021/jp3117825.

(187) Nowroozi, M. A.; Mohammad, I.; Molaiyan, P.; Wissel, K.; Munnangi, A. R.; Clemens, O. Fluoride Ion Batteries – Past, Present, and Future. *J. Mater. Chem. A* **2021**, 10.1039.D0TA11656D. https://doi.org/10.1039/D0TA11656D.

(188) Gopinadh, S. V.; Phanendra, P. V. R. L.; John, B.; Mercy, T. D. Fluoride-Ion Batteries: State-of-the-Art and Future Perspectives. *Sustainable Materials and Technologies* **2022**, *32*, e00436. https://doi.org/10.1016/j.susmat.2022.e00436.

(189) Franklin, A. D. Born Model Calculation of Defect Energies in CaF2. *Journal of Physics and Chemistry of Solids* **1968**, *29* (5), 823–841. https://doi.org/10.1016/0022-3697(68)90144-3.

(190) Catlow, C. R. A.; Norgett, M. J. Shell Model Calculations of the Energies of Formation of Point Defects in Alkaline Earth Fluorides. *J. Phys. C: Solid State Phys.* **1973**, *6* (8), 1325. https://doi.org/10.1088/0022-3719/6/8/002.

(191) Li, K.-D.; Xiao, H. Y.; Wang, L. M. Computer Simulation Study of Defect Formation and Migration Energy in Calcium Fluoride. *Nuclear Instruments and Methods in Physics Research Section B: Beam Interactions with Materials and Atoms* **2008**, *266* (12), 2698–2701. https://doi.org/10.1016/j.nimb.2008.03.101.

(192) Matar, S.; Réau, J.-M.; Lucat, C.; Grannec, J.; Hagenmuller, P. Synthese et Etude Des Proprietes de Conductivite Ionique Des Phases Appartenant Aux Systemes KBiF4 ⊠ BiF3 et RbBiF4 ⊠ BiF3. *Materials Research Bulletin* **1980**, *15* (9), 1295–1301. https://doi.org/10.1016/0025-5408(80)90034-3.

(193) Cox, P. A.; Catlow, C. R. A.; Chadwick, A. V. EXAFS and Molecular Modelling Studies of Rb1−xBixF1+2x. *JOURNAL OF MATERIALS SCIENCE* **1994**, *29* (10), 2725–2733. https://doi.org/10.1007/BF00356824.

(194) Netshisaulu, T. T.; Chadwick, A. V.; Ngoepe, P. E.; Catlow, C. R. A. Spectroscopic and Computer Modelling Studies of Mixed-Cation Superionic Fluorites. *J. Phys.: Condens. Matter* **2005**, *17* (41), 6575. https://doi.org/10.1088/0953-8984/17/41/026.

(195) Düvel, A. Ionic Conductivity and Structure of M1−xPbxF2 (M = Ca, Sr, Ba) Solid Solutions Prepared by Ball Milling. *Dalton Trans.* **2019**, *48* (3), 859–871. https://doi.org/10.1039/C8DT03759K.

(196)Catlow, C. R. A.; Moroney, L. M.; Tomlinson, S. M.; Chadwick, A. V.; Greaves, G. N. An EXAFS Study of the Effect of Temperature on Short Range Ordering in the Ionic Conductor, RbBiF4. In *EXAFS and Near Edge Structure III*; Hodgson, K. O., Hedman, B., Penner-Hahn, J. E., Eds.; Springer Proceedings in Physics; Springer: Berlin, Heidelberg, 1984; pp 435–438. https://doi.org/10.1007/978-3-642-46522-2_111.

(197)Dénès, G.; Madamba, M. C.; Muntasar, A.; Zhu, Z. Combined Use of Mössbauer Spectroscopy and X-Ray Diffraction for the Study of Order-Disorder in Tin(II)-Containing Fluoride Ion Conductors. *WIT Transactions on Engineering Sciences* **2005**, *51*, 279–288.

(198)De´ne`s, G. PbSn4F10: A New Disordered Fluorite-Type Fast Ion Conductor. *Journal of Solid State Chemistry* **1988**, *74* (2), 343–352. https://doi.org/10.1016/0022-4596(88)90364-7.

(199)Denes, G.; Yu, Y. H.; Tyliszczak, T.; Hitchcock, A. P. Sn-K and Pb-L3 EXAFS, X-Ray Diffraction, and 119Sn Mössbauer Spectroscopic Studies of Ordered β-PbSnF4 and Disordered Pb1-xSnxF2 (x = 0.3, 0.4) Solid Solutions and PbSn4F10: High Performance Fluoride Ion Conductors. *Journal of Solid State Chemistry* **1993**, *104* (2), 239–252. https://doi.org/10.1006/jssc.1993.1159.

(200)A. S. Radtke; G. E. Brown. Frankdicksonite, BaF2, a New Mineral from Nevada. *American Mineralogist* **1974**, *59*, 885–888.

(201)McDonald, R. C.; Hau, H. H. K.; Eriks, Klaas. Crystallographic Studies of Tin(II) Compounds. I. Crystal Structure of Tin(II) Fluoride, SnF2. *Inorg. Chem.* **1976**, *15* (4), 762–765. https://doi.org/10.1021/ic50158a003.

(202)Birchall, T.; Dines, G. Goldanskii-Karyagin Effect in α-SnF 2 : A Neutron Diffraction and Mössbauer Absorption Study. **1986**, *30*, 167–183.

(203)Catlow, C. R. A. Atomistic Mechanisms of Ionic Transport in Fast-Ion Conductors. *J. Chem. Soc., Faraday Trans.* **1990**, *86* (8), 1167–1176. https://doi.org/10.1039/FT9908601167.

(204)Soubeyroux, J. L.; Reau, J. M.; Matar, S.; Villeneuve, G.; Hagenmuller, P. Etude Par Diffraction Neutronique Des Solutions Solides K1−xBixF1+2xetRb1−xBixF1+2x. *Solid State Ionics* **1982**, *6* (1), 103–111. https://doi.org/10.1016/0167-2738(82)90102-3.

(205)Youngman, R. E.; Smith, C. M. Multinuclear NMR Studies of Mixed ${\text{Ca}}_{1\ensuremath{-}x}{\text{Sr}}_{x}{\text{F}}_{2}$ Crystals. *Phys. Rev. B* **2008**, *78* (1), 014112. https://doi.org/10.1103/PhysRevB.78.014112.

(206)Preishuber-Pflügl, F.; Wilkening, M. Mechanochemically Synthesized Fluorides: Local Structures and Ion Transport. *Dalton Trans.* **2016**, *45* (21), 8675–8687. https://doi.org/10.1039/C6DT00944A.

(207)Bräuniger, T.; Ghedia, S.; Jansen, M. Covalent Bonds in α-SnF2 Monitored by J-Couplings in Solid-State NMR Spectra. *Zeitschrift für anorganische und allgemeine Chemie* **2010**, *636* (13–14), 2399–2404. https://doi.org/10.1002/zaac.201000176.

(208)Neutron Diffraction Study of β-SnF2. *Zeitschrift für Kristallographie - Crystalline Materials* **1980**, *153* (1–2), 89–97. https://doi.org/10.1524/zkri.1980.0008.

(209)Wang, F.; Grey, C. P. Probing the Mechanism of Fluoride-Ion Conduction in LaF_3 and Strontium-Doped LaF_3 with High-Resolution ^{19}F MAS NMR. *Chem. Mater.* **1997**, *9* (5), 1068–1070. https://doi.org/10.1021/cm970044f.

(210)Leger, J. M.; Haines, J.; Atouf, A.; Schulte, O.; Hull, S. High-Pressure x-Ray- and Neutron-Diffraction Studies of ${\mathrm{BaF}}_{2}$: An Example of a Coordination Number of 11 in ${\mathit{AX}}_{2}$ Compounds. *Phys. Rev. B* **1995**, *52* (18), 13247–13256. https://doi.org/10.1103/PhysRevB.52.13247.

(211)Greis, O.; Petzel, T. Ein Beitrag zur Strukturchemie der Selten-Erd-Trifluoride. *Zeitschrift für anorganische und allgemeine Chemie* **1974**, *403* (1), 1–22. https://doi.org/10.1002/zaac.19744030102.

(212)Jean-Maurice Reau; Paul Hagenmuller. Fast Ionic Conductivity of Fluorine Anions with Fluorite- or Tysonite-Type Structures. *Reviews in Inorganic Chemistry* **1999**, *19* (1–2), 45–78. https://doi.org/10.1515/REVIC.1999.19.1-2.45.

(213)Achary, K. R.; Rao, Y. B.; Kamadurai, R. K.; Patro, L. N. Mechanochemical Synthesis and Fluoride Ion Conductivity Studies in SrSnF4 Polymorphs. *J. Phys. Chem. C* **2023**, *127* (16), 7816–7822. https://doi.org/10.1021/acs.jpcc.3c00056.

(214)Schwartz, H. L.; Miller, T. M.; Bederson, B. Measurement of the Static Electric Dipole Polarizabilities of Barium and Strontium. *Phys. Rev. A* **1974**, *10* (6), 1924–1926. https://doi.org/10.1103/PhysRevA.10.1924.

(215)Pooke, D. M.; Devine, S. D. Inner Displacement and the Internal Strain Tensor in the Fluorite Structure. *J. Phys. C: Solid State Phys.* **1984**, *17* (20), 3531–3543. https://doi.org/10.1088/0022-3719/17/20/006.

(216)Williamson, G. K.; Hall, W. H. X-Ray Line Broadening from Filed Aluminium and Wolfram. *Acta Metallurgica* **1953**, *1* (1), 22–31. https://doi.org/10.1016/0001-6160(53)90006-6.

(217)Maniammal, K.; Madhu, G.; Biju, V. X-Ray Diffraction Line Profile Analysis of Nanostructured Nickel Oxide: Shape Factor and Convolution of Crystallite Size and Microstrain Contributions. *Physica E: Low-dimensional Systems and Nanostructures* **2017**, *85*, 214–222. https://doi.org/10.1016/j.physe.2016.08.035.

(218)Wilkening, M.; Düvel, A.; Preishuber-Pflügl, F.; Da Silva, K.; Breuer, S.; Šepelák, V.; Heitjans, P. Structure and Ion Dynamics of Mechanosynthesized Oxides and Fluorides. *Zeitschrift für Kristallographie - Crystalline Materials* **2017**, *232* (1–3), 107–127. https://doi.org/10.1515/zkri-2016-1963.

(219)Düvel, A.; Wilkening, M.; Uecker, R.; Wegner, S.; Šepelák, V.; Heitjans, P. Mechanosynthesized Nanocrystalline BaLiF 3 : The Impact of Grain Boundaries and Structural Disorder on Ionic Transport. *Physical Chemistry Chemical Physics* **2010**, *12* (37), 11251–11262. https://doi.org/10.1039/C004530F.

(220)Lees, J. K.; Flinn, P. A. Mössbauer Effect in Tin Compounds: Interpretation of Isomer Shifts and Determination of the Nuclear Radius Change in 119Sn. *J. Chem. Phys.* **1968**, *48* (2), 882–889. https://doi.org/10.1063/1.1668729.

(221)Greenwood, N. N. *Mössbauer Spectroscopy*; Springer Science & Business Media, 2012.

(222)*Mössbauer Spectroscopy in Materials Science*; Miglierini, M., Petridis, D., Eds.; Springer Netherlands: Dordrecht, 1999. https://doi.org/10.1007/978-94-011-4548-0.

(223)Fournes, L.; Grannec, J.; Mirambet, C.; Lestienne, B.; Hagenmuller, P. Etude Par Re´sonance Mo¨ssbauer Des Fluorures Ternaires Du Syste`me SrF2SnF2. *Journal of Solid State Chemistry* **1991**, *93* (1), 30–36. https://doi.org/10.1016/0022-4596(91)90270-R.

(224)Voronin, B. M.; Volkov, S. V. Ionic Conductivity of Fluorite Type Crystals CaF2, SrF2, BaF2, and SrCl2 at High Temperatures. *Journal of Physics and Chemistry of Solids* **2001**, *62* (7), 1349–1358. https://doi.org/10.1016/S0022-3697(01)00036-1.

(225)Sadoc, A.; Body, M.; Legein, C.; Biswal, M.; Fayon, F.; Rocquefelte, X.; Boucher, F. NMR Parameters in Alkali, Alkaline Earth and Rare Earth Fluorides from First Principle Calculations. *Phys. Chem. Chem. Phys.* **2011**, *13* (41), 18539. https://doi.org/10.1039/c1cp21253b.

(226)Scheidecker, R. W.; Berard, M. F. Interdiffusion in the System SrF2-BaF2. *Journal of the American Ceramic Society* **1976**, *59* (9–10), 431–433. https://doi.org/10.1111/j.1151-2916.1976.tb09511.x.

(227)Vegard, L. Die Konstitution der Mischkristalle und die Raumfüllung der Atome. *Z. Physik* **1921**, *5* (1), 17–26. https://doi.org/10.1007/BF01349680.

(228)Zahn, D.; Heitjans, P.; Maier, J. From Composites to Solid Solutions: Modeling of Ionic Conductivity in the CaF $_2$ -BaF $_2$ System. *Chem. Eur. J.* **2012**, *18* (20), 6225–6229. https://doi.org/10.1002/chem.201102410.

(229)Dénès, G.; Birchall, T.; Sayer, M.; Bell, M. F. BaSnF4 — A New Fluoride Ionic Conductor with the α-PbSnF4 Structure. *Solid State Ionics* **1984**, *13* (3), 213–219. https://doi.org/10.1016/0167-2738(84)90032-8.

(230)Patro, L. N.; Ravi Chandra Raju, N.; Meher, S. R.; Kamala Bharathi, K. Physical Properties of High Performance Fluoride Ion Conductor BaSnF4 Thin Films by Pulsed Laser Deposition. *Appl. Phys. A* **2013**, *112* (3), 727–732. https://doi.org/10.1007/s00339-013-7767-3.

(231) Patro, L. N.; Hariharan, K. Influence of Synthesis Methodology on the Ionic Transport Properties of BaSnF4. *Materials Research Bulletin* **2011**, *46* (5), 732–737. https://doi.org/10.1016/j.materresbull.2011.01.010.

(232) Ahmad, M. M.; Yamane, Y.; Yamada, K. Structure, Ionic Conduction, and Giant Dielectric Properties of Mechanochemically Synthesized BaSnF4. *Journal of Applied Physics* **2009**, *106* (7), 074106. https://doi.org/10.1063/1.3234393.

(233) Dénès, G.; Milova, G.; Madamba, M. C.; Perfiliev, M. Structure and Ionic Transport of PbSnF4 Superionic Conductor. *Solid State Ionics* **1996**, *86–88*, 77–82. https://doi.org/10.1016/0167-2738(96)00094-X.

(234) Ito, Y.; Mukoyama, T.; Funatomi, H.; Yoshikado, S.; Tanaka, T. The Crystal Structure of Tetragonal Form PbSnF4. *Solid State Ionics* **1994**, *67* (3), 301–305. https://doi.org/10.1016/0167-2738(94)90021-3.

(235) Cavaliere, P.; Sadeghi, B.; Shabani, A. Spark Plasma Sintering: Process Fundamentals. In *Spark Plasma Sintering of Materials: Advances in Processing and Applications*; Cavaliere, P., Ed.; Springer International Publishing: Cham, 2019; pp 3–20. https://doi.org/10.1007/978-3-030-05327-7_1.

(236) Nadeina, A.; Rozier, P.; Seznec, V. Facile Synthesis of a Common Na-Ion Battery Cathode Material Na3V2(PO4)2F3 by Spark Plasma Sintering. *Energy Technology* **2020**, *8* (5), 1901304. https://doi.org/10.1002/ente.201901304.

(237) Lalère, F.; Leriche, J. B.; Courty, M.; Boulineau, S.; Viallet, V.; Masquelier, C.; Seznec, V. An All-Solid State NASICON Sodium Battery Operating at 200 °C. *Journal of Power Sources* **2014**, *247*, 975–980. https://doi.org/10.1016/j.jpowsour.2013.09.051.

(238) Mikami, M.; Kinemuchi, Y.; Kubo, K.; Uchiyama, N.; Miyazaki, H.; Nishino, Y. Flash-Sintering of Antimony Telluride and Its Thermoelectric Properties. *Journal of Applied Physics* **2018**, *124* (10), 105104. https://doi.org/10.1063/1.5041970.

(239) Mikami, M.; Miyazaki, H.; Nishino, Y. Suppressed Atomic Diffusion in Flash Sintering of Bismuth Telluride. *Journal of the European Ceramic Society* **2022**, *42* (10), 4233–4238. https://doi.org/10.1016/j.jeurceramsoc.2022.03.036.

(240) Gao, N. F.; Li, J. T.; Zhang, D.; Miyamoto, Y. Rapid Synthesis of Dense Ti3SiC2 by Spark Plasma Sintering. *Journal of the European Ceramic Society* **2002**, *22* (13), 2365–2370. https://doi.org/10.1016/S0955-2219(02)00021-3.

(241) Jeong, K.; Lee, H.; Lee, C.; Wook, L. H.; Kim, H.; Lee, E.; Cho, M.-H. Ferroelectric Switching in GeTe through Rotation of Lone-Pair Electrons by Electric Field-Driven Phase Transition. *Applied Materials Today* **2021**, *24*, 101122. https://doi.org/10.1016/j.apmt.2021.101122.

(242) Wang, P.; Huang, Z.; Morita, K.; Li, Q.; Yang, M.; Zhang, S.; Goto, T.; Tu, R. Influence of Spark Plasma Sintering Conditions on Microstructure, Carbon Contamination,

and Transmittance of CaF2 Ceramics. *Journal of the European Ceramic Society* **2022**, *42* (1), 245–257. https://doi.org/10.1016/j.jeurceramsoc.2021.10.004.

(243)Thompson, P.; Cox, D. E.; Hastings, J. B. Rietveld Refinement of Debye–Scherrer Synchrotron X-Ray Data from Al2O3. *Journal of Applied Crystallography* **1987**, *20* (2), 79–83. https://doi.org/10.1107/S0021889887087090.

(244)Warren, B. E. *X-Ray Diffraction*; Courier Corporation, 2012.

(245)Juan Rodríguez-Carvajal. Recent Advances in Magnetic Structure Determination by Neutron Powder Diffraction. *Physica B : Condensed Matter* **1993**, *1–2* (192), 55–69. https://doi.org/10.1016/0921-4526(93)90108-I.

(246)Gravereau, P. Introduction à la pratique de la diffraction des rayons X par les poudres. 210.

(247)Kasnatscheew, J.; Streipert, B.; Röser, S.; Wagner, R.; Cekic Laskovic, I.; Winter, M. Determining Oxidative Stability of Battery Electrolytes: Validity of Common Electrochemical Stability Window (ESW) Data and Alternative Strategies. *Phys. Chem. Chem. Phys.* **2017**, *19* (24), 16078–16086. https://doi.org/10.1039/C7CP03072J.

(248)Tan, D. H. S.; Wu, E. A.; Nguyen, H.; Chen, Z.; Marple, M. A. T.; Doux, J.-M.; Wang, X.; Yang, H.; Banerjee, A.; Meng, Y. S. Elucidating Reversible Electrochemical Redox of Li6PS5Cl Solid Electrolyte. *ACS Energy Lett.* **2019**, *4* (10), 2418–2427. https://doi.org/10.1021/acsenergylett.9b01693.

(249)Méry, A.; Rousselot, S.; Lepage, D.; Dollé, M. A Critical Review for an Accurate Electrochemical Stability Window Measurement of Solid Polymer and Composite Electrolytes. *Materials* **2021**, *14* (14), 3840. https://doi.org/10.3390/ma14143840.

(250)Zhu, Y.; He, X.; Mo, Y. Origin of Outstanding Stability in the Lithium Solid Electrolyte Materials: Insights from Thermodynamic Analyses Based on First-Principles Calculations. *ACS Appl. Mater. Interfaces* **2015**, *7* (42), 23685–23693. https://doi.org/10.1021/acsami.5b07517.

(251)Hernández, G.; Johansson, I. L.; Mathew, A.; Sångeland, C.; Brandell, D.; Mindemark, J. Going Beyond Sweep Voltammetry: Alternative Approaches in Search of the Elusive Electrochemical Stability of Polymer Electrolytes. *J. Electrochem. Soc.* **2021**, *168* (10), 100523. https://doi.org/10.1149/1945-7111/ac2d8b.

(252)*Handbook of Reference Electrodes*; Inzelt, G., Lewenstam, A., Scholz, F., Eds.; Springer Berlin Heidelberg: Berlin, Heidelberg, 2013. https://doi.org/10.1007/978-3-642-36188-3.

(253)Grenier, A.; Porras Gutierrez, A. G.; Groult, H.; Dambournet, D. Modified Coin Cells to Evaluate the Electrochemical Properties of Solid-State Fluoride-Ion Batteries at 150°C. *Journal of Fluorine Chemistry* **2016**, *191*, 23–28. https://doi.org/10.1016/j.jfluchem.2016.09.006.

(254)Barcha, C. Étude de la stabilité des interfaces dans les batteries tout-solide au lithium. phdthesis, Université de Picardie Jules Verne, 2021. https://theses.hal.science/tel-03945249 (accessed 2023-05-23).

(255)Koshikawa, H.; Matsuda, S.; Kamiya, K.; Miyayama, M.; Kubo, Y.; Uosaki, K.; Hashimoto, K.; Nakanishi, S. Dynamic Changes in Charge-Transfer Resistance at Li Metal/Li7La3Zr2O12 Interfaces during Electrochemical Li Dissolution/Deposition Cycles. *Journal of Power Sources* **2018**, *376*, 147–151. https://doi.org/10.1016/j.jpowsour.2017.11.082.

(256)Kasemchainan, J.; Zekoll, S.; Spencer Jolly, D.; Ning, Z.; Hartley, G. O.; Marrow, J.; Bruce, P. G. Critical Stripping Current Leads to Dendrite Formation on Plating in Lithium Anode Solid Electrolyte Cells. *Nat Mater* **2019**, *18* (10), 1105–1111. https://doi.org/10.1038/s41563-019-0438-9.

(257)Schweidler, S.; de Biasi, L.; Schiele, A.; Hartmann, P.; Brezesinski, T.; Janek, J. Volume Changes of Graphite Anodes Revisited: A Combined Operando X-Ray Diffraction and In Situ Pressure Analysis Study. *J. Phys. Chem. C* **2018**, *122* (16), 8829–8835. https://doi.org/10.1021/acs.jpcc.8b01873.

(258)de Biasi, L.; Schiele, A.; Roca-Ayats, M.; Garcia, G.; Brezesinski, T.; Hartmann, P.; Janek, J. Phase Transformation Behavior and Stability of LiNiO2 Cathode Material for Li-Ion Batteries Obtained from In Situ Gas Analysis and Operando X-Ray Diffraction. *ChemSusChem* **2019**, *12* (10), 2240–2250. https://doi.org/10.1002/cssc.201900032.

(259)Zagorac, D.; Müller, H.; Ruehl, S.; Zagorac, J.; Rehme, S. Recent Developments in the Inorganic Crystal Structure Database: Theoretical Crystal Structure Data and Related Features. *J Appl Cryst* **2019**, *52* (5), 918–925. https://doi.org/10.1107/S160057671900997X.

(260)Jain, A.; Ong, S. P.; Hautier, G.; Chen, W.; Richards, W. D.; Dacek, S.; Cholia, S.; Gunter, D.; Skinner, D.; Ceder, G.; Persson, K. A. Commentary: The Materials Project: A Materials Genome Approach to Accelerating Materials Innovation. *APL Materials* **2013**, *1* (1), 011002. https://doi.org/10.1063/1.4812323.

(261)Chouvin, J.; Pérez Vicente, C.; Olivier-Fourcade, J.; Jumas, J.-C.; Simon, B.; Biensan, P. Deeper Insight on the Lithium Reaction Mechanism with Amorphous Tin Composite Oxides. *Solid State Sciences* **2004**, *6* (1), 39–46. https://doi.org/10.1016/j.solidstatesciences.2003.10.012.

(262)Flatscher, F.; Philipp, M.; Ganschow, S.; R. Wilkening, H. M.; Rettenwander, D. The Natural Critical Current Density Limit for Li 7 La 3 Zr 2 O 12 Garnets. *Journal of Materials Chemistry A* **2020**, *8* (31), 15782–15788. https://doi.org/10.1039/C9TA14177D.

(263)Zhao, F.; Sun, Q.; Yu, C.; Zhang, S.; Adair, K.; Wang, S.; Liu, Y.; Zhao, Y.; Liang, J.; Wang, C.; Li, X.; Li, X.; Xia, W.; Li, R.; Huang, H.; Zhang, L.; Zhao, S.; Lu, S.; Sun, X. Ultrastable Anode Interface Achieved by Fluorinating Electrolytes for All-Solid-State Li Metal

Batteries. *ACS Energy Lett.* **2020**, *5* (4), 1035–1043. https://doi.org/10.1021/acsenergylett.0c00207.

(264)Binninger, T.; Marcolongo, A.; Mottet, M.; Weber, V.; Laino, T. Comparison of Computational Methods for the Electrochemical Stability Window of Solid-State Electrolyte Materials. *Journal of Materials Chemistry A* **2020**, *8* (3), 1347–1359. https://doi.org/10.1039/C9TA09401F.

(265)Yang, Y.; Wu, Q.; Cui, Y.; Chen, Y.; Shi, S.; Wang, R.-Z.; Yan, H. Elastic Properties, Defect Thermodynamics, Electrochemical Window, Phase Stability, and Li+ Mobility of Li3PS4: Insights from First-Principles Calculations. *ACS Appl. Mater. Interfaces* **2016**, *8* (38), 25229–25242. https://doi.org/10.1021/acsami.6b06754.

(266)Schwietert, T. K.; Arszelewska, V. A.; Wang, C.; Yu, C.; Vasileiadis, A.; de Klerk, N. J. J.; Hageman, J.; Hupfer, T.; Kerkamm, I.; Xu, Y.; van der Maas, E.; Kelder, E. M.; Ganapathy, S.; Wagemaker, M. Clarifying the Relationship between Redox Activity and Electrochemical Stability in Solid Electrolytes. *Nature Materials* **2020**, *19* (4), 428–435. https://doi.org/10.1038/s41563-019-0576-0.

(267)Mohammad, I.; Witter, R.; Fichtner, M.; Reddy, M. A. Introducing Interlayer Electrolytes: Toward Room-Temperature High-Potential Solid-State Rechargeable Fluoride Ion Batteries. *ACS Appl. Energy Mater.* **2019**, *2* (2), 1553–1562. https://doi.org/10.1021/acsaem.8b02166.

(268)Boultif, A.; Louër, D. Powder Pattern Indexing with the Dichotomy Method. *J Appl Cryst* **2004**, *37* (5), 724–731. https://doi.org/10.1107/S0021889804014876.

(269)Kokunov, Yu. V.; Detkov, D. G.; Gorbunova, Yu. E.; Ershova, M. M.; Mikhailov, Yu. N. Synthesis and Crystal Structure of Calcium Trifluorostannate(II). *Doklady Chemistry* **2001**, *376* (4/6), 52–54. https://doi.org/10.1023/A:1018855109716.

(270)Bell, M. F.; DéNés, G.; Zhu, Z. Ionic Conductivity of the New Fluoride-Ion Conductor Casn2F6. *MRS Online Proceedings Library (OPL)* **2002**, *756*. https://doi.org/10.1557/PROC-756-EE3.5.

Résumé

Les batteries à ions fluors sont une nouvelle alternative aux batteries à ions lithium, introduite en 2011, dans lesquelles le Fluor est utilisé comme porteur de charge. Ces systèmes entrent dans la catégorie des batteries tout solides, c'est-à-dire que leur électrolyte est un matériau solide, ce qui induit un gain en sécurité, ainsi qu'en densité d'énergie. Le meilleur conducteur d'ion fluor connu à ce jour est $PbSnF_4$, et son isomorphe $BaSnF_4$ est lui aussi un excellent conducteur ionique. Dans cette thèse, nous explorons divers aspects de la famille de matériaux de structure $MSnF_4$. Tout d'abord, le polymorphe cubique de formule $BaSnF_4$ est étudié. Il est montré que cette structure est désordonnée et complexe. On met en lumière le mécanisme de transport ionique, qui repose fortement sur la présence d'étain dans la structure fluorite. Un nouvel isomorphe, $SrSnF_4$, est reporté pour la première fois, et l'étude des solutions solides $Ba_{1-x}Sr_xSnF_4$ permet de quantifier les effets de volume pour ces phases. La phase tétragonale, la plus conductrice, est ensuite examinée. Deux nouvelles voies de synthèses pour $BaSnF_4$ sont proposées. Les propriétés de stabilité électrochimique de ces produits sont ensuite explorées. Cette étude fournit des renseignements clés sur l'utilisation potentielle future du $BaSnF_4$ dans les batteries à ions de fluorure.

Summary

A new alternative to lithium ion batteries, introduced in 2011, is a system using fluoride as a charge carrier: fluoride ion batteries. These systems fall into the category of all-solid-state batteries, meaning that their electrolyte is a solid material, which induces a gain in safety, as well as in energy density. The best-known fluoride ion conductor to date is $PbSnF_4$, and its isomorph $BaSnF_4$ is the second best. In this thesis, we explore various aspects of the $MSnF_4$ family. First, the $BaSnF_4$ cubic polymorph is studied. It is shown that this structure is extremely disordered and complex. The ionic transport mechanism is demonstrated to be heavily on the presence of tin in the fluorite structure. A new isomorph, $SrSnF_4$, is reported for the first time, and the study of solid solutions $Ba_{1-x}Sr_xSnF_4$ allows for quantification of the effects of volume change in these phases. The tetragonal phase, which is most conductive, is then examined. Two new synthesis pathways for $BaSnF_4$ are proposed, both yielding a pure product and improving the conductivity, reaching up to 5.10^{-3} $S.cm^{-1}$. The electrochemical stability of these products is then explored. This study provides key information for future potential use of $BaSnF_4$ in fluoride ion batteries.